UNIVERSITY OF SOUTHAMPTON

FACULTY OF PHYSICAL AND APPLIED SCIENCES

Optoelectronics Research Centre

Novel Toroidal and Superconducting Metamaterials

Vassili Savinov

Thesis for the degree of Doctor of Philosophy

January 2014

UNIVERSITY OF SOUTHAMPTON

ABSTRACT

FACULTY OF PHYSICAL AND APPLIED SCIENCES

OPTOELECTRONICS RESEARCH CENTRE

Doctor of Philosophy

NOVEL TOROIDAL AND SUPERCONDUCTING METAMATERIALS

by Vassili Savinov

This thesis reports on new solutions for sensing and controlling the electromagnetic radiation, and explores some novel effects of electrodynamics, using metamaterials.

I have demonstrated the first superconducting metamaterial-based electro-optical modulator controlled by passing current through the network of meta-molecules. The metamaterial, fabricated out of thin niobium film, modulated the sub-terahertz radiation through magnetic-field-induced suppression of superconductivity as well as through thermal effect. Transmission modulation up to 45% has been observed and main mechanisms of modulation have been studied.

I have demonstrated a resonant radiation-harvesting bolometer for the sub-terahertz frequency range using a superconducting metamaterial fabricated out of thin niobium film. The strong electromagnetic interactions between the meta-molecules allowed harnessing of the radiation incident on the metamaterial and channeling it into a small radiation sensor, thus boosting the device sensitivity and selectivity. Bolometer sensitivity bandwidth of 1% has been achieved.

I have suggested and experimentally demonstrated a new type of quantum metamaterial that engages the quantization of magnetic flux trapped in the meta-molecules. The metamaterial, fabricated out of high-temperature superconductor YBCO, has been designed to display nonlinear response associated with switching between the magnetic flux states. Although switching experiments have not been performed, a detailed characterization of the metamaterial, including the study of superconducting metamaterial structures that model different switching states, has been conducted.

I have, for the first time, investigated highly nonlinear superconducting sub-terahertz metamaterial that exploits critical current and thermal nonlinearity. The metamaterial was fabricated out of thin niobium film with every meta-molecule containing wire segments of nanoscale thickness. The transmission change of up to 13% has been observed in response to ramping up the intensity of incident radiation to $8\,\mathrm{W/m^2}$.

I have developed a novel analytical formalism that, for the first time, linked the reflection and the transmission of the metamaterial with the microscopic multipole excitations taking into account the electric, magnetic and toroidal multipoles of the constituent meta-molecules. A planar superconducting metamaterial with strong toroidal dipole response has been fabricated to test the formalism experimentally, and a very good agreement between the experiment and the analytical predictions has been observed.

I have, for the first time, numerically and analytically studied the non-radiating configuration observed in the microwave experiment with the toroidal void metamaterial. It has been found that the non-radiating configuration is non-trivial and results from the destructive interference between the co-located electric and toroidal dipoles. Such non-radiating configurations shall allow designing high-Q metamaterial resonances and the generation of oscillating vector-potential for the study of the time-dependent Aharonov-Bohm effect.

Contents

List of Figures

List of Tables

DECLARATION OF AUTHORSHIP

I, Vassili Savinov, declare that the thesis entitled "Novel Toroidal and Superconducting Metamaterials" and the work presented in the thesis are both my own, and have been generated by me as the result of my own original research. I confirm that:

- this work was done wholly or mainly while in candidature for a research degree at this University;
- where any part of this thesis has previously been submitted for a degree or any other qualification at this University or any other institution, this has been clearly stated;
- where I have consulted the published work of others, this is always clearly attributed;
- where I have quoted from the work of others, the source is always given. With the exception of such quotations, this thesis is entirely my own work;
- I have acknowledged all main sources of help;
- where the thesis is based on work done by myself jointly with others, I have made clear exactly what was done by others and what I have contributed myself;
- parts of this work have been published as the journal papers and conference contributions listed in Appendix O.

Signed: _____

Date: _____

Acknowledgments

I am grateful to Prof. N. I. Zheludev for his advice, guidance and patience during my studies, as well as for all the opportunities he has given me over these years. I am also grateful to Prof. P. A. J. de Groot who has been my co-supervisor during the first half of my studies and has given me plenty of advice and unique insights into fields of superconductivity and magnetism. I deeply indebted to Dr. V. A. Fedotov for all his help and many discussions that helped me to become a better researcher. I am very grateful to Dr. K. Delfanazari for his insightful suggestions and comments regarding my work. I am also very grateful to Dr. A. R. Buckingham and Dr. A. Tsiatmas for teaching me a lion's share of the experimental techniques I have used over the course of my doctoral work. I would like to thank all students and academics in the Nanophotonics group for their help on innumerable occasions when I needed advice or just someone to talk to.

I would like to thank my family and my friends for their support during my studies.

Finally, but very importantly, I would like to thank my beautiful wife Aigul, for all the love and support she has given me ever since I met her, and as of recently, for my wonderful son Danyal.

Chapter 1

Introduction

1.1 Motivation

Sensing, routing and manipulating the electromagnetic radiation lies at the heart of modern science and technology. Over the past century, various materials and material composites have been studied and successfully adopted for the ever increasing degree of control over the electromagnetic waves, providing us with everything from consumer electronics and internet, to Large Hadron Collider. Metamaterials represent a next step in this evolution.

Before proceeding it is necessary to define the term 'metamaterial'. The (electromagnetic) metamaterials are arrays[1] of man-made structures tailored to exhibit a desired electromagnetic response [1]. The size and the spacing of the basic building blocks of the metamaterials, the meta-molecules, are always chosen to be sufficiently smaller than the wavelength of the driving electromagnetic excitations, which ensures that metamaterials respond as homogeneous electromagnetic media, or homogenous boundaries (in case of two-dimensional metamaterials).

Whilst the topic of man-made sub-wavelength composites can be traced back to J. C.

[1]The arrays can be periodic or random [2]. Three-, two- or even one-dimensional arrays have been referred to as metamaterials by various researchers [3].

Figure 1.1: ***Early examples of millimeter-wave 'metamaterials' created by J. C. Bose [4, 5].*** ***(a)*** *Linear polarizer made from a book with inserted sheets of tin-foil.* ***(b)*** *Polarization rotator made from twisted jute.*

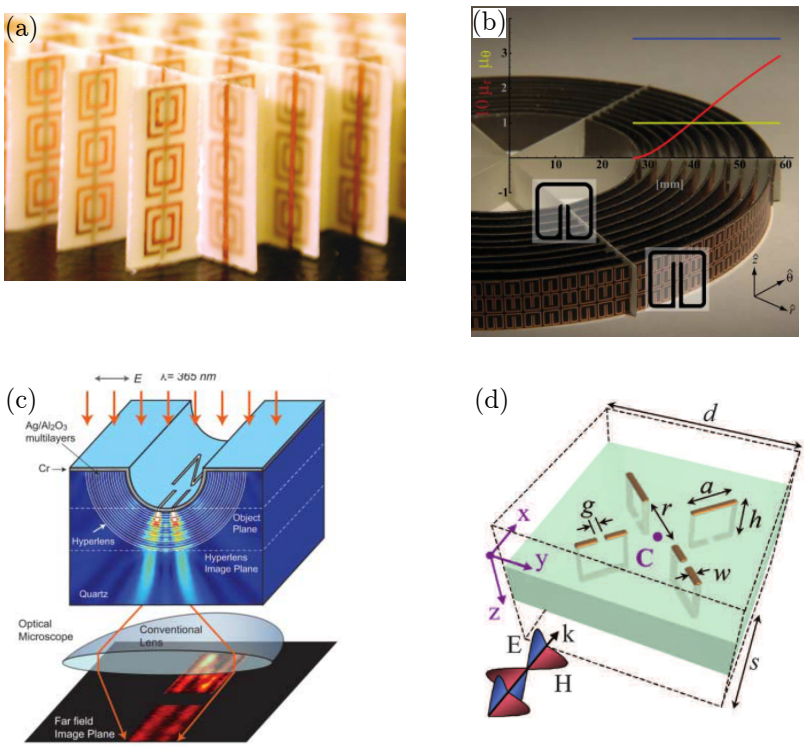

Figure 1.2: ***Selected examples of the metamaterial research in the fundamental electrodynamics.*** ***(a)*** *First demonstration of a medium with negative refractive index [7].* ***(b)*** *First metamaterial invisibility cloak for the microwave spectrum [11].* ***(c)*** *First demonstration of the sub-diffraction imaging with metamaterial hyperlens [16].* ***(d)*** *First demonstration of the toroidal dipole excitation in a toroidal metamaterial [17].*

Bose [4, 5] (also see Fig. 1.1), the modern field of electromagnetic metamaterials began, arguably, with the experimental demonstration of the left-handed metamaterial [6, 7] (Fig. 1.2a), i.e. a metamaterial with simultaneously negative permittivity and permeability, and, consequently, a negative index of refraction[2]. Since then the field of metamaterial research has been growing rapidly facilitating the exploration of fundamental electrodynamic phenomena, such as cloaking[3] [10–12] (Fig. 1.2b), superlenses [13, 14], hyperlenses [15, 16] (Fig. 1.2c) and the toroidal metamaterials [17] (Fig. 1.2d). At the same time, the metamaterial research has provided a wealth of practical solutions[4], for radiation generation [23] (Fig. 1.3a), modulation [24] (Fig. 1.3b), sensing [25] (Fig. 1.3c) and nonlinear electromagnetic response [26] (Fig. 1.3d).

This thesis aims to add to both strands of metamaterial research with demonstration of new ways to sense and modulate the sub-terahertz radiation using superconducting metamaterials (Chap. 3), as well as exploiting metamaterials to shed new light on the electrodynamics of the toroidal dipole excitations (Chap. 4) and on the quantization of

[2]The basic properties of the left-handed electromagnetic media have been explored theoretically by V. G. Veselago as far back as 1967 [8], but without offering a concrete physical example of a left-handed electromagnetic medium.

[3]It should be noted that electromagnetic cloaking has been already discussed in 1961 by L. S. Dolin [9].

[4]Practical applications of metamaterials are now a vast and growing area of research, so only selected references are presented here. For a more detailed overview see reviews in Refs. [1, 18–22]

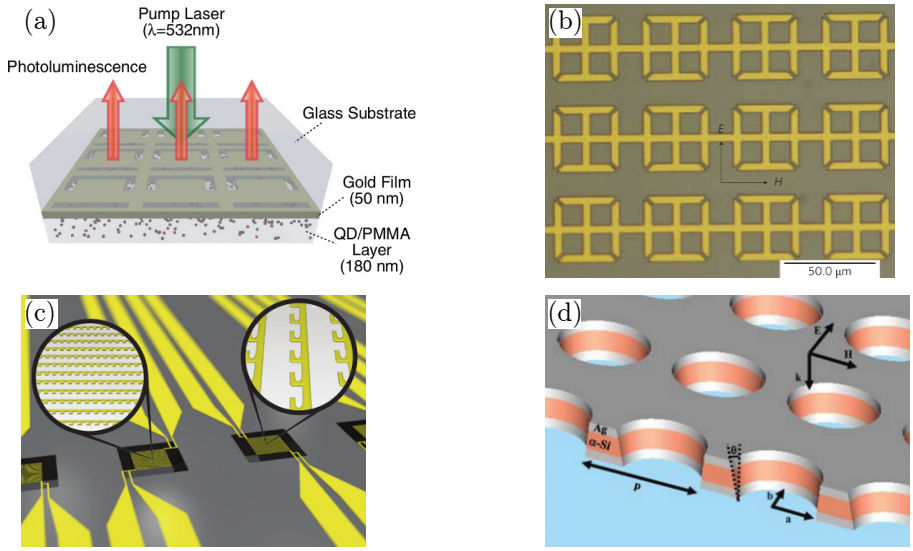

Figure 1.3: ***Selected examples of the metamaterial research in the applied electrodynamics.*** ***(a)*** *Experimental demonstration of the near-infrared plasmonic metamaterial enhancing the luminescence of the quantum dots through the Purcell effect [23].* ***(b)*** *Electrically controlled terahertz metamaterial modulator based on charge carrier injection into semiconducting substrate [24].* ***(c)*** *Metamaterial metal-based near-infrared bolometer [25].* ***(d)*** *Near-infrared fishnet metamaterial with sub-picosecond nonlinear response due to fast carrier dynamics in the semiconductor substrate [26].*

magnetic flux in superconductors (Chap. 5). The rest of this chapter will provide brief introduction into the field of superconductivity (Sec. 1.2) which will play an important role for the rest of the thesis. The chapter ends with an overview of the thesis structure, in Sec. 1.3.

1.2 Introduction to superconductivity

This section gives a brief introduction into the topic of superconductivity, more in-depth introductions can be found in Refs. [27, 28].

1.2.1 Basic properties

The superconductivity was discovered by H. K. Onnes in 1911 [28]. He and his team have noticed that the resistance of mercury vanished abruptly when it was cooled down to the boiling temperature of helium. This is one of the hallmarks of the superconductivity, common to all superconductors: the resistance to the direct electrical currents (DC-resistance) is zero[5] below the critical (transition) temperature (assuming no applied magnetic field).

Another hallmark of the superconductivity is the exclusion of the sufficiently weak magnetic fields by the superconductors - the Meissner-Ochsenfeld effect [28]. Inside the

[5]The lower bound for the characteristic decay time of (direct) currents in superconductors has been estimated to lie around 10^5 years [27].

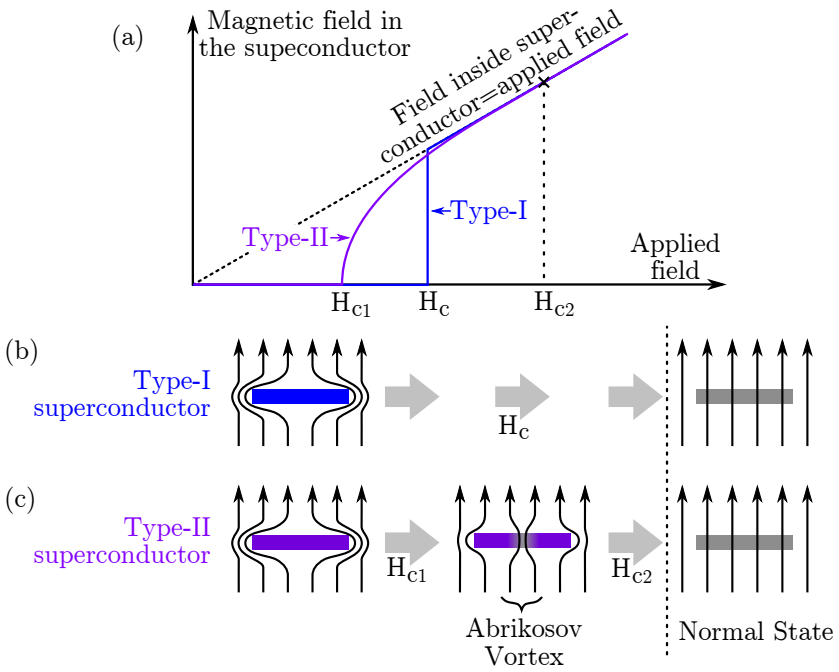

Figure 1.4: ***Screening of external (static) magnetic fields by the superconductors.*** ***(a)*** *Magnetic field inside the superconductor as a function of applied magnetic field. Type-I superconductors (blue curve) fully screen the applied field until its magnitude reaches the thermodynamic critical field (H_c) at which point the material enters the normal state and the applied field penetrates the sample completely. Type-II superconductors (violet curve) screen all applied field until it reaches lower critical field (H_{c1}). Above H_{c1}, the applied field begins to partially penetrate the superconductor in form of Abrikosov vortices. More and more vortices enter the superconductor as the applied field is increased. Once it reaches the upper critical field (H_{c2}) the material enters the normal state (applied field fully penetrates the sample).* ***(b)-(c)*** *Schematic illustrations of the screening of the applied field (vertical arrows) by the type-I (b) and type-II (c) superconductors.*

superconductors, the strength of any (weak) externally applied magnetic field decays exponentially on the scale of the penetration depth (λ; typically tens to hundreds of nanometers) due to screening by the loss-less electrical currents. The applied field is screened from the bulk of the superconductor both if the magnetic field is applied to the already superconducting sample, as well as if the sample in the normal state is first placed into the magnetic field and only then cooled down to superconductivity temperature. The appearance of the screening currents (to screen external magnetic field) upon the transition into the superconducting state shows that superconductors are different from perfect electrical conductors[6] (conductors with infinite conductivity) and that superconductivity is a distinct thermodynamic phase with internal energy depending on temperature as well as on the external magnetic field.

The superconductors[7] are divided into type-I and type-II superconductors depending

[6]Perfect electrical conductors, i.e. conductors with infinite (real-valued) conductivity, would prevent magnetic field within the sample from changing, but it could be non-zero. In case of superconductors, the magnetic field in the bulk of the material is always zero (provided the fields are sufficiently weak).

[7]There also exists a class of the so-called '1.5-superconductors', such as magnesium di-borade [29], which behave as both type-I and type-II superconductors, but on different scales. This is an active area

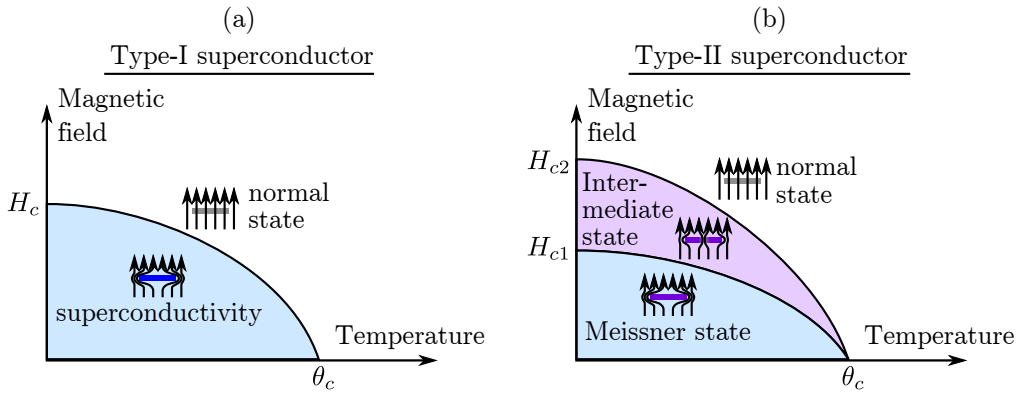

Figure 1.5: ***Phase diagram of the superconducting and the normal states as a function of temperature and applied magnetic field.*** ***(a)*** *Type-I superconductors.* ***(b)*** *Type-II superconductors. Intermediate state is also called the vortex state. Critical temperature is denoted with θ_c.*

on their behavior in strong magnetic fields. Figure 1.4a shows how the magnetic field inside the superconductors changes as a function of applied (static) field.

In case of type-I superconductors, the applied magnetic field with magnitude below the thermodynamic critical field (H_c) will be fully screened from within the superconductor. For higher applied fields the superconductivity will be suppressed and the material will enter the normal state thus allowing the applied field to fully penetrate into the sample. See Fig. 1.4b.

In case of type-II superconductors, the applied field will be fully screened until its magnitude reaches the lower critical field (H_{c1}). Above this value, the applied field will begin to partially penetrate the sample by creating highly regular domains of the material in the normal state within the otherwise superconducting sample. The domains in normal state are called the Abrikosov vortices [28], the magnetic flux threading each Abrikosov vortex is equal to a single flux quantum $\Phi_0 = h/2e \approx 2.07\,\mathrm{Wb}$ (h-Planck constant, e-electron charge). As the applied field is increased, more and more vortices will enter the sample. Finally, when the magnitude of the applied field will reach the upper critical field (H_{c2}), the *entire* material will enter the normal state, allowing the applied field to fully penetrate into it. See Fig. 1.4c.

Paradoxically, the thermodynamic critical field H_c is not related to the magnitude of the applied field. Instead, it is the measure of the difference in (Helmholtz) free energy between the material in the normal state and in the superconducting state. Consequently, H_c can be defined for both type-I and type-II superconductors. The relation between the measurable critical fields and the thermodynamic critical field of the type-II superconductors is often approximated by $H_c \approx \sqrt{H_{c1} \cdot H_{c2}}$ [27].

In almost all superconductors[8] the critical magnetic fields (H_c, H_{c1}, H_{c2}) are suppressed when temperature of the superconductor is increased, as is shown in Fig. 1.5a,b.

of research.

[8] In some exotic superconductors, such as rare-earth nickel boride carbides, increasing temperature may lead to increase in the critical magnetic field [30].

A common empirical approximation used to describe the relationship between the temperature (θ) and thermodynamic critical field is $H_c(\theta) = H_c(0) \cdot \left(1 - (\theta/\theta_c)^2\right)$, where θ_c is the critical temperature of the superconductor.

1.2.2 Critical current density

One of the most useful properties of superconductors is the ability to carry (direct) electrical currents without the Ohmic losses[9]. In practice, the superconductors can carry loss-less currents only as long as the currents are sufficiently small. Currents above the critical value suppress the superconductivity, and result in the re-appearance of the Ohmic losses. A common way to describe the current-carrying ability of superconductors is through the critical current density (J_c) [27].

As dictated by Ampère's law, current-carrying wire must be penetrated by magnetic field (created by the carried current). In case of type-I superconductors, this implies that the loss-less currents can be carried only in the surface layer of thickness of order of the penetration depth, since magnetic field cannot penetrate any deeper (Meissner-Ochsenfeld effect). The critical current density of type-I superconductors is therefore related to the thermodynamic critical field ($\mathbf{H}_c$).

Type-II superconductors can, in contrast, carry current in their bulk by allowing the magnetic field to penetrate the wire in form of Abrikosov vortices (see Fig. 1.4c). The current flowing through the type-II superconductor will exert Lorentz force on the vortices [27]. If the vortices move under the action of this force, there will be energy dissipation, which will cause superconductor to exhibit Ohmic losses despite remaining (partially) superconducting. The displacement of vortices can be eliminated by providing pinning sites, such as impurities and crystal lattice dislocations within the superconducting wire, that will hold the vortices in place. This is called *vortex pinning* [27]. As long as vortex pinning is strong enough to withstand the Lorentz force due to flowing current, the type-II superconductor will carry loss-less currents. Once the vortices start to move, the superconductor will seize to be loss-less. For this reason, the critical current in type-II superconductors is related to the strength of vortex pinning. All applications of superconductors that require carrying high loss-less (persistent) currents rely on type-II superconductors with strong vortex pinning [31].

1.2.3 Macroscopic quantum state

The third hallmark of the superconductivity is the macroscopic quantum state of the charge carriers. As dictated by the celebrated BCS microscopic theory of superconductivity [32], named after its co-inventors Bardeen, Cooper and Schrieffer, the electrons inside the superconductors occupy the ground state in pairs (Cooper pairs). Excitation of an electron inside the superconductor from the ground state requires a finite energy

[9] Oscillating currents are however subject to Ohmic losses even in superconductors.

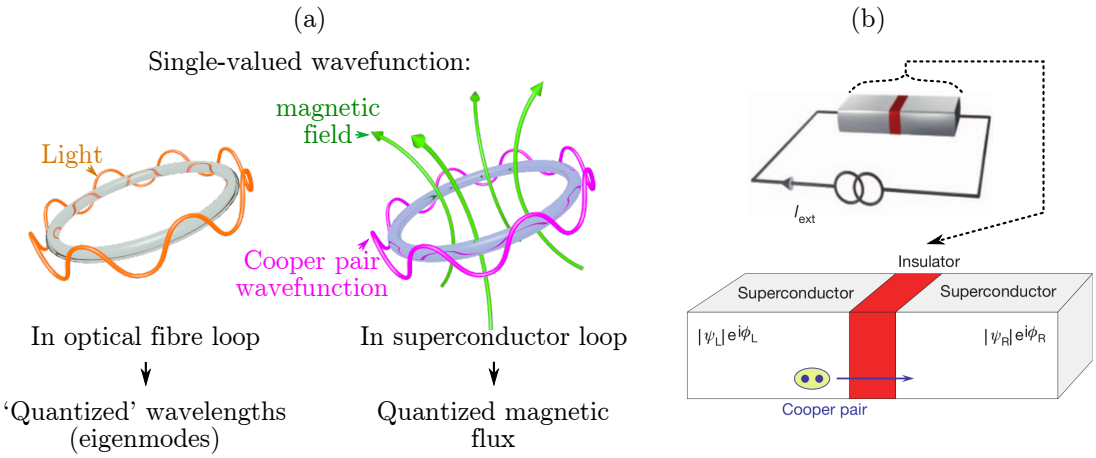

Figure 1.6: ***Phenomena related to macroscopic quantum state in superconductors.*** ***(a)*** *Requirement for single-valued Cooper pair wavefunction in a closed loop of superconducting wire (multiply connected superconductor), leads to quantization of magnetic flux through the loop. Similar mathematics lead to appearance of eigenmodes in a closed loop of optical fibre, i.e. quantized wavelengths of light allowed to propagate inside the fibre (e.g. Ref. [36]).* ***(b)*** *The interference between the Cooper pair wavefunctions on the different sides of the insulator barrier in the Josephson junction leads to highly nonlinear electric response (of the junction) [37].*

2Δ, which is known as superconducting energy gap and typically lies in the region[10] 1-60 meV. As a result of the existence of superconducting gap, the electrons in the superconducting ground state do not experience scattering by thermal excitations and impurities as long as the potential increase in electron energy, due to scattering, is less than 2Δ. Consequently, loss-less electrical currents can flow within the superconductors.

It is convenient to regard each Cooper pair as a single particle. Cooper pairs are made up of two electrons with opposite one-half spin ($S = \frac{1}{2}$), consequently the net spin of the pair is integer[11]. Cooper pairs can thus be treated as bosons. Inside the superconductors, all Cooper pairs condense into a macroscopic ground state and can *all* be described by a *single* (pseudo-) wavefunction[12]. The single macroscopic quantum state of the Cooper pairs leads to non-local electrodynamics within the superconductors, characterized by the coherence length[13] (ξ). Furthermore, the requirement for the wavefunction of all Cooper pairs to be single-valued leads to quantization of magnetic flux in multiply-connected superconductors[14] (see Fig. 1.6a).

One of the most striking consequences of the macroscopic quantum state of the Cooper pairs is the Josephson effect [27, 41], which describes how the Cooper pairs will

[10] Classical superconductors, discovered before 1980s, have energy gaps (2Δ) of just few meV [33]. Energy gaps (2Δ) higher than 10 meV are found in high-temperature superconductors, such as YBCO [34] and BSCCO [35].

[11] The net spin of each Cooper pair is zero in most superconductors, but some exotic superconductors such as UPt_3 [38] and Sr_2RuO_4 [39], have been demonstrated to have Cooper pairs with unit spin (S=1).

[12] This is the approach of the phenomenological Ginzburg-Landau theory, that has been shown to be a valid approximation of the more general BCS theory [27].

[13] Coherence length can be larger than micro-meter for some type-I superconductors such as Aluminium [33], or as small as few nano-meters for high-temperature superconductors [40].

[14] The topic of flux quantization will be discussed in more detail in Chap. 5.

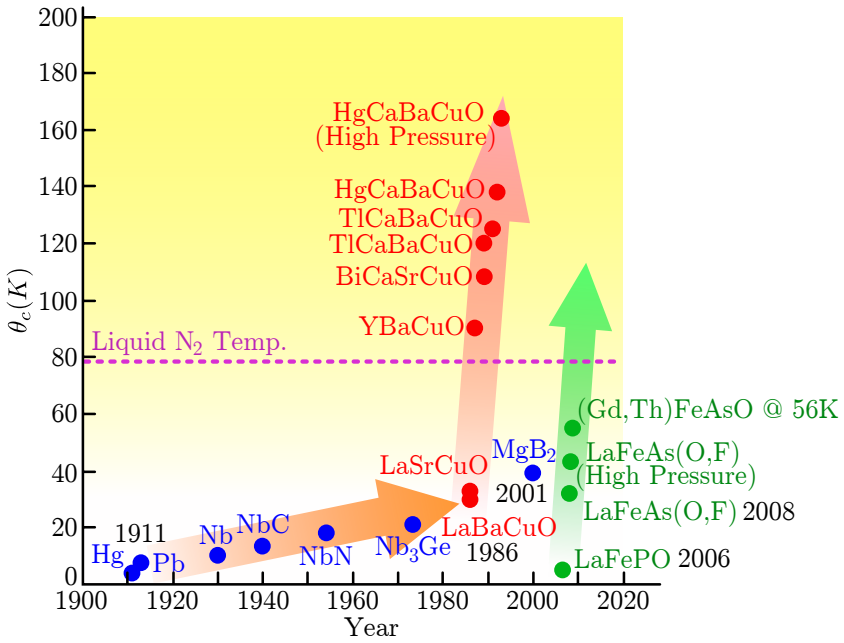

Figure 1.7: ***Rise in critical temperature of the superconductors over the past century.*** *The conventional superconductors are shown in blue, the cuprate high-temperature superconductors are shown in red, whilst pnictide (iron-based) superconductors are shown in green. An important mile-stone in the growth of superconducting critical temperature was the boiling point of liquid nitrogen (at 77 K), shown with the dashed horizontal line (pink). The image has been adopted from Ref. [42].*

tunnel through a small (thinner than the coherence length) junction made from a dielectric (or normal metal) barrier in the superconducting wire - the Josephson junction (see Fig. 1.6b). The current flowing through such a junction shows effects of the interference of the Cooper pair wavefunctions on either side of the junction, resulting in rich nonlinear behavior that now forms the basis of superconducting electronics [33, 41].

1.2.4 High-temperature superconductors

Figure 1.7 shows the growth of the maximum critical temperature of the superconductors over the last century [42]. The superconductors discovered before the 1980s are commonly called conventional, classical or low-temperature superconductors. The properties of the conventional superconductors have been successfully described by the BCS theory and are now well understood.

In 1986, Bednorz and Müller have discovered superconductivity with unusually high critical temperature in lanthanum-barium-copper-oxide or 'LBCO'. Their results were soon corroborated by other experimenters [42]. Further research into different cuprates, i.e. materials containing copper-oxide planes, lead to a wealth of new and exotic superconductors and sparked a rapid growth in the critical temperature of the superconductivity (see Fig. 1.7) [27, 42]. More recently, a new family of iron-based superconductors (pnictides) has been discovered and is now an active area of research [42].

High-temperature superconductivity remains an attractive field of research both due

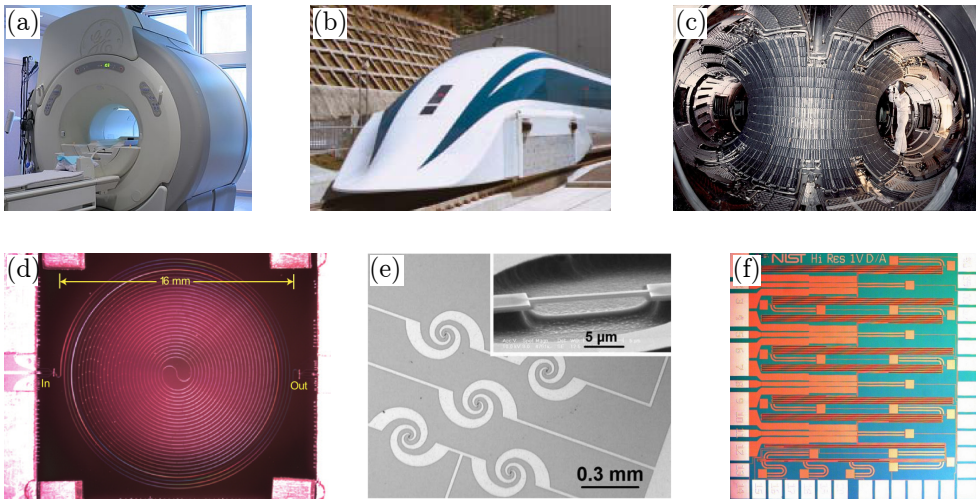

Figure 1.8: ***Selected applications of superconductors.*** ***(a)*** *Magnetic resonance imaging [43].* ***(b)*** *Superconducting maglev (magnetic levitation) train [44].* ***(c)*** *Tore Supra. Tokamak designed for nuclear fusion research (superconducting magnets are used to confine hot plasma) [45].* ***(d)*** *Low-noise superconducting microwave amplifier [46].* ***(e)*** *Terahertz-range superconducting bolometer (radiation sensor) [47].* ***(f)*** *Voltage standard based on Josephson effect [48].*

to great practical advantage of loss-less conduction at high temperature, but also because of rich and complicated behavior on the microscopic scale that gives rise to high-temperature superconductivity. At the moment of writing this thesis, there is no general microscopic theory of high-temperature superconductivity [42], however many properties of the high-temperature superconductors can be explained within the context of suitably modified BCS theory [27].

1.2.5 Applications of superconductors

The unique properties of superconductors make them ideally suited for a range of applications despite the need for cryogenic cooling. The three features of superconducting state that are utilized for the applications are the ability to carry persistent currents (zero DC-losses), low Joule losses and nonlinear response to currents oscillating at frequencies below the energy gap (up to terahertz range), and the Josephson effect.

The ability of superconductors to carry persistent currents without the Joule losses has been utilized to create powerful magnets that are necessary for magnetic resonance imaging (see Fig. 1.8a), levitating trains (see Fig. 1.8b) and plasma confinement (see Fig. 1.8c). Invention of the high-temperature cuprates, that could be cooled with much cheaper and more abundant liquid nitrogen, has also made it economically feasible to use superconductors for the distribution of electrical power [42].

Superconductors exhibit low losses and high nonlinearities in the radio and microwave spectra, which facilitates their use in high-quality resonators [49], and nonlinear devices such as amplifiers (see Fig. 1.8d). The transition from the superconducting to normal state is commonly accompanied by a large change in electrical resistance due to

small change in the temperature of the material. This property is routinely utilized for creation of highly-sensitive superconducting radiation detectors (see Fig. 1.8e; also see Ref. [50]).

The Josephson effect demonstrates the quantum mechanical interference of the charge carriers on the macroscopic scale, and can be used to create extremely accurate magnetometers [33,41], artificial atoms [37,51] as well as voltage standards based on frequency (see Fig. 1.8f). Furthermore, the Josephson junctions constitute the fundamental nonlinear components in the superconducting electronics, allowing to implement such basic electronic macro-components as amplifiers and frequency mixers [41].

A detailed review of the popular applications of the superconductors can be found in Ref. [42].

1.2.6 Superconductors used in this thesis: YBCO and niobium

In this thesis, the metamaterials were implemented out of two superconductors: niobium, low-temperature 'conventional' type-II superconductor with critical temperature of 9.2-9.3 K [33]; and yttrium-barium-copper-oxide or YBCO, high-temperature cuprate type-II superconductor with critical temperature[15] 80-87 K [52].

1.3 Thesis overview

This thesis is concerned with exploring the new applications of metamaterials both for fundamental and the applied electrodynamics. The research reported here has lead to demonstration of metamaterial-assisted radiation harvesting, a new type of electro-optical modulation, first single thin-film metamaterial with a strong toroidal dipole response, and to introduction of the new type of nonlinear metamaterial based on quantization of magnetic flux. The thesis is structured as follows.

Chapter 2 describes the main methods and the equipment used in the experiments, including the optical cryostat used to cool down the experimental samples, and the apparatus used for the spectroscopy of the metamaterials in the sub-terahertz range. The chapter also describes the manufacturing process used to create the superconducting metamaterials.

Chapter 3 explains the significance and the future potential of the terahertz/sub-terahertz technology, and demonstrates proof-of-principle solutions for sensing and controlling the sub-terahertz radiation using the superconducting metamaterials. The chapter demonstrates radiation harvesting, electro-optical modulation and a low-intensity nonlinear response in superconducting metamaterials working in the sub-terahertz range.

Chapter 4 describes the research on toroidal multipoles in metamaterials. An analytical formalism is derived to link the microscopic multipole excitations within the thin slabs of metamaterials to metamaterial transmission and reflection. The formalism is

[15] Critical temperature of YBCO depends greatly on the way it was synthesized. Maximum critical temperature achieved in YBCO is 93 K [27].

tested both experimentally and numerically, showing good agreement in both cases. Using the derived formalism, it is shown how far the design of the toroidal metamaterials can be simplified. Furthermore, a new class of metamaterials is demonstrated, where a narrow transparency window in the metamaterial transmission spectrum is achieved through the nearly-complete destructive interference between the electric dipole and the toroidal dipole (lowest member in the family of toroidal multipoles).

Chapter 5 introduces a new type of superconducting metamaterial potentially capable of quantum level nonlinear response underpinned by flux quantization. The response of the metamaterial is characterized in the low-intensity (linear) regime. The scale of expected change due to nonlinear switching is studied using additional metamaterial structures.

Chapter 6 summarizes the achieved results and proposes the future directions of research.

The appendix contains some technical parts taken out of the preceding chapters to make the main text easier to follow. The list of publications related to the research reported in this thesis can be found in App. O.

Chapter 2

Methods

This chapter explains the methods of manufacturing and experimental characterization of the superconducting metamaterials studied in this thesis.

Section 2.1 describes the cryogenic setup that was used to cool down the superconducting metamaterials. Section 2.2 describes the equipment and the calibration methods used for characterization of the electromagnetic response of metamaterials. Section 2.3 describes the methods and techniques used to manufacture the superconducting metamaterials.

2.1 Optical cryostat for superconducting metamaterials

Most metamaterials studied in this thesis were made out of superconductors and therefore needed to be cooled down to cryogenic temperatures for characterization. A closed-cycle optical cryostat was used to cool down the metamaterials. Figure 2.1 shows the schematic representation of the cryogenic setup. The cooling was achieved in two stages: first, the process cooling water, available in the laboratory, was used to cool down the helium vapour, second, the helium vapour cooled down the metallic cold-finger, to which the metamaterial was attached. In order to reach the required temperatures, the cold-finger and the metamaterial had to be isolated from the environment, which was achieved by keeping the inside of the cryostat under low pressure (typically below 5×10^{-6} mbar).

The temperature of the metamaterial was regulated using a resistive heater attached to the cold-finger. The heater was controlled by a temperature controller working in a feed-back loop. The controller measured the temperature of the cold-finger and adjusted the heating accordingly. The experimentally achievable (metamaterial) temperatures ranged from 4 K to room temperature.

The metamaterial, which was always in a shape of a thin (0.5 mm-1 mm) sapphire disk of diameter 30 mm, was clamped in the sample holder with a circular opening, as shown in Fig. 2.2a. The overlap between the sample holder and the edge of metamaterial was 0.5 mm. Indium wire was placed between the edge of the metamaterial and the sample holder. The indium was squeezed (and deformed) during clamping which lead to

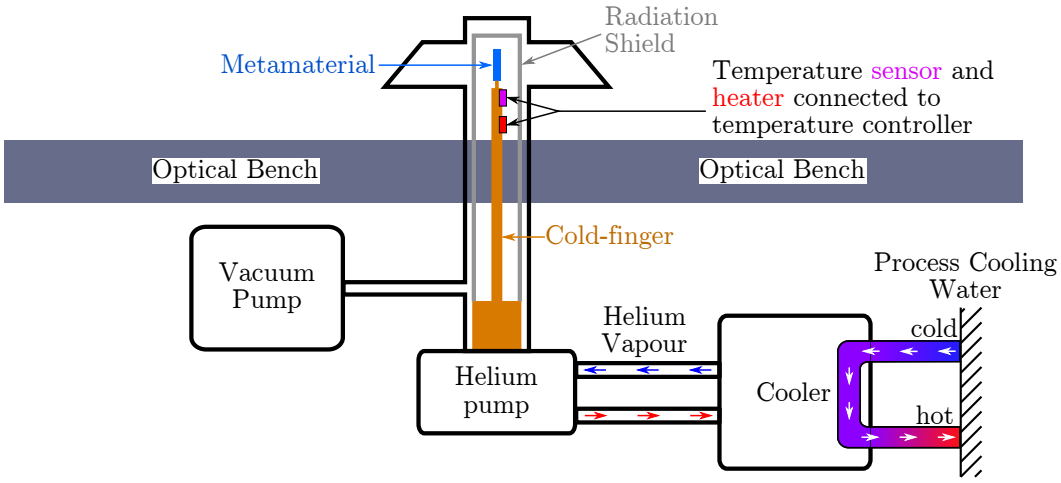

Figure 2.1: ***Optical cryostat for characterization of superconducting metamaterials.*** *A schematic representation of the main components of the cryostat. The cooler cools the helium vapour using the process cooling water. Helium vapour, circulated around by the helium pump, cools down the cold-finger. The metamaterial sample, attached to the cold-finger, is cooled at the same time. The temperature of the metamaterial is regulated by the temperature controller that uses the readings from temperature sensor to adjust the heating by heater attached to the cold-finger. The cold-finger and the metamaterial is kept under vacuum that is maintained by the vacuum pump. A radiation shield is placed between the outer wall of the vacuum chamber and the metamaterial/cold-finger to reduce heating via the black-body radiation.*

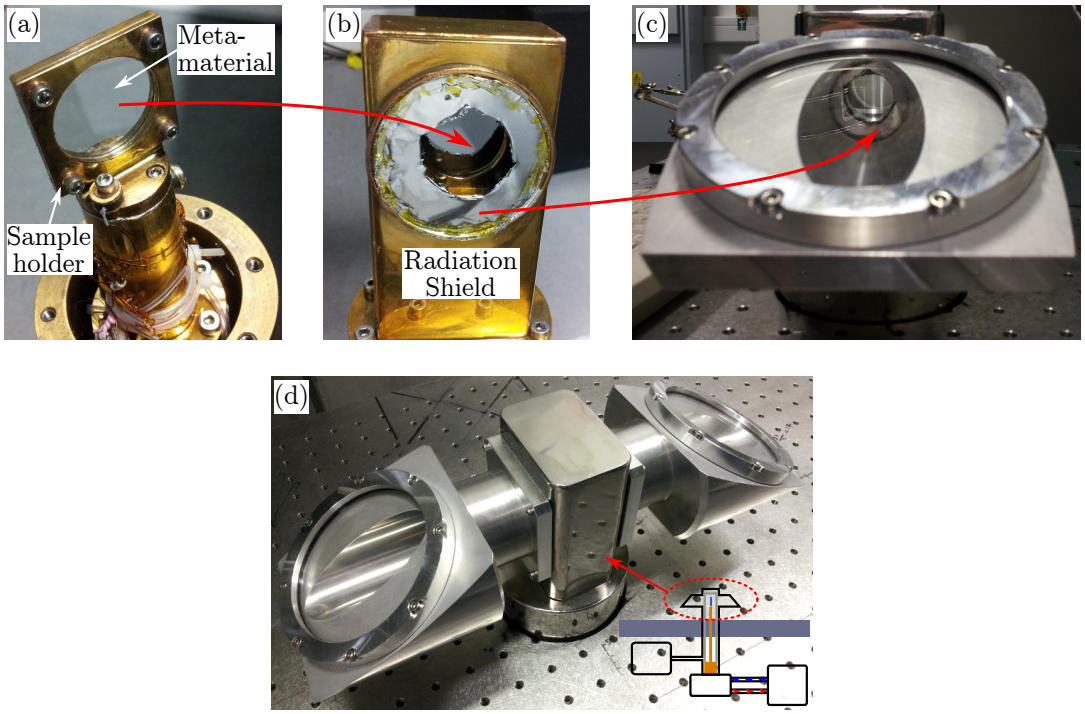

Figure 2.2: ***Housing the metamaterial inside the optical cryostat.*** ***(a)*** *Metamaterial, a thin (0.5-1 mm) sapphire disk with diameter of 30 mm, is clamped in the sample holder.* ***(b)*** *The sample holder with the metamaterial is protected by the radiation shield.* ***(c),(d)*** *Top part of the optical cryostat. The metamaterial and the radiation shield can be seen, through the fused silica windows, inside the cryostat in (c).*

a better thermal contact between the metamaterial and the sample holder. The sample holder was, in turn, screwed to the cold-finger.

The metamaterial and the cold-finger were protected from the black-body radiation, emitted by the surrounding objects at high temperature, using a metallic radiation shield (see Fig. 2.2b). The cold-finger with the attached metamaterial and the radiation shield was placed inside the optical cryostat (see Fig. 2.2c,d), which was fitted with tilted fused silica windows transparent for both visible light and the radiation from the target spectrum (75-110 GHz).

Temperature of the metamaterials

The temperature of the metamaterials in the experiments could not be measured directly, due to difficulty in attaching a thermal sensor to a small and brittle sapphire substrate firmly enough to establish a satisfactory thermal contact, whilst not obstructing the electromagnetic radiation incident on the metamaterial. Instead, in all experiments, the temperature of the cold-finger was taken as representative of the temperature of the metamaterial. The temperature of the metamaterial is likely to have been slightly higher than that of the cold-finger. Another systematic error in determining the temperature of the metamaterial, arose due to the pumping of the cryostat, which lead to periodic variations in the metamaterial temperature (roughly once per second).

The transmission of all superconducting metamaterials studied in this thesis depended strongly on their temperatures, one could therefore use the variations in metamaterial transmission to estimate the metamaterial temperature at any given time[1]. According to such estimates, at temperature $\theta = 4\,\mathrm{K}$, the amplitude of metamaterial temperature oscillations was roughly $\Delta\theta \approx 0.3\,\mathrm{K}$, increasing up to $\Delta\theta \approx 1\,\mathrm{K}$ for metamaterial temperature around $\theta = 10\,\mathrm{K}$, and then decreasing again to a fraction of a Kelvin for higher temperatures. The difference between the average temperature of the metamaterial and the readings of the temperature controller (i.e. the temperature of the cold-finger) was insignificant compared to the magnitude of $\Delta\theta$.

2.2 Sub-THz spectroscopy

The basic aim of spectroscopy is to determine the amount of (electromagnetic) radiation absorbed, transmitted and reflected by the material/device under examination. Most of the metamaterials discussed in this thesis have been studied using the same spectroscopic setup, shown in Fig. 2.3a, working in the frequency range 75-110 GHz. The setup consists of a microwave vector network analyzer, mm-wave (millimeter-wave) modules for up-conversion from microwave spectrum into the sub-THz spectrum, and the focusing horn antennae used to couple the sub-THz radiation from and into the free-space. For some of the experiments, the output power of the mm-wave modules was not sufficient. An

[1]The critical temperature of the superconductor-to-metal transition could be used as a known temperature calibration point.

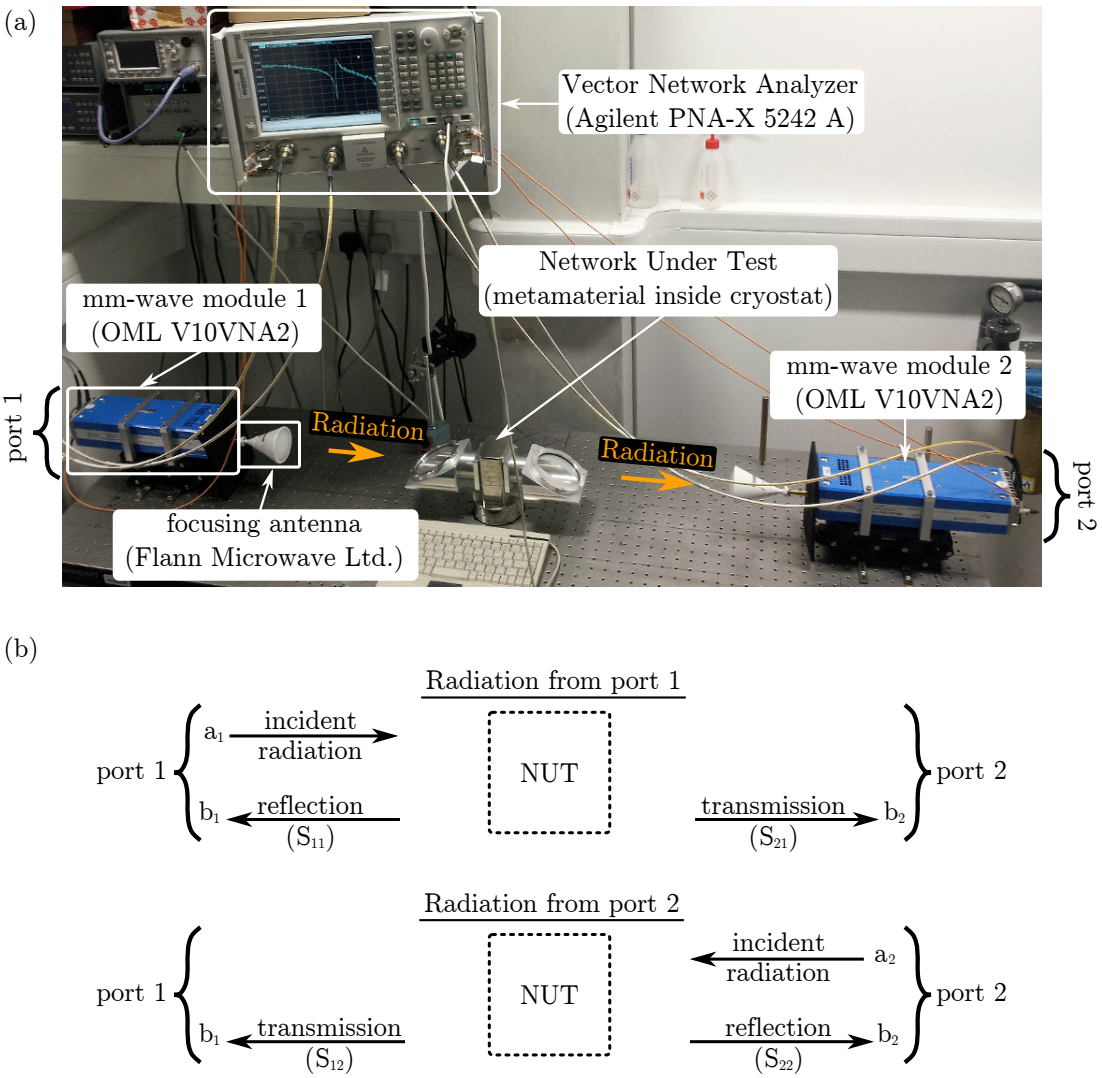

Figure 2.3: ***The setup for measuring the transmission and reflection of the metamaterials in the frequency range 75-110 GHz.*** ***(a)*** *Picture of the experimental setup for spectroscopic measurements.* ***(b)*** *Schematic representation of the setup as a two-port network that is used to characterize the Network Under Test (NUT).*

external power amplifier was then used to boost the magnitude of the emitted sub-THz radiation.

This section will provide a description of the main components of sub-THz spectroscopy setup.

Names of the spectra: microwaves, millimeter wave, sub-THz and terahertz

Before proceeding one should clarify the names of the electromagnetic spectra that will be used in the rest of the thesis. *Microwave* spectrum is usually defined to span frequency range 3-300 GHz [53]. *Millimeter wave* spectrum lies within the microwave spectrum, and covers the frequency range 30 GHz-300 GHz (wavelength range 1 mm-10 mm) [53]. The *terahertz* spectrum is commonly defined to lie in the frequency range

100 GHz-30 THz [54]. The *sub-terahertz (sub-THz)* spectrum is not officially defined (nevertheless this term is used, e.g. Ref. [54]). In this thesis, the term *sub-THz* spectrum will be used for frequency spectrum 75-110 GHz. The reason for such terminology lies in the fact that all the experimental results presented in this thesis within the sub-THz range, have a potential to be extended into the terahertz range without any significant modifications.

2.2.1 Vector network analyzer

The vector network analyzer (VNA) used for sub-THz spectroscopy was Agilent PNA-X 5242 A (Agilent Technologies, USA).

VNA is a device that allows to characterize the electromagnetic response, i.e. transmission and reflection, of an experimental sample, generically called Network Under Test (NUT), at different frequencies [55]. Usually VNA constitutes a two-port network, with each port capable of emitting and receiving the electromagnetic radiation. Two measurements (at each frequency) are required for a complete characterization of the NUT, with radiation being emitted first from port 1 and then from port 2 (see Fig. 2.3b). The measured quantities are: complex amplitude (power and phase) of the radiation emitted by port 1 (a_1), complex amplitude of the radiation received by port 1 (b_1) , complex amplitude of the radiation emitted by port 2 (a_2) and complex amplitude of the radiation received by port 2 (b_2). It is common to relate the four quantities through S-matrix (scattering matrix):

$$\begin{pmatrix} b_1 \\ b_2 \end{pmatrix} = \begin{pmatrix} S_{11} & S_{12} \\ S_{21} & S_{22} \end{pmatrix} \begin{pmatrix} a_1 \\ a_2 \end{pmatrix}$$

The components of the S-matrix are called the S-parameters. The S-parameters can be computed from the quantities measured in the experiments, as follows:

$$S_{11} = \frac{b_1}{a_1}, \text{ provided } a_2 = 0 \qquad S_{12} = \frac{b_1}{a_2}, \text{ provided } a_1 = 0$$

$$S_{21} = \frac{b_2}{a_1}, \text{ provided } a_2 = 0 \qquad S_{22} = \frac{b_2}{a_2}, \text{ provided } a_1 = 0$$

It follows that S_{11} and S_{22} represent the reflection of NUT, when it is irradiated from port 1 and from port 2 (respectively). Similarly, S_{21} and S_{12} represent the transmission of NUT, when it is irradiated from port 1 and from port 2 (respectively).

In an ideal case the VNA should measure only the electromagnetic response of the NUT, however, in reality, the signal has to travel from the signal synthesizer inside the VNA through several components, such as connecting cables, before and after it reaches the NUT. As a result, without any calibration, the electromagnetic response measured by the VNA would be the combined response of the NUT and the spectroscopic setup (cables, antennas etc.). A procedure called the two-port error correction [56] has been employed to remove the systematic errors due to the response of the VNA and other

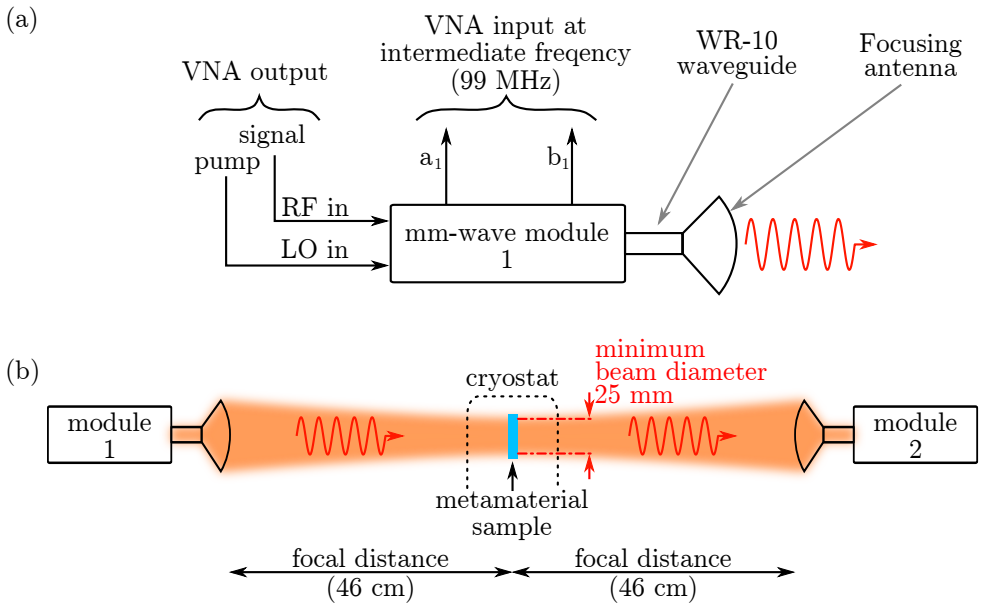

Figure 2.4: ***MM-Wave modules and antennae for sub-THz spectroscopy.*** ***(a)*** *Schematic of the single mm-wave module with an antenna. The VNA supplies the LO (local oscillator) and RF (radio-frequency) signals to the mm-wave module. The mm-wave module mixes the two input signals to produce the sub-THz radiation (75-110 GHz). The sub-THz radiation is routed into the focusing antenna through the waveguide. The output of the mm-wave modules (a_1 and b_1; or a_2 and b_2 for module 2) is returned to VNA as sinusoidal waves at an intermediate frequency (99 MHz).* ***(b)*** *The path of the radiation in sub-THz spectroscopy experiments. The antennae, connected to the mm-wave modules, focus the radiation into a spot size of $\sim 25\,mm$ at a focal distance 46 cm (from the tip of the antenna). The metamaterial (inside the cryostat) is placed in the focal plane of both antennae.*

parts of the spectroscopic setup from the experimental measurements. The procedure is built into the software of the VNA. It involves carrying out measurements on a set of standard samples. Once calibrated, the VNA is capable of removing the systematic errors, provided the full S-matrix is measured.

As one can see from Fig. 2.3b, measurement of the full S-matrix involves measuring the transmission and reflection of the NUT by illuminating it from both ports (sequentially). For the experiments on the nonlinear response of the metamaterials, presented in Sec. 3.5, an external power amplifier had to be used to reach higher level of radiation intensity. The amplifier will be described in more detail in Sec. 2.2.7, here it is sufficient to state that the power amplifier only allowed the radiation to pass in one direction. The two-port error correction could therefore not be used in the experiments involving the power amplifier (since the full S-matrix could not be measured).

2.2.2 Millimeter wave modules and antennae

The VNA used in the experiments could not produce sub-THz radiation in the 75-110 GHz range. External millimeter wave (mm-wave) modules (OML V10VNA2, OML Inc., USA) were used to up-convert the frequency of radiation from the microwave range

(VNA output) into the sub-THz range.

Figure 2.4a shows the schematic representation of the mm-wave module. The module worked by mixing two microwave outputs from the VNA, the signal (RF) and the pump (LO), to generate sub-THz radiation, which was coupled into the waveguide (WR-10) and routed to the custom-made horn antenna (Flann Microwave Ltd., UK). The readings of the two sensors in the mm-wave module (a_1 and b_1 in the mm-wave module 1 and the equivalent a_2 and b_2 in the mm-wave module 2) were returned to the VNA at an intermediate frequency[2] of 99 MHz.

Figure 2.4b shows the path of sub-THz radiation in the experiment. The horn antenna focused the sub-THz radiation into a spot of diameter $\sim 25\,\text{mm}$ at a focal distance of 46 cm, from the tip of the antenna. The metamaterial, inside the cryostat, was placed exactly between the two antennae, 46 cm away from either one, so it was always in the focal plane. The polarization of the sub-THz radiation was always vertical, i.e. perpendicular to the optical bench (see Fig. 2.3a).

2.2.3 Tilted Brewster windows for reducing unwanted reflections

The transparent fused silica windows of the cryostat were tilted with respect to path of the incident sub-THz radiation (see Fig. 2.2d and Fig. 2.3a) in order to reduce the reflection of the incident radiation. The angle of the tilt was the Brewster angle, at which the incident (p-polarized) radiation is not reflected from the dielectric [57]. Assuming that radiation propagates in free-space with refractive index $n_0 = 1$, and that the refractive index of the dielectric is n, the Brewster angle is given by $\theta_B = \arctan\left(\frac{n}{n_0}\right) = \arctan(n)$. The refractive index of the fused silica (in the sub-THz range) is $n = 1.95$ [58, 59], leading to $\theta_B = 63°$.

2.2.4 Transmission spectrum of the empty optical cryostat

Figure 2.5 shows the electromagnetic response of the cryostat - the transmission spectrum measured by passing the sub-THz radiation through the cryostat, as shown in Fig. 2.3a, but *without* the metamaterial inside it. The electromagnetic response of the cryostat distorted all transmission spectra of metamaterials measured in the cryostat.

In most experiments, the electromagnetic response of the cryostat has been filtered out of the experimental measurements by measuring the transmission with and without the metamaterial, and using the cubic fit[3] of the second measurement to normalize the first measurement.

In case of the woodcut metamaterial, described in Chap. 5, the low-temperature transmission (below the critical temperature) was normalized with respect to high-

[2]For example, the output of sensor b_1 was a radio frequency wave at frequency 99 MHz. The amplitude and phase of this wave were directly related to the amplitude and phase of the sub-THz radiation that was received by the mm-wave module 1.

[3]Using cubic fit for normalization is preferential to using the actual transmission spectrum of the empty cryostat because the cubic fit is smooth, so normalizing with respect to the cubic fit will not introduce new errors (e.g. errors due to spurious echoes) into the spectra that are normalized.

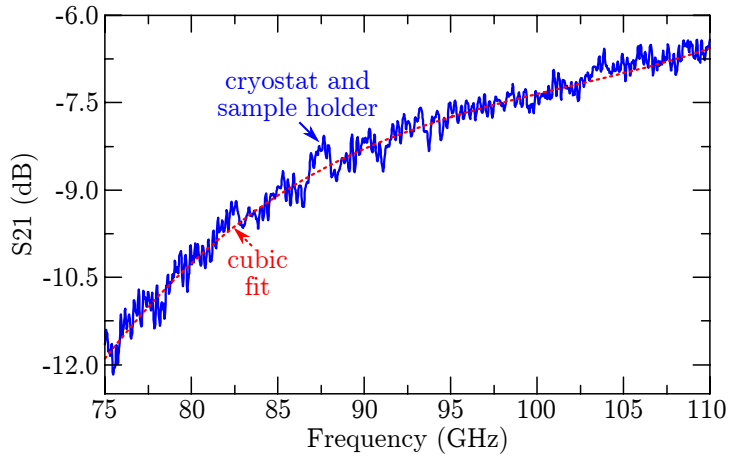

Figure 2.5: ***The transmission spectrum of the empty cryostat.*** *The solid (blue curve) is the experimental measurement, the dashed (red) curve is the cubic fit used to normalize other transmission traces.*

temperature transmission (above the critical temperature). Since the high-temperature transmission spectrum of this metamaterial was relatively featureless, such normalization did not distort the low-temperature spectra significantly, but it did remove any repeated features in the transmission spectra (such as the response of the cryostat).

2.2.5 Spurious echoes and gating

As one can see from Fig. 2.3a and Fig. 2.4b, the metamaterial samples were always illuminated at normal incidence. This lead to spurious reflections between the metamaterial samples and the antennae. Additionally, there were reflections between the two antennae even in the absence of the metamaterial. These reflections (echoes) lead to (rapid) periodic modulation of the measured transmission spectra in the frequency domain, as one can see in Fig. 2.5.

To reduce the noise due to echoes the transmission spectra were gated. Gating involves transforming the transmission trace into time-domain, at which point the spurious echoes, that arrive after the main transmitted pulse, can be suppressed. The procedure of gating is built into the software of the VNA. The effect of gating on the transmission trace is illustrated in Fig. 2.6a-c using the transmission of the planar toroidal metamaterial (discussed in Sec. 4.3).

The reflection spectra of the metamaterials were contaminated by spurious echoes to a significantly greater degree. The modulation due to echoes was stronger and it was more difficult to apply gating, because, in time domain, some of the spurious echo peaks overlapped with the main reflection peak. For this reason, only the transmission measurements of metamaterials will be analyzed in this thesis.

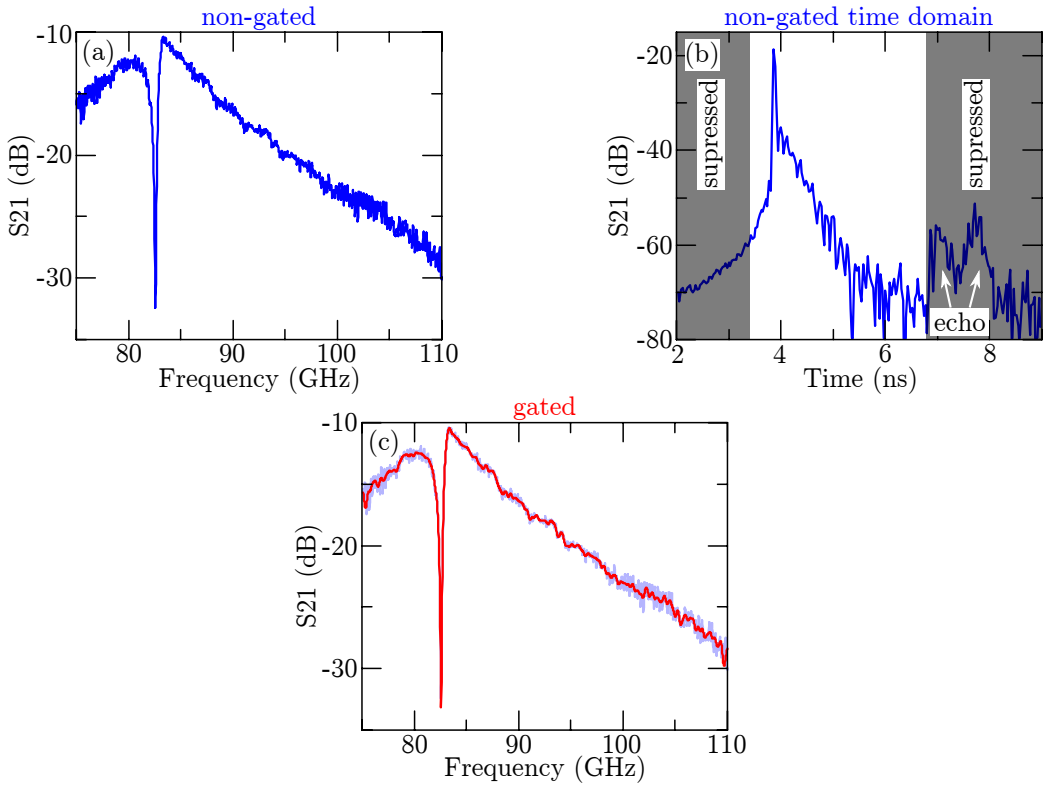

Figure 2.6: ***Gating the transmission trace (S21) to filter out the contribution due spurious echoes.*** ***(a)*** *The transmission trace of the planar toroidal metamaterial (discussed in Sec. 4.3) before gating.* ***(b)*** *The transmission trace (a) in time domain. The grayed-out area contains spurious echoes (e.g. peaks at* $7 - 8\,ns$*). The gated trace is obtained by suppressing the grayed-out area and converting the trace back into the frequency domain.* ***(c)*** *The gated transmission trace in frequency domain (red). The original non-gated trace is shown in faint blue colour on the background.*

2.2.6 Measuring transmission at a fixed frequency as a function of time

For some of the measurements reported in this thesis, it was necessary to measure how the transmission of the metamaterial changed in time. To achieve this, the VNA was switched into time-sweep mode and was triggered externally using a signal generator. The maximum achievable temporal resolution was $2.4\,\mu s$ per point.

One can estimate the maximum frequency, at which the transmission of the metamaterial may have changed, so that it could still be reliably detected by the VNA. As dictated by the Nyquist sampling rate [60], the period of the maximum detectable frequency was twice the temporal resolution of VNA $f_{max} = 1/(2 \times 2.4\,\mu s) = 208\,kHz$, but the actual limit of the maximum detectable frequency of transmission modulation was lower. For example, assume that the value of the metamaterial transmission ($T(t)$; here time is denoted with t), that was measured by the VNA, was simply the average of the instantaneous metamaterial transmission ($T^{(i)}(t)$) over the period $\tau = 2.4\,\mu s$:

$$T(t) = \frac{1}{\tau} \int_{t-\tau/2}^{t+\tau/2} dt'\, T^{(i)}(t')$$

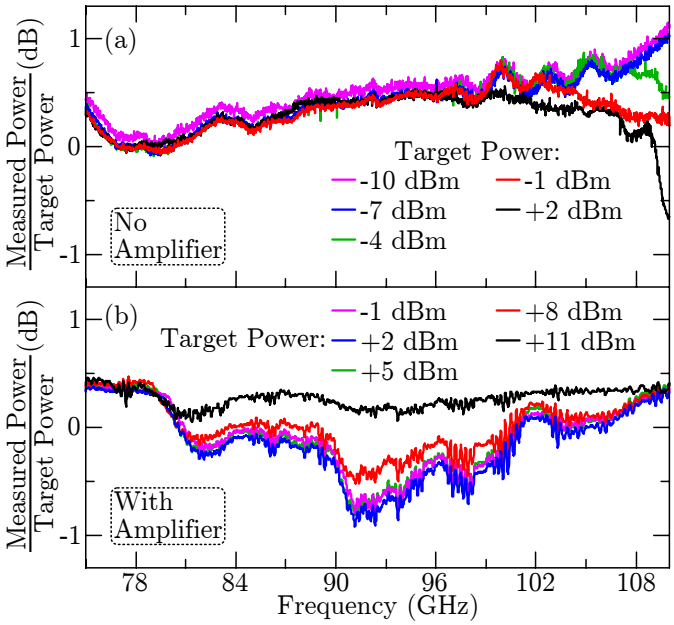

Figure 2.7: ***Output power of the mm-wave module and the power amplifier.*** ***(a)*** *The deviation of the output power level of the mm-wave module from the target power level. Five curves for five target power levels are presented (-10 dBm, -7 dBm, -4 dBm, -1 dBm, 2 dBm). The curves are created by dividing the measured output power by the target power.* ***(b)*** *The deviation of the output power level of the power amplifier (attached to mm-wave module) from the target power level.*

Assume that the instantaneous transmission oscillates sinusoidally with frequency f, i.e. $T^{(i)} = T_0 \sin(2\pi t f)$. In this case:

$$T(t) = \frac{\sin(\pi f \tau)}{\pi f \tau} \times T_0 \sin(2\pi f t) = \mathrm{sinc}(f\tau) \times T_0 \sin(2\pi f t)$$

The observed amplitude of transmission modulation will therefore be lower than the actual transmission modulation due to pre-factor $\mathrm{sinc}(\tau f)$. At $f = 100\,\mathrm{kHz}$, $\mathrm{sinc}(2.4\,\mu\mathrm{s} \times 100\,\mathrm{kHz}) \approx 0.9$, so the observed amplitude of transmission modulation will be 90% of the actual amplitude. Based on this estimate, one can define cut-off frequency, above which the transmission modulation cannot be measured reliably (using VNA) as $f_{cut-off} = 100\,\mathrm{kHz}$.

2.2.7 Available beam power and the external power amplifier

In this section it will be explained how the power (and intensity) of the radiation, reaching the metamaterials inside the cryostat, was controlled.

The power of the sub-THz radiation that was channeled into the focusing antennae, could be monitored using a waveguide-coupled power sensor (Agilent W8486A) which was controlled by the external power meter (Agilent E4416A). The power meter was used to calibrate the VNA, which allowed to control the power of sub-THz radiation produced by the mm-wave modules. Figure 2.7a shows the deviation of the output

power level of the mm-wave module (controlled by the calibrated VNA) from the target power level (that was put into the VNA). The deviation stayed within $\pm 1\,\mathrm{dB}$.

The maximum output power[4] of the mm-wave modules could not exceed +3 dBm. To achieve a higher level of radiation power, an external power amplifier was used (Millitech AMP-10-02130N, Millitech, USA). The amplifier was attached between the mm-wave module and the antenna, and allowed to achieve output power levels of up to +11 dBm. Figure 2.7b shows the deviation of the output power level of the external amplifier (attached to mm-wave module) from the target power level.

The deviation of the output power level from the target power level was repeatable (both with and without the amplifier), so in cases when the level of output power needed to be known with precision, the curves in Fig. 2.7a,b were used to correct for the power level deviation manually.

Next it will be explained how the power and the intensity of radiation reaching the metamaterials inside the cryostat were calculated. By measuring the transmission spectrum of the empty cryostat, *without* the metamaterial holder, and comparing it to the transmission spectrum measured without the cryostat in the path of radiation (i.e. transmission through the free space), it was established that the radiation propagated through the empty cryostat without any significant[5] reflection or absorption (i.e the opening in the cryostat was large enough to let the beam pass unhindered). It was therefore assumed, that the total power of radiation, that reached the metamaterial, was equal to the power measured by the power meter and multiplied by the square-root[6] of losses measured in the transmission through the cryostat *with* empty sample holder. For example, Fig. 2.5 shows that the level of transmission of the cryostat without the metamaterial at frequency 96 GHz was equal to -7.7 dB. If the power of radiation coming out of the mm-wave module (or out of the amplifier) was 0 dBm, then it was assumed that the power in the beam that reached the metamaterial was $0\,\mathrm{dBm} + (-7.7\,\mathrm{dB}/2) = -3.85\,\mathrm{dBm}$ (or $640\,\mu\mathrm{W}$). If the intensity of the radiation reaching the metamaterial was required, it was assumed that the beam power was spread uniformly over the metamaterial area (circle with diameter 30 mm), so that in the case chosen as an example (frequency 96 GHz, input power 0 dBm), the radiation intensity at the metamaterial plane would be $640\,\mu\mathrm{W}/\left(\pi \times (15\,\mathrm{mm})^2\right) = 0.91\,\mathrm{W/m^2}$.

[4] Throughout the thesis, the radiation power will be given in 'dBm', that is decibels relative to 1 mW. For example, +3 dBm corresponds to $10^{(+3/10)} \times (1\,\mathrm{mW}) = 2.0\,\mathrm{mW}$.

[5] The difference between the transmission through the free-space and through the cryostat differed by no more than 0.8 dB which was within the typical error level arising due to imperfect alignment of the antennae.

[6] The path of the radiation from the emitting mm-wave module to the centre of the cryostat, contained the same attenuating factors as the path of propagation from the centre of the cryostat to the receiving mm-wave module. Taking the square-root of the full attenuation thus allowed to estimate the attenuation experienced by the sub-THz beam after propagation for half the distance, i.e. up to the centre of the cryostat (where the metamaterial would have been placed).

2.3 Manufacturing of sub-THz superconducting metamaterials

2.3.1 Materials used for manufacturing

Two types of superconductors were used to manufacture the metamaterials described in the following chapters: niobium and YBCO (see Sec. 1.2.6).

The metamaterials out of niobium have been manufactured by photolithographically patterning thin niobium film (280-300 nm thick) on a sapphire substrate. The substrates were disks of 0.5 mm thickness with diameter of 30 mm. Clean sapphire substrates were ordered from PI-KEM Ltd. (UK), and were then coated with thin niobium film by Star Cryoelectronics (USA).

The metamaterials out of YBCO have been manufactured using the photolithography to pattern YBCO film on a sapphire substrate. The thickness of the YBCO film was 300 nm. The sapphire substrate was a disk of diameter 30 mm and thickness 1 mm. Both the YBCO film coating and the substrate itself have been ordered from Theva (Germany).

2.3.2 Manufacturing metamaterials using photolithography

The work-flow for manufacturing the metamaterials, outlined in Fig. 2.8, can be decided into the design stage, the resist deposition stage, and the etching and verification stage.

At the design stage, the metamaterial response was modeled numerically (using COMSOL 3.5a) to find the correct geometry. Then a photolithographic mask, based on this geometry, was designed by me[7] and implemented by Compugraphics (UK).

During the resist deposition stage, the sapphire substrates with superconductor films were cleaned and then spin-coated with a 1 μm thick layer of photo-resist (S1813). The coated sample was then pre-baked at temperature 90°C for 30 min and exposed to UV radiation through the photolithographic mask. The fluence of UV radiation was $110\,\mathrm{mJ/cm^2}$. The exposed photo-resist was washed off with the developer MF-319 (samples were bathed in the developer for 55 sec). In most cases, the sample with the developed photo-resist was then post-baked at 90°C for 15-25 min.

One of the two etching techniques has been used to remove exposed superconducting film during the etching and verification stage. For niobium films, I have used both the reactive ion etching (Oxford Instruments Plasmalab 80 Plus; 10 cc of SF_6, pressure 30 mTorr, RF power 85 W for 4 min.) and ion beam etching (Oxford Instruments Ionfab 300 Plus; pressure below 10^{-5} mbar, RF power 230 W, accelerating voltage 302 V for 55 min.). For YBCO films only the ion beam etching was used (same recipe as for niobium but etching time was 22 min.). In both cases, after etching, the remaining photo-resist was removed by sonication in acetone or by exposing the sample to

[7]The mask for the woodcut metamaterial described in Chap. 5 was designed in collaboration with Dr. A. R. Buckingham.

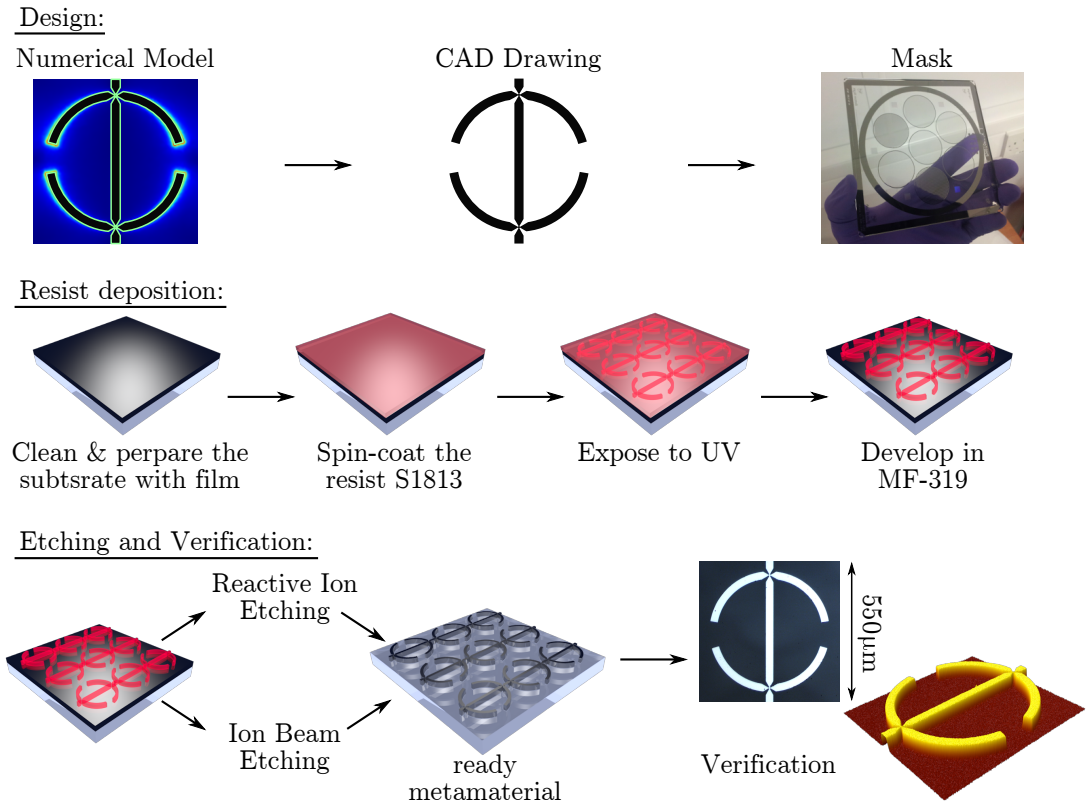

Figure 2.8: ***Work-flow for manufacturing the metamaterials using ultraviolet (UV) photolithography.*** *The process is separated into three stages. First, the model is designed and modeled on computer, and then converted into a mask (**Design**). Then the photo-resist is deposited onto the sapphire substrate with superconductor film, and patterned using exposure to UV radiation through the mask, the exposed film is then washed off in the MF-319 developer (**Resist deposition**). Finally, the superconductor film not protected by the resist is etched away using either reactive ion etching or ion beam etching and the quality of the ready metamaterial sample is verified under optical microscope and under three-dimensional profiler (**Etching and Verification**).*

oxygen plasma (ashing). The ready metamaterials were then characterized using either the stylus profiler (KLA-Tencor P.16) or the optical interference microscope (ZeMetrics ZeScope).

The techniques used for manufacturing the metamaterials allowed to achieve line-widths of around 2 μm, which was sufficient for metamaterial designs described in this thesis.

Selective etching of niobium metamaterials

Whilst in most cases of manufacturing the metamaterials, all of the exposed superconductor film had to be removed, for metamaterials described in Sec. 3.5 only partial removal of the niobium film was required, at some specific points in the metamaterial sample. Here I will describe how this metamaterial was manufactured. The details of metamaterial design will be presented in Chap. 3.

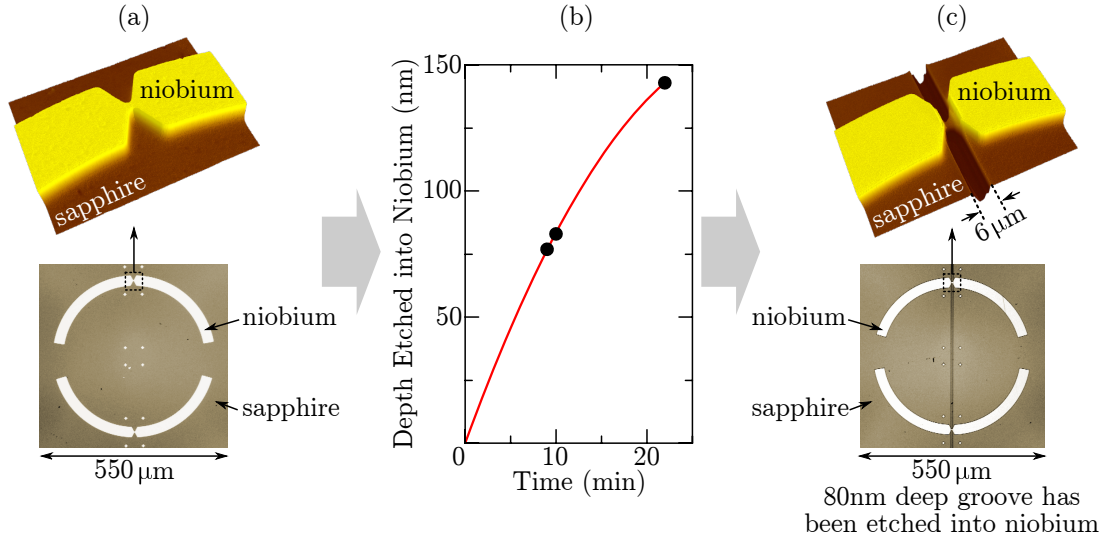

Figure 2.9: ***Selective etching of niobium metamaterial.*** ***(a)*** *The unit cell of the niobium metamaterial on sapphire substrate before the selective etching. The bottom plot shows the optical microscope picture of the unit cell and the top plot shows the 3D scan of the constriction within the unit cell.* ***(b)*** *The rate of etching of niobium film using the ion beam etching.* ***(c)*** *The unit cell of the niobium metamaterial after etching. Most of the metamaterial remains unchanged apart from the groove that was etched into the niobium film at the locations of constrictions. The sapphire substrate was also etched by the ion beam (which is why the groove carries on after the niobium film ends).*

First, the basic niobium metamaterial sample has been manufactured (see Fig. 2.9a) following the process outlined in the beginning of this section (see Fig. 2.8). Apart from the metamaterial design, the sample also contained the alignment marks. The ready metamaterial was then covered with another layer of photo-resist and patterned using a different mask that protected most of the metamaterial except for the points, where the film had to be thinned down[8]. The second mask was aligned with respect to metamaterial with the precision of $2-3\,\mu$m using the alignment marks etched into the metamaterial when it was first made.

After the second round of photo-resist deposition, the metamaterial was subjected to the second round of etching. This time, the duration of etching had to be carefully monitored to make sure that the exposed niobium film was thinned down, but not removed completely. It was found that only the ion beam etching allowed to selectively etch the niobium film at a uniform rate (reactive ion etching tended to produce isolated islands of niobium). Several experiments have been conducted with varying etch durations. The resulting etch rate is shown in Fig. 2.9b. Apart from the time of etching, all the other parameters were the same as in the first round of etching.

The result of second round of etching is shown in Fig. 2.9c, the metamaterial was thinned down at the points of interest and the rest of the design remained unchanged.

[8]In the specific case of the metamaterial I have manufactured using the selective etching, the second round of photolithography exposed 6 µm wide grooves in the metamaterial, whilst protecting the rest of it.

2.3.3 Attaching electrical contacts to the metamaterials

In the next chapter (Sec. 3.3 and Sec. 3.4) I will describe the metamaterials controlled by the electrical signals. Here I will explain how the electrical contacts were attached to the metamaterials.

Since both the cryostat and the sample holder were metallic, extra care had to be taken to avoid electrical contact between the wires attached to the metamaterial and the cryostat (which was grounded). In practice this lead to a significant amount of manipulation of the contact wires at the stage of loading the metamaterial into the cryostat, putting a significant mechanical stress on the electrical contacts. It has been found that soldering the metallic wires to the metamaterial (using both normal solder and indium) as well as gluing the wires to the metamaterials using the silver paint, did not provide the contacts with sufficient mechanical strength (the wires kept falling off). The conductive epoxy (Circuit Works CW2400), on the other hand, allowed to attach the wires very firmly to the metamaterial whilst, at the same time, enabling strong electrical contact, with contact resistances as low as $1-2\,\Omega$ (at cryogenic temperatures). Consequently, the conductive epoxy was used to attach all electrical contacts to the metamaterials reported in this thesis.

2.4 Numerical modeling of electromagnetic response of the metamaterials

This section briefly describes the method used to model (simulate) the electromagnetic response of the metamaterials. The response has been simulated by solving the 3D Maxwell equations using the Finite Element Method (FEM). The solver that was used for FEM simulations was the commercially available software COMSOL 3.5a.

Figure 2.10 shows the typical geometry that was used to find the electromagnetic response of planar metamaterials. The geometry contains a single unit cell of the metamaterial at the origin, and the tunnel of free-space above and below the unit cell. The boundaries in the x- and y-directions have been modeled as periodic boundaries, which implies that metamaterial was modeled as being infinitely large. The boundaries at either end of the tunnel (boundaries that are perpendicular to z-axis) have been modeled as scattering boundaries. Scattering boundaries allow the radiation incident on the boundary to pass through without any reflection, which models scattering into the free-space. One can also launch an electromagnetic wave from the scattering boundary, which models the incident radiation. The transmission and reflection of the metamaterial was calculated by integrating the Poynting vector over the scattering boundaries. The scattering boundaries were always positioned no closer than 3-5 wavelengths away from the metamaterial in order to ensure that only the far-field radiation would reach them.

The electromagnetic response of different materials (from which the metamaterials

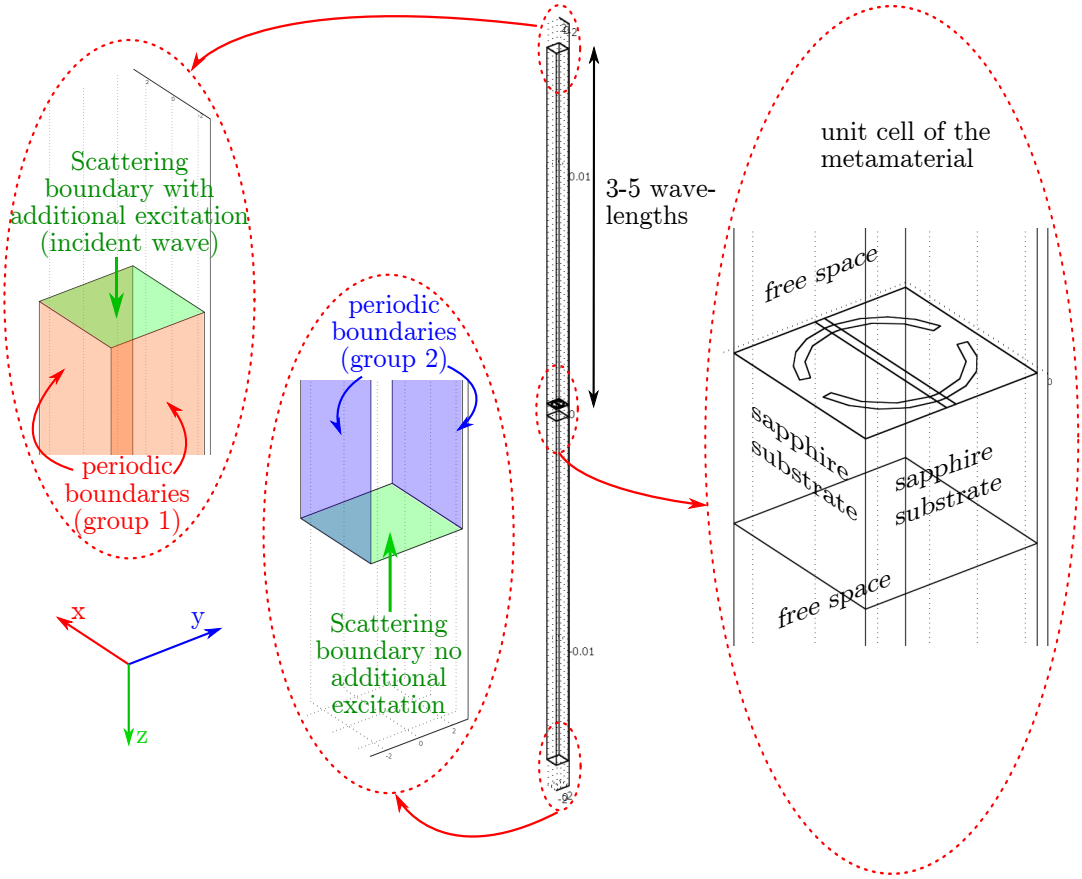

Figure 2.10: ***Numerical modeling of electromagnetic response of metamaterials in COMSOL.*** *The figure shows a typical geometry that was simulated in COMSOL to calculate the electromagnetic response of the metamaterial. Unless stated otherwise, the size of metamaterials was assumed to be infinite, so only the response of the single unit cell needed to be simulated with periodic boundary conditions. Consequently, the simulated geometry consisted of a long free-space 'tunnel with a single metamaterial unit cell in the middle. Scattering boundary conditions were used to simulate radiation scattering into the free space at the ends of the tunnel, as well as to launch the plane wave radiation incident on the metamaterial.*

were made) was modeled through complex-valued dielectric constants[9].

The correctness of the numerical solution has been verified by comparing it against the experimental data (if available) and by changing the size of the simulation (increasing the number of finite elements). In the latter case, if the increase in the size of the simulation did not change the electromagnetic response of the metamaterial, one could conclude that the solution was trustworthy.

[9]The specific constants used in different simulations will be given in the descriptions of simulation results in the following chapters.

Chapter 3

Nonlinear Effects in Superconducting Metamaterials

3.1 Introduction

Since its birth more than a decade ago, the field of metamaterial research has undergone a rapid growth with demonstration of such exotic effects as cloaking, negative refractive index and magnetism at optical frequencies [1, 19]. Now the attention of researchers is turning from passive metamaterials to active metadevices, with functionality applicable to tuning, switching and sensing the electromagnetic radiation [21]. The terahertz technology stands to gain most from these advances. Terahertz radiation, typically defined to lie in frequency range from 100 GHz to 30 THz [54], could have applications in security, biomedical imaging, atmospheric sensing, astrophysics, analytical chemistry, and communications, but its proliferation is hampered by a lack of switching and modulation solutions [54, 61–63]. This is the so-called 'terahertz gap', and it could potentially be closed through the development of active terahertz metamaterials [21, 64].

Following a decade of research, several types of active terahertz metamaterials have been identified, including the reconfigurable metamaterials, liquid crystal-loaded metamaterials, semiconductor/graphene-based metamaterials, and superconducting metamaterials (see Refs. [21,64]). The superconducting metamaterials, i.e. metamaterials made from superconductors, are of particular interest in the terahertz range due to low Joule losses, sub-nanosecond nonlinear response [65–67] and sensitivity to a wide range of external stimuli, including light, magnetic field and temperature [21, 68]. The inherent drawback of superconducting metamaterials is the need for cryogenic temperatures to sustain superconductivity, however the modern closed-cycle cryostat technology allows to create autonomous systems that house the superconducting devices and the cryocooler whilst consuming only the electrical power. In selected fields, such as microwave engineering, these combined systems can outperform the room-temperature counterparts even with the penalty for the cryogenic cooling factored in [69]. The potential for applications of the superconducting metamaterials will therefore depend on the cost/benefit

analysis of the metamaterial functionality against the penalty for cooling.

In this chapter, the research on active superconducting metamaterials for the subterahertz (sub-THz) range is reported and analyzed. Using superconducting metamaterials out of niobium, sensing (Sec. 3.3) and modulation (Sec. 3.4) of the sub-THz radiation, as well as nonlinear sub-THz response (Sec. 3.5), are demonstrated. Since all the metamaterials studied in this chapter are derived from the asymmetrically-split ring metamaterial [2, 70, 71], its basic properties are reviewed in Sec. 3.2. Possible improvements of the asymmetrically-split ring metamaterials are briefly discussed in Sec. 3.6. All active metamaterials demonstrated in this chapter rely on the nonlinear electrical response of superconductors. The remainder of this introductory section summarizes the main mechanisms of the nonlinear response of the superconductors to high current densities.

Nonlinear response of the superconductors to high current densities

The main mechanisms of the nonlinear electrical response of superconductors can be separated into three categories[1]:

Heating: Provided the applied current is not constant in time, even a superconductor will exhibit Ohmic losses, which will lead to increase in its temperature [27]. Rising temperature will decrease the number of Cooper pairs and increase the number of quasiparticles (normal electrons, that are not parts of the Cooper pairs), leading to even higher Ohmic losses. This type of nonlinear response has been utilized in the operation of the metamaterial bolometer (Sec. 3.3), electro-optical modulator (Sec. 3.4) and nonlinear sub-THz metamaterial (Sec. 3.5).

Decreased minimum excitation energy (intrinsic nonlinearity): In Sec. 1.2.3 it was stated that a minimum energy of $E_{min} = 2\Delta$ was required to excite the electron from the superconducting ground state (i.e. to destroy a Cooper pair and create two quasiparticles instead). This is true in the absence of the net electrical current. The presence of current imparts a net drift velocity v_D on all electrons inside the superconductor. This additional kinetic energy leads to the reduction in the minimum energy needed to excite the electron from the superconducting ground state $E_{min} = 2 \cdot (\Delta - p_F v_D)$ [27], where p_F if the Fermi momentum of the superconducting ground state. The reduction in E_{min}, in turn, leads to change in the ratio of quasi-particles and Cooper pairs, thus changing the conductivity of the superconductor.

Nonlinearities related to Abrikosov vortices: Abrikosov vortices are islands of non-superconducting material, penetrated by the magnetic field, within the otherwise

[1] In case of granular superconductors such as cuprates (e.g. YBCO) the nonlinear response is often dominated by a yet another (different) mechanism that relates to tunneling of Cooper pairs between the grains of the material [40, 72].

superconducting medium (see Sec. 1.2.1). Electrical currents flowing within the superconductors exert Lorentz force on Abrikosov vortices. Energy dissipation occurs if the vortices move in response to this force. One mechanism of nonlinear response related to Abrikosov vortices lies in electrical current exceeding the lower critical field of the superconductor (H_{c1}; see Sec. 1.2.1), which leads to creation of Abrikosov vortices, which, in turn, increases the energy dissipation. Another mechanism lies in non-trivial displacement of the Abrikosov vortices under the action of electrical current. In the most basic approximation the dynamics of vortices in superconductors can be described by viscous motion in a pinning potential. If the pinning potential is not harmonic, that is if the vortex displacement is not proportional to the magnitude of local current density, the relation between the energy dissipation in superconductor and the magnitude of applied current will not be quadratic, resulting in current-dependent (effective) conductivity. This type of nonlinear response is utilized in the operation of the electro-optical modulator (Sec. 3.4).

A more detailed review of the different mechanisms of nonlinear response in superconductors, including the relationships between the nonlinear change in conductivity and the applied electromagnetic field, can be found in the discussion section of Ref. [73].

3.2 Properties of asymmetrically-split ring metamaterial

Figure 3.1a shows a microwave-range asymmetrically-split ring (ASR) metamaterial and its transmission spectrum (measured at normal incidence of radiation). The metamaterial is created by cutting asymmetric arcs out of metallic rings arranged in a planar array on a dielectric substrate. Three resonant modes are clearly distinguishable in the transmission spectrum of the ASR metamaterial in Fig. 3.1a. The corresponding current density distributions within the ASR meta-molecules are shown in Fig. 3.1b. Modes I and III are the symmetric modes, meaning that the currents in the metallic arcs of each meta-molecule oscillate in phase. Mode II is an anti-symmetric mode, with currents in the metallic arcs of the meta-molecules oscillating in anti-phase. The anti-symmetric current oscillations in mode II lead to reduced net radiation scattering by the metamaterial, thus trapping the electromagnetic energy at the metamaterial plane in form of magneto-inductive waves (waves propagating between resonators, i.e. meta-molecules, coupled through mutual induction [74]), and creating a transparency window in metamaterial's transmission spectrum (see Fig. 3.1a). Mode II is therefore called the *trapped mode* [71, 75–77]. The extent, to which the trapped mode can be excited in ASR metamaterials, depends on the degree of asymmetry between the metallic arcs (difference in arc length) and on Ohmic losses in the metal used to implement the metamaterial[2] [71]. Due to the asymmetric shape of the transparency window, the trapped mode in ASR

[2]Dielectric losses in the substrate affect the quality of the trapped mode in the same way as Ohmic losses in the metal.

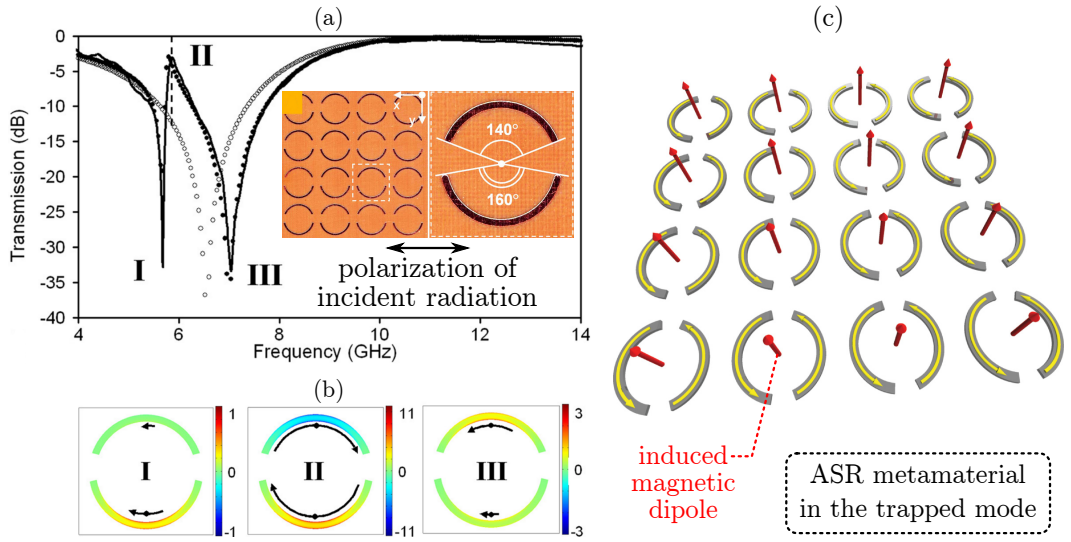

Figure 3.1: ***Asymmetrically-split ring (ASR) metamaterial.*** ***(a)*** *Microwave-range ASR metamaterial and its transmission spectrum (adopted from Ref. [71]). Mode II is the trapped mode.* ***(b)*** *The current density distribution within the unit cells of the ASR metamaterial in each of the three resonant modes (adopted from Ref. [71]).* ***(c)*** *Artistic impression of the interacting ASR meta-molecules (unit cells) at the trapped mode (adopted from Ref. [78]). The interactions between the meta-molecules can be represented by the interactions between the magnetic dipoles induced in each unit cell.*

metamaterials is also commonly referred to as the *Fano mode* [77].

The nature of the three resonant modes of the ASR metamaterial can be understood by considering the resonant response of the isolated metallic arcs that make up the ASR metamaterial. The first resonant mode of the metallic arcs, driven by the electric field polarized along them, occurs when the wavelength of the driving radiation is twice as long as the electrical length[3] of the arcs. The ASR metamaterial is made up of two kinds of arcs, with slightly different lengths, therefore there will be two modes with closely spaced frequencies at which one of the two kinds of arcs will be in resonance. These two modes correspond to mode I and mode III in Fig. 3.1a. The metamaterial transmission will be reduced in both mode I and mode III due to increased scattering from the metallic arcs driven at resonance. Mode II arises as a result of rapid variation in phase[4] of the currents induced in the metallic arcs in the vicinity of the resonance. Due to difference in the resonant frequency of the asymmetric arcs, the currents excited in them will be sufficiently out of phase at frequencies between mode I and mode III, for net scattering of the metamaterial to be reduced, which will lead[5] to mode II accompanied by the

[3]If the ASRs were suspended in vacuum, then the electrical length of the arcs would equal the geometrical length. Placing the ASR onto a substrate with dielectric constant $\epsilon_r > 1$ will lead to electrical length being longer then the geometrical length. The net effect of the substrate will be in reducing the resonant frequency of the arc.

[4]The same variation in phase is commonly observed in harmonic oscillators driven at frequencies close to the resonant frequency [79].

[5]The current distribution within the single ASR can always be decomposed into a linear combination of symmetric mode (induced currents in phase in both arcs) and the anti-symmetric mode (induced currents in anti-phase). The amplitude of the excited anti-symmetric mode will be strongest when the

characteristic transparency window in metamaterial transmission spectrum.

In the trapped mode, the meta-molecules of the ASR metamaterial effectively behave as an array of out-of-plane magnetic dipoles (see Fig. 3.1c). Due to orientation, these dipoles only interact with each other without radiating into the far-field (except at the edges of metamaterial). As a result of the magnetic dipole-dipole interactions, at the trapped mode, the ASR metamaterial responds not as a set of isolated resonators, but as a single planar electromagnetic cavity. Furthermore, it has been shown that the response of the ASR metamaterials depends on the physical size of the sample, i.e. the number of meta-molecules in the metamaterial plane. The increase in the number of meta-molecules leads to dramatic narrowing of the trapped mode resonance, the so-called *spectral collapse* [70]. Such response in metamaterials is commonly called the *collective response* (or *collective mode*) [80], and the wider class of metamaterials exhibiting the collective response is called the *coherent metamaterials* [2].

The three metamaterials that will be discussed in the subsequent sections of this chapter have been derived from the same ASR metamaterial design (see Fig. 3.3b, Fig. 3.7a and Fig. 3.11a). The main parameters of the ASR metamaterial are the unit cell size, the radius of the ASR as well as the width and the length of the metallic strips that make up the ASR. Since all of the experimental work reported in this thesis targeted the proof-of-principle demonstrations rather than optimization of a single design, the parameters such as unit cell size, the radius of the ASR and the length of the longer arc of the ASR have been adopted[6] from Fedotov *et al.* [71]. The length of the shorter arc has been chosen as a result of simulations, in such a way as to provide trapped mode response with high quality-factor[7]. Finally, the width of the asymmetric arcs has been chosen to be 10 times larger than the smallest width that can be (reliably) achieved with the process adopted for manufacturing the metamaterials (see Sec. 2.3). Such choice made the metamaterial designs easily reproducible.

3.3 Radiation-harvesting sub-THz metamaterial bolometer

Despite the terahertz gap, numerous types of terahertz and sub-THz detectors were developed over the past century. These include the photoconductive antennas, the detectors based on Schottky diodes, the semi- and superconducting bolometers, and many others (see Table 3.1). The focus of this section will be on superconducting

phase difference between the currents induced in the arcs of the ASR is largest, i.e. in the frequency range between mode I and mode III. To a good approximation, mode II corresponds to maximum excitation of the anti-symmetric current mode.

[6] All lengths were multiplied by a scaling constant to account for high permittivity of the substrate and to shift the resonant frequency into the 90-100 GHz range.

[7] Quality factor is calculated from $Q = \nu_0/\Delta\nu$, where ν_0 is the resonant frequency and $\Delta\nu$ is the full width at half maximum of the transmission resonance. Increasing the length of the shorter arc towards the length of the longer arc tends to increase the quality factor of the trapped mode response, but this trend will ultimately be suppressed by the Joule losses in the metamaterial [71].

Detection Method	Active Medium	Principle of Operation	Advantages / Disadvantages
Terahertz time-domain spectroscopy	Semiconductor, superconductor, nonlinear optical crtystal	Gated detection in time domain	A: Coherent detection (phase and amplitude). D: Only works for periodic signals.
Schottky diodes	Semiconductor	Heterodyne detection	A: Coherent detection. High spectral selectivity. D: Requires pumping from local oscillator (LO).
Superconducting tunneling junctions	Superconducting tunneling junctions	Tunneling and/or breaking the Cooper pairs. Both heterodyne and direct detection are possible.	A: Low noise. Low LO power. Coherent detection. High spectral selectivity. D: Requires cooling. Less established technological platform (compared to semiconductor electronics).
Semiconducting bolometers	Semiconductor	Temperature-dependent change in resistivity of semiconductors.	A: Mature technology. High sensitivity. Low noise. Can work as coherent or incoherent detector. D: Typically requires cooling.
Superconducting bolometers	Superconductor	Rapid change in resistivity during the superconducting transition.	A: Very high sensitivity and very low noise. Can work as coherent or incoherent detector. D: Requires cooling.

Table 3.1: ***Comparison of the mature technologies for detection of terahertz and sub-THz radiation.*** *The considered technologies are: terahertz time-domain spectroscopy [81], Schottky diodes [82,83], superconducting tunneling junctions [50,82], semiconducting bolometers [82,84], superconducting bolometers [50,82,84].*

bolometers.

Bolometer is a type of radiation sensor that converts the energy of the incident radiation into heat, detecting the latter as the signal. In the superconducting bolometers, the detection relies on the rapid change in the electrical resistance of the materials during the superconducting-to-normal phase transition (triggered by heating the bolometer with radiation). The superconducting bolometers are amongst the most sensitive detectors available for the terahertz and sub-THz spectrum with Noise Equivalent Power[8] (NEP) reaching as low as $10^{-19} - 10^{-20}\,\mathrm{W}/\sqrt{\mathrm{Hz}}$ [85,86].

Reducing the size of the bolometers helps to reduce their intrinsic noise level. However, the reduction of the bolometer size leads to reduced coupling to free-space radiation (and thus a weaker signal). A simple, but bulky, way of overcoming this challenge lies in using a combination of a lens and an antenna to capture the radiation from the target spectrum and to route it into the bolometer [50,82,87–89] (see Fig. 3.2). In this section

[8]See the sub-section 'Noise performance' on p. 42 for the explanation on how NEP describes to the performance of a bolometer.

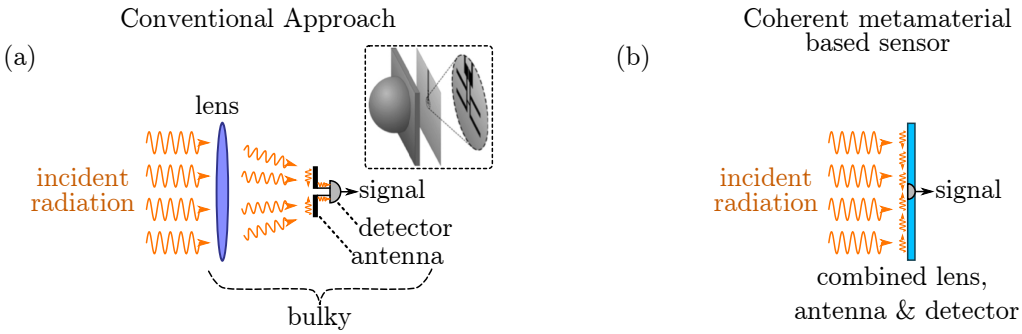

Advantages of using (dielectric) lens to couple radiation into the detector:

- Low (energy) loss
- Broadband
- Easy to fabricate

Disadvantages:

- Large lens size in all three dimensions (of order of the wavelength of the target spectrum).

Advantages of using coherent metamaterial to couple radiation into the detector:

- Thin (small size)
- High spectral selectivity
- Monolithic and robust

Disadvantages:

- Low coupling efficiency (non-zero metamaterial reflection, transmission and absorption in the non-detecting part of the metamaterial)

Figure 3.2: ***Comparison of the conventional radiation detector (a) and the coherent metamaterial bolometer (b).*** *In the second case the metamaterial effectively combines the functions of the antenna and the lens as well as houses the radiation detector, making the end-device significantly more compact. The inset in (a) has been adopted from Ref. [87]. The main advantages and disadvantages of both approaches are listed below the sub-figures. See Ref. [88] for a review of use of dielectric lenses to couple terahertz radiation into small bolometers.*

it will be demonstrated how a coherent metamaterial can be used to achieve the same aim of coupling radiation from the large area into a small detector, but using only a single compact monolithic device (see Fig. 3.2).

The results presented in this section have been published in Ref. [90].

3.3.1 Metamaterial bolometer design and experimental setup

The metamaterial bolometer, shown in Fig. 3.3, was created by photolithographic patterning of thin niobium film (280 nm thickness) on a sapphire substrate (disk of thickness 0.5 mm and diameter 30 mm; see Sec. 2.3 for further manufacturing details) with a design based on asymmetrically-split ring metamaterial [2, 71, 76, 91]. All the split-ring resonators in the metamaterial array were connected by a continuous niobium (sensing) wire. The arcs of the split-rings were tapered down to widths of $3 - 7\,\mu$m at the points of crossing with the sensing wire in order to increase the heating produced by sub-THz currents at these locations (thus increasing the sensitivity). The metamaterial sample contained 1189 split-ring resonators, with the number or resonators being limited only

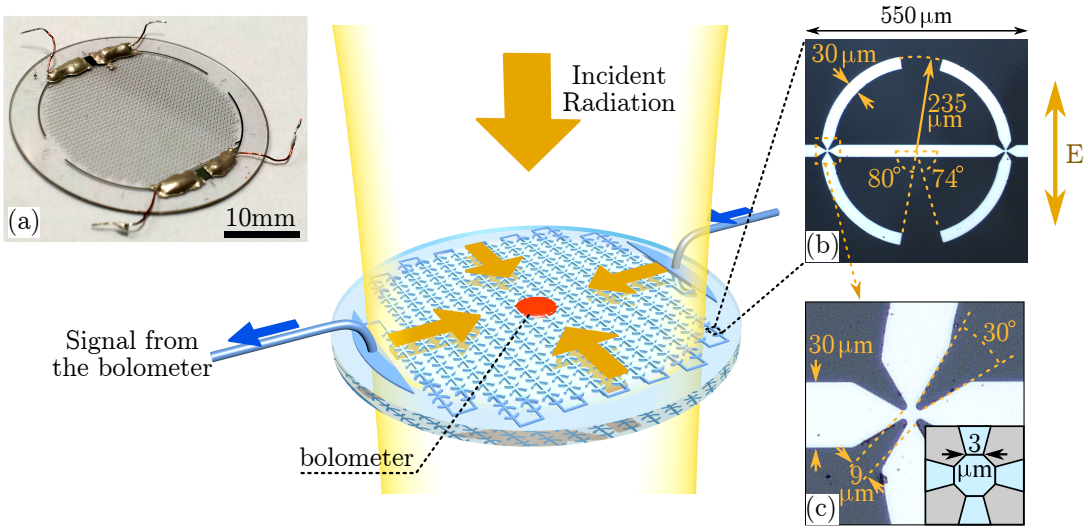

Figure 3.3: ***The design and principle of operation of the superconducting bolometer combined with a coherent metamaterial.*** *The main figure shows the artist's impression of the device in action. The radiation incident on the metamaterial is trapped in the cavity-like mode at the metamaterial plane, and is then routed into the bolometer located on the metamaterial surface. The signal wire that runs through the metamaterial allows to extract bolometer readings.* ***(a)*** *Picture of the manufactured device.* ***(b)*** *Microscope picture of the unit cell of the metamaterial (darker area is sapphire substrate, lighter area is the niobium film). The asymmetrically-split ring metamaterial is merged with a signal wire. The intersections of the signal wire with the asymmetric arcs are tapered down to increase the sensitivity of the bolometer. The polarization of incident radiation is shown with a vertical arrow (labeled 'E').* ***(c)*** *The zoom of the taper. The tapering angle is* $30°$*. The photolithographic mask was designed to achieve tapering down to an octagon with* $3\,\mu m$ *sides (see the inset).*

by the overall size of the metamaterial[9]. Although the strength of the resonant response in asymmetrically split-ring metamaterials is known to depend on the size of the array, the quality factor[10] of the response typically becomes saturated[11] as the number of resonators in the metamaterial exceeds 10^3 [70, 92]. It was therefore not practical to increase the number of split-rings beyond the number presented in this work. Furthermore, since the response of a lossy ASR metamaterial does not change significantly with number of unit cells once the latter exceeds 10^3, the ASR metamaterials discussed in this thesis could be modeled as infinite-sized (modeling single unit cell with periodic boundary conditions).

For characterization, the metamaterial was placed inside a closed-cycle optical cryostat, which provided the temperature control within the range from 4.5 K to room temperature (see Sec. 2.1 and Sec. 2.2 for details of the experimental setup). The role of superconducting bolometer was carried out by the voltage-bias induced hot-spot, created

[9]The size of the ASR unit cell was $550\,\mu m \times 550\,\mu m$, due to constraints on space inside the cryostat all experimental samples had to be disks with diameter of 30 mm, 1189 was the maximum number of unit cells that could be fitted onto the substrate whilst leaving space for the sensing wire and the contact pads.

[10]Quality factor is calculated from $Q = \nu_0/\Delta\nu$, where ν_0 is the resonant frequency and $\Delta\nu$ is the full width at half maximum of the transmission resonance.

[11]The saturation occurs mostly due to finite Ohmic losses in the metamaterial [92].

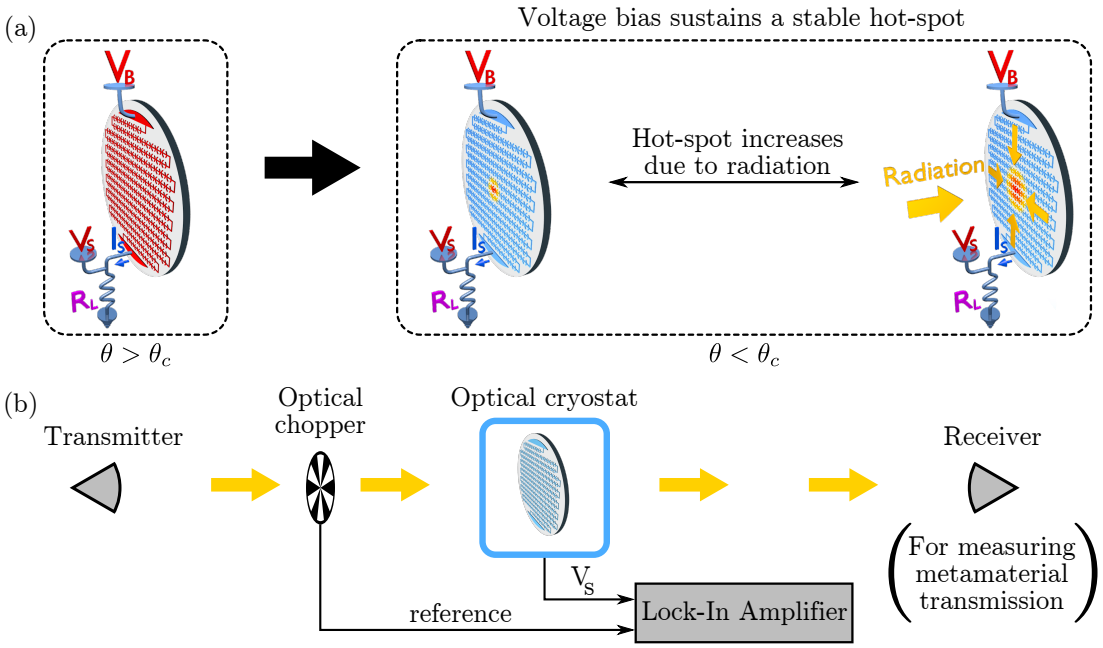

Figure 3.4: ***Experimental characterization of the superconducting metamaterial bolometer.*** ***(a)*** *Establishing the hot-spot on the surface of the metamaterial. Metamaterial is brought above niobium's critical point (θ_c), then bias voltage (V_B) is applied across the metamaterial and the load resistor (R_L). After that, the temperature of the metamaterial is lowered below θ_c whilst maintaining the bias. Most of niobium entered the superconducting state, but a small hot-spot of niobium in the normal state remained. The size (and resistance) of the hot-spot changed in response to incident radiation.* ***(b)*** *The experimental set up. Optical chopper was used to modulate the radiation. Output of the bolometer was recovered using the lock-in amplifier. The metamaterial was housed inside the optical cryostat, the rest, including the load resistor, remained at room temperature.*

following the procedure outlined in Fig. 3.4a. To create the hot-spot, the metamaterial was placed in series with a load resistor (R_L) and biased with constant voltage bias (V_B), whilst keeping it at temperature above the critical point of niobium ($\theta_c \approx 9\,\mathrm{K}$). The metamaterial was then cooled down below the critical temperature, whilst maintaining the voltage bias. As a result of this procedure, a single stable hot-spot, sustained by heat dissipation due to voltage bias, developed in the superconducting sensing wire [93]. The bolometer operated by thermalizing[12] the incident radiation in the hot-spot, which lead to a change in hot-spot's size and therefore its resistance. The latter was detected by measuring the signal voltage (V_s) across R_L using a lock-in amplifier for detection, and an optical chopper for modulation of the incident radiation (see Fig. 3.4b).

3.3.2 Experimental Results

Figure 3.5a shows the transmission of the metamaterial bolometer at zero voltage bias. The metamaterial displays a wide transmission stop-band with a narrow transparency window at frequency $\nu_0 = 95.7\,\mathrm{GHz}$. The transparency window is a typical Fano res-

[12] Converting electromagnetic energy into heat.

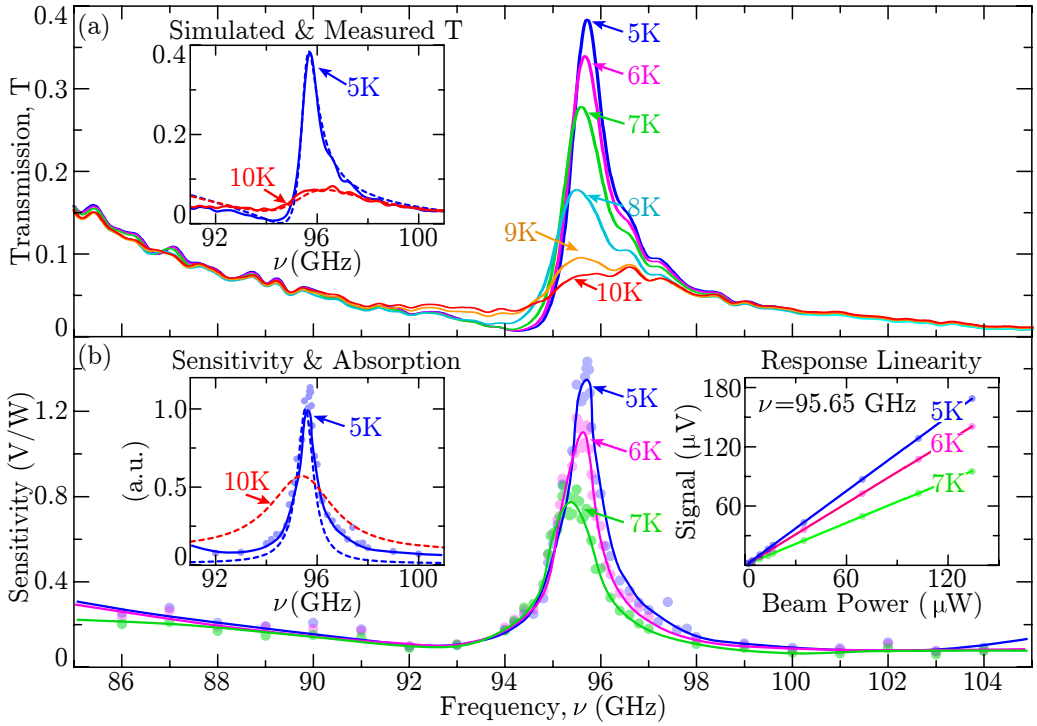

Figure 3.5: ***Transmission of the metamaterial and the sensitivity of the metamaterial bolometer.*** ***(a)*** *Main plot shows the transmission of the metamaterial at different temperatures, in case of zero voltage bias. The inset compares the measured (solid curves) and the simulated (dashed curves) transmission at temperatures* 5 *K and* 10 *K.* ***(b)*** *Main plot shows the sensitivity of the metamaterial bolometer with bias voltage* $V_B = 4\ V$ *and load resistor* $R_L = 100\,\Omega$ *for different temperatures.* ***Inset on the left*** *compares the measured sensitivity of the bolometer at temperature* 5 *K (data points and the solid guide for the eye) to the simulated absorption (dashed curves) of the metamaterial at temperatures* 5 *K and* 10 *K. All quantities are in arbitrary units.* ***Inset on the right*** *compares the bolometer signal measured with the lock-in amplifier (component of* V_s *at the frequency of the chopper), to the integrated power of the incident beam to illustrate the linearity of the bolometric response of the metamaterial.*

onance [77]. It arises from the interference between the subradiant collective mode of the anti-symmetric current oscillations in the arcs of the split-rings, and the free-space-coupled superradiant mode created by the symmetric current oscillations. The Fano resonance is highly sensitive to Ohmic losses, which is demonstrated by a rapid collapse of the transmission window (see Fig. 3.5a) when the temperature is ramped from 5 K to 10 K across the superconducting transition of niobium. The electromagnetic response of metamaterial could be reliably reproduced by numerically solving the Maxwell's equations[13] as is demonstrated on the inset in Fig. 3.5a for the metamaterial temperatures $\theta = 5\,\mathrm{K},\ 10\,\mathrm{K}$.

Following the standard terminology, one can define the sensitivity of metamaterial bolometer as $S = V_s/P$, where P is the power delivered by the incident radiation and V_s

[13]COMSOL 3.5a was used for simulations. The material constants were as follows: the dielectric constant of sapphire was taken to be $\tilde{\epsilon}_r = 9.73 \times \left(1 - \mathrm{i}1.3 \times 10^{-7}\right)$ [94], the conductivity of niobium was taken to be $\tilde{\sigma}_{Nb,5K} = (1.09 - \mathrm{i}1.56) \times 10^8$ S/m and $\tilde{\sigma}_{Nb,10K} = 3.44 \times 10^7$ S/m [95], for temperatures 5 K and 10 K, respectively.

is the voltage measured across the load resistor in series with the metamaterial bolometer (see Fig. 3.4a). The sensitivity of the metamaterial was characterized with bias voltage[14] $V_B = 4\,\mathrm{V}$ and load resistor $R_L = 100\,\Omega$ (see Fig. 3.4a). Although it was not possible to determine the position of the hot-spot, its size, relative to the size of the metamaterial, could be estimated[15] directly from the ratio of metamaterial resistance at any given temperature and the metamaterial resistance at temperature slightly above niobium's critical point. Given the values of V_B and R_L, the relative size of the hot-spot stayed within 4-5% for temperatures in the range 5-7 K (at higher temperatures the hot-spot became unstable). Thus, most of the metamaterial remained superconducting even with the established hot-spot. The response of the metamaterial bolometer was linear within the available range of incident radiation power (see inset on the right in Fig. 3.5b).

The sensitivity of the metamaterial bolometer is shown on Fig. 3.5b. It was measured with total power of the incident beam below $100\,\mu\mathrm{W}$ (see App. B). The size of the beam cross-section was comparable with the opening in the optical chopper used to modulate the beam. As a result, the power of the modulated beam did not go up to 100% during the 'open' position of the chopper, and did not drop down to zero during the 'shut' position of the chopper. All these effects have been compensated for by using the procedure described in App. B. One should note that the source of rapid oscillations of sensitivity in Fig. 3.5b is not the experimental error, but the spurious reflections between the various components of the system (such as, for example, reflections between the antenna and the metamaterial) which lead to slight differences in the magnitude of the radiation power that was incident on the metamaterial. These oscillations could be resolved[16] and were reproducible. The actual experimental error in the measurement of sensitivity was around $\pm 3\%$.

The efficiency of the metamaterial bolometer in utilizing the power of incident radiation towards heating the niobium wire, can be shown to be around 0.3% (see App. C). To improve efficiency in future designs one should increase the coupling between the neighboring ASRs by packing them more densely (see Sec. 3.6), which would increase the rate of energy transfer between the ASRs (so a higher proportion of energy would reach the thermalizing part of the metamaterial before being lost to Ohmic losses). A further boost in efficiency may be achieved by integrating the metamaterial with a reflective mirror which would allow the radiation to pass through the bolometer twice.

[14] See App. A for the motivation behind the choice of the bias voltage and the load resistance.

[15] The DC-resistance (i.e. zero frequency resistance) of niobium in the normal state changes very little with temperature below 20 K. Since the DC-resistance of the superconducting niobium is zero, one can estimate the size of the hot-spot created by bias voltage from the ratio of hot-spot resistance, to the resistance of metamaterial at 10 K.

[16] The period of oscillations was approximately $0.2 - 0.3\,\mathrm{GHz}$.

3.3.3 Discussion

Radiation Harvesting: Experimental evidence

The crucial feature of the work reported here, which sets it apart from the numerous implementations of hot-spot bolometers (for example, see [47, 96–99]), as well as from the previously reported metamaterial-based bolometers [25, 100–102], is the collective response of the metamaterial. The asymmetrically-split ring metamaterial, studied in this work, exhibits a collective mode of excitation, involving a large number of split-ring resonators in the vicinity of the hot-spot, which interact through out-of-plane magnetic dipoles induced by the asymmetric currents (see Sec. 3.2). The collective mode of the metamaterial allows to enhance the sensitivity of the bolometer by collecting and channeling the energy of the incident radiation into the hot-spot. Simultaneously, the selectivity[17] of the bolometer is significantly boosted due to the spectral collapse exhibited by the asymmetric split-ring metamaterials [70]. This principle of operation will be called the 'radiation harvesting'.

As one can see from Fig. 3.5b, the metamaterial bolometer operated at sensitivity of order 1 V/W with a sharp frequency-selective response (fractional sensitivity bandwidth[18] is about 1% at temperature 5 K). Strong spectral selectivity indicates the involvement of a large section of the metamaterial array outside the hot-spot, where the superconducting state was preserved. Indeed, if only the hot-spot area participated in the detection, the spectral response of the bolometer would be much broader and would correspond to the absorption[19] (A) of the (unbiased) metamaterial at the temperature at which the hot-spot is maintained, i.e. slightly greater than 9 K (see the inset in Fig. 3.5b). I argue that the electromagnetic interactions between the meta-molecules facilitate harvesting of energy by a large number of meta-molecules in the superconducting state and channeling it to the hot-spot area, which is kept in the normal state (by the voltage bias). The strong selectivity of the metamaterial bolometer is therefore experimental evidence for radiation harvesting.

Radiation harvesting: Numerical example

The claim of radiation harvesting is further substantiated by simulating the absorption of radiation in the isolated asymmetrically-split ring resonator at temperature 10 K and the same resonator surrounded by the superconducting asymmetrically-split rings at temperature 5 K. Four structures were simulated: single ASR at 10K, ASR at 10K surrounded by 8 ASRs at 5 K (3×3), ASR at 10 K surrounded by 24 ASRs at 5 K (5×5), ASR at 10 K surrounded by 48 ASRs at 5 K (7×7). The absorption of the central ASR is presented in Fig. 3.6a for all four array types.

[17] Increased sensitivity in the narrow frequency range.

[18] Ratio of the -3 dB bandwidth the centre frequency of bolometer sensitivity curve.

[19] The absorption (A) is given by the energy conservation: $A = 1 - T - R$ where T and R are the normalized transmission and reflection of the metamaterial sample.

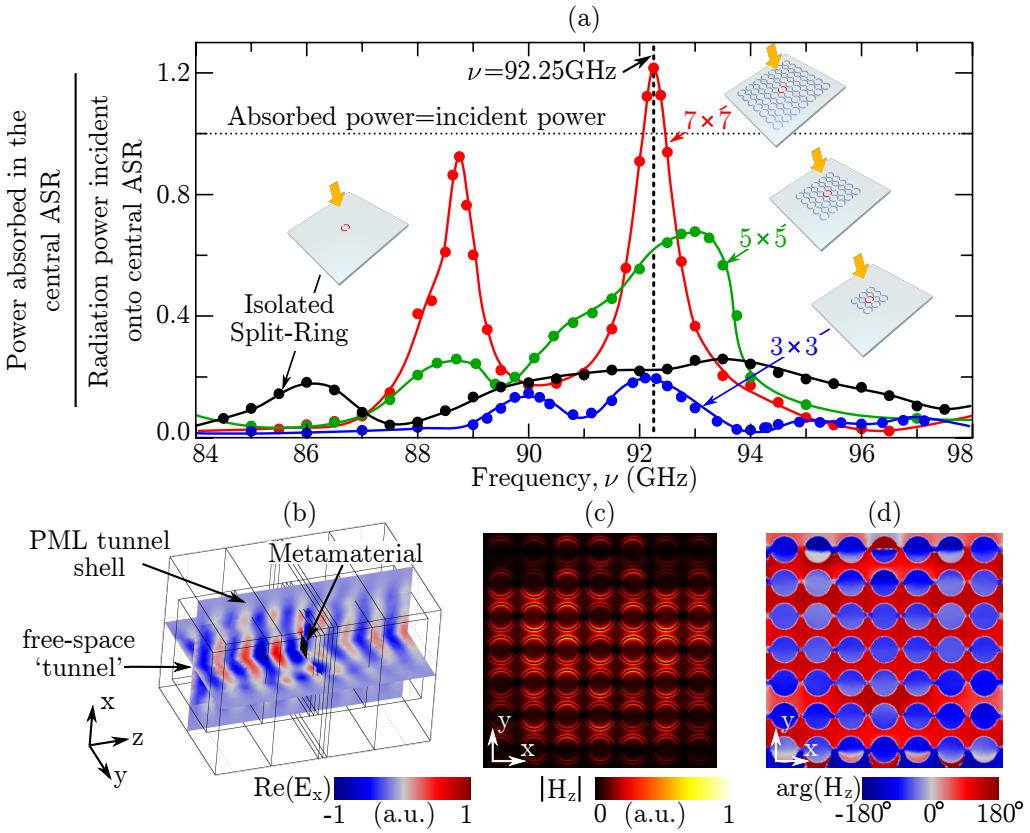

Figure 3.6: ***Numerical illustration of radiation harvesting.*** ***(a)*** *The graph shows the dissipated power in the asymmetrically-split ring (ASR) resonator with conductivity equal to niobium conductivity at temperature* 10 *K, when it is placed in the centre of an array where all remaining ASR resonators have conductivity equal to niobium conductivity at* 5 *K. Different curves correspond to arrays of various sizes. In all cases, the ASRs are placed onto sapphire substrate. The dissipated power is normalized with respect to the power of radiation (geometrically) incident onto the central unit cell.* ***(b)*** *The geometry and the solution, for the case of illumination of the* 7×7 *array at frequency* 92.25 *GHz. The finite-sized array of ASRs and the tunnel of free-space before and after the array, were surrounded by the shell of Perfect Matched Layer (PML) which absorbed the scattered radiation. The color-map shows the real part of the x-polarized electric field.* ***(c),(d)*** *Magnitude and phase of z-component of magnetic field* (H_z) *at the metamaterial surface for the case of* 7×7 *array at frequency* 92.25 *GHz.*

The absorption of the single lossy ASR (10 K) is relatively featureless, however when the lossy ASR is surrounded by the array of superconducting ASRs two clear peaks appear in the absorption spectrum. Increase in the number of surrounding ASRs leads to increase in height and decrease in width of the absorption peaks. One therefore concludes, that, as expected, the surrounding rings have a profound influence on the energy dissipation in the lossy ring (through the magnetic dipole-dipole interactions [78, 92]).

It is instructive to examine the simulation results in detail for the case of the largest array[20] that could be simulated (7×7). Figure 3.6b shows the geometry that was

[20]Simulating even larger array of ASRs would have required computers with operating memory larger than was available.

simulated in COMSOL. Unlike in all other simulations for this thesis (see Sec. 2.4), the electromagnetic response of the full array had to be simulated (instead of simulating the response of a single unit cell). Scattering boundaries and the Perfectly Matched Layers (PMLs) were used to emulate scattering of radiation into the free space at the edges of the array. Figure 3.6b also shows the color-map of the real part of the electric field that drives the metamaterial sample. One should note that the wave-front approaching the metamaterial is flat, i.e. the metamaterial is illuminated by the 'plane-wave radiation'.

Figures 3.6c,d show the amplitude and the phase of the magnetic field perpendicular to the metamaterial plane at the higher-frequency absorption resonance (92.25 GHz; see Fig. 3.6a). One can see that this mode corresponds to a relatively uniform excitation (if one discounts the edge effects) with magnetic field piercing through the centers of the ASRs and returning back around the edges (of the ASRs). This means that all ASRs oscillate as magnetic dipoles. Therefore, the higher-frequency absorption resonance of the 7×7 array corresponds to the trapped mode resonance. A similar analysis of the resonance at 88.75 GHz (see Fig. 3.6a) shows that this lower-frequency absorption resonance corresponds to induced current flowing in anti-phase in the meta-molecules from different rows of the metamaterial. The absorption resonance at 88.75 GHz will therefore disappear[21] in the infinite-sized ASR metamaterial.

Noise performance

An important parameter of any radiation detector is the noise-equivalent power (NEP), which determines its sensitivity limit [103, 104]. For example, if the noise equivalent power of the detector is NEP $= 1\,\mathrm{nW}/\sqrt{\mathrm{Hz}}$, it means that to measure the radiation power of 1 nW with the signal-to-noise ratio of 1:1, one has to collect the signal for 1 s (e. g. set 1 s integration time on the lock-in detector). Increasing the integration time to 4 s would allow to detect 0.5 nW signal with the 1:1 signal-to-noise ratio.

The specific sources of noise for cryogenic bolometers have been discussed by Low and Hoffman [105], finer non-equilibrium corrections have later been provided by Mather [106]. In this work, the bolometer was operated at temperature of $\theta = 10\,\mathrm{K}$ with the typical hot-spot resistance of $R = 140\,\Omega - 200\,\Omega$. The signal was detected as the voltage drop across the bolometer, so the Johnson noise was the main limiting factor $NEP_{Johnson} = \sqrt{4k_B\theta R/S^2} \sim 0.3\,\mathrm{nW}/\sqrt{\mathrm{Hz}}$, where $S \sim 1\,V/W$ is the sensitivity of the bolometer (see Fig. 3.5b) and k_B is the Boltzmann constant. Such level of noise, however, by no means imposes the fundamental limit. Indeed, the superconducting bolometers, working in electro-thermal feedback and in strong isolation from the heat sink, are amongst the most sensitive detectors, with NEP levels reaching as low as $10^{-19} - 10^{-20}\,\mathrm{W}/\sqrt{\mathrm{Hz}}$ [85, 86]. The focus of this work lied not in reducing the NEP of the superconducting bolometers, but in showing how the metamaterial allows to dramatically shape the selectivity of the bolometers, and, at the same time, to greatly increase

[21] Different unit cells cannot display different excitations in an infinite-sized metamaterial since this is incompatible with the translational symmetry of the infinite-sized metamaterial array.

the bolometer absorption cross-section. I argue that combining the coherent metamaterial (presented here) with the state-of-the-art superconducting bolometer would produce a device with a superior specific detectivity[22] (D^*) [103].

3.3.4 Summary

In summary, a superconducting light-harvesting bolometer was demonstrated in this section. The coherent response of the metamaterial allowed to effectively collect the incident sub-THz radiation from the narrow target spectrum band and channel it into the small sensitive hot-spot, whilst rejecting the background radiation. This concept allows to combine the harvesting device, filter, antenna and the bolometer in a single robust package that can be manufactured in one lithography step. The approach presented in this section could greatly influence the design of the next generation of terahertz/sub-THz bolometers.

3.4 Modulation of sub-THz radiation with superconducting metamaterial

Fast and effective radiation modulators have now been developed for most parts of electromagnetic spectrum, from microwaves up to visible, with the exception of terahertz/sub-THz range [54, 63, 107]. Here, the solutions are only beginning to emerge.

Over the past two decades terahertz wave modulation has been demonstrated using microwave electronics [63, 108], charge carrier injection into semiconductors and graphene [109–113], optical nonlinearities [114–117], and liquid crystals [118, 119]. Several metamaterial modulators loaded with liquid crystals [120, 121], semiconductors [122–134], and relying on mechanical displacement have also been presented [20,135–138] (also see Ref. [64]). All of these approaches have drawbacks. Optically controlled modulators are clearly bulky. Electrically controlled modulators perform well for single-mode beams (i.e. small beam cross-section), but cannot be scaled up to modulate large cross-section beams, due to intrinsic (distributed) capacitance and resistance.

In this section, I will demonstrate a superconducting sub-THz radiation modulator, which has no intrinsic capacitance and low Ohmic losses, and thus is potentially capable of efficiently modulating large-area terahertz/sub-THz beams at high frequency. The results reported in this section have been published in Ref. [91].

3.4.1 The design and transmission of superconducting metamaterial modulator

Figures 3.7a-c show the design and the principle of operation of the metamaterial electro-optical modulator. It is a planar array of sequentially connected asymmetrically-split

[22] $D^* = \frac{\sqrt{A}}{NEP}$, where A is the area of the detector and NEP is the noise equivalent power (in units $\mathrm{W}/\sqrt{\mathrm{Hz}}$).

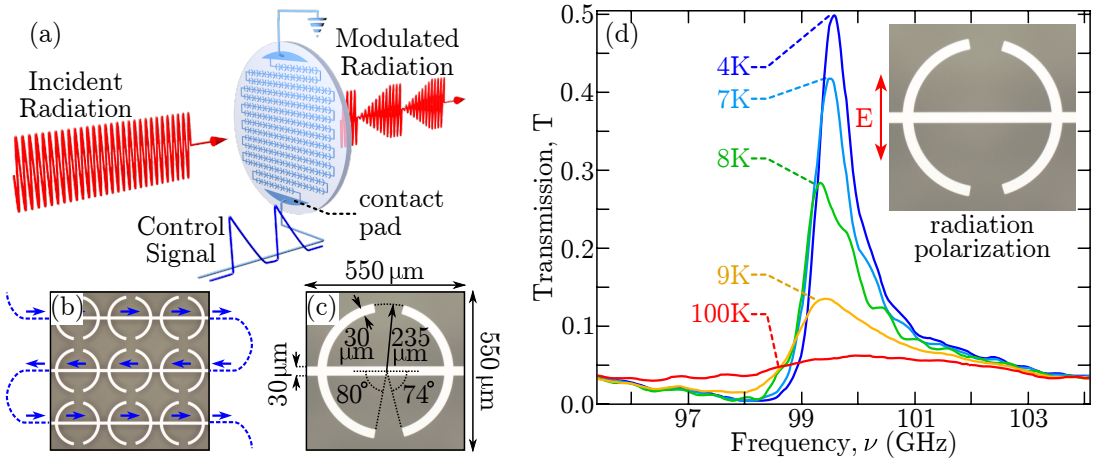

Figure 3.7: ***Electro-optical modulator based on superconducting metamaterial.*** ***(a)*** *Artist's impression of the metamaterial modulator in action. Sub-THz radiation is modulated by passing current through a planar metamaterial array, fabricated lithographically from superconducting niobium.* ***(b)*** *Optical microscope image of the metamaterial's unit cell. Bright parts show patterned niobium film on (darker) sapphire substrate. Blue arrows indicate the path of the electric current through the network of meta-molecules.* ***(c)*** *Details of the meta-molecule geometry.* ***(d)*** *Metamaterial transmission spectra with no applied control signal below and above the critical temperature of phase transition in niobium ($\theta_c \approx 9\,K$).*

ring resonators, similar to the metamaterial bolometer described in Sec. 3.3. The sample has been fabricated by optical lithographic patterning of a 280 nm thick niobium film deposited onto a sapphire substrate in shape of a thin disk of thickness 0.5 mm and diameter 30 mm (the metamaterial occupied a smaller area of radius 11 mm). The macroscopic design of the metamaterial was the same as for metamaterial bolometer shown in Fig. 3.3a.

For characterization, the manufactured sample was housed inside the optical cryostat, and its transmission has been measured in a free-space setup with sub-THz radiation at normal incidence (see Sec. 2.1 and Sec. 2.2 for details of the experimental setup). Figure 3.7d shows the metamaterial transmission spectrum for a range of substrate temperatures. At temperature $\theta = 4\,\mathrm{K}$, the metamaterial displays a narrow asymmetrically-shaped 50% transmission peak (Fano resonance) that is centered at frequency $\nu = 99.5\,\mathrm{GHz}$. When the temperature is increased towards the superconductor-to-metal phase transition point ($\theta_\mathrm{C} \approx 9\,\mathrm{K}$), the transmission peak broadens, and its magnitude drops rapidly. In the normal state, where Joule losses in niobium are high [95,139], the resonance is completely suppressed, and transmission level of the array does not exceed 10%.

All asymmetrically-split rings of the metamaterial network are sequentially connected by a (control) wire, as illustrated in Fig. 3.7a,b. This allows running the control current simultaneously through the entire metamaterial array. The control wire is perpendicular to the polarization state of incident electromagnetic wave and does not affect the Fano resonance, provided no current is running through the control loop. The cross-

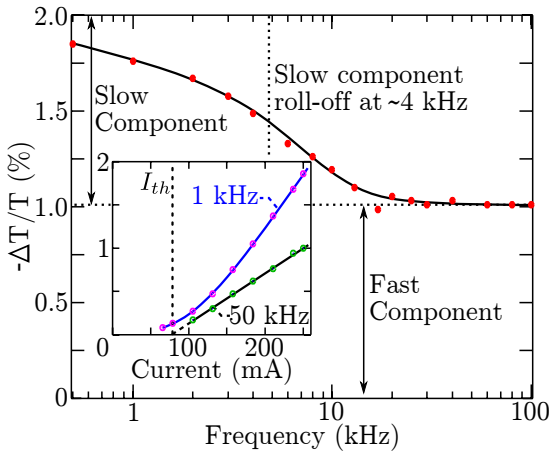

Figure 3.8: ***Electro-optical modulation in sub-critical regime at ν=99.5 GHz.*** *Amplitude of the metamaterial transmission change as a function of frequency of the (sinusoidal) control signal. The horizontal dashed line separates the fast and slow components of response. The vertical dashed line marks the roll-off of the slow modulation component at ~ 4 kHz.* ***Inset:*** *Amplitude of the transmission change as a function of the peak modulation current for modulation frequencies of 1 kHz and 50 kHz.*

ing point of the control wire with the split rings is chosen deliberately to be at the anti-node of the oscillating currents driven by the sub-THz radiation[23]. This maximizes the influence of the control current on the transmission of the metamaterial by changing the conductivity inside the meta-molecules where it matters most.

Depending on the magnitude of the control signal, the modulation of the metamaterial transmission could be achieved in two different ways which will be discussed in Sec. 3.4.2 and Sec. 3.4.3.

3.4.2 Sub-critical modulation

The modulation of the metamaterial transmission has been studied at the lowest achievable substrate temperature of $\theta = 4\,\mathrm{K}$. At this temperature, the electrical response of the metamaterial was linear[24] as long as the control current did not rise above the critical current[25] of $\sim 0.5\,\mathrm{A}$. The modulation of the metamaterial transmission using control currents below this critical value will be called the 'sub-critical' regime of modulation.

The sub-critical modulation of metamaterial transmission was studied at the trapped mode resonance ($\nu_0 = 99.5\,\mathrm{GHz}$). Applied control currents were sinusoidal with amplitudes of up to 250 mA and frequencies ranging between 0.5 kHz and 100 kHz. Figure 3.8 shows the amplitude of metamaterial's transmission change at the peak of trapped mode resonance. The plot reveals two mechanisms of transmission modulation in the sub-critical regime: the slow mechanism with the roll-off at $\sim 4\,\mathrm{kHz}$, and a fast, frequency-independent mechanism.

[23] See the current distribution for mode II in Fig. 3.1a.

[24] For low control currents, the electrical response of the metamaterial was equivalent to a resistor $R = 3.1\,\Omega$ (including the contact resistance) in series with an inductor $L = 3.2\,\mu\mathrm{H}$.

[25] The critical current of the metamaterial will be discussed in Sec. 3.4.3

The slow sub-critical modulation mechanism can be explained by considering the heat diffusion at the electrical contact pads (see Fig. 3.7a). In the sub-critical regime of operation, the whole of the metamaterial modulator is in the superconducting state and therefore exhibits extremely low Ohmic losses. However, the wires feeding the control signal into the metamaterial have non-zero resistance, and therefore heat up when current flows through them. One can estimate the time it takes for the heat generated in the contact pads to diffuse from the edge of the metamaterial to its centre. Given the distance from contact pads to metamaterial centre $r = 11\,\mathrm{mm}$, and assuming thermal diffusivity of sapphire $\kappa = 0.12\,\mathrm{m}^2/\mathrm{s}$ [140], the diffusion time is $\tau_d = r^2/4\kappa = 250\,\mu\mathrm{s}$. In the case of continuously oscillating control signal, τ_d corresponds to 4 kHz, which agrees well with the roll-off of the slow sub-critical modulation mechanism (see Fig. 3.8). One therefore concludes that the slow component of transmission modulation in the sub-critical regime is due to heating of the metamaterial by the power dissipated in the contact pads.

It is argued here, that the fast sub-critical transmission modulation mechanism can be explained by the suppression of superconductivity in the magnetic field induced within the niobium wire by the control current. In the case of weak magnetic field, the change in niobium sub-THz conductivity will be proportional to the magnitude of the field, and therefore to the amplitude of the control current. One can assume that the metamaterial transmission modulation will be proportional to small changes in niobium conductivity. Consequently, in the absence of heating (i.e. at modulation frequencies above 10 kHz), the transmission modulation of metamaterial will be proportional to the amplitude of the control current. By contrast, at low modulation frequencies, where the heating mechanism prevails, the relation between transmission modulation and the control current amplitude should become at least quadratic as dictated by Joule's law. This is exactly what we observed in the experiments (see inset to Fig. 3.8). Using the literature data for high-frequency conductivity of niobium [95], and its response to applied magnetic field [141], one can estimate the sub-critical transmission modulation due to fast modulation mechanism to be 3% (see App. E), which compares well[26] to the experimentally observed 1% (see Fig. 3.8).

The transmission change of the metamaterial in response to control current at frequency 50 kHz reveals a non-zero current threshold of about $I_{th} = 80\,\mathrm{mA}$ (see inset to Fig. 3.8). This feature can be attributed to the appearance of the Abrikosov vortices (small domains of niobium in the normal state), which enter the path of the resonantly induced sub-THz currents at the intersections between the control wire and the arcs of the split-ring meta-molecules. Abrikosov vortices are responsible for scattering the sub-THz currents, so there will be no transmission modulation until vortices enter the wire. Given the dimensions of the control wire and using the published data for niobium [142, 143], one arrives at the vortex-entry threshold current of $I_w = 17\,\mathrm{mA}$ (see App. D). Since the control wire effectively widens at the intersections, this value (I_w)

[26] Given the simplicity of the model used for estimation in App. E

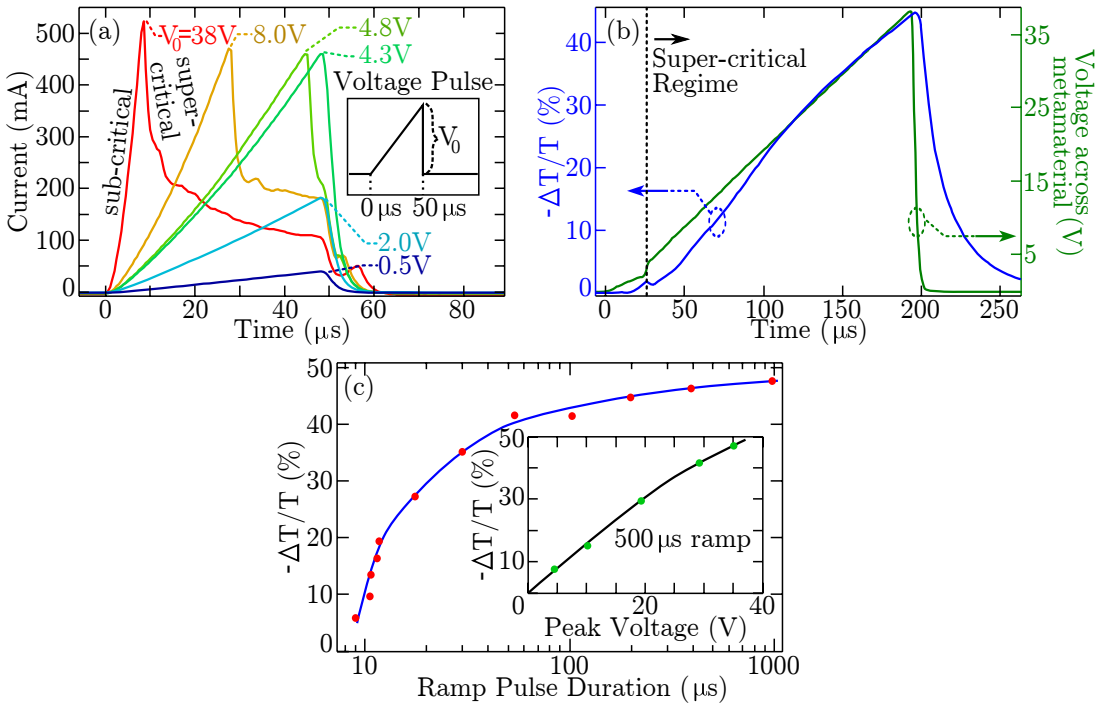

Figure 3.9: ***Electro-optical modulation in super-critical regime at ν=99.5 GHz.*** ***(a)*** *Transient electrical current through the metamaterial (at temperature $\theta = 4\,K$) in response to ramped voltage pulses (as shown on the schematic in the inset).* ***(b)*** *Dynamics of the metamaterial transmission change (blue) corresponding to a 200 µs long control voltage ramp applied across the metamaterial (green). The kinks in both curves at 26 µs signify the onset of super-critical regime.* ***(c)*** *Amplitude of metamaterial transmission modulation as a function of the voltage ramp duration at 38 V peak value. The inset shows the change in the transmission achieved with a 500 µs long voltage ramps of different amplitudes.*

serves only as a rough estimate of the observed threshold current (I_{th}).

3.4.3 Super-critical modulation

Figure 3.9a shows the electrical current established in metamaterial at substrate temperature $\theta = 4\,K$ in response to 50 µs long ramped control voltage pulse (see inset on Fig. 3.9a). Initially, the current through the metamaterial follows the applied voltage (sub-critical regime), but when the current exceeds the critical value of $\sim 500\,mA$, the metamaterial resistance increases abruptly, resulting in a sharp drop in current despite the rising voltage. This second regime of operation will be called 'super-critical'.

The super-critical modulation of metamaterial transmission has also been characterized at the trapped mode resonance ($\nu_0 = 99.5\,GHz$). Applied control signal was in the form of voltage ramps of duration from 10 to 1000 µs, with peak voltage of up to 40 V. The ramp repetition rate was kept low ($\sim 25\,Hz$) to prevent the metamaterial from overheating.

Figure 3.9b illustrates the dynamics of the metamaterial transmission change for the case of a 200 µs long ramp pulse: the transmission decreases progressively with the applied voltage dropping by 45% towards the end of the ramp. The kinks in the

transmission and voltage curves mark the transition from the sub-critical regime to the super-critical regime. Voltage ramps of the same magnitude, but different pulse durations, produced peak transmission changes ranging from -10% (10 μs ramps) to almost -50% (millisecond-long ramps; see Fig. 3.9c). The transmission suppression could also be controlled with the amplitude of the ramp pulse, as illustrated in the inset to Fig. 3.9c. The dependence of the maximum transmission change on the voltage ramp amplitude was fairly linear revealing the onset of saturation at about 30 V. In all cases, the relaxation of the ramp-induced transmission change had exponential-like (thermal) dynamics with decay time shorter than 25 μs (see Fig. 3.9b and App. F).

I argue that the super-critical regime of modulation involves a superconducting-to-normal phase transition triggered in the metamaterial by ramping up the current. Indeed, switching from the sub-critical to the super-critical regime takes place at about 500 mA, corresponding to critical current density of 6×10^6 A/cm^2 for wire cross section of 280 nm $\times$ 30 μm. This agrees with the directly measured critical current density of 3×10^6 A/cm^2 reported by Zhuravel *et al.* for niobium metamaterials [144]. The transition to the normal state typically starts at a small defect in the wire and rapidly spreads until it reaches the final size, which is a function of the applied bias voltage [93, 145]. The DC-resistance (zero frequency resistance) of niobium in the normal state changes very little with temperature below 20 K. Since the DC-resistance of the superconducting niobium is zero, one can estimate the size of the hot-spot created by bias voltage from the ratio of hot-spot resistance to the resistance of metamaterial at 10 K. Even for the longest ramp pulses (with peak amplitude of 38 V), no more than 20% percent of metamaterial went into normal state. Based on numerical modeling of metamaterial's transient thermal response (see App. F), one can conclude that, during a super-critical ramp pulse, the mean temperature of sapphire substrate increased by less than 1 K. Such change can account for no more than 5% reduction in metamaterial transmission (see Fig. 3.7d).

The transmission modulation in the super-critical regime can be explained as follows. The experimentally observed transmission modulation is a result of the collective response of the entire metamaterial array. Its high-Q resonance corresponds to the excitation of anti-symmetric current modes in all the split-ring meta-molecules [71], which trap the radiation in the plane of the metamaterial array in the form of magneto-inductive surface waves (trapped mode; see Sec. 3.2). Such waves were shown to mediate interactions between the meta-molecules, making the metamaterial response very sensitive to any changes in the array [2, 70]. Consequently, when only few meta-molecules undergo the transition to the normal state, the locally increased Joule losses draw energy from the entire metamaterial array, and therefore affect its transmission by a far greater proportion than one would expect from purely geometrical considerations[27]. After the control pulse ends, the heat from niobium film escapes into the sapphire substrate through the contact thermal resistance (R_θ) formed between the two materials. As a re-

[27] The same effect has been demonstrated in a superconducting metamaterial bolometer in Sec. 3.3.

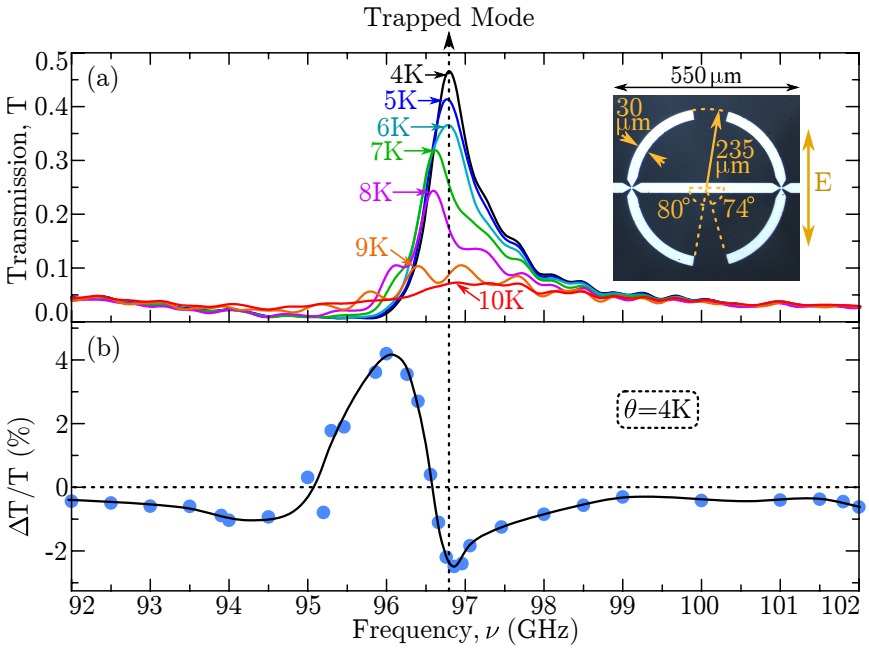

Figure 3.10: ***Behavior of the metamaterial modulator with constrictions under sub-critical regime of electro-optical control.*** ***(a)*** *Transmission of the metamaterial without the control signal. The inset shows the unit cell of the manufactured metamaterial (same as in Fig. 3.3).* ***(b)*** *Transmission modulation amplitude of the metamaterial with constrictions as a function of frequency of sub-THz radiation. The metamaterial is driven with sinusoidal control current at frequency 10 kHz, with amplitude of 100 mA. Modulation was measured at substrate temperature of $\theta = 4$ K.*

sult, the transmission of the metamaterial is restored to the original value. The observed transmission relaxation time of $20 - 25\,\mu s$ allows to estimate $R_\theta = 3 \times 10^{-3}\,\mathrm{K.m^2/W}$ (see App. F). This is significantly larger than some of the values reported for other low-temperature superconductors on sapphire substrates [146], indicating possible improvements for the future implementations. Assuming that heat can be withdrawn sufficiently fast from the sapphire substrate and ignoring the time it takes to induce a superconducting-to-normal phase change (this process can occur at sub-nanosecond rates [147–149]), the $25\,\mu s$ cooling time sets the maximum possible modulation bandwidth in the super-critical regime at 40 kHz.

3.4.4 Frequency-dependent electro-optical control in the sub-critical regime using metamaterial modulator with constrictions

The superconducting metamaterial bolometer described in Sec. 3.3 could also be used for electro-optical modulation. The main experimental results for the transmission modulation using this metamaterial will be presented below.

It can be shown (App. E), that the amplitude of sub-critical modulation in the asymmetrically-split ring (ASR) metamaterial modulators depends on the magnitude of the control current relative to the critical current of the metamaterial. Due to constrictions in the metamaterial bolometer from Sec. 3.3, its critical current (110 mA) is significantly

lower[28] than the critical current of the ASR metamaterial modulator *without* constrictions (500 mA; see Sec. 3.4.3). As a result, stronger transmission modulation can be achieved using ASR metamaterial *with* constrictions (from Sec. 3.3), than using the ASR metamaterial *without* constrictions, for the same magnitude of the control current. This has allowed to characterize the sub-critical transmission modulation in the metamaterial *with* constrictions not only at frequencies where the modulation was strong (at the trapped mode resonance), but also away from the metamaterial resonance, where the modulation was weak.

Figure 3.10a shows the transmission spectrum of the ASR *with* constrictions. Compared to metamaterial *without* constrictions, the trapped mode resonance (at $\nu_0 = 96.8\,\mathrm{GHz}$) is slightly red-shifted due to extra capacitance provided by the constrictions[29].

Figure 3.10b shows the amplitude of transmission modulation of the metamaterial *with* constrictions as a function of frequency of sub-THz radiation. As one would expect, the maximum transmission modulation[30] occurs near the trapped mode resonance.

Apart from lower magnitude of the required control signal, the metamaterial modulator *with* constrictions demonstrated similar transmission modulation performance to the metamaterial modulator *without* constrictions. The only noteworthy difference[31] was that, in metamaterial *with* constrictions, the transmission relaxation time following super-critical ramps was $\tau = 33\,\mu\mathrm{s}$, suggesting the thermal resistance of $R_\theta \approx 5 \times 10^{-3}\,\mathrm{K.m^2/W}$ (see Sec. 3.4.3 and App. F).

3.4.5 Summary

In this section it was demonstrated that by running current though a network of metamolecules in a superconducting metamaterial, one could achieve strong and fast modulation of sub-THz radiation passing through the metamaterial. Experimental proof-of-principle demonstration of such modulation has been provided, and the underlying physical mechanisms of the effect have been identified. The suggested approach to modulation can be extended to modulating terahertz radiation with high-temperature superconductor metamaterials [150, 151].

Compared to recently demonstrated semiconductor-based metamaterial modulators [122, 152–154], the superconducting metamaterial modulator described here achieved

[28] At the constrictions, the width of the niobium wire is reduced from 30 μm to $3-7\,\mu\mathrm{m}$. Correspondingly, the critical current of the wire is reduced by the same proportion.

[29] The metamaterial was contaminated and had to be cleaned between the transmission modulation experiments (reported here) and the bolometer experiments (reported in Sec. 3.3). The contamination in the constrictions could not be removed completely which explains further red-shift in metamaterial transmission spectrum evident in Fig. 3.5a.

[30] Relative transmission modulation is actually larger around 96.0 GHz, but this corresponds to the dip in metamaterial transmission, so the difference in transmitted radiation in 'on' and 'off' states is greatest at the trapped mode ($\nu_0 = 96.8\,\mathrm{GHz}$).

[31] The thermal resistance between the niobium film and sapphire substrate measured for the metamaterial with constrictions differs slightly from the value determined for metamaterial without constrictions (see 3.4.3). This difference is explained by slight variation in the bonding strength between the niobium and sapphire in the two samples.

similar rate and depth of modulation with a much larger active area (and therefore much lower control power per active metamaterial area) due to the virtual absence of a capacitive response. The same property makes the demonstrated approach well suited to the situations where the transmission modulation of a large area is required[32], and offers an advantage over the existing schemes of terahertz-range electro-optical modulation based on optical and microwave mixing [63].

I was unable to demonstrate modulation rates beyond 100 kHz due to limited bandwidth of the equipment, but I argue that the mechanism of conductivity modulation exploiting the self-induced magnetic field is extremely fast. Indeed, the Abrikosov vortices in niobium have been reported to propagate as fast as 2000 m/s [155], which brings the rate of the potential transmission modulation in the superconducting metamaterial into the VHF frequency band.

3.5 Giant nonlinear response in sub-THz superconducting metamaterials

Materials with nonlinear electromagnetic response are of key importance for fast information processing. Nonlinear mixing of signals (also called heterodyning) has been a major technological development in radio electronics, fueling the growth of world-wide radio communications [156]. Basic nonlinear electronic components such as diodes and transistors form the bedrock of modern digital electronics [156]. More recently, the developments in nonlinear optics have driven the rapid expansion in the field of photonics with wide-ranging applications from spectroscopy [157] to world-wide-web [158].

For a long time the nonlinear terahertz response of materials has remained relatively under-explored due to lack of easily-accessible sources of intense terahertz waves. The introduction of the tilted-pulse-front optical rectification has been a major advancement in the field of terahertz and sub-THz technology [159–163]. This technique has for the first time provided access to terahertz radiation powerful enough to study the nonlinear response of materials using a tabletop setup, and is now driving research in the field of material science [164]. Before this research can be translated into technological applications, for example in medicine, the level of required terahertz power will have to be reduced. Metamaterials provide a way to achieve the reduction in the required terahertz power, by concentrating the electromagnetic energy on the sub-wavelength scale (within the meta-molecules), thus significantly enhancing any natural nonlinearity of the underlying material [21].

Several groups have already demonstrated nonlinear terahertz metamaterials based on VO_2 [165], semiconductors [166], and superconductors[33] [168, 169]. However, the level of radiation intensity needed to observe the nonlinear response still remains high.

[32] Such as imaging and spatially multiplexed communications.

[33] Experiments on nonlinear response in microwave superconducting metamaterials have also been reported [144, 167].

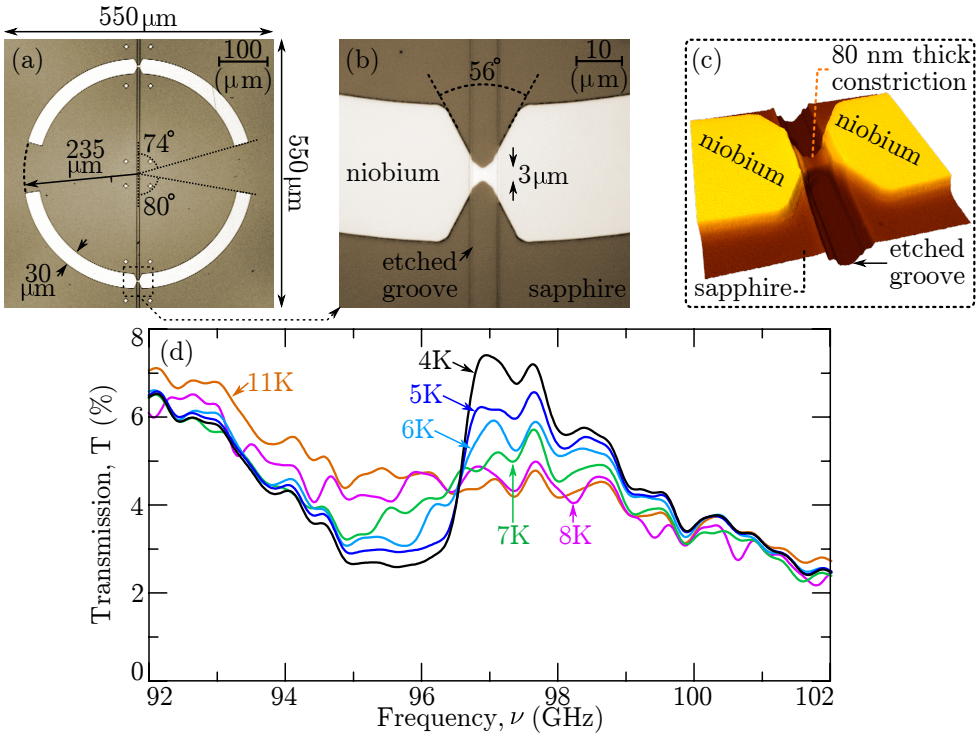

Figure 3.11: ***Design and linear (low-intensity) transmission of the selectively-etched asymmetrically-split ring metamaterial.*** ***(a)*** *The microscope picture of the metamaterial unit cell. Lighter areas are the niobium film (300 nm thick), darker areas are the sapphire substrate (0.5 mm thick).* ***(b)*** *Magnified junction in the asymmetric arc.* ***(c)*** *Interference microscope profile of the junction (colour indicates height).* ***(d)*** *Transmission spectrum of the metamaterial measured at low intensity of incident radiation (less than* $1\ W/m^2$*). Rapid oscillations in the transmission are caused by reflections between metamaterial and antennas.*

In this section, it will be demonstrated how a multi-stage photolithography process can be used to enhance the nonlinear response of the superconducting metamaterial, thus allowing to observe nonlinear sub-THz response at significantly lower intensity than in the previously reported demonstrations.

3.5.1 Sample design and linear response

Figures 3.11a-c show the design of the manufactured nonlinear superconducting metamaterial. It has been manufactured in two stages. In the first stage, the thin niobium film (300 nm thick) on sapphire substrate (0.5 mm thick) was photolithographically patterned into planar array of asymmetrically-split ring (ASR) resonators. By design, the niobium strips in each ASR meta-molecule were tapered down from widths of 30 μm to 3 μm wide constrictions, located at points of anti-nodes of the oscillating currents driven by the sub-THz radiation (see Fig. 3.1b). In the second stage of photo-lithography, a narrow groove was etched into each meta-molecule, with the rest of the metamaterial remaining unchanged (see Sec. 2.3 for manufacturing methods). As a result, the thickness

of the constrictions in each meta-molecule was reduced to just[34] 80 nm (see Fig. 3.11b,c).

For characterization, the manufactured sample was housed inside the optical cryostat, and its transmission has been measured in a free-space setup with low-intensity[35] sub-THz radiation at normal incidence (see Sec. 2.1 and Sec. 2.2 for details of the experimental setup). Figure 3.11d shows the metamaterial transmission spectrum for a range of substrate temperatures. At temperature $\theta = 4\,\mathrm{K}$, the selectively-etched metamaterial displays an asymmetrically-shaped transmission peak around $\nu = 97.4\,\mathrm{GHz}$. When the metamaterial temperature is increased towards niobium's superconductor-to-metal phase transition point ($\theta_\mathrm{C} \approx 9\,\mathrm{K}$), the peak flattens until it vanishes completely.

3.5.2 Measurement of the nonlinear response

This section will describe the procedure that was used to extract the nonlinear response of the metamaterial.

An external radiation power amplifier had to be used in order to achieve sufficient radiation intensity (see Sec. 2.2.7). Since the amplifier only allowed the radiation to pass in one direction, the two-port error correction could not be applied (see Sec. 2.2.1). An alternative way to eliminate the systematic errors due to uncalibrated VNA and amplifier, is to assume that these errors can be described by a product of frequency-dependent factor $A(\nu)$ and a quantity that is proportional[36] to the intensity of radiation that reached the receiver: $\mathcal{I} \cdot T$, where $\mathcal{I}$ is the intensity of radiation that reached the metamaterial and T is the metamaterial transmission. In this case, the uncalibrated signal measured by the VNA on the receiving port will be given by:

$$S_{uncal}\left(\nu, P, \theta\right) \propto A\left(\nu\right) \cdot \mathcal{I} \cdot T(\nu, \mathcal{I}, \theta)$$

where θ is the metamaterial temperature. Next, one can use the fact that conductivity of niobium will virtually seize to depend on temperature[37] and on current density just above the superconducting transition, e.g. at $\theta > 9.2\,\mathrm{K}$. Hence the transmission of the metamaterial, at temperature $\theta \gtrsim 11\,\mathrm{K}$, will be virtually independent of temperature and of the incident radiation intensity: $T(\nu, \mathcal{I}, \theta \gtrsim 11\,\mathrm{K}) = T_{11\,K}(\nu)$. As a result, one can extract the normalized transmission of the metamaterial from uncalibrated measurements:

$$\frac{T(\nu, \mathcal{I}, \theta)}{T_{11\,K}(\nu)} = \frac{S_{uncal}\left(\nu, \mathcal{I}, \theta\right)}{S_{uncal}\left(\nu, \mathcal{I}, \theta \gtrsim 11\,\mathrm{K}\right)}$$

[34] Due to finite manufacturing tolerance and inhomogeneities of the niobium film, the thickness of the selectively-etched constrictions varied from 60 nm to 100 nm over the metamaterial area. Thickness of 80 nm is therefore a representative value of the constriction thickness.

[35] Less than $1\,\mathrm{W/m^2}$.

[36] The intrinsic assumption here is that the signal detected by the radiation sensor in the mm-wave module (see Sec. 2.2.2) is proportional to the intensity of incident radiation. This assumption has been verified (found to be justified) by measuring the signal on the detector when the radiation was passed through the absorbing foam with a known transmission coefficient (see App. G).

[37] The electrical resistivity of most metals, including niobium (in the normal state), changes very little with temperature, when the temperature decreases to few tens of Kelvin.

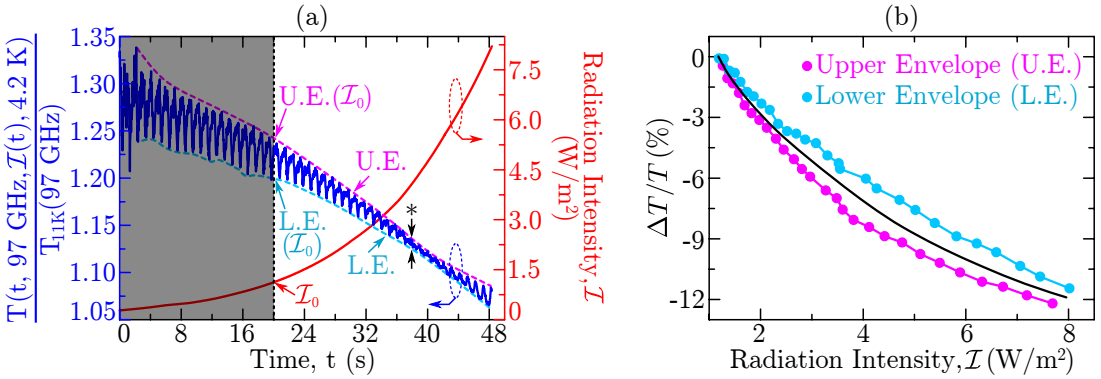

Figure 3.12: ***Change in normalized metamaterial transmission due to intensity of incident radiation at frequency ν=97 GHz and temperature θ=4.2 K. (a) Left axis (blue):*** *Metamaterial transmission as a function of time at frequency 97 GHz and temperature 4.2 K, normalized with respect to transmission at temperature 11 K. Oscillations in transmission are caused by the cryostat pump. The envelopes of the oscillations of metamaterial transmission are labeled as U.E. (upper envelope) and L.E. (lower envelope).* ***Right axis (red):*** *Intensity of radiation incident on metamaterial ($\mathcal{I}$). The grayed-out area marks the region that was not reliable enough to include in the analysis. The edge of the grayed-out area corresponds to reference point for both the envelope curves and for the intensity ($\mathcal{I}_0 = 1.12\ W/m^2$). The oscillations of metamaterial transmission due to cryostat pump are minimized at time $t = 38\ s$ ($\mathcal{I} = 4.11\ W/m^2$). This point is labeled with '*'.* ***(b)*** *Change in metamaterial transmission as a function of radiation intensity. Scattered points with connecting lines (blue and pink) show the change in the upper and lower envelopes of the normalized transmission trace from sub-figure (a), relative to envelope values at intensity $\mathcal{I}_0$ (see (a)). The average between the two envelope curves, shown with a solid black curve, will be defined as the intensity-dependent relative change of metamaterial transmission ($\Delta T/T$) at frequency $\nu = 97\ GHz$ and temperature $\theta = 4.2\ K$.*

In reality, the temperature oscillations due to cryostat pump (see Sec. 2.2.4) added another layer of complexity, since the metamaterial temperature could not be held constant. It was convenient to separate the dependence of metamaterial transmission on temperature into dependence on average temperature ($\bar{\theta}$) and dependence on pump-related temperature oscillations. The latter could be described as explicit dependence on time (t). Thus the normalized transmission of the metamaterial became:

$$\frac{T(\nu,\mathcal{I},\theta)}{T_{11\,K}(\nu)} \quad \rightarrow \quad \frac{T(t,\nu,\mathcal{I},\bar{\theta})}{T_{11\,K}(\nu)}$$

Figure 3.12a shows $T(t,\ 97\,\mathrm{GHz},\ \mathcal{I}(t),\ 4.2\,\mathrm{K})/T(97\,\mathrm{GHz};\ 11\,\mathrm{K})$, the ratio of the metamaterial transmission at temperatures 4.2 K and 11 K as a function of time (t), measured with slowly increasing intensity of incident radiation ($\mathcal{I} = \mathcal{I}(t)$) at a fixed frequency $\nu = 97\,\mathrm{GHz}$. The fast oscillations of the normalized transmission appear as a result of metamaterial temperature oscillations due to cryostat pump. The slow decline of the normalized transmission is caused by the increasing intensity of incident radiation (see Fig. 3.12a). Measurements at very low intensities of radiation were noisy due to performance of the power amplifier, so only the data measured with intensity higher than or equal to $1.12\,\mathrm{W/m^2}$ ($\mathcal{I}_0$) was used in the following analysis.

The aim of the experiment is to extract the relative change in metamaterial trans-

	Lowest	Highest
Power At Metamaterial Plane:	-1 dBm 0.79 mW	+7.4 dBm 5.5 mW
Intensity: (30mm diameter crossection)	1.1 W/m^2	7.8 W/m^2
Peak Electric Field:	0.29 V/cm	0.77 V/cm
Power Per Unit Cell:	-35 dBm 0.34 μW	-26 dBm 2.4 μW

Table 3.2: ***Minimum and maximum radiation power used in the measurement of the nonlinear response of metamaterial.***

mission ($\Delta T/T$) due to change in radiation intensity ($\mathcal{I}$). In principle, the relative intensity-dependent change in metamaterial transmission is given by:

$$\Delta T/T = \frac{\frac{T(\nu,\mathcal{I},\theta)}{T_{11\,K}(\nu)} - \frac{T(\nu,\mathcal{I}_0,\theta)}{T_{11\,K}(\nu)}}{\frac{T(\nu,\mathcal{I}_0,\theta)}{T_{11\,K}(\nu)}} = \frac{T(\nu,\mathcal{I},\theta) - T(\nu,\mathcal{I}_0,\theta)}{T(\nu,\mathcal{I}_0,\theta)}$$

The analysis is complicated by the oscillations in metamaterial transmission due to cryostat pump. However, the influence of the pump is eliminated, if one analyzes the *envelopes* of the normalized transmission trace (see Fig. 3.12a), since in this case one compares the transmission at the same points in the cycle of cryostat oscillations (hence the temperature of metamaterial will be the same). The upper and lower envelopes of the normalized transmission trace are outlined in Fig. 3.12a. Figure 3.12b shows the relative change in envelopes with respect to envelope value at the minimum intensity used in the experiments ($\mathcal{I}_0$). The difference between the two resulting curves is small enough, to define the relative change in metamaterial transmission as the average between the two envelope curves (see Fig. 3.12b).

The method of measuring the nonlinear response outlined in this section has been tested on an absorbing carbon foam in App. G.

3.5.3 Nonlinear response

The nonlinear response of the metamaterial has been measured with intensity of incident radiation ranging from 1.12 W/m^2 to 7.77 W/m^2 (see Table 3.2).

Figures 3.13a,b show how the metamaterial transmission changes with increasing radiation intensity for different metamaterial temperatures and at different frequencies of incident radiation. Despite the low intensity of radiation used in the experiment, the transmission of the metamaterial changed by up to 13.3%, as the intensity was ramped from 1.12 W/m^2 to 7.77 W/m^2 (see Fig. 3.13a).

Figure 3.13a shows that the nonlinear (intensity-dependent) change in metamaterial transmission is quite sensitive to changes in temperature of the substrate. The nonlinear response is prominent at temperature 4 K, but vanishes before the substrate temperature

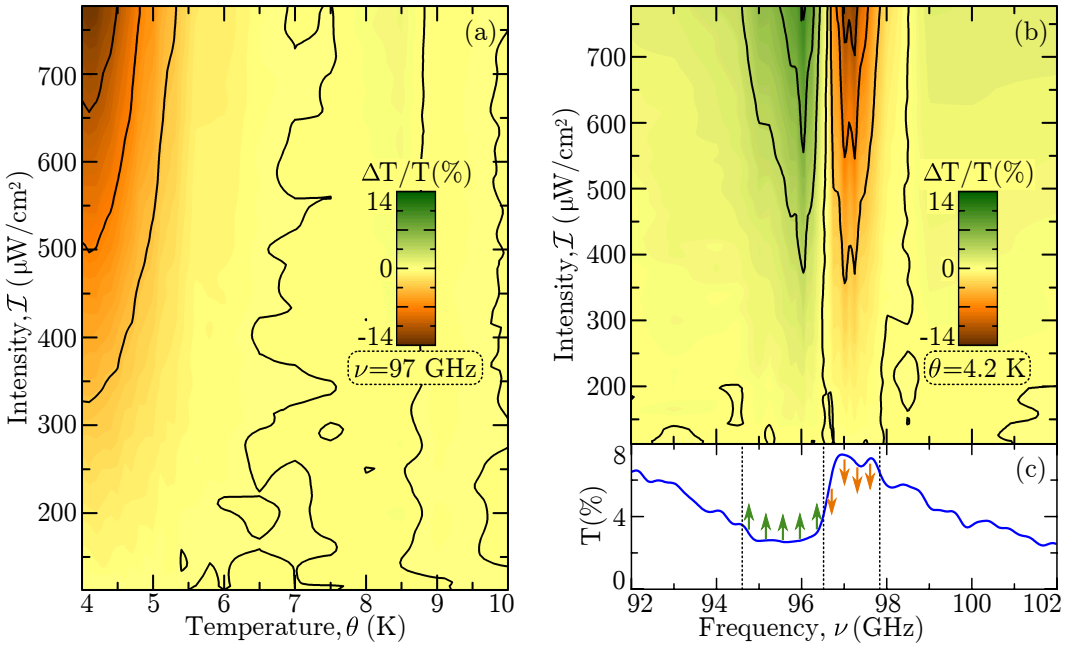

Figure 3.13: ***Nonlinear response of the metamaterial.*** ***(a)*** *Relative change in metamaterial transmission as a function of temperature (θ) and radiation intensity ($\mathcal{I}$) at a fixed frequency $\nu = 97$ GHz. Largest change in transmission, $\Delta T/T = -13.3\%$, occurs at $\mathcal{I} = 7.77$ W/m^2 and $\theta = 4.1$ K.* ***(b)*** *Relative change in metamaterial transmission as a function of radiation intensity and frequency (ν) at a fixed temperature $\theta = 4.2$ K. Largest negative change in transmission, $\Delta T/T = -12.2\%$, occurs at $\mathcal{I} = 7.77$ W/m^2 and $\nu = 97.3$ GHz. Largest positive change in transmission, $\Delta T/T = 10.5\%$, occurs at $\mathcal{I} = 7.77$ W/m^2 and $\nu = 96.0$ GHz.* ***(c)*** *Transmission of the metamaterial in the linear regime, at substrate temperature of $\theta = 4$ K (from Fig. 3.11d).*

reaches 6.5 K. Such a strong link between the nonlinear transmission change and the temperature of the metamaterial can be explained either by reduced critical temperature of the constrictions[38] (i.e. constrictions enter the normal state at temperature ~ 6.5 K), or by increased sub-THz Joule losses in niobium at higher temperature (higher losses lead to lower currents being induced in the meta-molecules, which, in turn, leads to lower nonlinear response). In reality, both of these effects are likely to contribute.

Figures 3.13b,c show that the increased radiation intensity, modifies the metamaterial transmission spectrum in the same way as increasing the temperature (see Fig. 3.11d), i.e. the transmission peak at frequency 97 GHz is lowered, whilst the transmission dip at 96 GHz is raised. The rest of the spectrum remains unchanged, showing that the nonlinearity of the metamaterial response is a resonant effect that is closely related to large radiation-induced currents that are forced to flow through narrow constrictions in the meta-molecules.

[38] The critical temperature of superconducting niobium films begins to drop significantly when the film thickness becomes comparable to the coherence length of the niobium (~ 40 nm) [170, 171].

Heating of the constrictions

Thermal resistance between the sapphire substrate and the niobium film established in the previous section[39] ($R_\theta \approx 4 \times 10^{-3}\,\mathrm{K.m^2/W}$), can be used to study the dynamics of heat transfer within the selectively-etched metamaterial.

A key question is whether the observed nonlinearity is a result of heating or high radiation-induced currents (i.e. currents comparable to the critical current). The former would only allow for slow variations in metamaterial transmission (on micro-second scale), whilst the latter could be utilized for sub-nanosecond routing and switching of sub-THz radiation [65–67].

Consider a small strip of niobium at temperature $\theta = 4\,\mathrm{K}$. Let the thickness, length and width of the strip be h, l, and w, respectively. Let the current density through the strip oscillate with amplitude equal to the critical current density for niobium: $J_c \approx 6 \times 10^6\,\mathrm{A/cm^2}$ (see Sec. 3.4.3). Assume that the conductivity of the strip is $\tilde{\sigma}_0 = (1.96 - \mathrm{i}2.10) \times 10^8\,\mathrm{S/m}$ (see App. E). The time-averaged power dissipated at the strip will be $P = \Re(J_c^2/\tilde{\sigma}_0)/2 \times hlw$. Assume that the temperature of the strip is constant (on average), then all the power dissipated by the current has to flow into the substrate as heat. The corresponding temperature difference between the strip and the substrate will be $\Delta\theta = R_\theta P/(lw) = hR_\theta\Re(J_c^2/\tilde{\sigma}_0)/2$. The nominal thickness of selectively-etched constrictions is $h = 80\,\mathrm{nm}$, giving $\Delta\theta = 1370\,\mathrm{K}$, which is more than 100 times larger than the critical temperature of niobium (9 K). This estimate shows that in my experiment, conducted with continuous wave radiation (slowly changing intensity), the small constrictions will always go into normal state due to heating, before the critical current density is reached. It should be noted, however, that the constriction height (h) can be potentially reduced by a factor of 2-5 (with further etching), the thermal resistance can be reduced by several orders of magnitude [146], and a different superconductor (with higher critical temperature) can be used. All together it means that, whilst in the experiment reported here, the nonlinear effects are almost certainly due to heating, further optimization may tip the balance in favor of nonlinearities due to large current densities. In any case, the fast nonlinear response due to large current densities can be observed with short (micro-second scale) bursts of radiation [65, 66].

Next, I will calculate the extent, to which the niobium film was heated in the experiments reported here. The power supplied to each unit cell of the metamaterial varied between $P = 0.32\,\mu\mathrm{W}$ and $2.4\,\mu\mathrm{W}$ (see Table 3.2). The contact area of the (remaining) niobium film with the sapphire substrate was $A \sim 3.5 \times 10^{-8}\,\mathrm{m^2}$, per unit cell. One can therefore conclude that even full absorption of the incident power would have heated the niobium film by $\Delta\theta = R_\theta P/A = 0.03 - 0.3\,\mathrm{K}$. Such a small increase in temperature is clearly not significant enough to change the metamaterial transmission[40] (see

[39] Thermal resistances of $3 \times 10^{-3}\,\mathrm{K.m^2/W}$ and $5 \times 10^{-3}\,\mathrm{K.m^2/W}$ have been measured for the metamaterial electro-optical modulators with and without constrictions, respectively (see Sec. 3.4.3 and Sec. 3.4.4). The average between these two values will be used here.

[40] Such a change in temperature is smaller than the estimated amplitude of the temperature oscillations

Fig. 3.11d). On the other hand, this power would be more than sufficient to heat up the small selectively-etched constrictions with contact area $A_\times \sim 3.9 \times 10^{-11}\,\mathrm{m}^2$.

Figure 3.12a shows that the oscillations of metamaterial transmission due to cryostat pump decrease in amplitude as the radiation intensity is increased. At intensity of $\mathcal{I} \approx 4.11\,\mathrm{W/m}^2$ (this point is marked with '*' in Fig. 3.12a), the oscillations in the normalized metamaterial transmission are of the same amplitude as for metamaterial above the critical temperature, i.e. when it is in the normal state[41]. This effect can be explained by constrictions in the asymmetrically-split rings entering the normal state, whilst the rest of the niobium remains in the superconducting state. Once in the normal state, the resistance of the constrictions will not depend strongly on the temperature. Provided the resistance of the constrictions, in the normal state, dominates over the resistance of the rest of the meta-molecule[42], the metamaterial transmission will seize to respond to temperature oscillations (due to cryostat pump) as soon as constrictions will enter the normal state. Assuming that the conductivity of niobium in the normal state, just above the critical temperature, is[43] $\sigma_n = 3.44 \times 10^7\,\mathrm{S/m}$, one can estimate the resistance of the single constriction: $R_\times \approx 0.4\,\Omega$. Assuming that the current excited in the meta-molecules ($I_\times$) is just high enough to keep the constrictions in the normal state ($\Delta\theta \approx 5\,\mathrm{K}$) allows to calculate the power dissipated at each constriction $P_\times = I_\times^2 R_\times/2 = \Delta\theta \cdot A_\times/R_\theta = 0.05\,\mu\mathrm{W}$, as well as the amplitude of the induced current $I_\times = \sqrt{2A_\times\Delta\theta/R_\times R_\theta} \approx 0.5\,\mathrm{mA}$. This current should be compared with the critical current of the constrictions, which, at $\theta = 4\,\mathrm{K}$, will be $I_c \sim J_c \times w \times h \approx 14\,\mathrm{mA}$. One can therefore deduce that the absolute maximum radiation intensity, required to excite current equal or greater than the critical current in the constrictions, would be $\left(4.11\,\mathrm{W/m}^2\right) \times (14/0.5)^2 = 3\,\mathrm{kW/m}^2$.

Comparison with other nonlinear superconducting metamaterials

The selectively-etched metamaterial demonstrated in this section, showed more than 10% change in transmission when the intensity of the incident radiation was increased from $\sim 1\,\mathrm{W/m}^2$ to $\sim 8\,\mathrm{W/m}^2$ (peak strength of electric field change from 300 mV/cm to 800 mV/cm; power per unit cell change from -35 dBm to -26 dBm). Nonlinear response at such a low level of radiation intensity compares favourably with previously demonstrated nonlinear superconducting metamaterials in the microwave [172,173] (90% change in transmission with power per unit cell increasing from +10 to +20 dBm), and in the terahertz spectrum [168, 169] (more than 99% change in transmission with peak

due the cryostat pump (see Sec. 2.1).

[41] When the (average) temperature of metamaterial was slightly above the critical point of niobium, the (relative) magnitude of oscillations in metamaterial transmission due to cryostat pump was of order 1%-0.5%. The magnitude of oscillations in metamaterial transmission at point marked with '*' in Fig. 3.12a is approximately 0.6%.

[42] Basic calculations show that the resistance of the constrictions in the normal state will be at least 6 times larger than the resistance of the rest of the ASR meta-molecule at temperature 4 K.

[43] Using the same normal state conductivity of niobium as for the superconducting metamaterial bolometer from Sec. 3.3.

field strength changing from 1 kV/cm to 30 kV/cm).

The order of nonlinear response

The potential practical applications of nonlinear sub-THz metamaterials will depend greatly on the nature of the nonlinear response. In particular it is important to know the order of the nonlinearity, i.e. what power of local electric field (**E**) contributes to the current density (**J**) in the constitutive equation (Greek indices stand for x, y, z):

$$(\mathbf{J})_\alpha = \sum_\beta \sigma^{(1)}_{\alpha,\beta} (\mathbf{E})_\beta + \underbrace{\sum_{\beta,\gamma} \sigma^{(2)}_{\alpha,\beta,\gamma} (\mathbf{E})_\beta (\mathbf{E})_\gamma}_{quadratic\,nonlinearity} + \underbrace{\sum_{\beta,\gamma,\zeta} \sigma^{(3)}_{\alpha,\beta,\gamma,\zeta} (\mathbf{E})_\beta (\mathbf{E})_\gamma (\mathbf{E})_\zeta}_{cubic\,nonlinearity} + ...$$

where the various conductivity tensors, such as $\sigma^{(1)}_{\alpha,\beta}$, $\sigma^{(2)}_{\alpha,\beta,\gamma}$, $\sigma^{(3)}_{\alpha,\beta,\gamma,\zeta}$, by definition do not depend on the magnitude of the electric field.

As was deduced in the preceding section, the most likely origin of the intensity-dependent change in the transmission of nonlinear sub-THz metamaterial presented in this thesis, is the heating of the selectively-etched constrictions. This corresponds to cubic nonlinearity [73]. In general, depending on the dominating mechanism of the nonlinearity in superconductor, the order of nonlinear response can be quadratic, cubic or even higher [73].

The main aim of the work presented in this section, was the proof-of-principle demonstration of the low-intensity nonlinear response in a superconducting sub-THz metamaterial. Future work should be directed at achieving stronger nonlinear response of the right kind, i.e. nonlinearity of a suitable order[44].

3.5.4 Summary

This section demonstrated low-intensity nonlinear response in the superconducting metamaterial driven by the sub-THz radiation. It has been shown that the main mechanism of the nonlinear response, in the presented experiments, is the local heating of the thin superconducting constrictions. Experiments with short bursts of radiation are required to study the faster nonlinear processes.

The strength of nonlinear response in the metamaterial presented here compares favourably with results demonstrated by other researchers. With the low Joule losses [95], and sub-nanosecond relaxation rates in superconducting films [65–67], the superconducting metamaterials offer a great potential for the development of fast nonlinear switching and data processing solutions for the now rapidly expanding field of terahertz technology.

[44] For example, it may be undesirable to have a nonlinear metamaterial with nonlinear response dominated by odd-order nonlinearity, since one of the harmonics that will appear as a result of such nonlinearity will be oscillating at the same frequency as the original (driving) signal which may lead to unwanted interference.

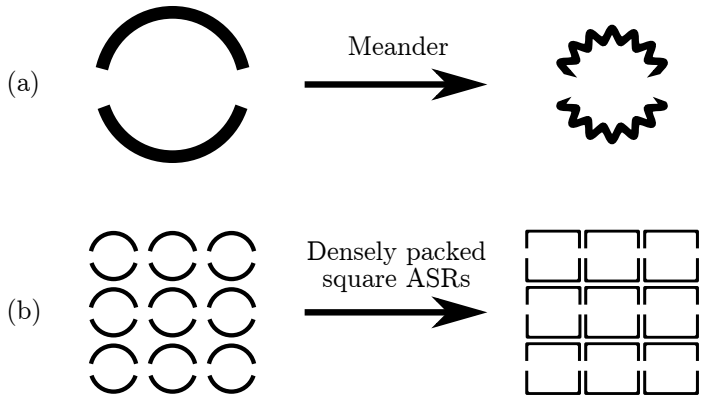

Figure 3.14: ***Possible design approaches aimed at improving the performance of the ASR metamaterials. (a)*** *The physical size of the ASRs can be reduced by meandering the asymmetric arcs. Reduced size of the ASRs will lead to reduced radiation losses and, therefore, to higher quality resonant response.* ***(b)*** *The shape of the ASRs can be altered to allow for more denser packing of the ASRs in the metamaterial. For example, the ASRs can be made square-shaped, which will allow to pack them densely in the metamaterial with square lattice. Such packing will allow for better confinement of the electromagnetic energy at the surface of the metamaterial.*

3.6 Possible future improvements to ASR metamaterials

This section will briefly describe the possible modifications to ASR metamaterial design that may improve the functionality demonstrated in the preceding sections of this chapter.

Two strategies for improving the ASR metamaterial design are shown in Fig. 3.14 and are discussed in the paragraphs below:

Smaller unit cell: High-quality response of the ASR metamaterials is crucial for all applications discussed in the preceding sections since it allows to achieve high concentration of electromagnetic energy, which is necessary to utilize the nonlinear response of the superconductors. The quality factor of metamaterial's resonant response is ultimately limited by Ohmic losses and by radiation losses. Implementing the metamaterials out of superconductors helps to reduce the Ohmic losses. Shrinking the physical size of the of the ASRs (without increasing the resonant frequency) will reduce the radiation losses[45]. The simplest way of achieving the reduction in size of ASRs is to introduce a meander into the asymmetric arcs, as is shown in Fig. 3.14a.

Denser packing: It has been shown in Ref. [80] that the reduction in spacing between the ASRs will lead to stronger confinement of electromagnetic energy at the metamate-

[45]The ASRs in the ASR metamaterial scatter mostly through the induced electric dipole [71, 92]. In electrodynamics, the electric dipole is given by the product of the amplitude of oscillating charge density and the separation of the positive and negative charges [174]. Therefore reducing the volume occupied by the charge density (i.e. the size of the ASR) will lead to smaller electric dipole (less scattering) even if the magnitude of charge oscillations will remain unchanged.

rial plane, which is crucial for utilization of the nonlinear response of superconductors. Such confinement can be achieved by making ASRs square-shaped and packing them into a very dense lattice, as is shown in Fig. 3.14b.

3.7 Conclusions

In this chapter I have demonstrated how the behaviour of the superconductors, combining low Joule losses with high sensitivity and nonlinearity, can be utilized to create a range of active terahertz metamaterials.

I have demonstrated radiation sensing, radiation modulation and low-intensity nonlinear response, thus covering the three basic types of devices required in any electromagnetic spectrum. All demonstrations have been carried out using similar structures and similar manufacturing methods, which allowed for a high degree of cross-comparison.

The work carried out in this chapter has focused on the proof-of-principle demonstrations of superconducting metamaterials as a natural platform for novel terahertz spectrum devices.

Chapter 4

Toroidal Excitations in Metamaterials

4.1 Introduction

Toroidal dipole is a peculiar electromagnetic excitation that cannot be presented in terms of the standard electric and magnetic multipoles [175–177]. First described by Ya. B. Zeldovich in 1957 [178], it can be visualized as current flowing along the meridians of an infinitesimally small torus[1] or, equivalently, as an infinitesimally small closed loop of magnetization[2] (see Fig. 4.1c). Toroidal dipole has been predicted to have a number of intriguing properties: static toroidal dipole is held responsible for parity violation in atomic spectra [179–181]; interactions between static toroidal dipole and oscillating magnetic dipole are claimed to violate Newton's Third Law[3] [182]; whilst different opinions exist on whether oscillating charge-current configurations involving toroidal dipole could radiate non-compensated vector potential in the absence of electromagnetic fields [183, 184].

The toroidal dipole is usually omitted in classical electrodynamics [174, 185]. This omission has recently been shown to be unjustified with the demonstration of the so-called *toroidal metamaterials*: the metamaterial structures specifically designed to exhibit strong toroidal dipole excitations. The first toroidal metamaterial has been demonstrated in the microwave spectrum [17], followed by further demonstrations at

[1] A meridian of a torus is the circle created by intersection of the torus with a plane that stretches from the axis of rotational symmetry of the torus to infinity. The definition is visualized in App. H.

[2] This alternative representation of the toroidal dipole is sometimes more convenient for analysis. Appendix M demonstrates the application of this definition in establishing the angular momentum of a toroidal dipole in external electromagnetic field.

[3] The detailed explanation of this claim can be found in Sec. 7.2.3 and Sec. 7.2.4 in Ref. [182]. To summarize, the author shows that as a result of electromagnetic interaction (between the static toroidal dipole and oscillating magnetic dipole) the static toroidal dipole will experience a force whilst the oscillating magnetic dipole will not. This may be viewed as a violation of Newton's Third Law, since the magnetic dipole effectively pushes the toroidal dipole without experiencing an equal and opposite force in return. The author notes that momentum of the whole system (magnetic dipole, toroidal dipole and the electromagnetic field) however, remains conserved at all times.

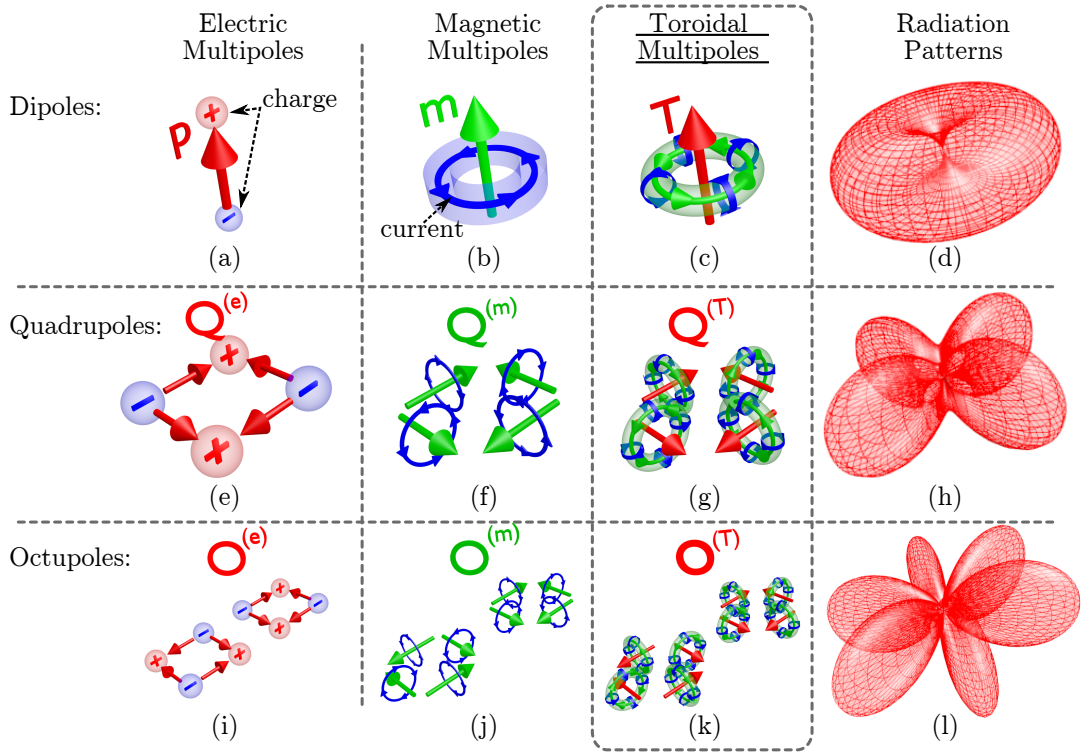

Figure 4.1: ***Three families of dynamic multipoles.*** *The three columns on the left show the charge-current distributions that give rise to the electric (**p**), magnetic (**m**) and toroidal (**T**) dipoles, electric ($\mathbf{Q}^{(\mathbf{e})}$), magnetic ($\mathbf{Q}^{(\mathbf{m})}$) and toroidal ($\mathbf{Q}^{(\mathbf{T})}$) quadrupoles as well as the electric ($\mathbf{O}^{(\mathbf{e})}$), magnetic ($\mathbf{O}^{(\mathbf{m})}$) and toroidal ($\mathbf{O}^{(\mathbf{T})}$) octupoles. The toroidal dipole (**T**), is created by the oscillating poloidal current - the current that flows along the meridians of a torus. The next member of the toroidal multipole family, the toroidal quadrupole ($\mathbf{Q}^{(\mathbf{T})}$), is created by the anti-aligned pairs of toroidal dipoles. The toroidal octupole ($\mathbf{O}^{(\mathbf{T})}$), in turn, is created out of the anti-aligned toroidal quadrupoles. The column on the (far) right shows the patterns of radiation (i.e. intensity as a function of direction) emitted by the various harmonically oscillating multipoles (for quadrupoles, only the radiation associated with the off-diagonal component of the second-rank quadrupole moment tensor is shown, for octupoles only the radiation associated with the component of the third-rank octupole moment tensor, with two repeated indices and the third distinct index, is shown).*

microwave [186–188] and at optical frequencies [189–192].

Like the conventional electric and magnetic multipoles, the toroidal dipole originates from the electric charge-current distribution. Nevertheless, the toroidal dipole is fundamentally different from the electric and magnetic multipoles (see Fig. 4.1). At the same time, however, the radiation pattern of the toroidal dipole is indistinguishable from that of the electric dipole to any distant observer [183]. Consequently, combinations of destructively interfering electric and toroidal dipoles, allow to explain the localized distributions of oscillating currents that do not emit into the free-space. As a result, understanding of the toroidal dipole excitations could have significant benefits for many fields of photonics where local field enhancement is key, including surface plasmon sensors [193–195], nanolasers [196], nonlinear optics of metallic nanoparticles [197–202], as well as for a wide class of organic and inorganic media containing constitutes with el-

ements of toroidal symmetry, such as biologically important molecules, fullerenes and bacteriophages. This calls for the development of a theory that links the microscopic toroidal excitations to the macroscopic response of the material such as transmission and reflection.

In this chapter, I derive an analytical formalism which provides a quantitative link between the microscopic multipole excitations within the metamaterials and the macroscopic metamaterial response. Following the derivation, the formalism is tested on an infrared toroidal metamaterial, in Sec. 4.2. Building on the derived formalism, in Sec 4.3, it is proved that the toroidal dipole excitations can only be observed in metamaterials with three-dimensional unit cells, and the simplest kind of such a metamaterial is demonstrated. Finally, Sec. 4.4 describes the first experimental observations of the non-trivial non-radiating charge-current excitations based on destructive interference of the electric and the toroidal dipoles in the toroidal metamaterial. The formalism derived in the preceding sections is used to verify the destructive interference.

4.2 Multipole decomposition of metamaterial response

Following the recent experimental demonstration of the dynamic toroidal dipole excitation in a toroidal metamaterial [17], the interest in this peculiar current excitation has been growing rapidly [186–191]. Yet, there still exists no theory to link the microscopic toroidal dipole excitations to the macroscopically observable properties of the metamaterial such as transmission and reflection. Instead, the researchers have analyzed the scattered power from the single unit cells of the metamaterial, integrated over all directions, as if the unit cell was isolated. This approach does allow for a *qualitative* comparison between macroscopic and microscopic response of the metamaterial, especially in cases where there is a dominant contribution from a single multipole (e.g. only the toroidal dipole in Ref. [17]), but it fails if there are several competing multipole contributions to metamaterial response, which are all of similar magnitude.

In this section, a rigorous formalism will be developed to fill this gap. By starting from the scattered fields of isolated multipoles, the amplitude and phase of the radiation scattered by an array of such multipoles are calculated. The scattered radiation is then related to metamaterial transmission and reflection. Similar problems, of calculating the scattered radiation from arrays of metallic resonators, have been addressed in the past using Fast Multipole Method (FMM) [203–207], and periodic Green's functions for the Helmholtz equation [208–210]. What makes this approach different is that it yields expressions sufficiently compact to be suitable not only for computer-aided calculations (like FMM), but also for the purely analytic evaluation[4]. At the same time, the presented approach accounts not only for the conventional multipoles but also for the elusive toroidal multipoles (see Fig. 4.1c,g,k).

[4]See Sec. 4.3.1 for an example of an analytic calculation that utilizes the formalism derived in this section.

The validity of the obtained formalism is verified using a test case study of a metamaterial (see Sec. 4.2.2), which reveals that the contribution of the toroidal dipole is crucial for the correct interpretation of the reflection and the transmission spectra of a certain class of metamaterials.

The results reported in this section have been prepared for submission to a journal and a pre-print was made available on-line [211].

4.2.1 Relation between the microscopic multipolar excitations and macroscopic metamaterial response

A general expression will now be derived for the electromagnetic field scattered by a two-dimensional array of identical charge-current excitations that are represented by a finite series of previously known dynamic multipoles. For the case of a passive materials (and metamaterials), these multipoles will have been induced by normally incident plane-wave radiation. It is assumed that the multipole moments can either be extracted from the numerical simulation of the induced currents, or calculated from the dynamics of charge and current densities anticipated for the meta-molecules of a known geometry [212–216]. In the interest of brevity, only the key steps of the derivation will be demonstrated, yielding the expression for the radiation from a two-dimensional array of toroidal dipoles. After this, the full expression, that includes all other multipoles, will simply be stated (further details of the derivation are described in App. I, J, K).

The derivation begins from the far-field distribution of the electric field radiated by a single oscillating toroidal dipole, which has been derived by Radescu and Vaman[5] [176]:

$$\mathbf{E}(\mathbf{r}) = \frac{-\mathrm{i}\mu_0 c^2 k^3}{3\sqrt{2\pi}} \cdot \frac{\exp\left(-\mathrm{i}kr\right)}{r} \cdot \sum_{m=0,\pm1} T_{1m} \left[\mathbf{Y}_{1,2,m} + \sqrt{2}\mathbf{Y}_{1,0,m}\right] \tag{4.1}$$

$$T_{1,\pm1} = \frac{1}{\sqrt{2}} \left(\mp T_x + \mathrm{i}T_y\right) \tag{4.2}$$

$$T_{1,0} = T_z \tag{4.3}$$

$$\mathbf{T} = \frac{1}{10c} \int d^3r \, \left[\mathbf{r}\left(\mathbf{r}.\mathbf{J}\right) - 2r^2\mathbf{J}\right] \tag{4.4}$$

Here μ_0 is the magnetic permeability of vacuum, c is the speed of light, $\mathbf{r}$ is the vector connecting the location of the dipole with the observer and $\mathbf{Y}_{l,l',m}$ are the spherical vector harmonics that allow to represent any vector field on the surface of the unit sphere in a similar way, as spherical harmonics allow to represent any scalar field on the surface of the unit sphere [175, 176, 217] (also see App. I.3). Toroidal dipole moment is denoted by $\mathbf{T}$, whilst $\mathbf{J}$ is the current density that gives rise to such dipole. All quantities are

[5]The current derivation is based on Eq. (3.15) from Ref. [176]. However, that equation is for the arbitrary time-dependence and is given in CGS units. A simplified version of Eq. (3.15) from Ref. [176], for the harmonic time-dependence, and in SI units, can be found in App. I.1 (Eq. (I.7)). Equation (4.1) is a single linear term of Eq. (I.7) for the case $l = 1$ and $n = 0$.

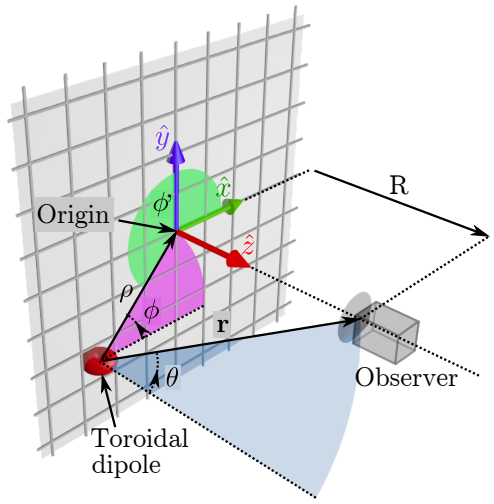

Figure 4.2: ***Calculating scattering from a two-dimensional planar array of toroidal dipoles.*** *A single toroidal dipole is represented by its radiation pattern. The vectors connecting the dipole to the observer and to the origin of the array are* $\mathbf{r}$ *and* ρ*, respectively. The observer is located at distance* R *from the array. The vector* $\mathbf{R}$ *is perpendicular to the array plane. The position of the observer relative to the dipole in spherical polar coordinates is* (r, θ, ϕ)*. The position of the dipole relative to the origin of the array in cylindrical polar coordinates is* (ρ, ϕ')*.*

specified in SI units. Complex-valued harmonic time-dependence, given by $\exp(+\mathrm{i}\omega t)$, is assumed, where ω is the angular frequency and $k = 2\pi/\lambda = \omega/c$ is the wavenumber.

The total field radiated by an infinitely large planar array of toroidal dipoles ($\mathbf{E}_s$) is obtained by summing the contributions from all the dipoles at the position of the observer. It is assumed that all dipoles oscillate in phase (i.e. the multipole array is induced by the plane wave radiation at normal incidence), and that the unit cell of the array (separation between dipoles) is sufficiently smaller than the wavelength to replace the sum over the unit cells with an integral over the array area (Δ^2 denotes the area of the unit cell).

$$\mathbf{E_s} = \sum_{\mathbf{r}} \mathbf{E}(\mathbf{r}) \approx \frac{1}{\Delta^2} \int_{array} d^2 r \, \mathbf{E}(\mathbf{r}) \tag{4.5}$$

It is convenient to work in the coordinate system where the array of dipoles lies in the xy-plane and the incident/scattered radiation propagates along the z-axis (see Fig. 4.2). Explicit evaluation of the relevant[6] spherical vector harmonics produces [176] (also see App. I.3):

$$\mathbf{Y}_{1,2,\pm1} + \sqrt{2}\mathbf{Y}_{1,0,\pm1} = \begin{pmatrix} \pm\sqrt{\frac{3}{10}}Y_{2,\pm2} \mp \sqrt{\frac{1}{20}}Y_{2,0} \mp Y_{0,0} \\ -\mathrm{i}\sqrt{\frac{3}{10}}Y_{2,\pm2} - \mathrm{i}\sqrt{\frac{1}{20}}Y_{2,0} - \mathrm{i}Y_{0,0} \\ -\sqrt{\frac{3}{10}}Y_{2,\pm1} \end{pmatrix}$$

[6] That is, the spherical vector harmonics that describe the electric field emitted by the toroidal dipole (Eq. (4.1))

$$\mathbf{Y}_{1,2,0}+\sqrt{2}\mathbf{Y}_{1,0,0}=\begin{pmatrix}\sqrt{\frac{3}{20}}Y_{2,1}-\sqrt{\frac{3}{20}}Y_{2,-1}\\ -\mathrm{i}\sqrt{\frac{3}{20}}Y_{2,1}-\mathrm{i}\sqrt{\frac{3}{20}}Y_{2,-1}\\ -\sqrt{\frac{2}{5}}Y_{2,0}+\sqrt{2}Y_{0,0}\end{pmatrix}$$

The spherical vector harmonics are presented in the Cartesian basis with column entries indicating the x-, y- and z-components (from top to bottom respectively), $Y_{l,m}$ are the standard spherical harmonics [176, 218]. The basic integral that needs to be calculated in Eq. (4.5), after substitution of Eq. (4.1), is:

$$I_{l,m}=\int\limits_{array} d^2r\, Y_{l,m}\exp\left(-\mathrm{i}kr\right)/r \tag{4.6}$$

One can show that this integral can be re-written as (see App. J):

$$\begin{aligned}I_{l,m}&=\int_0^{2\pi}d\phi'\int_0^{\infty}\rho d\rho\, Y_{l,m}\left(\theta,\phi'+\pi\right)\exp\left(-\mathrm{i}kr\right)/r\\&=\pi\delta_{m,0}\sqrt{\frac{2l+1}{\pi}}\left(\hat{\mathbf{R}}.\hat{\mathbf{z}}\right)^l\sum_{s=0}^{\infty}a_s^{(l)}\int_R^{\infty}dr\left(\frac{R}{r}\right)^s\exp\left(-\mathrm{i}kr\right)\end{aligned} \tag{4.7}$$

Where ρ and ϕ' are the radius and the angle specifying the position of the toroidal dipoles in the planar array (over which the integration is carried out), r is the distance between the observer and the toroidal dipole, θ is the angle between the line connecting the observer to a toroidal dipole and a normal to the array, and R is the distance from the observer to the array. All variables are annotated in Fig. 4.2. The unit vector pointing from the array towards the observer is $\hat{\mathbf{R}}=\mathbf{R}/R$. Index l can take positive integer values ($l=1,2,3...$), index m can take any integer values in the range $-l\leq m\leq l$, but the Kronecker delta will vanish unless m is zero ($\delta_{m,0}=1$ for $m=0$, otherwise $\delta_{m,0}=0$). The nature and value of coefficients $a_s^{(l)}$ is not important here, but their sum is given by $\sum_{s=0}^{\infty}a_s^{(l)}=1$ (see App. J).

To proceed, one needs to assume that the wavenumber is complex-valued and that its imaginary part is negative ($\Im(k)<0$), which is equivalent to assuming that radiation propagation occurs in space with losses. The losses can be marginally small, but a non-zero (negative) value of the imaginary part of k is necessary for the convergence of the family of integrals shown below:

$$\int_R^{\infty}dr\left(\frac{R}{r}\right)^s\exp\left(-\mathrm{i}kr\right)\cong\frac{\exp\left(-\mathrm{i}kR\right)}{\mathrm{i}k},\quad s=0,1,2...\text{ and }\Im\left(k\right)<0 \tag{4.8}$$

Equation (4.8) is exactly correct for $s=0$, but is correct only up to order $O\left(\lambda/R\right)$ for $s\geq 1$. However, this is not an issue, since one is only interested in the far-field radiation ($R\gg\lambda$). Note that up to order $O\left(\lambda/R\right)$, the value of the integral above does not depend on s. Substitution of Eq. (4.8) into Eq. (4.7) results in:

$$I_{l,m} \approxeq \frac{\pi\delta_{m,0}\left(\hat{\mathbf{R}}.\hat{\mathbf{z}}\right)^{l}}{\mathrm{i}k} \cdot \sqrt{\frac{2l+1}{\pi}} \cdot \exp\left(-\mathrm{i}kR\right) \tag{4.9}$$

Substitution of Eq. (4.1) into Eq. (4.5) and use of Eq. (4.9) allows to derive the far-field component of the electric field scattered by an array of identical toroidal dipoles:

$$\mathbf{E_s} = \frac{\mu_0 c^2 k^2}{4\Delta^2} \cdot \sqrt{2} \cdot \begin{pmatrix} T_{1,1} - T_{1,-1} \\ \mathrm{i}\left(T_{1,1} + T_{1,-1}\right) \\ 0 \end{pmatrix} \cdot \exp\left(-\mathrm{i}kR\right)$$

Further simplification, using Eq. (4.2), produces the final form:

$$\mathbf{E_s} = -\frac{\mu_0 c^2 k^2}{2\Delta^2}\,\mathbf{T}_{\parallel}\,\exp\left(-\mathrm{i}kR\right) \tag{4.10}$$

The subscript $(...)_{\parallel}$ denotes the projection of the vector into the plane of the array. If one assumes the coordinate system shown in Fig. 4.2, where the array lies in the xy-plane, the projection of the toroidal dipole is given by $\mathbf{T}_{\parallel} = T_x\hat{\mathbf{x}} + T_y\hat{\mathbf{y}}$ (i.e. the z-component is dropped since it is perpendicular to the array). In general, $\mathbf{T}_{\parallel} = \mathbf{T} - \left(\mathbf{T}.\hat{\mathbf{R}}\right)\hat{\mathbf{R}}$.

Repeating the same derivation steps for other multipoles leads to the following result (note that the fourth linear term corresponds to Eq. (4.10)):

$$\begin{aligned}\mathbf{E}_s = \frac{\mu_0 c^2}{2\Delta^2} \cdot \Bigg[& -\mathrm{i}k\mathbf{p}_{\parallel} + \mathrm{i}k\hat{\mathbf{R}} \times \left(\mathbf{m}_{\parallel} - \frac{k^2}{10}\mathbf{m}_{\parallel}^{(1)}\right) - k^2\left(\mathbf{T}_{\parallel} + \frac{k^2}{10}\mathbf{T}_{\parallel}^{(1)}\right) + \\ & + k^2\left(\mathbf{Q}^{(\mathbf{e})}.\hat{\mathbf{R}}\right)_{\parallel} - \frac{k^2}{2}\hat{\mathbf{R}} \times \left(\mathbf{Q}^{(\mathbf{m})}.\hat{\mathbf{R}}\right)_{\parallel} - \frac{\mathrm{i}k^3}{3}\left(\mathbf{Q}^{(\mathbf{T})}.\hat{\mathbf{R}}\right)_{\parallel} + \\ & + \mathrm{i}k^3\left(\left(\mathbf{O}^{(\mathbf{e})}.\hat{\mathbf{R}}\right).\hat{\mathbf{R}}\right)_{\parallel} - \frac{\mathrm{i}k^3}{180}\hat{\mathbf{R}} \times \left(\left(\mathbf{O}^{(\mathbf{m})}.\hat{\mathbf{R}}\right).\hat{\mathbf{R}}\right)_{\parallel}\Bigg] \cdot \\ & \cdot \exp\left(-\mathrm{i}kR\right)\end{aligned} \tag{4.11}$$

Equation (4.11) describes electric field emitted by an infinitely large two-dimensional array of meta-molecules (or any sub-wavelength emitters) with induced oscillations of charge-current density approximated by first 8 dynamic multipoles. It contains 10 terms corresponding to the electric ($\mathbf{p}$), toroidal ($\mathbf{T}$) and magnetic ($\mathbf{m}$) dipoles, electric ($\mathbf{Q}^{(\mathbf{e})}$), magnetic ($\mathbf{Q}^{(\mathbf{m})}$) and toroidal ($\mathbf{Q}^{(\mathbf{T})}$) quadrupoles, electric ($\mathbf{O}^{(\mathbf{e})}$) and magnetic ($\mathbf{O}^{(\mathbf{m})}$) octupoles[7], and the so-called mean square radii of toroidal ($\mathbf{T}^{(1)}$) and magnetic ($\mathbf{m}^{(1)}$) dipoles, which are the lowest-order corrections retained to account for the finite size of the meta-molecules [176] (see App. K for integrals used to find the multipole moments from the current density). Further multipole contributions to the radiation by an array of multipoles can be found in the same way.

[7]The toroidal octupole has not been included as it is a higher order multipole. The contribution of the toroidal would be of the same order as that of the magnetic hexadecapole (next one up after octupole), for example.

Using Eq. (4.11), the radiation transmitted and reflected by the two-dimensional array, when it is illuminated by normally incident plane wave, can be found by adding up the incident radiation with the radiation scattered by the array:

$$\begin{aligned} \mathbf{E}_{reflected} &= [\mathbf{E}_s]_{\hat{\mathbf{R}}=-\hat{\mathbf{k}}} \\ \mathbf{E}_{transmitted} &= [\mathbf{E}_s]_{\hat{\mathbf{R}}=\hat{\mathbf{k}}} + \mathbf{E}_{incident} \end{aligned}$$

where $\hat{\mathbf{k}} = \mathbf{k}/k$ points in the direction of propagation of the incident radiation.

4.2.2 Test Case: Infrared toroidal metamaterial

This section will demonstrate the application of the formalism derived in the preceding section, using a test case metamaterial designed to exhibit strong toroidal dipole dominated resonance (toroidal resonance) in the long-wavelength infrared part of the spectrum. The reason for choosing to tailor the design of the test case metamaterial to infrared spectrum, despite the rest of the work in this thesis targeting the sub-THz spectrum, is to demonstrate the performance of the derived formalism in the regime where metals suffer from significant Ohmic losses. In Sec. 4.3.2, it will be demonstrated that the derived formalism also performs well in the range where Ohmic losses of metals are low.

The unit cell of the metamaterial array, shown in Fig. 4.3, contains a three-dimensional complex-shaped gold resonator embedded in SU-8 polymer. The main features of the design are similar to the four-split-ring design proposed by Kaelberer *et al.* [17] (shown in Fig. 1.2d). The current design was optimized for the novel metamaterial fabrication technique SAMPL[8] [220]. As a result, each of the four split rings was replaced with a pair of split rings of highly asymmetric shape, which allowed to reduce the effect of losses and maximize the contribution of the toroidal dipole moment towards metamaterial response.

The transmission and reflection of the array of such meta-molecules were simulated in $14.5\,\mu\text{m} - 23.5\,\mu\text{m}$ range of wavelengths using a full 3D Maxwell's equations solver, COMSOL 3.5a (see App. N for material constants used for the simulation). The numerical model also provided data on spatial distribution of the current density within the metamaterial, which was used to calculate dynamic multipole moments induced in each meta-molecule (see App. K).

[8] Self-Aligned Membrane Projection Lithography [219,220]. The target surface is patterned into small cavities and a lithographic membrane is introduced on top of each cavity. The instances (shadows) of the membrane are then deposited onto walls of the cavity through directional evaporation. The metamaterial design in Fig. 4.3 is taylored to SAMPL process similar to the one reported in Ref. [220]. The cavities in this case will be in shapes of microscopic cubes in SU8 polymer. The gold will be evaporated onto the walls of the cubes though a membrane. The cross-shaped void formed by the gold resonators (see Fig. 4.3d) will be the walls separating the four cubes. Finally, the cubic cavities will be filled with the SU-8 polymer.

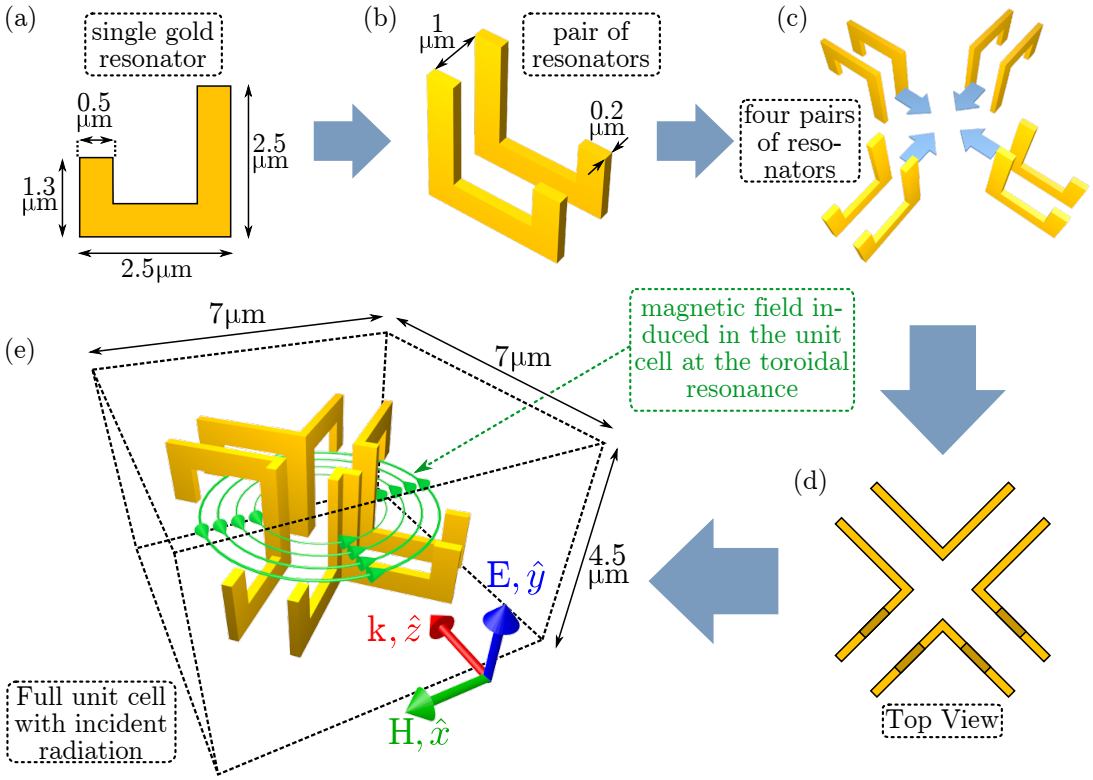

Figure 4.3: ***The design of the unit cell of the test-case toroidal metamaterial.*** ***(a)*** *The most basic building block of the unit cell. L-shaped resonator out of gold.* ***(b)*** *The L-shaped resonators are put in pairs with* 1 μm *separation between them.* ***(c)-(d)*** *Four pairs of resonators are combined to make a single large resonator. The two pairs of resonators at the front end are oriented in the usual way (same as in (a) and (b), with the split pointing up), the two pairs of resonators at the rear end are turned up-side down before merging into the large resonator.* ***(e)*** *The full unit cell, which consists of the large gold resonator at the centre, embedded into the SU-8 polymer. The metamaterial is created by translating and replicating the unit cell along the x- and y-axis. The metamaterial is driven by the plane-wave radiation propagating along the* $\hat{\mathbf{z}}$*-axis and polarized along* $\hat{\mathbf{y}}$*-axis. The configuration of the magnetic field that gives rise to the toroidal dipole excitation in the metamaterial, is schematically illustrated with green field-lines.*

The simulated transmission and reflection spectra of the metamaterial are shown in Fig. 4.4a,b as solid curves, revealing two distinct resonances located at around 21.0 μm and 17.4 μm. The simulated spectra are well matched by the transmission and reflection calculated from the radiation scattered by the induced multipoles (using Eq. (4.11)), shown as dashed curves in Fig. 4.4a. Small discrepancies are attributed to somewhat limited accuracy of extracting the induced current distribution from the numerical model and to the omission of higher order multipoles[9].

Figure 4.4c shows the intensity that would be scattered by the various multipoles, induced in the unit-cells of the test-case metamaterial, if they were individually placed in an array (with the same period as the metamaterial array). For example, the 'toroidal dipole' curve in Fig. 4.4c shows the intensity of the plane-wave radiation that would be

[9]The dashed curves in Fig. 4.4a include contributions from all multipoles included in Eq. (4.11), but there are more multipoles of even higher order, e.g. hexadecapoles etc.

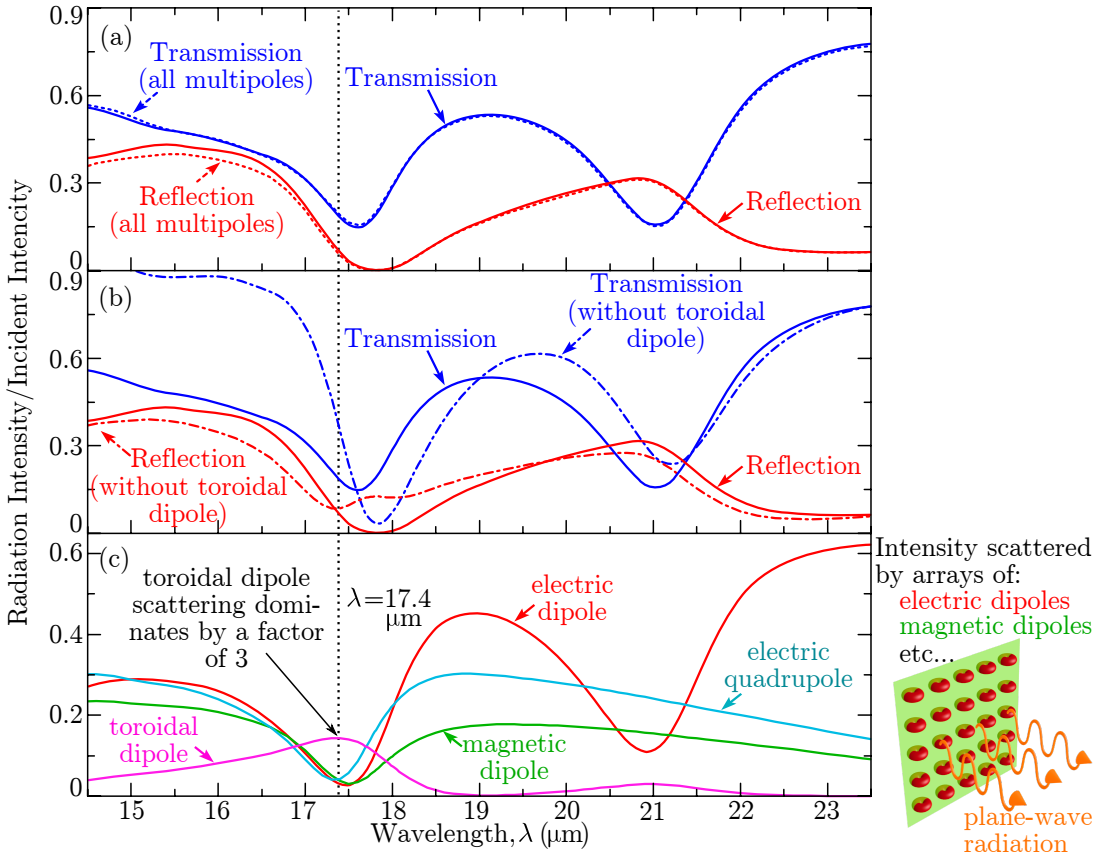

Figure 4.4: ***Macroscopic and microscopic electromagnetic response of the test-case toroidal metamaterial.*** ***(a)*** *Transmission (blue) and reflection (red) of the metamaterial. The solid curves are obtained directly from the simulation, the dashed curves are obtained from the multipole moment calculations using Eq. (4.11).* ***(b)*** *The comparison of the directly calculated metamaterial transmission/reflection to the response obtained from multipole moment calculations that included just the electric and magnetic multipoles, i.e. without the toroidal dipole.* ***(c)*** *The plot displays the intensity of the (plane-wave) radiation that would be scattered by each of the four multipoles if they were (individually) placed in an array with the same unit cell dimensions as in the test-case metamaterial. The concept is illustrated in the inset on the right-hand side. The radiation intensity in all plots is normalized with respect to incident radiation.*

scattered by an array that contains *only* the toroidal dipoles, with the same amplitude as the toroidal dipoles induced in the meta-molecules of the test-case metamaterial. From Fig. 4.4c one can see that the shorter-wavelength resonance, at 17.4 μm, corresponds to strong toroidal response, since the radiation scattered by the toroidal dipoles is more than three times larger than scattering of any other multipole. Consequently, the toroidal dipole excitation must play the key role in forming the macroscopic response of the metamaterial at this wavelength.

The method of data presentation in Fig. 4.4c allows for simple comparison between the magnitudes of the total metamaterial reflection and the radiation scattered by different multipoles. However, one should note that the curves in Fig. 4.4c will not add up to metamaterial reflection (in Fig. 4.4a,b) because the interference between the various plane-waves (due to different multipoles) needs to be taken into account. To demon-

strate the importance of the toroidal dipole contribution to the response of the test-case metamaterial one can compare the simulated transmission and reflection spectra of the metamaterial (solid lines in Fig. 4.4b) to the spectra calculated from the radiation scattered by just the electric and magnetic multipoles, i.e. without the toroidal dipole (dash-dot curves in Fig. 4.4b). As one can see, from Fig. 4.4b, the solid curves and the dash-dot curves clearly do not display the same behaviour. Therefore the correct electromagnetic response of the test-case metamaterial cannot be explained in the frame of the standard multipole expansion (electric and magnetic multipoles only) and the notion of the toroidal dipole is necessary for the correct interpretation of metamaterial's macroscopic response.

4.2.3 Summary

In summary, a fully analytical formalism was developed, that allows to calculate the transmission and reflection properties of thin sheets of metamaterials and material composites, based on the dynamic multipole decomposition of charge-current densities induced in their structure by an incident electromagnetic wave. In addition, a case study was provided, which demonstrated that the contribution of the toroidal dipole is necessary for the correct interpretation of the reflection and the transmission spectra of a certain class of metamaterials.

It can be argued, that since the current density distribution that gives rise to the toroidal multipoles is fundamentally different from that of the electric and magnetic multipoles, incorporation of the toroidal multipoles into analysis of the scattered radiation, may help to capture some additional dynamics of the current density of the scattering source (such as meta-molecule or nanoparticle). This, in turn, will assist the understanding of the microscopic mechanisms of the light-matter interactions in the complex nano-photonic structures.

4.3 Planar toroidal metamaterial

The meta-molecule designs of most toroidal metamaterials demonstrated to-date are three-dimensional (see Sec. 4.1 for references) which makes them difficult to manufacture, especially on micro- and nano-scale. This, in turn, hampers further study of the intriguing properties of toroidal dipoles in the infrared and the optical parts of the electromagnetic spectrum. The reason for the complexity of toroidal metamaterial designs lies in the nature of the toroidal dipole. Figure 4.1c shows that the current configuration that gives rise to the toroidal dipole is the poloidal current, i.e. current flowing along the meridians of a torus, which is intrinsically a three-dimensional structure[10].

Some progress has been made in implementing toroidal metamaterials in '2.5-dimensional' designs, which rely on several aligned planar metamaterial layers [187, 191].

[10] Torus cannot be embedded into a plane.

Whilst, clearly a simplification, these metamaterials are still challenging to manufacture due to requirement for precise alignment between the layers.

In this section, it will be proved that the scattering from the toroidal dipole excitations cannot be observed using purely two-dimensional free-standing metamaterials, and an implementation of the next simplest kind of toroidal metamaterial will be demonstrated: a planar metamaterial on a substrate of suitably chosen thickness.

4.3.1 Toroidal dipole excitations in planar metamaterials

In this sub-section it will be demonstrated that toroidal dipole excitations cannot be observed in a planar free-standing metamaterial, i.e. a metamaterial cut out of an infinitely thin metal sheet.

Assume that the planar metamaterial lies in the xy-plane and that it is driven with normally incident monochromatic plane-wave radiation at frequency ν (angular frequency ω, wavelength λ, wavenumber $k = 2\pi/\lambda$). The toroidal dipole moment ($\mathbf{T}$) induced in each unit cell of the metamaterial is obtained by integrating the current density ($\mathbf{J}$) within the unit cell (see App. K):

$$(\mathbf{T})_\alpha = T_\alpha = \frac{1}{10c} \int\limits_{unit\,cell} d^3r \, \left[(\mathbf{r}.\mathbf{J})\, r_\alpha - 2r^2 J_\alpha \right]$$

Where c denotes the speed of light. The Greek letter indices, such as α, will be used to denote the Cartesian components of the vectors and tensors (i.e. $\alpha = x$, y or z). Both $(\mathbf{T})_\alpha$ and T_α refer to α-th component of toroidal dipole moment.

It is convenient to introduce the following tensor:

$$K_{\alpha,\beta,\gamma} = K_{\beta,\alpha,\gamma} \equiv \int\limits_{unit\,cell} d^3r \, \left[r_\alpha r_\beta J_\gamma \right]$$

Toroidal dipole moment is then represented by:

$$T_\alpha = \sum_\beta \left(K_{\alpha,\beta,\beta} - 2K_{\beta,\beta,\alpha} \right) / 10c$$

Integrals for calculating all lower order multipoles, up to magnetic octupole, are presented in App. K. From there one can see that apart from the toroidal dipole moment, the tensor $K_{\alpha,\beta,\gamma}$ only contributes to two other multipole moments: the magnetic quadrupole moment ($\mathbf{Q}^{(m)}$) and the electric octupole moment ($\mathbf{O}^{(e)}$).

If the planar metamaterial lies in the xy-plane at $z = 0$, the induced current density within the metamaterial will be constrained to flow in the xy-plane and will vanish for $z \neq 0$. In this case, the only non-zero (distinct) components of $K_{\alpha,\beta,\gamma}$, will be $K_{x,x,x}$, $K_{x,y,x}$, $K_{y,y,x}$, $K_{y,y,y}$, $K_{y,x,y}$, $K_{x,x,y}$. The components of the toroidal dipole, magnetic quadrupole and electric octupole moments, which will contribute to the radiation scat-

tered by the planar metamaterial, will then be (see Sec. 4.2.1 and App. K):

$$\begin{aligned}
T_x &= \left(K_{x,y,y} - K_{x,x,x} - 2K_{y,y,x}\right)/10c \\
T_y &= \left(K_{y,x,x} - K_{y,y,y} - 2K_{x,x,y}\right)/10c \\
Q^{(m)}_{xz} &= -\left(K_{x,y,x} - K_{x,x,y}\right)/3c \\
Q^{(m)}_{yz} &= \left(K_{x,y,y} - K_{y,y,x}\right)/3c \\
O^{(e)}_{xzz} &= \mathrm{i}\left(3K_{x,x,x} + K_{y,y,x} + 2K_{x,y,y}\right)/30kc \\
O^{(e)}_{yzz} &= \mathrm{i}\left(3K_{y,y,y} + K_{x,x,y} + 2K_{y,x,x}\right)/30kc
\end{aligned}$$

Substituting these components into Eq. (4.11) allows to calculate the net contribution of the toroidal dipole, magnetic quadrupole and electric octupole excitations to the radiation scattered by the metamaterial:

$$\begin{aligned}
\mathbf{E}_s^{\left(\mathbf{T}+\mathbf{Q}^{(m)}+\mathbf{O}^{(e)}\right)} =& \hat{\mathbf{x}}\frac{\mu_0 c^2}{2\Delta^2}\cdot\left[-k^2 T_x - \frac{k^2}{2}\overbrace{(-1)}^{\hat{\mathbf{z}}\times\hat{\mathbf{y}}=-\hat{\mathbf{x}}} Q^{(m)}_{yz} + \mathrm{i}k^3 O^{(e)}_{xzz}\right]\cdot\exp\left(-\mathrm{i}kR\right) + \\
&+ \hat{\mathbf{y}}\frac{\mu_0 c^2}{2\Delta^2}\cdot\left[-k^2 T_y - \frac{k^2}{2}\overbrace{(+1)}^{\hat{\mathbf{z}}\times\hat{\mathbf{x}}=+\hat{\mathbf{y}}} Q^{(m)}_{xz} + \mathrm{i}k^3 O^{(e)}_{yzz}\right]\cdot\exp\left(-\mathrm{i}kR\right) = \\
=& \mathbf{0}
\end{aligned}$$

The net contribution to scattered radiation is zero in all cases. Therefore, whilst there may exist planar metamaterials such that normally incident radiation will induce toroidal dipole excitations in metamaterial's unit cells, the same current configuration that gave rise to the toroidal dipole moment, will also give rise to the magnetic quadrupole and to the electric octupole moments, so that the *net* scattered radiation due to these three multipoles will be zero.

4.3.2 Design and characterization of planar toroidal metamaterial

A basic, but nevertheless routinely overlooked, feature of planar metamaterials is the substrate, which is usually a thin low-loss dielectric wafer. A common practice is to concentrate on the dynamics of current oscillations inside the conductive part of the metamaterial, assuming that the dielectric substrate is a relatively inert part of the environment. This assumption does not always apply. At a certain frequencies, for which the radiation wavelength (inside the dielectric) matches the thickness of the substrate, a well-known Fabry-Perot cavity resonance will occur[11]. Provided the resonant mode of the metamaterial is designed to occur close to the Fabry-Perot resonance of the substrate (and is of comparable or smaller bandwidth), the two resonant modes will

[11] Fabry-Perot resonance occurs due to establishment of the 'standing wave' resonance inside the dielectric slab. Multiple reflections from the dielectric-air interfaces add up constructively/destructively leading to maxima/minima in transmission (and reflection) of the dielectric slab [57].

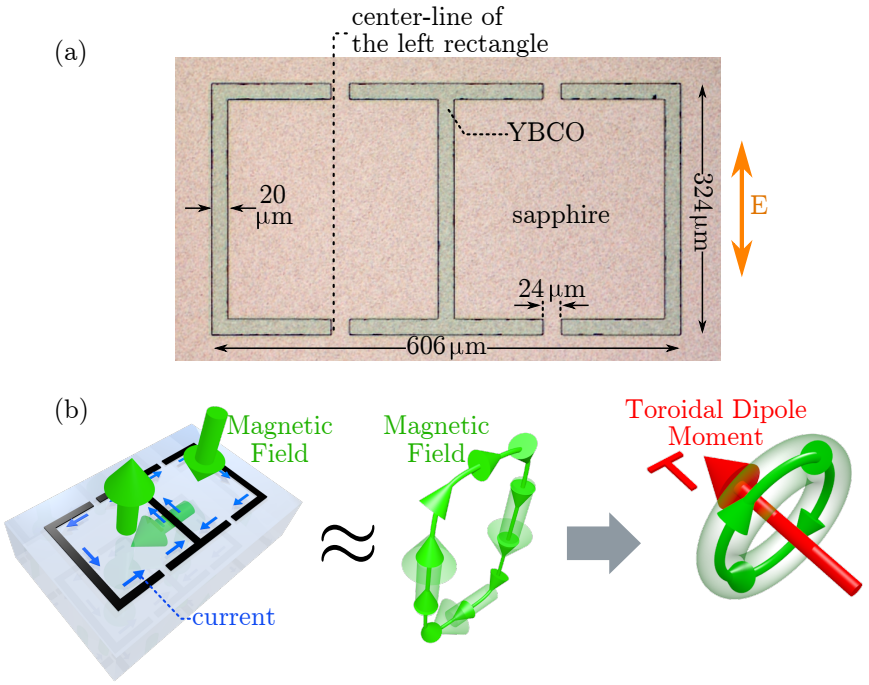

Figure 4.5: ***The design of the planar toroidal superconducting metamaterial.*** ***(a)*** *A microscope picture of the unit cell of the metamaterial (unit cell size is* $702\,\mu m \times 393\,\mu m$*). The vertical arrow labeled 'E' denotes the polarization of incident radiation. The dashed vertical line shows the midpoint of the left rectangle, thus high-lighting the asymmetric positioning of the split.* ***(b)*** *Artist's impression of the anti-symmetric mode of the metamaterial, which is excited in the experiment. The current oscillations in the two rectangles give rise to two out-of-plane magnetic dipoles (shown with green arrows). The displacement currents in the substrate constitute a third magnetic dipole. As a result, the anti-symmetric mode gives rise to oscillating closed loop of magnetic field. Such a configuration of magnetic field, in turn, gives rise to the toroidal dipole moment (labeled with 'T').*

hybridize into a single mode, which will no longer be confined to the conductive part of the metamaterial.

In Sec. 4.3.1 it was shown that it is not possible to observe a contribution of the toroidal dipole excitations to the radiation scattered by a planar (free-standing) metamaterial. However, this limitation can be circumvented by combining a planar metamaterial with an appropriately chosen dielectric substrate so that the full metamaterial design becomes 'three-dimensional'. This means that the resonant mode, i.e. the conduction and displacement currents excited in the metamaterial and its substrate at resonance, will have a finite extent in the direction of propagation of the incident radiation.

To demonstrate this feature, a planar metamaterial has been designed and implemented out of 300 nm thick film of high-temperature superconductor yttrium-barium-copper-oxide (YBCO), on a 1 mm thick sapphire substrate (see Sec. 2.3 for manufacturing methods). The unit cell of the metamaterial, shown in Fig. 4.5a, consists out of two asymmetrically-split rectangles. The asymmetry of the position of the splits allows to excite an anti-symmetric mode with plane wave radiation at normal incidence. Figure 4.5b schematically depicts the distribution of induced currents within the meta-

molecules in the anti-symmetric mode. The currents induced in the two rectangles of the meta-molecules flow in the opposite directions, which reduces the net radiation losses of the metamaterial, leading to enhancement of the anti-symmetric mode (i.e. higher amplitude of current oscillations). The low sub-THz losses in the sapphire substrate and in the superconducting YBCO serve to strengthen the anti-symmetric mode even further.

The oscillations of current in the two rectangles at the anti-symmetric mode, give rise to two opposing magnetic dipoles, pointing out of and into the metamaterial plane. Through design of the metamaterial, the anti-symmetric mode was tuned[12] to occur near the Fabry-Perot resonance of the substrate. Consequently, at the anti-symmetric mode, the substrate of the metamaterial essentially acts as a third magnetic dipole. Figure 4.1c shows that the toroidal dipole corresponds to a oscillating loop of magnetization and can therefore be considered as several magnetic dipoles arranged in a loop. The three magnetic dipoles induced in the anti-symmetric mode of the planar metamaterial in Fig. 4.5b constitute a close approximation of such circular arrangement of dipoles. Consequently, the planar metamaterial in Fig. 4.5a shall scatter radiation due to toroidal dipole excitation.

For experiments, the metamaterial has been placed into the optical cryostat and its transmission was measured at temperatures 5-100 K. The measured transmission is shown in Fig. 4.6a as a function of frequency and temperature. Below 80 K, where YBCO enters the superconducting state, a sharp resonance appears in metamaterial's transmission spectrum and strengthens as the temperature is decreased. The peak in metamaterial transmission at $\sim 83\,\mathrm{GHz}$ corresponds to the anti-symmetric mode depicted schematically in Fig. 4.5b.

To verify the expected scattering due to toroidal dipole excitation at the anti-symmetric mode, the response of the metamaterial was simulated numerically, on COMSOL 3.5a, using realistic material parameters[13]. The simulation allowed to calculate the metamaterial transmission as well as the multipole excitations induced in the metamaterial by the incident radiation. Figure 4.6b compares the measured transmission of the metamaterial at temperature $\theta = 5\,\mathrm{K}$ to transmission obtained directly from the simulation and to the transmission calculated from the radiation scattered by the multipoles induced in the metamaterial (using Eq. (4.11)). The three curves show close agreement around the anti-symmetric resonant mode of the metamaterial.

Figure 4.6c shows the intensity of radiation scattered by the leading multipole excitations induced in the metamaterial. The three leading multipole contributions to the radiation scattered by the metamaterial at the anti-symmetric mode are: the electric

[12]The frequency of the metamaterial resonance is easily shifted by changing the physical size of the meta-molecule. Making the meta-molecules larger reduces the resonant frequency, and vice verse.

[13]Dielectric constant of the sapphire was taken to be $\epsilon_r = 9.3$, the minimum physically justified value [94]. Conductivity of YBCO has been taken from the value reported in Ref. [221] for thin-film YBCO at frequency 87 GHz. To get a good agreement with experiment, the imaginary part of conductivity had to be reduced by 30%, so the actual value used was $\sigma_{YBCO} = (0.3 - \mathrm{i}2.8) \times 10^7\,\mathrm{S/m}$.

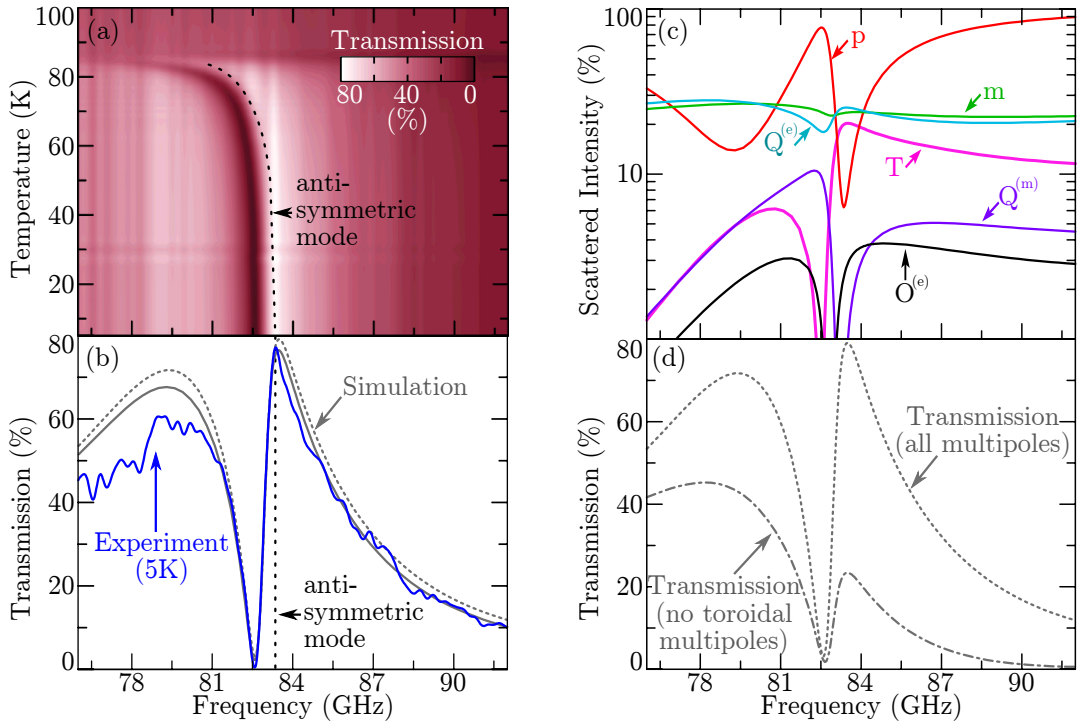

Figure 4.6: ***Characterization of the planar toroidal superconducting metamaterial.*** ***(a)*** *Measured transmission of the metamaterial as a function of frequency and temperature.* ***(b)*** *Metamaterial transmission at temperature 5 K (blue) compared with simulated transmission (gray; solid line - direct numerical result; dashed line - transmission calculated from multipole decomposition).* ***(c)*** *Intensity of the radiation scattered by each of six leading multipole excitations when placed in an array (***p****-electric dipole,* **m***-magnetic dipole,* **T***-toroidal dipole,* $\mathbf{Q}^{(\mathbf{e})}$*-electric quadrupole,* $\mathbf{Q}^{(\mathbf{m})}$*- magnetic quadrupole,* $\mathbf{O}^{(\mathbf{e})}$*-electric octupole).* ***(d)*** *Transmission of the metamaterial calculated from multipole scattering with (dashed line) and without (dash-dot line) the input of the scattering by the toroidal multipoles.*

quadrupole ($\mathbf{Q}^{(e)}$), magnetic dipole (**m**) and the toroidal dipole (**T**). Whilst the intensity of radiation scattered by the toroidal dipole excitation never exceeds that of the electric quadrupole and the magnetic dipole, the contribution of the toroidal dipole is quite significant. This point is illustrated in Fig. 4.6d by comparing the transmission spectrum calculated from the radiation scattered by all the multipoles (dashed curve), and the transmission spectrum calculated from the radiation scattered by just the electric and magnetic multipoles, i.e. without the toroidal multipoles (dash-dot curve). Here (Fig. 4.6d), as in Sec. 4.2.2, the transmission of the metamaterial cannot be faithfully represented without accounting for the toroidal dipole excitations. Furthermore, according to additional simulations (not shown here), the radiation scattered by the toroidal dipole could be made 50% stronger than of any other multipole if the substrate thickness was just 70 μm thicker.

4.3.3 Summary

It was demonstrated that scattering of radiation due toroidal dipole excitation cannot be observed in single-layer planar free-standing metamaterials, i.e. metamaterials made

from single thin sheet of metal. However, it was also shown that this limitation can be circumvented using planar metamaterials *on* a suitably chosen dielectric substrate. An experimental demonstration of such planar toroidal metamaterial on a suitable substrate has been presented and characterized. The strong contribution of the toroidal dipole excitation to the radiation scattered by the planar metamaterial has been verified numerically. The work reported here demonstrates how the design of the toroidal metamaterials can be considerably simplified up to a point where the toroidal metamaterials can be manufactured in a single lithography procedure.

4.4 Non-Radiating configurations based on multipole interference in toroidal metamaterial

Engaging strongly resonant interactions allows dramatic enhancement of functionalities of many electromagnetic devices. The resonances, however, can be dampened by Joule and radiation losses. While in many cases Joule losses may be minimized by the choice of constituting materials, controlling radiation losses is often a bigger problem. Recent solutions include the use of coupled radiant and sub-radiant modes yielding narrow asymmetric Fano resonances in a wide range of systems: from defect states in photonic crystals [222], and optical waveguides with mesoscopic ring resonators [223], to nanoscale plasmonic and metamaterial systems exhibiting interference effects akin to electromagnetically-induced transparency [77].

This section will demonstrate a new class of artificial electromagnetic media with ultra-narrow resonances, namely toroidal metamaterials, that exploit interference between co-located and coherently oscillating electrical and toroidal dipolar modes. The interference between the electrical and toroidal dipolar modes leads to characteristically *symmetric*[14] Lorentzian transparency lines in the response of the new metamaterials. More interestingly, such metamaterials are a long-awaited implementation of the 'non-trivial non-radiating charge-current configurations', which were predicted, by Afanasiev and Stepanovsky, to generate waves of gauge-irreducible electromagnetic vector potential in the absence of electromagnetic fields [183].

Realization of the non-trivial non-radiating charge-current configuration has been suggested to enable testing of the *dynamic* Aharonov-Bohm effect [183]. The *static* Aharonov-Bohm effect, described by Y. Aharonov and D. Bohm in 1959 [224], predicts that the phase of the electron wavefunction will change as it propagates in a space with zero electromagnetic field, but non-zero vector potential. This effect has been successfully verified by several experimenters including the famous electron-holography experiment reported by A. Tonomura *et al.* [225]. The static Aharonov-Bohm effect showed that, in magnetostatics, the vector potential has an independent physical significance, i.e. it contains more information than one can recover from just the magnetic

[14] As opposed to the asymmetric Fano-type resonances more commonly encountered in the metamaterials with high-quality response [77].

field. The observation of the dynamic Aharonov-Bohm effect would allow to demonstrate the independent physical significance of both scalar and vector potentials in the *electrodynamics*.

The idea behind the metamaterial was conceived by Dr. V. A. Fedotov. The manufacturing and the experiments were conducted by Dr. V. A. Fedotov and Dr. A. V. Rogacheva. My input into this project came through using the analytical formalism developed in Sec. 4.2.1 to verify the destructive interference between the electric and the toroidal dipoles, and through extensive discussions at the stage of interpreting the experimental results. Our findings have been published in Ref. [226].

4.4.1 Resonant transparency in toroidal metamaterials

Despite the fundamental differences between the charge-current distributions that induce the electric and toroidal dipoles, their radiation patterns are identical to any distant observer (see Sec. 4.1). Thus, when the poloidal current mode (toroidal dipole) and bipolar charge distribution (electric dipole) are co-located and oscillate coherently at the same frequency, the net radiation emitted by such a charge-current configuration can be reduced to zero through the destructive interference between the electric and the toroidal dipoles [183, 227]. This suggests an interesting opportunity of creating artificial electromagnetic materials, which exhibit isolated transparency bands when the radiation losses are suppressed through the interference of toroidal and electric dipolar emission. Such mechanism of transparency and resonant dispersion is somewhat different from the one more typically encountered in plasmonic and metamaterial systems mimicking electromagnetically-induced transparency. There, the transparency is caused by the interference between the two spectrally separated multipolar modes, i.e. the transparency is caused by the interference of the scattered radiation due to two resonant eigenmodes of the system with slightly different eigenfrequencies, which leads to a sharp *asymmetric* Fano resonance on the background of another, much wider, resonant band [77]. Here, by contrast, the interfering electric and toroidal dipoles are both spatially and spectrally co-located, i.e. the electric and toroidal dipole excitations correspond to the same resonant eigenmode, leading to the *symmetric* transparency line.

This novel mechanism of radiation suppression is demonstrated for metamaterials based on a dumb-bell-shaped aperture element. The element is cut out of a thin metal plate and resembles a meridional cross-section of a toroidal void (see Fig. 4.7a). This is a very special electromagnetic system in which the incident wave polarized parallel to the symmetry axis of the aperture induces both electric and toroidal dipolar moments. Indeed, the electric field of the wave drives charge separation across the waist of the aperture, which gives rise to an oscillating electric dipole moment oriented along the symmetry axis of the aperture (see Fig. 4.7a). The charge displacement also gives rise to counter-rotating (poloidal-like) currents oscillating along the edges of the circular cuts, as shown in Fig. 4.7a. The poloidal currents, in turn, give rise to the toroidal dipole,

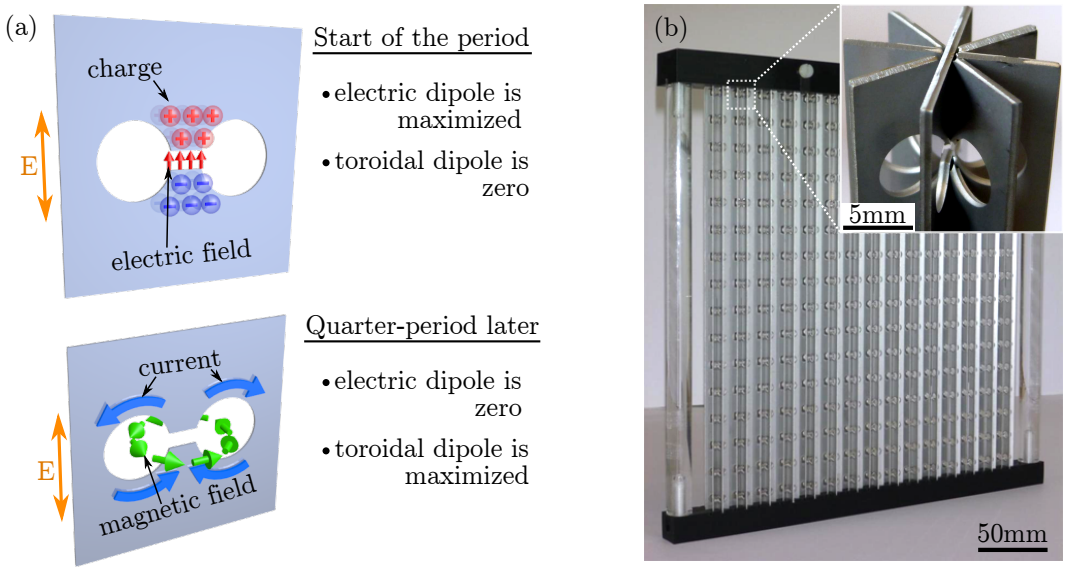

Figure 4.7: ***Toroidal void metamaterial.*** ***(a)*** *Metal screen with a dumbbell-shaped aperture - the basic structural element of the toroidal void metamaterial. Vertical arrows labeled 'E' denote the polarization of the incident radiation. The charge-current oscillations at the transparency resonance are shown at the beginning of the (oscillation) period and quarter of the period later. The build-up of charge and zero current at the beginning of the period, leads to a maximum in electric dipole and a zero toroidal dipole. Quarter-period later, the charge build-up is gone so the electric dipole is zero. At the same time the currents set up due to relaxation of the charge build-up lead to a maximum in toroidal dipole. Oscillations of the toroidal dipole are thus a quarter-period behind the electric dipole (in this mode).* ***(b)*** *Photograph of the assembled metamaterial slab, an array of* 15×16 *toroidal aperture-based meta-molecules. Inset shows a close-up view of one of the array's columns with 8-fold symmetry.*

which oscillates coherently with the electric dipole but lags quarter of a period behind it. It can be shown that the radiation of such electric and toroidal dipoles will always interfere destructively both in the near- and the far-field (see App. L). The amplitude of the poloidal currents increases resonantly when the wavelength of incident radiation (λ) approaches the circumference of the aperture $\sim 4\pi R$ (where R is the radius of the circular cuts) leading to the enhancement of toroidal emission, which in principle can be made to cancel electric dipolar scattering completely.

In reality, an electromagnetic wave incident onto a planar metamaterial made from dumbbell-shaped apertures (Fig. 4.7a), would induce numerous multipoles other than the electric and the toroidal dipole. Most notably, the pair of counter-rotating currents, that lead to the toroidal dipole (Fig. 4.7a), would also lead to the magnetic quadrupole[15]. The scattering contribution from this multipolar current mode (magnetic quadrupole) can be effectively suppressed in an aperture-based structure of higher rotational symmetry such as, for example, 4-fold or 8-fold symmetric toroidal meta-molecules shown in Fig. 4.8a and Fig. 4.8b. This was demonstrated by modeling numerically the interaction

[15]This relates directly to the proof in Sec. 4.3.1 regarding the impossibility of observing net contribution to scattered radiation from the toroidal dipole excitations in planar metamaterials. In the current case, the scattering from the toroidal dipole would be canceled out by the scattering from the magnetic quadrupole.

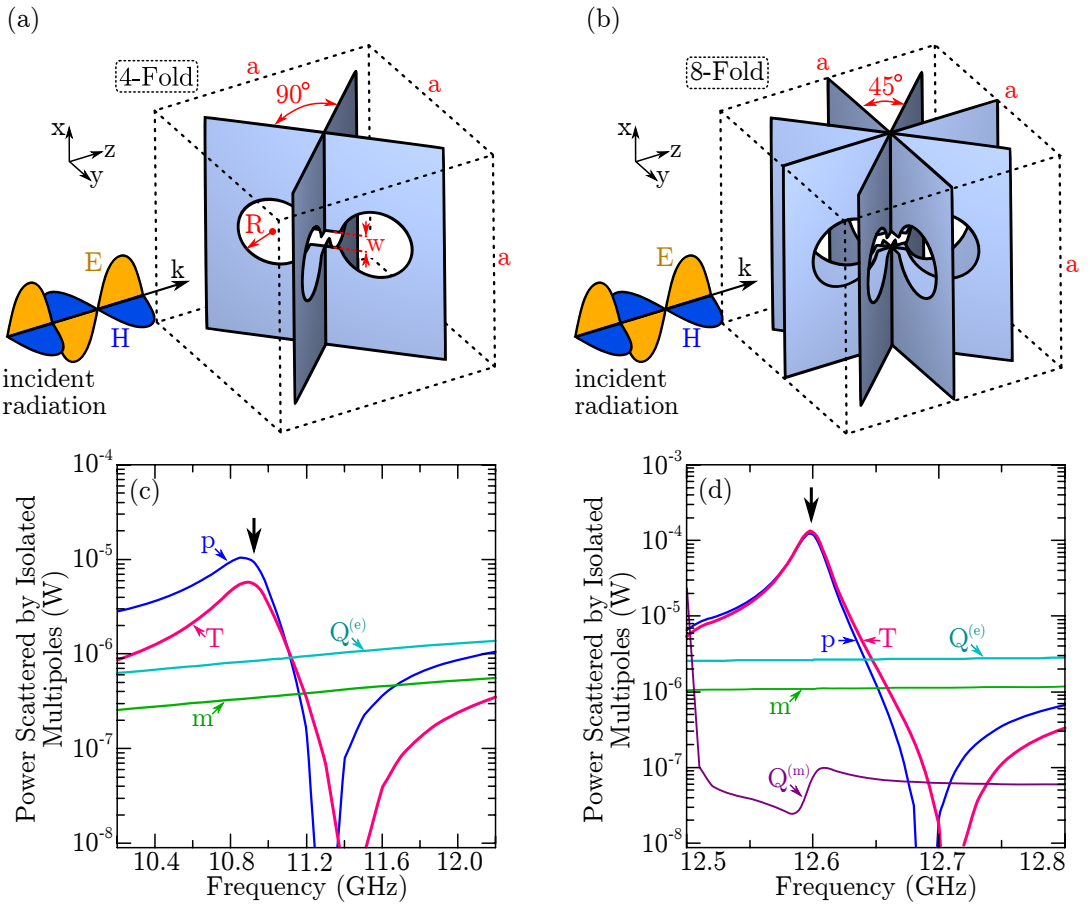

Figure 4.8: ***Multipole excitations in toroidal void metamaterials.*** *Panels* ***(a)*** *and* ***(b)*** *show metamaterial's unit cell with 4-fold (a) and 8-fold (b) symmetry; a=16.5 mm, R=2.5 mm, w=1.2 mm, separation between the centers of the circular cuts is 7.0 mm. Panels* ***(c)*** *and* ***(d)*** *show dispersions of multipolar scattering rates calculated for 4 strongest multipoles induced in 4-fold* ***(c)*** *and 8-fold* ***(d)*** *symmetric meta-molecules (***p***-electric dipole,* ***m****-magnetic dipole,* ***T****-toroidal dipole,* $\mathbf{Q}^{(\mathbf{e})}$*-electric quadrupole,* $\mathbf{Q}^{(\mathbf{m})}$*- magnetic quadrupole). Arrows indicate locations of the corresponding transparency resonances. Note that here the power scattered by the single unit cell in all directions, is presented (as opposed to scattering from an array of unit cells used in previous sections).*

of the meta-molecules assembled in two-dimensional arrays (slabs of toroidal metamaterials) with a normally incident linearly polarized plane wave. The slabs were described through periodic boundary conditions applied to the corresponding unit cell's facets in X and Y directions, as indicated in Figs. 4.8a and 4.8b. The dumbbell-shaped aperture resonators forming 4-fold and 8-fold symmetric toroidal void meta-molecules were assumed to be cut in infinitely thin sheets of perfect electric conductor in accordance with the design specifications[16]. Electromagnetic response of the metamaterial slabs

[16]The length-scale of the design, which ultimately determined the resonant frequency, was chosen based on what could be manufactured and characterized. Experimentally it was easier to characterize small metamaterials (with small unit cells), due to ease of alignment. With smaller metamaterials it was also easier to ensure that the metamaterial would be excited with plane-wave radiation at normal incidence (as in the model). On the other hand, it was easier to manufacture metamaterials with larger unit cells.

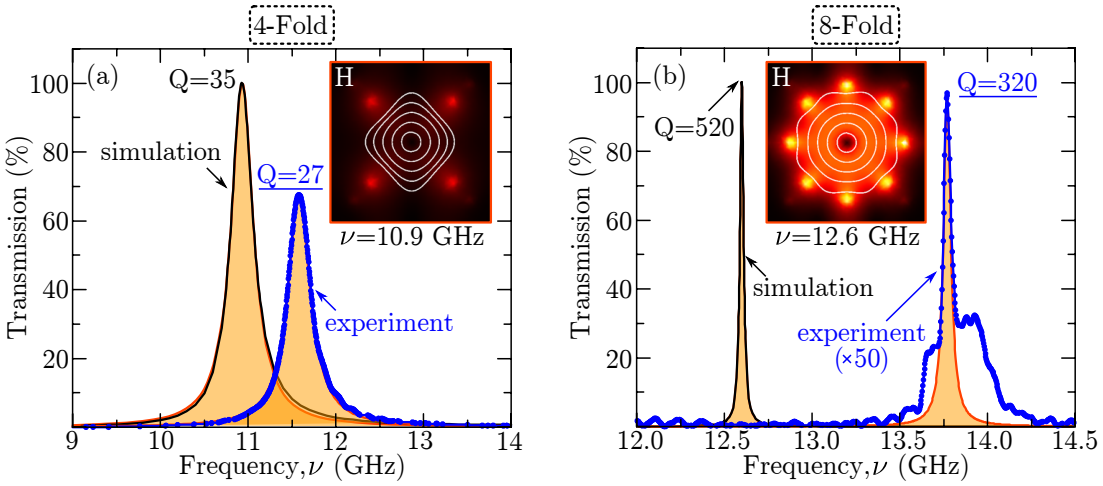

Figure 4.9: ***Transmission response of toroidal void metamaterials.*** ***(a)*** *The simulated (black solid line) and the measured (blue solid line with data-points) transmission spectra of the 4-fold symmetric metamaterial slabs. Orange-filled areas represent the symmetric Lorentz line profiles fitting the simulation and the experimental data. The inset shows the simulated distribution of magnetic field lines and magnetic field intensity* $|\mathbf{H}|$ *within the unit cell of the four-fold symmetric meta-molecule (top view), corresponding to resonantly excited mode at the transmission resonance at frequency* 10.9 *GHz.* ***(b)*** *The corresponding experimental and simulation data for the 8-fold symmetric metamaterial slabs.*

was simulated using commercial full three-dimensional Maxwell equations solver based on the finite element method, COMSOL 3.5a. The simulations also provided data on the densities of electrical currents induced in the metamaterials by the incident wave, which was used to calculate the power scattered by the conventional multipoles and by the toroidal dipole, associated with each meta-molecule[17].

The results of the calculations are shown in Fig. 4.8c,d as the power that would be scattered in all directions by isolated multipoles with the same magnitude as the multipoles excited in the unit-cells of the metamaterials with 4-fold and 8-fold symmetric meta-molecules (respectively). The calculations showed that, in the metamaterial with 4-fold symmetric meta-molecules, the emission of the standard multipoles other than the electric dipole ($\mathbf{p}$) is small (see Fig. 4.8c). Close to the resonance, at 10.9 GHz, the electric quadrupole ($\mathbf{Q}^{(e)}$) and the magnetic dipole ($\mathbf{m}$) exhibit scattering rates that are factors of 10 and 30 smaller than that of the electric dipole, whilst the scattering rate of the magnetic quadrupole ($\mathbf{Q}^{(m)}$) is a factor of 10^5 weaker than the electric dipole scattering. Toroidal dipole provides the second strongest contribution at the resonance, being responsible for more than 30% of the total scattering. Its presence can be detected in the near-field as closed loops of magnetic field-lines confined within the meta-molecule and threading the circular sections of the apertures (see the inset to Fig. 4.9a). Qualitatively similar response is observed in the 8-fold symmetric toroidal void metamaterial (see Fig. 4.8d), but the scattering of the toroidal dipole becomes even

[17]See App. I.2 for the equation used to find the scattered power. The integrals used to find the multipole moments are listed in App. K.

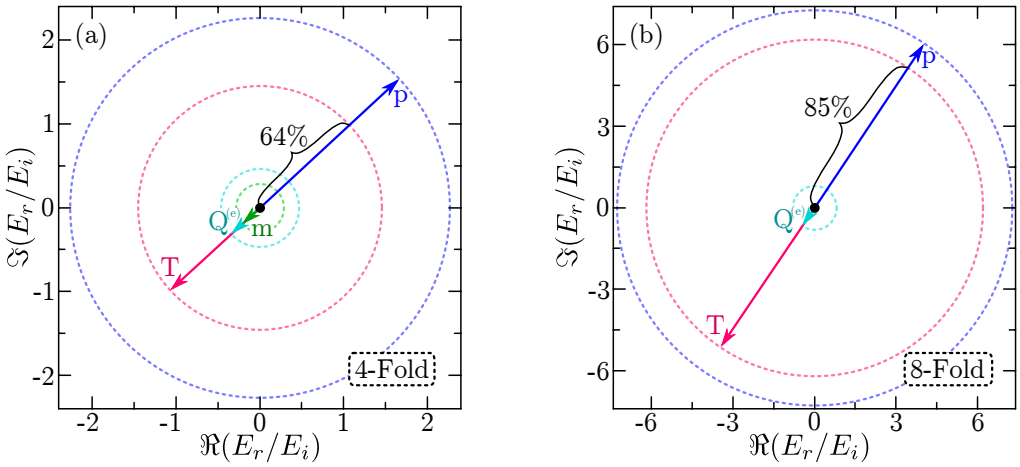

Figure 4.10: ***Contributions of the leading multipole excitations to the reflection of the toroidal void metamaterials at the point of maximum transmission.*** ***(a)*** *Multipole contributions to the reflection of the four-fold toroidal void metamaterial (shown in Fig. 4.9a). Each arrow is a phasor-like representation of the radiation (electric field) scattered back by the corresponding multipole excitations. The sum of all phasors allows to calculate the amplitude and phase of the radiation reflected by the four-fold toroidal void metamaterial. Horizontal axis expresses the real part of the phasors, whilst vertical axis expresses the imaginary part.* ***(b)*** *Multipole contributions to the reflection of the eight-fold toroidal void metamaterial (shown in Fig. 4.9b). The radiation scattered by all multipoles in (a) and (b) has been calculated using Eq. (4.11) and was normalized with respect to amplitude of the incident field (E_i).*

stronger.

The calculations also show that, at the resonance, the complete destructive interference of radiated fields takes place in a loss-less toroidal metamaterial (implemented out of perfect electric conductor). This corresponds to the total transparency of the toroidal metamaterial. For instance, for the 4-fold symmetric system the prevailing electric dipolar scattering is canceled on about 64% by toroidal scattering and on 36% by scattering from other multipoles (see Fig. 4.10a) creating a background-free resonant transparency peak with symmetric Lorentzian profile and quality factor[18] $Q \approx 35$ (Fig. 4.9a), which is already quite high by the standard of the microwave metamaterials. In the metamaterial composed of 8-fold symmetric meta-molecules, electric and toroidal dipolar scattering is mutually canceled on 85% (see Fig. 4.10b), leading to a transparency peak with $Q \approx 520$ (Fig. 4.9b). The increased role of toroidal dipolar mode in the 8-fold symmetric structure is also evident from the calculated magnetic near-field map (compare the insets in Fig. 4.9a and Fig. 4.9b).

The appearance of the transparency resonances due to electric-toroidal dipolar interference was confirmed with experiments conducted in the microwave part of the spectrum. The toroidal metamaterials were constructed from strips of thin stainless steel plates with dumbbell-shaped apertures. The stainless steel strips, which had the thickness of 0.8 mm, were patterned using chemical etching and assembled into columns of

[18] Quality factor is calculated from $Q = \nu_0/\Delta\nu$, where ν_0 is the resonant frequency and $\Delta\nu$ is the full width at half maximum of the transmission resonance.

4-fold and 8-fold symmetric structures. The metamaterial slabs were formed out of 15 columns, each column containing 16 toroidal meta-molecules (see Fig. 4.7b). All dimensions of the design features were identical to those used in the modeling (Fig. 4.8), except for the finite thickness of the stainless steel strips. The transmission spectra of the metamaterial samples were measured in Emerson & Cuming microwave anechoic chamber using vector network analyzer (Agilent E8364B) and a pair of broadband linearly polarized horn antennas (Schwarzbeck Mess-Elektronik BBHA 9120D) equipped with dielectric lens collimators. The experimental data shows a very good qualitative agreement with the theory reproducing fully the main features of the metamaterials' response predicted by the modeling: the appearance of narrow isolated bands of transparency with symmetric Lorentzian profile and very large Q-factor, which reaches a record-high value of 320 in the case of 8-fold symmetric metamaterial (see Fig. 4.9). The slight shift of the observed resonances towards higher frequencies is attributed to the shortening of the outer effective circumference of the apertures due to non-zero area of the intersection between the metal strips in the assembled meta-molecules (resulting from the finite thickness of the strips). Somewhat lower Q-factors measured for the toroidal metamaterials result from the inhomogeneous broadening of the resonances due to fabrication tolerances and imperfections of the sample assemblies. The latter is also responsible for the incomplete transparency, as well as the appearance of the broad asymmetric pedestal of the high-fidelity resonance. For example, given 0.2% variation of the resonance frequency among 8-fold symmetric meta-molecules in the assembled array (which correspond to the fabrication tolerance of 0.06 mm), the amplitude of its transmission resonance would reduce to 4% with the Q-factor dropping to about 300. Other factors that limited transparency in the experiment are residual curvature of the incident wavefront and diffusive scattering from the metamaterial structures.

4.4.2 Discussion

It should be noted that simultaneous presence of co-located electric and toroidal dipolar excitations in metamaterials presented in this section may create a unique situation, where vector potential $\mathbf{A}$, generated outside the arrays, is non-zero even though the scattered electromagnetic fields are completely canceled via the destructive interference. Indeed, although the electromagnetic field emission characteristics of oscillating electric and toroidal dipoles are identical, the vector-potential fields they produce are quite different [183, 228] (also see App. L). Under the condition of total coherent cancellation of their radiation, the resulting vector potential propagating in the far-field is given by:

$$\mathbf{A}(\mathbf{r},t) \overset{O(1/r)}{=} -\frac{\mathbf{r}k^2}{r^3}\left(\mathbf{r}.\mathbf{T}\right)\exp\left(\mathrm{i}\left[\omega t - kr\right]\right)$$

The complete expression for $\mathbf{A}$, featuring also the near-field contributions, can be found in App. L.

The discussion on the independent physical significance of the vector potential started

from the famous paper by Aharonov and Bohm [224] and has developed into an active research topic that attracted a large number of publications (see, for example, [229–231] and references therein). In particular, it was theoretically shown that the Aharonov-Bohm effect due to time-varying vector potential of a coherent light source could be used for quantum-nondemolition detection of photons emitted by the source [232]. Intriguingly, Afanasiev and Stepanovsky suggested [183], that time-dependent electromagnetic potentials produced by their non-trivial non-radiating system of collocated electric and toroidal dipolar excitations "... can be used as a new channel for information transfer (by modulating the phase of the charged particle wavefunction) and for the performance of time-dependent Aharonov-Bohm-like experiments.". Those predictions were disputed by Marengo and Ziolkowski, who argued "... that electrodynamically not only the fields but also the associated potentials are unobservable everywhere in the exterior of a spatially localized non-radiating source" and "... Aharonov-Bohm effects associated with non-radiating potentials are possible only in static situations" [184]. Resolving this apparent controversy and further understanding the role of time-dependent electromagnetic potentials would require practical realization of non-trivial non-radiating sources, which have so far remained merely a peculiar theoretical concept.

It is suggested here that the observed resonant transparency phenomenon is the first example of the manifestation of the non-trivial non-radiating charge-current excitation, and that the toroidal void metamaterial arrays operating at the transparency resonance could serve as the source of the non-compensated vector-potential. Even though in case of metamaterials presented here the destructive interference between electric and toroidal dipole moments does not lead to the complete cancellation of their scattering, the residual dipolar radiation is suppressed by higher multipoles. So the structure can be viewed as a combination of perfect destructive interference between the electric and the toroidal dipoles (which should generate the vector potential of interest), combined with the interference of the small remainder of the electric dipole with the higher order multipoles. Due to the two-dimensional periodicity of the metamaterial arrays, in the current case, the non-trivial component of the vector-potential field is expected to localize in the plane of the metamaterial structure.

4.4.3 Summary

In summary, a class of metamaterials has been identified, that supports a novel mechanism of resonant electromagnetic transparency. The transparency mechanism exploits the destructive interference between the spatially and spectrally co-located and coherently oscillating electric and toroidal dipoles, and leads to narrow (due to low Ohmic losses) and characteristically symmetric Lorentzian transparency lines with quality factors exceeding 300. Such mode of resonant excitation corresponds to a long-awaited implementation of the non-trivial non-radiating charge-current configuration, that has been predicted to generate waves of gauge-irreducible vector potential in the absence of

scattered (reflected) electromagnetic fields.

4.5 Conclusions

In this chapter, an analytical formalism has been developed for calculation of transmission and reflection properties of electromagnetic metamaterials. The formalism has been tested both numerically and experimentally showing good agreement in both cases. Building on the newly developed formalism, it has been demonstrated that toroidal dipole excitations can only be observed in metamaterials with three-dimensional unit cells. The simplest kind of such metamaterial, from the point of view of manufacturing, has been designed, manufactured and tested.

This chapter also reports on the first experimental realization of the non-trivial non-radiating configuration using toroidal metamaterials. The expected cancellation of metamaterial scattering due to interference between the toroidal dipole and the electric dipole has been verified using the formalism developed in the preceding sections.

The research into toroidal metamaterials is still in its infancy, and the main application of these metamaterials remains the experimental verification of intriguing properties of toroidal dipoles (e.g. time-dependent Aharonov-Bohm effect using non-radiating configuration based on toroidal and electric dipoles). However even at this early stage, one can identify some practical applications. The toroidal metamaterials tend to display sharp resonant response accompanied by concentration of electromagnetic field in a relatively large volume inside the meta-molecule[19], which can be utilized for creating lasing metamaterials [192], metamaterial sensors and metamaterials with nonlinear electromagnetic response.

[19] By contrast, a number of other meta-molecule designs demonstrate electromagnetic field enhancement at resonant frequency, but the volume in which the enhanced field is concentrated, tends to be small (e.g. bow-tie antennas [233]).

Chapter 5

Quantum Flux Exclusion Metamaterial: Towards Quantum-Level Nonlinearity

5.1 Introduction

The coherent nature of the macroscopic quantum state of charge carriers within the superconductor dictates that the magnetic flux through a closed superconducting loop will be an integer multiple of the flux quantum $\Phi_0 \equiv h/2e \approx 2.1 \times 10^{-15}$ Wb, where h is the Plank's constant and e is the charge of the electron [28, 33]. This is known as flux quantization. First demonstrated by Deaver and Fairbank [234], as well as by Doll and Näbauer [235], flux quantization is now accepted as one of the fundamental phenomena of the superconducting state. Combined with the Josephson effect, flux quantization forms the basis for the operation of SQUIDs[1] and is therefore crucially important for high-precision magnetometry [236], superconducting electronics [33, 41] and quantum computing [51].

The unique feature of flux quantization is that, through Φ_0, it firmly links the physical size of an object (i.e. the area of the loop) to the magnitude of the magnetic field. In the case of electrodynamics, this corresponds to a link between the intensity of the electromagnetic radiation and the geometry. Whilst there exist other phenomena sensitive to the magnitude of the electromagnetic fields (e.g. ferromagnetism), the flux quantization stands out because it is a *universal* (i.e. material-independent) property of superconductors.

In this chapter I will introduce the *flux exclusion quantum metamaterial*, a superconducting metamaterial designed to utilize flux quantization as a source of its switching functionality. The term 'quantum metamaterial' is somewhat ambiguous. In the narrowest sense, this is a metamaterial comprised of meta-molecules that can exists in quantum

[1] Superconducting QUantum Interference Device.

mechanical states for significantly longer periods of time than the period of the electromagnetic excitation that drives the metamaterial [237]. In a broader sense however, a quantum metamaterial could be defined as a metamaterial that allows observation of novel quantum mechanical phenomena on a macroscopic scale. The flux exclusion quantum metamaterial, described in this chapter, falls into the second category. Unlike the other recently discussed superconducting quantum metamaterials [238–249], the design proposed here does not require Josephson junctions, making it much simpler to fabricate and scale into large arrays, but should still be capable of demonstrating a purely quantum mechanical effect of flux quantization.

The chapter is organized in the following way. Section 5.2 describes the origin of flux quantization in closed superconducting loops. Section 5.3 describes how the phenomenon of flux quantization can be utilized in nonlinear superconducting metamaterials and presents a specific implementation - the woodcut metamaterial. The low-intensity electromagnetic response of the woodcut metamaterial is studied in the same section. An alternative design of the flux exclusion metamaterial is suggested in Sec. 5.4. The results are summarized in Sec. 5.5. The findings presented in this chapter, apart from Sec. 5.4, have been published in Ref. [250].

5.2 Flux quantization in closed superconducting loops

This section will briefly describe the nature of flux quantization and discuss its role in the electromagnetic response of closed superconducting loops.

5.2.1 Origin of flux quantization

According to phenomenological Ginzburg-Landau theory [28,33,251], the superconducting charge carriers (Cooper pairs) can be described by a single complex-valued wavefunction $\psi(\mathbf{r}) = \sqrt{n_s(\mathbf{r})} \times \exp\left(\mathrm{i}\phi\left(\mathbf{r}\right)\right)$, where $\mathbf{r}$ is the position vector inside the superconductor, $n_s(\mathbf{r})$ is the density of the Cooper pairs and $\phi\left(\mathbf{r}\right)$ is the phase of the wavefunction. The current density due to Cooper pairs is then given by [33]:

$$\begin{aligned}\mathbf{J}_s &= -\frac{\mathrm{i}e\hbar}{m}\left(\psi^\dagger\nabla\psi - \psi\nabla\psi^\dagger\right) - \frac{4e^2}{m}n_s\mathbf{A} \\ &= \frac{2en_s}{m}\left(\hbar\nabla\phi - 2e\mathbf{A}\right)\end{aligned} \tag{5.1}$$

Where e is the electron charge, $\hbar$ is the reduced Planck constant, m is the mass of a single Cooper pair and $\mathbf{A}$ is the vector potential related to the magnetic field ($\mathbf{B} = \nabla \times \mathbf{A}$).

Consider a closed superconducting loop (i.e. a ring out of superconducting wire), threaded by magnetic flux Φ, as shown in Fig. 5.1. Wavefunction of the Cooper pairs ($\psi(\mathbf{r})$) must be single-valued at every point in the superconducting wire, which means

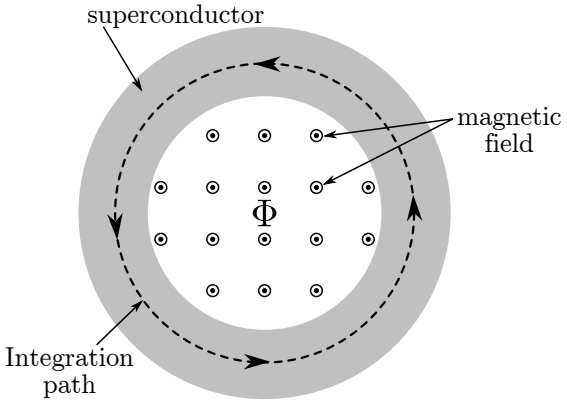

Figure 5.1: ***Superconducting loop with (net) magnetic flux*** Φ ***threading through it.***

that the phase of the wavefunction ($\phi(\mathbf{r})$) may change only by multiples of 2π as one goes around the loop. Integrating the gradient of ϕ along the closed loop therefore results in (see Fig. 5.1 for integration path):

$$\oint dl\,\hat{l}.\nabla\phi = 2\pi \times k, \quad k = 0, \pm 1, \pm 2. \tag{5.2}$$

If the magnitude of the magnetic field threading the loop in Fig. 5.1 is sufficiently small, and the thickness of the superconducting wire is sufficiently large[2], then the magnetic field will be screened from within the bulk of the wire. Let the integration path shown in Fig. 5.1 lie deep enough inside the superconductor for external magnetic field to be screened, so that current density ($\mathbf{J}_s$) would be negligible along the path. Integrating $\mathbf{J}_s$ (from Eq. (5.1)) along this path will then result in[3]:

$$\oint dl\,\hat{l}.\mathbf{J_s} = 0 = \frac{2en_s}{m}\left(\hbar\,(2\pi k) - 2e\left[\int d^2r\,\hat{\mathbf{n}}.\mathbf{B}\right]\right) = \frac{2en_s}{m}\left(\hbar\,(2\pi k) - 2e\Phi\right)$$

It thus follows that the flux through the superconducting loop will be an integer multiple of the flux quantum:

$$\Phi = 0, \pm\Phi_0, \pm 2\Phi_0, \ldots \quad \Phi_0 = \pi\hbar/e \approx 2.1 \times 10^{-15}\,\mathrm{Wb}$$

The flux quantization in superconducting loops is therefore a consequence of a requirement for single-valued wavefunction of the Cooper pairs.

[2]Inside the superconductor the magnetic field will decay exponentially on the scale of the penetration depth (see Sec. 1.2.1). For YBCO, the typical penetration depth is several hundred nanometers [221].

[3]Unit vector $\hat{\mathbf{n}}$ is perpendicular to the plane that contains the integration path.

5.2.2 Magnetic flux states of the superconducting loop

One can understand the electromagnetic response of a closed superconducting loop in the equilibrium by considering its Gibbs free energy[4] (G) as a function of applied magnetic flux. The approach presented here is adopted from Silver and Zimmerman [253].

In general, the change in Gibbs free energy of a system as a result of change in the strength of applied magnetic field ($\mathbf{H}$) is given by $\Delta G = -\int d^3r \int_{\mathbf{H}_0}^{\mathbf{H}_1} d\mathbf{H}.\mathbf{M}$, where the first integral runs over the volume (that contains the system) and $\mathbf{M}$ is the magnetization of the system [252]. In the case of a closed loop with current I, the expression for the change in free energy can be shown to be $\Delta G = -\int I\, d\Phi_a$, where Φ_a is the applied magnetic flux (threading the loop). The total magnetic flux through the closed superconducting loop will consist from the applied flux and the screening flux $\Phi_s = LI$, where L is the inductance of the loop. The total flux through the loop will be an integer multiple (m) of Φ_0: $\Phi_{total} = \Phi_a + LI = m\Phi_0$. If one considers the equilibrium behaviour of the loop at a fixed number of flux quanta ($m = const$), the integration with respect to Φ_a may be exchanged for integration with respect to I, resulting in: $\Delta G = LI^2/2$. Therefore, the free energy of the superconducting loop is given by[5] $G = G_0 + LI^2/2$, where G_0 is the constant of integration. Substituting $I = (\Phi_{total} - \Phi_a)/L = (m\Phi_0 - \Phi_a)/L$, results in:

$$G(\Phi_a;\, m) = G_0 + \frac{(\Phi_a - m\Phi_0)^2}{2L} \tag{5.3}$$

Equation (5.3) explicitly shows that the superconducting loop can exist in different flux states, each corresponding to a different integer value of m.

Different flux states of the loop may overlap. The degree of such overlap depends on the critical current and on the inductance L. The maximum free energy of the superconducting loop is reached when it carries critical current: $G_{max} = G_0 + LI_c^2/2$. It is therefore convenient to define the free energy in such a way as to have $G = 0$ when $I = I_c$:

$$G(\Phi_a;\, m) = \frac{(\Phi_a - m\Phi_0)^2}{2L} - \frac{LI_c^2}{2} \tag{5.4}$$

Figures 5.2a-c show the schematic representation of the free energy as defined in Eq. (5.4). Three cases can be distinguished depending on the magnitude of LI_c. If $LI_c < \Phi_0/2$ then the transition between the different flux states will require the loop to remain in the normal state for a finite period of time, because the magnitude of the applied flux that forces the loop into the normal state is too low to allow the restoration of superconducting state with a quantized magnetic flux through the loop. Magnitude of the applied flux will have to be increased (or decreased) before the restoration of superconducting state will be possible. If $LI_c = \Phi_0/2$ then as soon as superconductivity

[4] Gibbs free energy is used here because it is minimized in the equilibrium for a system at constant temperature and constant generalized force, which in this case is the applied magnetic field [252].

[5] In the most basic analysis, L is the geometrical inductance of the loop. In a more detailed analysis, L should include the contribution due to free energy of the section of the loop that will switch into normal state to let the flux into the loop [253].

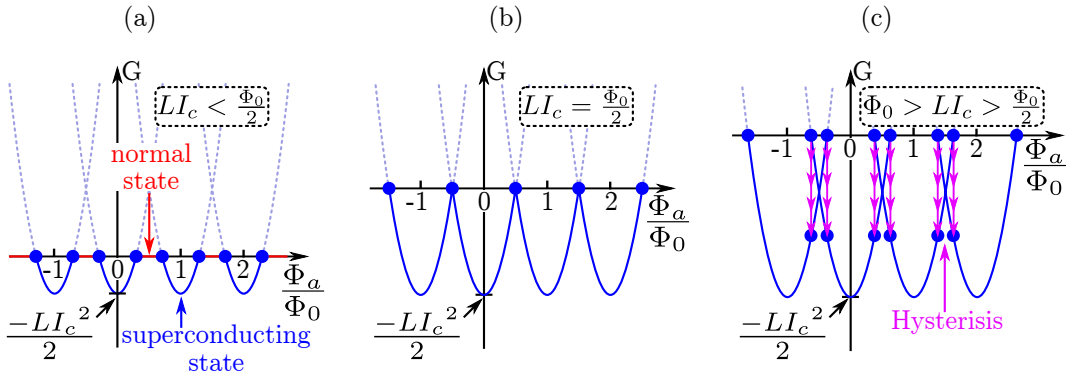

Figure 5.2: ***Magnetic flux states of a closed superconducting loop as a function of applied flux*** Φ_a***.*** *The three plots show the free energy (G), in solid blue lines, that corresponds to superconducting loops with* $LI_c < \Phi_0/2$*,* $LI_c = \Phi_0/2$ *and* $\Phi_0 > LI_c > \Phi_0/2$ *in sub-figures* ***(a)-(c)****, respectively. Here L is the inductance of the loop and* I_c *is the critical current of the loop. In all sub-figures, each parabola corresponds to a distinct flux state that a superconducting loop can be in. To switch between the neighboring states of a superconducting loop, the current flowing through the loop has to reach the critical value, which corresponds to zero free energy (G=0). The points of transition between the states are labeled with filled blue circles. In sub-figure (a) the neighbouring states of the loop are not connected, so the transition between the states involves the loop becoming non-superconducting for a finite period of time. In sub-figure (c) the states of the loop overlap leading to hysteresis in transitions between the states. The parabolas that correspond to distinct flux states are made to look the same in all three cases to high-light the fact, that the effect of different values of* LI_c *is to 'shift' the horizontal axis up or down.*

in the loop is suppressed by the applied flux, it becomes possible for the superconducting state to be restored, but in a higher flux state. If $LI_c > \Phi_0/2$ then the different flux states begin to overlap and it becomes possible to jump from one flux state to the next one, however the critical current still has to be reached before such a jump is allowed. Consequently a hysteresis appears in the switching between the different flux states.

5.2.3 Flux exclusion and flux penetration in the driven superconducting loop

Section 5.2.2 analyzed the equilibrium response of the closed superconducting loop to an applied field. This section will describe the dynamic behaviour.

Consider a single superconducting loop in the time-varying magnetic field perpendicular to the loop (as in Fig. 5.1). In a much simplified picture, when resistive losses and kinetic inductance of the Cooper pairs are neglected, the response of the closed superconducting loop to ramped magnetic field ($\mathbf{B}_a$) will be similar to that sketched in Fig. 5.3. At low magnitudes of the applied field the magnitude of the total magnetic flux through the loop ($|\Phi|$) will be close to zero. As the amplitude of the applied field increases past the critical value B^*, the flux through the loop will increase to a flux quantum. After that, the magnitude of the flux through the loop will grow in jumps, increasing by Φ_0 as the amplitude of the applied field is increased. One can distinguish two regimes: when the flux through the loop is zero despite the applied magnetic field

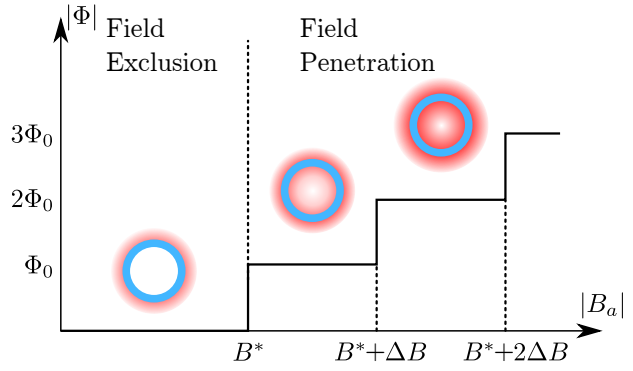

Figure 5.3: ***Flux exclusion in the superconducting loop.*** *Idealized response of the closed superconducting loop to an applied magnetic field of amplitude $|B_a|$. At low amplitudes of the applied field, the magnitude of the total flux through the loop $|\Phi|$ stays close to zero. When the amplitude of the applied field increases to a critical value B^*, the magnitude of the flux through the loop jumps to one flux quantum Φ_0. Further jumps occur every time the amplitude of the applied magnetic field increases by ΔB. The insets are artistic impressions of the magnetic field configuration (red) around the superconducting loop (blue).*

and the regime when flux through the loop is greater than zero. These two cases will be referred to as flux exclusion and flux penetration regimes.

The critical value B^* will depend on the mechanism of flux penetration into the loop. Let the applied field (B_a) oscillate harmonically in time. At lower oscillation frequencies, for type-II superconductors, magnetic field will be able to slip into the loop in form of Abrikosov vortices, but the propagation speeds of vortices inside the superconductors are too low [155, 254] to penetrate through the width of a realistic superconducting wire during a single 10 pico-second cycle (i.e. oscillation frequency of around 100 GHz). At high frequencies, the only way for the magnetic field to penetrate the closed superconducting loop is through local suppression of the superconducting state. This is a fast process limited by the nonequilibrium electron-phonon interaction time, which is about 1 ps in high-temperature superconductors [255, 256]. The superconducting state will be suppressed when the current in the closed loop reaches the critical value I_c. It follows, that when the applied magnetic field reaches $B^* = LI_c/S$, where L is the inductance of the closed loop and S is the area encircled by the loop, the superconductivity in the wire will be suppressed and the first magnetic flux quantum will enter the loop. After the penetration by the first quantum, the remaining field to be screened will be $B^* - \Delta B$, where $\Delta B = \Phi_0/S$. The required screening current will therefore be $I = I_c - \Phi_0/L$, i.e. lower than the critical current (assuming $\Phi_0 \leq 2LI_c$), consequently, the superconductivity in the loop will be restored. Following the first jump, there will be a new jump in flux through the loop every time the strength of the applied field reaches $B^* + m\Delta B$, where m is an integer. Such behaviour has been demonstrated in the lower frequency range in Refs. [257, 258]. Clearly, the most interesting behavior will be observed for the loops where $B^* \approx \Delta B$ (or $LI_c \approx \Phi_0$).

5.3 Flux quantization in nonlinear superconducting metamaterial

Silver and Zimmerman have previously investigated the applications of the single closed superconducting loops with nonlinear response due to flux quantization [253]. Building on this work, the rest of this chapter will describe how the nonlinear response of the closed superconducting loops can be used as a source of nonlinearity in the metamaterials.

In the simplest implementation of the metamaterial that relies on flux quantization in superconducting loops, one encloses the superconducting wire loop into a resonant split-ring resonator thus creating a meta-molecule. This meta-molecule will be a building block of the two-dimensional flat metamaterial array, which will be called the flux exclusion metamaterial. For normal radiation incidence on the array of such meta-molecules, the magnetic field of the incident wave does not penetrate the array and therefore is not directly engaged in the flux quantization. However, an incident electromagnetic wave polarized along the split-ring resonator gap will drive an oscillating current in the resonator that will produce oscillating magnetic field embraced by the split ring. The superconducting wire loop inside the split ring will respond depending on the amplitude of the generated magnetic field and therefore depending on the incident wave intensity: it will block the field penetration into the ring at low levels of magnetic flux, or will allow penetration at high levels, thus ensuring nonlinear nature of the response. As a result, in the flux penetration regime, the closed loop will be continuously driven by the oscillating magnetic field from one flux state to the next one, up and down the ladder shown in Fig. 5.3.

It shall be noted that electromagnetic functionality of the flux exclusion quantum metamaterial described here is distinctively different from the artificial atoms (flux qubits) based on Josephson junctions, where the flux through the superconducting loop (interrupted by a Josephson junction) can be treated as a quantum mechanical variable analogous to the displacement in quantum harmonic oscillator [37, 41, 51]. In case of these artificial atoms, the resonant response is created by the absorption of single photons of incident radiation with the energy that corresponds to separation between the energy levels of the artificial atom. In the present case, the resonant properties of the metamaterial are derived from the outer split-ring resonator of the meta-molecule which, at high frequency, acts as an LC circuit. Nonlinearity here is a result of inductance being a function of intensity: higher intensity levels of incident wave create higher magnetic flux through the split ring. At certain level of excitation the applied flux can drive transitions between the different quantum flux states of the inner loop, thus dynamically modifying the inductance and the resonant properties of the LC circuit (meta-molecule).

The scale of potential switching in the flux quantization metamaterial has been il-

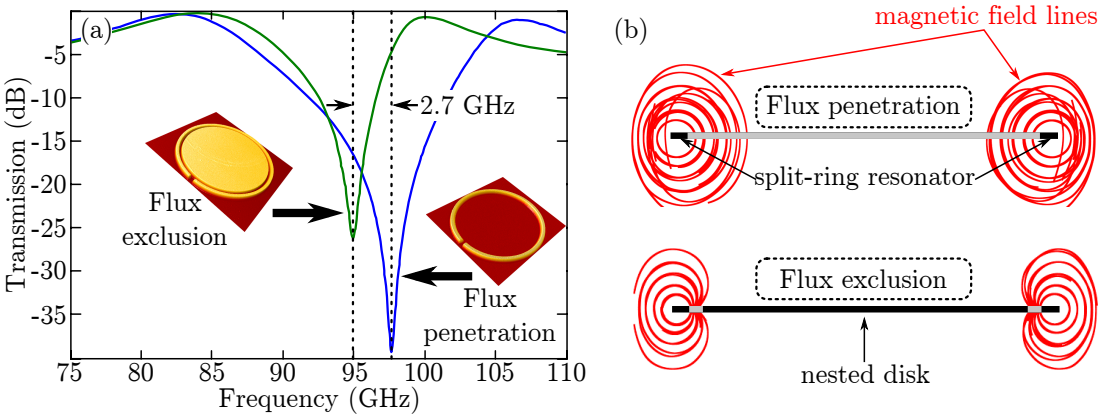

Figure 5.4: ***Switching in the flux exclusion superconducting quantum metamaterial (computer simulation). (a)*** *Resonant curves correspond to two limiting regimes (modeled by two different metamaterials), the flux exclusion regime (low intensity, green curve) and flux penetration regime (high intensity, blue curve). The insets show the unit cells of the metamaterials used to model the regimes. Both metamaterials were simulated as a thin yttrium-barium-copper-oxide film (at temperature 77 K) on 1 mm-thick sapphire substrate. The unit cell sizes were 240 μm×240 μm. Outer and inner radii of the split-ring resonators were 100 μm and 92 μm, respectively. The radius of the nested disk was 89 μm. The size of the gap in the split ring was 8 μm. The metamaterials were driven by the normally-incident radiation with electric field polarized along the gap in the split-ring resonators.* ***(b)*** *The side view of the distribution of magnetic field at the resonance of the two metamaterials.*

lustrated by modeling[6] the metamaterial response using two simpler structures that served as limiting cases for the flux exclusion and the flux penetration regimes. First metamaterial modeled the flux penetration regime. It was an array of split-ring resonators without the superconducting wire loop inside. Second metamaterial modeled the flux exclusion regime. It also was an array of split-ring resonators, but in addition, each resonator embraced a superconducting disk blocking the flux penetration through its center. In both cases, the modeling was carried out assuming that the metamaterial structures were manufactured from thin films of high-temperature superconductor yttrium-barium-copper-oxide (YBCO) on sapphire substrate. The reason for choosing YBCO for modeling and, later, for implementation of the flux exclusion metamaterials, is that it remains superconducting at a relatively high temperature (up to 80-90 K) and because, in YBCO, the transition to normal state and the subsequent relaxation into the superconducting state can occur at pico-second time-scale[7]. The full 3-dimensional

[6]Rigorous modeling of the time-dependent electromagnetic response of the superconductor can be achieved by coupling Maxwell's equations with the Time-Dependent Ginzburg-Landau (TDGL) equations [27, 259]. These are coupled nonlinear time-dependent partial differential equations that describe the temporal evolution of the current density and the density of superconducting (and normal) charge carriers within the superconductor. It should be noted however that TDGL are only strictly applicable to superconductors at temperatures very close to transition temperature and with vanishing superconducting energy gap (the so-called gapless superconductivity).

[7]High-current induced suppression of superconductivity (i.e. destruction of the Cooper pairs) in yttrium-barium-copper-oxide can occur on the scale of few pico-seconds [260]. Following the suppression of superconductivity, the recombination time of the Cooper pairs can be as short as 1-3 ps [261]. The relaxation time is usually limited by the time it takes the phonons (left after Cooper pair recombination) to escape into the substrate. This effect can be reduced by thinning down a small section of the loop (as

simulation of metamaterial transmission (carried out with COMSOL 3.5a), using the two-fluid model of superconductivity of YBCO (taken from Ref. [263]) and a realistic permittivity for sapphire[8], illustrates the potential switching in Fig. 5.4a. Blocking the flux penetration through the area embraced by the split ring results in a 2.7 GHz shift of the transmission resonance. Such a shift would correspond to switching from flux penetration state to the flux exclusion state in the flux quantization metamaterial with meta-molecules consisting of superconducting loops embraced by the split rings. Figure 5.4b shows the redistribution of the magnetic field in the meta-molecule that would arise due to switching.

The possibility of switching from flux exclusion to flux penetration states (see Fig. 5.3) can be discussed in the context of the split ring metamaterial with nested disks, even though a working design shall contain nested loops, because the disks can be viewed as a limiting case of the loops with thick borders. To observe the switching, the incident radiation shall drive the flux quantization metamaterial to such a level that flux applied to the disk exceeds Φ_0. Simultaneously, the electrical current density in the outer perimeter of the disk shall reach the critical value that destroys superconductivity thus allowing the magnetic field to penetrate inside. From modeling the response of split-ring metamaterial with nested disks (shown in Fig. 5.4a), it was estimated that, at resonance, the amplitude of the flux applied to the nested disks would reach Φ_0 at incident radiation intensity level of $\sim 0.5\,\mathrm{W/m^2}$. At such radiation intensity, the current density in the outer perimeter of the disk will be of the order of $10^4\,\mathrm{A/cm^2}$. This is much smaller than the critical current density of YBCO, which is approximately $10^6\,\mathrm{A/cm^2}$ at temperature 77 K [264].

5.3.1 Woodcut metamaterial design and sample manufacturing

Metamaterial design: To approach the regime where flux quantization will be observable ($LI_c \approx \Phi_0$) one could operate the metamaterial very close to superconductor's critical temperature θ_c, thus lowering the critical current density J_c. However, increasing the temperature leads to suppressed switching as Joule losses dampen the metamaterial resonance [76, 150, 265]. To go around this problem, a different flux exclusion quantum metamaterial had to be designed, that was more complex than just the pattern of loops enclosed by the split rings, used in the preceding sub-section to explain the principle of operation. Here, instead of enclosing a single superconducting loop, every split ring of the design embraced a cluster (mesh) of smaller superconducting loops, resembling a wood cut, as shown in Fig. 5.5a. In this design, the switching will be achieved si-

in Sec. 3.5), so that the superconducting-to-normal transition only occurs there. Operation at frequencies of 100 GHz should therefore be possible. By contrast, in niobium (for example), the recombination of the Cooper pairs takes longer than 100 ps [262].

[8]For the purposes of modeling, sapphire permittivity was taken as $\epsilon_r = 10.35$ because the sapphire substrates used in the experiments were polished with random orientation of the crystalline axis to the surface, so the permittivity could potentially lie anywhere within the range $9.3 \leq \epsilon_r \leq 11.4$ [94].

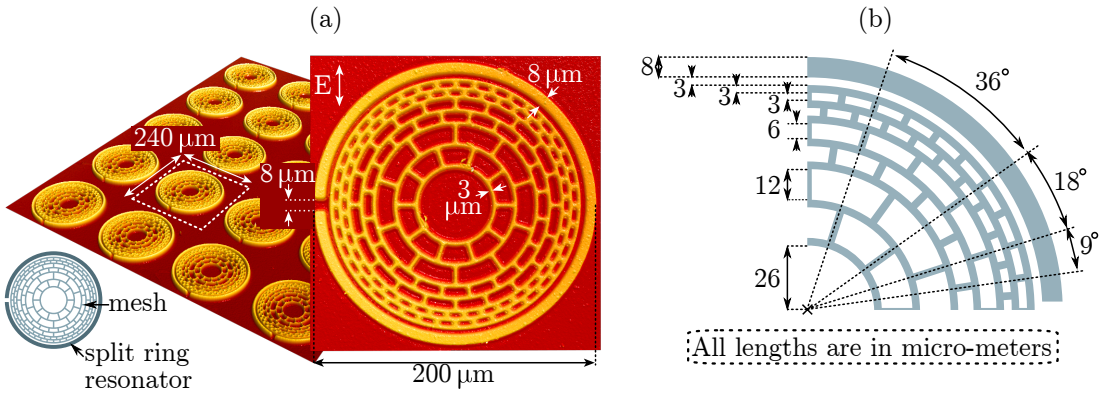

Figure 5.5: ***Design and implementation of the Woodcut superconducting quantum metamaterial.*** ***(a)*** *The interference microscope picture of a fragment of the woodcut metamaterial (colour expresses height). The metamaterial is created by patterning 300 nm thick YBCO film deposited onto 1 mm thick sapphire substrate. The area covered by the metamaterial is a disk with diameter of 30 mm.* ***(b)*** *Details of the woodcut metamaterial design.*

multaneously in a number of small loops. As loops become smaller the same applied magnetic *flux* induces larger screening currents in them. Making the loops very small thus allows the screening currents to reach the critical value necessary for the suppression of superconductivity at the level of applied flux close to Φ_0. The magnetic field generated by the split-ring resonators will be strongest near the split-ring resonator wire and will become weaker towards the centre of the meta-molecules (centre of the mesh). To compensate for this, the area of the loops closer to the centre of the mesh increases, so that the magnetic flux applied to the outer and the inner loops of the mesh is of comparable magnitude. This could help to achieve the cascade switching, where the flux first penetrates the outer loops of the mesh, then the loops in the next belt[9] of the mesh and so on. The neighbouring belts of the mesh are counter-rotated with respect to each other in order to reduce the anisotropy of the mesh. This design will be called the woodcut metamaterial.

Manufactured metamaterial sample: The woodcut metamaterial was manufactured according to the design shown in Fig. 5.5 by photolithographically patterning a 300 nm-thick YBCO film deposited onto a 1 mm-thick sapphire substrate. Ion beam etching was used to remove the YBCO film exposed after the photolithography. Further details of manufacturing process are given in Sec. 2.3. Figure 5.5a shows a 3D scan of the manufactured metamaterial sample. The outer and inner radii of the split-ring resonators were 100 µm and 92 µm respectively; the gap in the split-ring resonators was 8 µm wide. The outer radius of the mesh was 89 µm. All the wire-strips inside the mesh, were designed to be 3 µm wide, but due to manufacturing uncertainties, most notable on the outer edge of the mesh (see Fig. 5.5a), the wire width was slightly greater. The metamaterial unit cell size was 240 µm × 240 µm.

[9]Collection of loops at the same distance from the centre of the mesh, i.e. a 'circle' of loops.

Full 3-dimensional simulations show that in this metamaterial structure, at temperature 77 K, near the resonant frequency of $\sim$ 95 GHz, at the incident radiation intensity of $\sim 10\,\mathrm{kW/m^2}$, the flux switching should be observed: the current through the outer rim of the mesh will reach the critical current[10] of 10 mA at the same time when the amplitude of the magnetic flux applied to outer loops of the mesh will be of order Φ_0.

5.3.2 Experimental characterization and discussion

The level of intensity of $\sim 10\,\mathrm{kW/m^2}$, required to demonstrate switching, was not achievable in setup used for metamaterial characterization (see Sec. 2.2.7), so the electromagnetic properties of the woodcut metamaterial were characterized only at low intensity, in the flux exclusion regime (see Fig. 5.3). To evaluate the potential switching of electromagnetic properties from the flux exclusion to the flux penetration regimes, the two regimes were *experimentally* modeled by comparing the measured transmission of the split-ring metamaterial and the metamaterial with split-ring resonators containing the field-blocking nested disks (inside the split rings). These two reference metamaterials represent the two extremes of the woodcut metamaterial operation: the flux exclusion and the flux penetration regimes.

All three metamaterials shared the same unit cell and split ring dimensions and were manufactured by the same technological process (see Sec. 2.3). The free-space low-temperature electromagnetic response of the three metamaterials in the 75 GHz-110 GHz frequency range was characterized following the methods described in Sec. 2.1 and Sec. 2.2. The intensity of incident radiation reaching the metamaterials was of the order of $0.5\,\mathrm{W/m^2}$ (see Sec. 2.2.7).

The measured transmission of the three metamaterials is shown in Fig. 5.6a,b. The metamaterials demonstrated a clear Lorentzian-like resonant dip in transmission, that shifted towards the lower frequencies and became shallower as the temperature reached the critical temperature of the superconductor (83 K).

The scale of the expected change in the transmission of the woodcut metamaterial upon flux switching is illustrated in Fig. 5.6a,c. The experiment (Fig. 5.6a) and numerical simulation (Fig. 5.6c) show that flux penetration would lead to a shift in the resonance frequency of the metamaterial array. Experimentally observed value of the potential shift is about 7 GHz for temperatures below 60 K, and decreasing towards the critical temperature. This shift is well replicated by calculations. Some minor discrepancies between the experimentally measured and the calculated characteristics of the metamaterial response are explainable by experimental tolerance of the fabrication process (widths of lines and gaps in the designs) and by simplifications of the two-fluid model of superconductivity that, for example, does not account for anisotropy of the material's response.

[10] Critical current density of $J_c \sim 10^6\,\mathrm{A/cm^2}$ and wire cross-section of $3\,\mu\mathrm{m} \times 300\,\mathrm{nm}$.

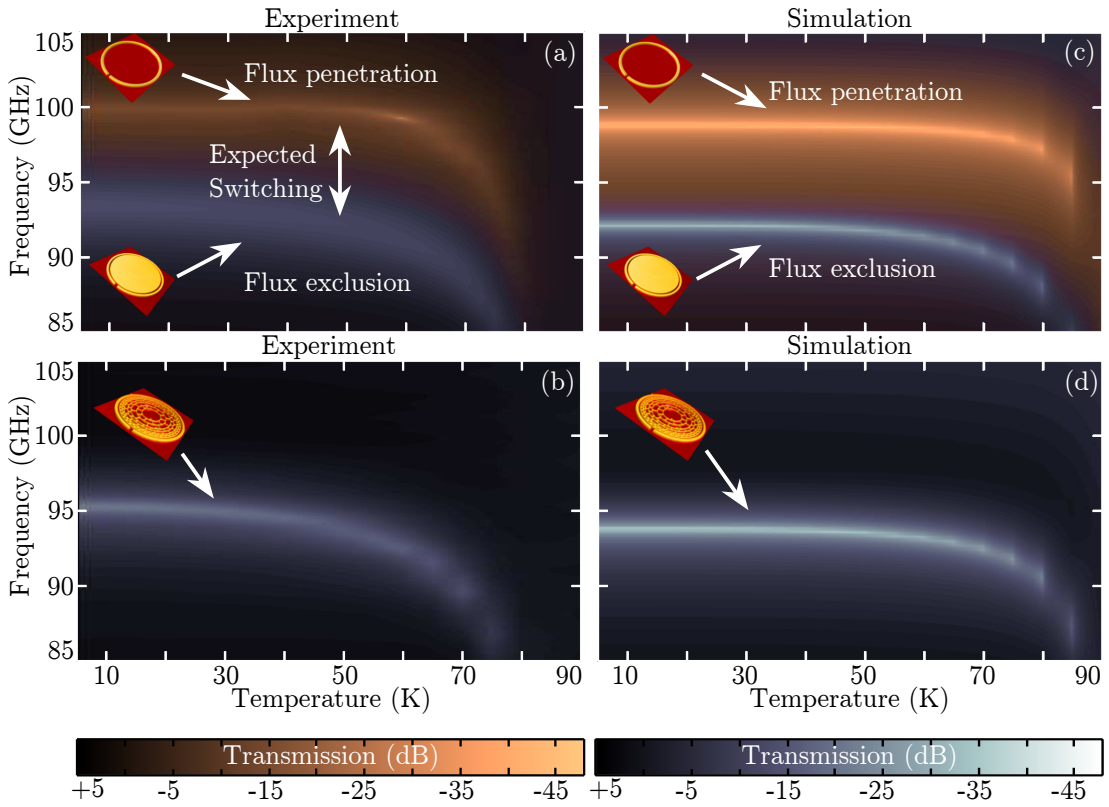

Figure 5.6: ***Electromagnetic properties of the woodcut metamaterial and of the reference metamaterial structures.*** ***(a)*** *Experimentally observed transmission of the split-ring superconducting metamaterials with and without the nested disk (blue and yellow respectively).* ***(b)*** *Experimentally observed transmission of the woodcut metamaterial.* ***(c)*** *Simulated transmission of the split-ring resonator metamaterial with and without the nested disk.* ***(d)*** *Simulated transmission of the woodcut metamaterial. In all cases level of transmission is expressed through colour.*

Upon reaching the excitation level of $\sim 10\,\mathrm{kW/m^2}$ the woodcut metamaterial should exhibit a similar $\sim 7\,\mathrm{GHz}$ shift in transmission resulting in $\sim 20\,\mathrm{dB}$ of transmission change[11]. However, the exact dynamics of this shift, which is likely to take the form of a hysterectic nonlinear response, are difficult to predict. It will have to be investigated both theoretically and experimentally in the future.

At this stage it shall be noted, that experimentally observed transmission spectra for the woodcut metamaterial (Fig. 5.6b) are closely matched by the transmission spectra of the split-ring metamaterial with field-blocking disk (Fig. 5.6a), as should be expected for the flux exclusion regime. Simultaneously, the experimentally measured transmission of the woodcut metamaterial (Fig. 5.6b) is faithfully replicated by numerical calculations based on *linear* response of all constituent materials (Fig. 5.6d). One therefore concludes that, as expected, at incident radiation intensity level of $0.5\,\mathrm{W/m^2}$ the woodcut metamaterial remains in the flux exclusion state.

As far as I am aware this is the first observation of the quantum phenomenon of

[11]The difference between the transmission of the woodcut metamaterial at resonance and away from resonance (i.e. 7 GHz away from resonance) reaches 20 dB in the superconducting state (see Fig. 5.6b)

flux exclusion affecting the macroscopic properties of a metamaterial. Here one can see a good corroboration between the computed (Fig. 5.6d) and experimentally measured values (Fig. 5.6b) of woodcut metamaterial transmission. The good agreement between the full 3-dimensional Maxwell calculations and experimental spectra indicates a high quality of the samples and thus a non-destructive nature of the fabrication process. This gives confidence that switching between the flux states of the closed superconducting loops will be observable in the woodcut metamaterial at the higher intensity levels.

5.4 Future work on flux exclusion metamaterials

This section will describe the future work which will simplify and improve the design of the flux exclusion metamaterials.

The requirement $LI_c \approx \Phi_0$ (see Sec. 5.2.2 and Sec. 5.2.3) imposes a limit on the inductance of the closed loops. The typical strip-wire width that can be achieved by photolithographically patterning thin superconductor film is about 2 μm and the achievable film thickness[12] is about 100 nm. With critical current density of order 10^6 A/cm^2, the typical critical current of the closed superconducting loop implemented using photolithography is $I_c \sim 1 - 10$ mA. Consequently, the typical inductance of the closed loop should be $L \approx \Phi_0/I_c \sim 0.1 - 1$ pH, which corresponds to a loop of radius of few micro-meters. Such inductance is significantly smaller than the inductance of the meta-molecules used to implement the metamaterials in the 75-110 GHz range (about 500 pH). As a result, in order to observe significant change in the properties of the metamaterial due to switching between the flux states of the closed loops, one has to use either many closed loops together (as in the woodcut metamaterial), or one has to rely on changes in properties other than inductance.

Figures 5.7a,b show how a closed superconducting loop can be used as a nonlinear resistor. A section of the closed loop is designed to have a smaller cross-section than the rest of the loop. Two current-carrying wires are attached to the loop. The positioning of the attached wires is such that the resistance[13] of the non-constricted section of the loop (R_l) is comparable to the resistance of the constricted section (R_{jtn}), which will be called the junction. This is achieved by making the path of the current through the non-constricted section longer than the path through the junction, which compensates for reduced cross-section of the junction. The effective resistance of the loop will be $R_{eff} = R_l R_{jtn}/(R_l + R_{jtn})$.

As long as the applied current (I_a), through the closed loop resistor, is low enough for loop to remain superconducting, the current through the non-constrained section of the loop will be $I_l = I_a R_{jtn}/(R_l + R_{jtn}) - I_s$ and the current through the junction will be $I_{jtn} = I_a R_l/(R_l + R_{jtn}) + I_s$. The screening current I_s will ensure that magnetic

[12] Here it is presumed that most of the loop is made out of thick film with only a small section of the loop selectively etched in order to reduce the critical current.

[13] Here it is assumed that the loop will be driven by oscillating currents, therefore even the currents flowing through the superconductor will be subject to Ohmic losses (see Sec. 1.2).

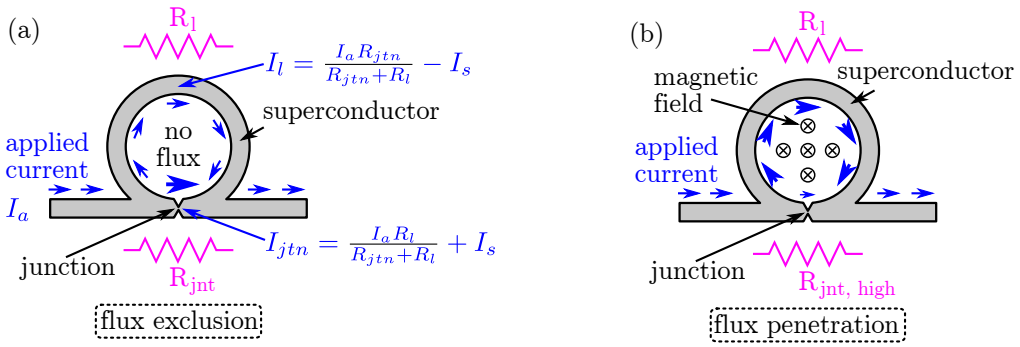

Figure 5.7: ***Closed superconducting loop as a nonlinear resistor. (a)*** *The superconducting loop in the flux exclusion state with applied bias current. The cross-section of the wire that makes up the loop is reduced at one point to form the junction. The junction has low critical current and high resistance (R_{jtn}). The current-carrying wires are attached to the loop in such a way, that the current flowing through the non-constricted section of the loop meets resistance (R_l) that is comparable to R_{jtn}. In the flux exclusion state, the currents flowing through the junction (I_{jtn}) and through the non-constrained (I_l) section will be balanced with the additional screening current (I_s), in such a way, that the net magnetic flux through the loop will be zero.* ***(b)*** *The superconducting loop in the flux penetration state. Once the magnitude of the applied current through the junction exceeds the critical current, the junction will enter into the normal state and its resistance will increase ($R_{jtn} \rightarrow R_{jtn,high}$) leading to increase in the effective resistance of the closed loop. At the same time, the magnetic field will enter the closed loop. After the magnetic flux penetration, the superconductivity in the junction may be restored provided the flux trapped in the loop is an integer multiple of Φ_0.*

flux through the loop is zero. The superconductivity in the junction will be suppressed when the current flowing through the junction will exceed the critical current. As a result of the suppression of superconductivity, the resistance of the junction will be increased, leading to increase in the R_{eff}. Following the transition of the junction into the normal state, the magnetic flux will enter the closed loop. The superconductivity in the junction could then be restored provided the magnitude of the flux trapped in the loop is an integer multiple of Φ_0 (see Sec. 5.2.2 and Sec. 5.2.3). A thorough study of the dynamics of such closed superconducting loops, used as resistors, has been provided by Silver and Zimmerman [253].

The closed superconducting loop with a nonlinear resistance, shown in Fig. 5.7, can be incorporated into various metamaterial designs including the split-ring metamaterial as well as the asymmetrically-split ring metamaterial. In this section, the analysis will focus on embedding the closed loops into the asymmetrically-split ring metamaterial because the high-quality resonant response, typical to this metamaterial (see Chap. 3 and Sec. 3.2 in particular), should allow to observe nonlinear response at low level of radiation intensity. Figures 5.8a-c show the design of the asymmetrically-split ring metamolecule with the embedded closed superconducting loops. The metamaterial shall be implemented out of 300 nm thick film of YBCO on 1 mm thick sapphire substrate (same as the woodcut metamaterial). The closed superconducting loops are created by removing the YBCO film within the wire strips that make up the asymmetrically-split rings. The loops are positioned in the midpoints of the strips, where the largest currents

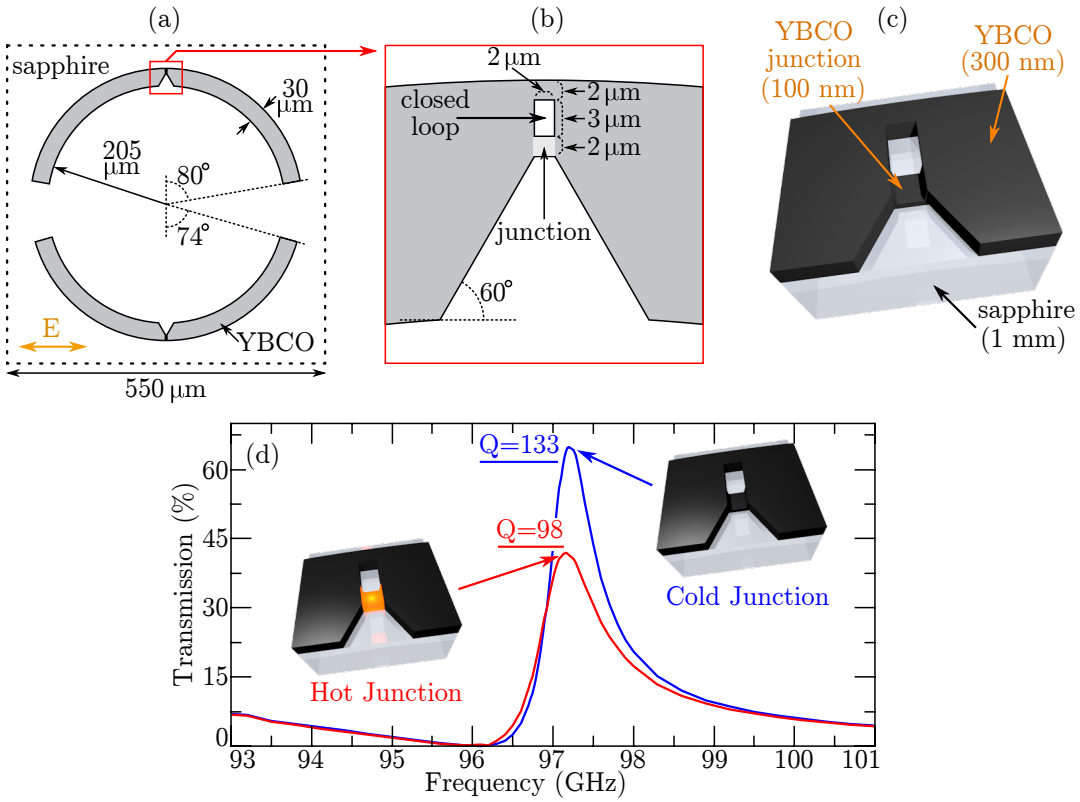

Figure 5.8: ***Asymmetrically-split ring flux exclusion metamaterial.*** ***(a)*** *The unit cell of the asymmetrically-split ring metamaterial. Grey areas denote thin YBCO film (300 nm thick). White area is the sapphire substrate (1 mm thick). Orange arrow labeled 'E' denotes the polarization of the incident radiation.* ***(b),(c)*** *Close-ups of the closed superconducting loop embedded into the asymmetrically-split ring. The thickness of the YBCO film is reduced to 100 nm at the bottom part of the loop (junction).* ***(d)*** *The transmission of the metamaterial at temperature 77 K. The blue curve corresponds to all of the metamaterial being at temperature 77 K (cold junction). The red curve (lower peak) corresponds to most of the metamaterial being at temperature 77 K, apart from the junctions which are at temperature 90 K (hot junction). The quality factors of metamaterial response are $Q = 133$ and $Q = 98$ for the case of cold junction and hot junction, respectively.*

will be induced by the incident radiation[14]. The wire strips are tapered around the the closed loops in order to ensure small critical current of the closed loops. One side of each loop is further thinned down to 100 nm (thus creating the junctions).

Figure 5.8d shows the simulated[15] transmission spectrum of the metamaterial at temperature 77 K for the case when the junctions are in the superconducting state (as the rest of the metamaterial) and for the case when the junctions are in the normal state (i.e. at 90 K), while the rest of the metamaterial still remains superconducting. According to simulation, at the intensity of incident radiation of 40 W/m^2, the magnitude of the

[14] See Sec. 3.2 and Fig. 3.1b in particular.

[15] Conductivity of YBCO is obtained using the model from Ref. [263], the dielectric constant of sapphire was $\tilde{\epsilon}_r = 9.3 \times (1 - \mathrm{i}2 \times 10^{-7})$ [94]. COMSOL 3.5a was used to numerically solve the Maxwell's equations. The metamaterial was driven with normally incident plane-wave radiation with polarization perpendicular to the symmetry axis of the meta-molecule (as is shown in Fig. 5.8a with letter 'E').

induced current that is forced through the junctions will reach the critical current[16]. The magnitude of magnetic flux applied to the closed loops[17] will reach Φ_0 at approximately the same level of intensity of incident radiation. Thus the condition $LI_c \approx \Phi_0$ is satisfied. It should be noted that the required intensity of radiation is only 5-6 times greater than the maximum achievable intensity in the sub-terahertz spectroscopy setup used for metamaterial characterization in this thesis (see Table 3.2).

The exact dynamics of the metamaterial response are difficult to anticipate, but an estimate can be made by noting that the transition of the junctions to normal state leads to change in the quality factor[18] of metamaterial response from $Q = 133$ to $Q = 98$ (see Fig. 5.8d). One can approximate the complicated dynamics of the asymmetrically-split ring metamaterial with a single one-dimensional sinusoidally driven oscillator with a nonlinear damping term (γ). The evolution of such oscillator will be described by the following equation [79]:

$$\ddot{x} + \gamma(x) \cdot \dot{x} + \omega_0^2 x = F \cdot \sin(\omega t) \tag{5.5}$$

Where x is the 'displacement' of the oscillator, ω_0 is the angular resonant frequency of the non-damped oscillator, F is a constant and t is time. In case of harmonic oscillators, the relationship between the quality factor of the resonant response and the damping term is given by[19] $Q = \omega_0/\gamma$. Thus the change of quality factor from 133 to 98 corresponds to change of the damping term from $\gamma = \omega_0/133$ to $\gamma = \omega_0/98$.

Figure 5.9 shows the numerical solution of Eq. (5.5) for three different damping terms: γ is constant (case A), γ increases when the displacement of the oscillator (x) crosses a certain threshold and remains high until x decreases (case B), and γ increases and then decreases whilst x grows (case C). Case B models the simple suppression of the superconductivity in the junction. Case C models the event of transition between the two flux states of the closed loop, i.e. initially the damping is low, then the superconductivity in the junction is suppressed and damping becomes high, later still the superconductivity in the junction is restored so the damping returns to lower level. The numerical solutions in Fig. 5.9 all reach $|x|^2 = 1$ at the maximum. This is achieved not by normalization, but by controlling the amplitude of the driver: $F = 0.2993$, 0.3577, 0.3372 for cases A, B, C, respectively.

The results of numerical simulation in Fig. 5.9 suggest that the flux penetration and the transition between the different flux states of the closed loops, in the asymmetrically-split ring flux exclusion metamaterial, can be detected by monitoring the quality factor

[16]Critical current density $J_c \approx 10^6\,\mathrm{A/cm^2}$ (YBCO at 77 K) with wire cross-section $2\,\mu\mathrm{m} \times 100\,\mathrm{nm}$ lead to critical current $I_C = 2\,\mathrm{mA}$.

[17]The 'applied magnetic flux' refers to the magnitude of magnetic flux that will enter the superconducting loop once the superconductivity in the junction is suppressed (see Fig. 5.7b).

[18]$Q = \nu_0/\Delta\nu$, where ν_0 is the resonant frequency and $\Delta\nu$ is the full width at half maximum of the transmission resonance.

[19]One can show that $Q = \omega_0/\gamma$ follows from the definition of the quality factor (i.e. energy stored divided by energy lost per cycle). The approximation $Q \approx \nu_0/\Delta\nu$ used throughout the thesis is correct provided the value of the Q-factor is large. One can show that for the driven damped harmonic oscillator $\nu_0/\Delta\nu \approx Q - 1/2Q + ...$

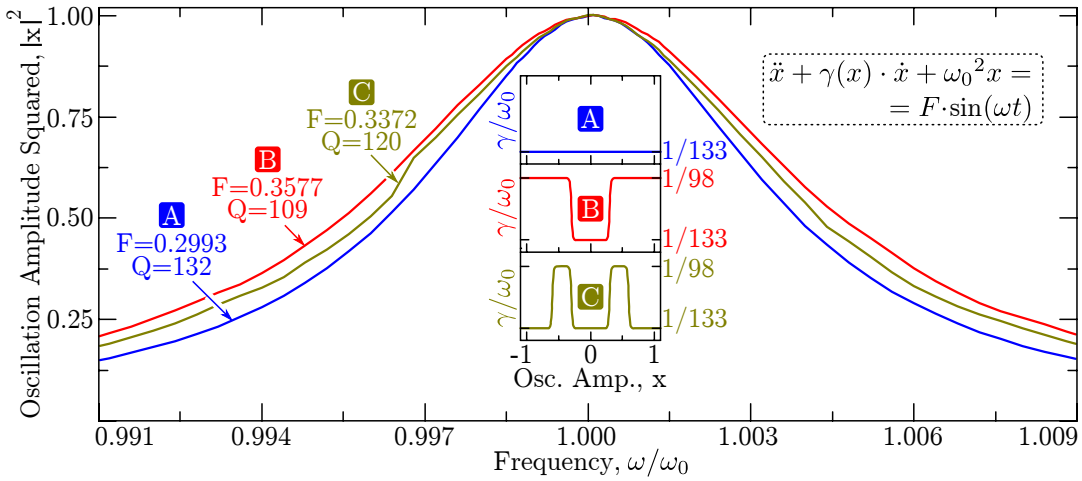

Figure 5.9: ***Response of the oscillator with a variable damping term*** $\gamma(x)$ ***- model for the dynamics of asymmetrically-split ring flux exclusion metamaterial.*** *The three curves show the amplitude squared of the numerical solution for the equation* $\ddot{x}+\gamma(x)\cdot\dot{x}+\omega_0^2 x = F\cdot\sin(\omega t)$ *for three different damping terms (A, B, C). The damping terms are plotted in the inset. To ensure the same maximum amplitude of oscillations in all cases (max* $\left(|x|^2\right)=1$*), the amplitude of the driving signal was* $F = 0.2993, 0.3577, 0.3372$ *for the damping terms A, B, C respectively. The quality factor of the oscillator response is denoted with* Q*.*

of the resonant response of metamaterial as a function of radiation intensity[20]. As the radiation intensity increases from below $10\,\mathrm{W/m^2}$ to $100-200\,\mathrm{W/m^2}$ the quality factor will initially decrease (case A $\rightarrow$ case B) and then increase (case B $\rightarrow$ case C). The level of frequency resolution required to register such changes in the quality factor of metamaterial response is of order[21] of 50 MHz, which is detectable on the Vector Network Analyzer (VNA) used for the sub-terahertz spectroscopy in this thesis[22]. Alternatively one may aim to detect the nonlinear response via generation of harmonics, or intermodulation distortion. This however, will involve serious modifications to the spectroscopy setup, and shall be investigated in the future.

5.5 Conclusion

In conclusion, a new type of superconducting metamaterial capable of quantum level nonlinear response underpinned by flux quantization has been designed, modeled, manufactured from a high-temperature superconductor and characterized in low-intensity, flux exclusion regime. Measurements on model metamaterial samples have demonstrated the extent of change in metamaterial's transmission upon switching. A second metamaterial design, potentially capable of nonlinear response at lower intensity of incident

[20] The amplitude of the transmission peak is also likely to change as a function of intensity, but it is harder to measure such a change (see App. G).

[21] Change in quality factor from $Q = 110$ to $Q = 120$ for the resonant frequency $\nu_0 \approx 100\,\mathrm{GHz}$ corresponds to change in the width of resonance from $100\,\mathrm{GHz}/110$ to $100\,\mathrm{GHz}/120$, which is approximately 80 MHz.

[22] The frequency resolution of the VNA was 22 MHz in all experiments described in this thesis. The VNA can be configured to operate with even higher frequency resolution.

radiation, has been proposed.

The metamaterials with nonlinear response that engages the phenomenon of flux quantization, could find applications in metrology, linking the intensity of incident radiation to the geometry of the meta-molecules, and in active devices for controlling THz and sub-THz radiation.

Chapter 6

Conclusions and Outlook

6.1 Summary

The aim of this thesis was to design new solutions for the applied and the fundamental electrodynamics by harnessing the potential of the metamaterials.

The applied metamaterial solutions presented in this thesis targeted the relatively under-explored sub-THz/terahertz spectrum, that is expected to have numerous applications in many fields of technology including security [54], communications [63] and biomedical imaging [62]. The demonstrated results are:

- Large-area electro-optical modulation of sub-THz radiation incident on the superconducting metamaterial. Modulation rate of 100 kHz and modulation depth of 45% has been demonstrated.
- Enhancement of radiation sensor performance via radiation harvesting in coherent superconducting metamaterials.
- Nonlinear response in a sub-THz superconducting metamaterial at radiation intensity below $10\,\mathrm{W/m^2}$.

The results of this thesis that relate to fundamental electrodynamics are:

- An analytical formalism was developed, that links the transmission and the reflection of the metamaterial with the microscopic multipole excitations within the constituent meta-molecules. Apart from the electric and magnetic multipoles, the formalism includes the contribution from the toroidal multipoles, which are necessary for the complete multipole expansion. The developed formalism, for the first time, allows to study toroidal multipole excitations in the metamaterials on a *quantitative* level.
- It was proved that toroidal dipole excitations could not be observed in two-dimensional metamaterials. The next simplest kind of metamaterials, where the toroidal dipole response could be observed, has been identified, implemented and experimentally characterized.

- A new class of metamaterials has been demonstrated, that display resonant transparency due to destructive interference between the co-located toroidal and electric dipoles.
- The flux exclusion quantum metamaterial, has been introduced, and studied both theoretically and experimentally (in the low-intensity regime).

6.2 Outlook

The work reported in this thesis focused on the proof-of-principle demonstrations. Consequently, there is room for further research in all of the topics that were discussed in the preceding chapters. Some of the suggestions for the future work will be listed below.

The electro-optical modulator and the low-intensity nonlinear superconducting metamaterial, described in this thesis, allow to control the sub-THz radiation incident on the metamaterial. Due to the ability of these metamaterials to modulate sub-THz/terahertz[1] beams with large cross-section, they can potentially form the basis of the high-throughput directional communication systems [63], that utilize spatial multiplexing [266], and therefore rely on radiation with large cross-section beams.

The radiation-harvesting metamaterial bolometer, presented in the thesis, demonstrates how the performance of the bolometer, for example selectivity, can be drastically improved by combining it with the metamaterial. Such boost of the radiation sensor performance could be of great utility for the next generation of terahertz imaging systems in surveillance, quality control and medicine [62].

A significant part of this thesis has been dedicated to deriving the relationship between the metamaterial transmission and reflection, and the microscopic multipole excitations, including the toroidal dipole excitations, within the meta-molecules. Building on this platform, one can study the occurrence of constituents with toroidal topology (capable of displaying toroidal dipole excitations) in various metamaterial systems, thin slabs of natural materials and in suspensions of biological cells. From the topological point of view, torus is the next simplest shape after the sphere (i.e. after a 'blob'), the molecules and living cells with toroidal shape should therefore be ubiquitous in nature.

The toroidal void metamaterials, described in this thesis, demonstrate the destructive interference between the co-located electric and toroidal dipoles. Such dipole configurations have been predicted to enable observation of the time-dependent Aharonov-Bohm effect [183]. It is of fundamental importance to test this prediction in the experiment, as it could have paradigm-shifting repercussions for the electromagnetism (by establishing the independent physical nature of the vector potential in electrodynamics).

The flux exclusion quantum metamaterials, introduced in this thesis, could potentially display nonlinear response dictated by the geometry of the metamaterial rather

[1] To operate in the terahertz spectrum, the metamaterials would have to be implemented out of high-temperature superconductors such as YBCO, that retain the superconducting properties well into the terahertz range (e.g. Ref. [151]).

than by material parameters. One could therefore link the intensity of the radiation driving the quantum flux exclusion metamaterial, to the geometry of that metamaterial, thus creating a new way of measuring the intensity of electromagnetic radiation.

Appendix

A Load resistance and bias voltage for the metamaterial-based bolometer

This appendix will explain the method used to choose the suitable bias voltage and load resistance for the metamaterial-based bolometer described in Sec. 3.3.

The electrical circuit equivalent of the metamaterial bolometer is shown in Fig. A.1a. The signal voltage is given by $V_s = V_B R_L/(R_L + R_{MM})$, where V_B is the bias voltage, R_L is the load resistance and R_{MM} is the resistance of the metamaterial, i.e. the resistance of the hot-spot that is responsible for sensing the radiation (see Fig. 3.4a). The sensitivity is given by:

$$S = \left|\frac{dV_s}{dP}\right| = \left|\frac{dQ}{dP} \cdot \frac{dR_{MM}}{dQ} \cdot \frac{dV_s}{dR_{MM}}\right| \tag{A.1}$$

Where P is the (total) power of radiation incident on the metamaterial and Q is the rate of heat dissipation at the hot-spot. The first factor in the above expression (dQ/dP) describes how effectively the energy from the cavity-like mode, established on the metamaterial surface, couples into the hot-spot.

The second factor (dR_{MM}/dQ) in Eq. (A.1) describes how effectively the heat dissipated at the hot-spot is converted into change in hot-spot resistance. The heat dissipation rate at the metamaterial is $Q = (V_B - V_s)\, I = V_B I - R_L I^2$, where $I = V_B/(R_L + R_{MM})$ is the current through the metamaterial and through the load resistor[2]. The second factor can therefore be evaluated in the following way:

$$\begin{aligned}\frac{dR_{MM}}{dQ} &= \left(\frac{d}{dQ}\right)\left(\frac{V_B - V_S}{I}\right) = \left(\frac{1}{V_B - 2R_L I} \cdot \frac{d}{dI}\right)\left(\frac{V_B - R_L I}{I}\right) \\ &= \frac{V_B}{(2R_L I - V_B)\, I^2} = \frac{V_B}{(R_L - R_{MM})\, I^3} \\ &= \frac{(R_L + R_{MM})^3}{V_B^2 \cdot (R_L - R_{MM})}\end{aligned}$$

The third factor (dV_s/dR_{MM}) in Eq. (A.1) describes how much the change in re-

[2]The equipment detecting changes in V_s is assumed to have sufficiently large input resistance to ignore the difference in current flowing though the metamaterial and through the load resistor.

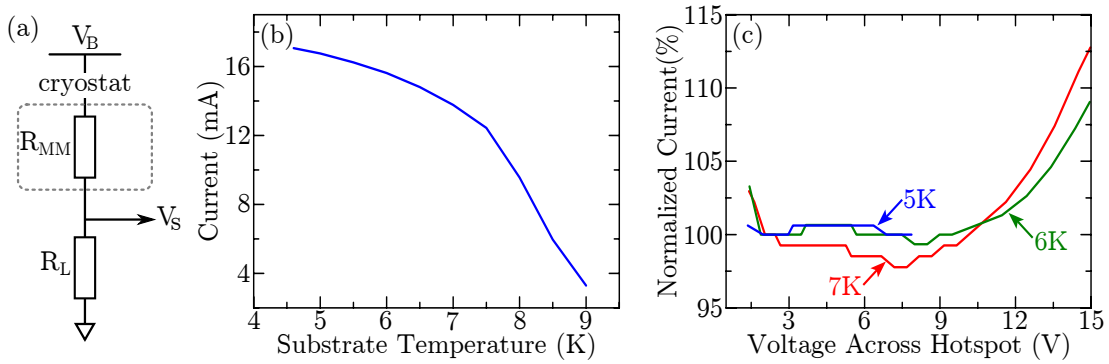

Figure A.1: ***Electrical properties of hot-spots in the metamaterial bolometer.*** ***(a)*** *The electrical circuit equivalent to the metamaterial bolometer shown in Fig. 3.4a.* ***(b)*** *The current through the metamaterial bolometer at $V_B = 4$ V bias as a function of temperature.* ***(c)*** *Current through the metamaterial as a function of voltage across the hot-spot.*

sistance of the hot-spot influences the change in signal voltage. Expressing the signal voltage as a function of the metamaterial resistance allows to evaluate the third factor:

$$\frac{dV_s}{dR_{MM}} = \left(\frac{d}{dR_{MM}}\right)\left(V_B \cdot \frac{R_L}{R_L + R_{MM}}\right) = -\frac{V_B R_L}{(R_L + R_{MM})^2}$$
$$= -\left(\frac{R_L I}{V_B}\right) \cdot I$$

Factor dR_{MM}/dQ is maximized for $R_{MM} \approx R_L$. It has been previously shown [93], that for large enough voltage-biased hot-spots on long superconducting strips, the current through the hot-spot does not depend on voltage (it only depends on substrate temperature and material constants). The same effect has been observed in the experiments reported here: the current through the hot-spot in the metamaterial changed by less than 5% when voltage across the hot-spot was varied from $V_B = 2\,\mathrm{V}$ up to $12\,\mathrm{V}$ (see Fig. A.1b,c). Thus, to a good approximation, current (I) could be taken to be constant at any fixed substrate temperature. In this case, dV_s/dR_{MM} was maximized for largest possible $R_L I/V_B$. Simultaneously, the current-dependent voltage drop across the load resistor imposed the lower limit on V_B, i.e. the bias voltage had to be large enough to force current I through the load resistor R_L, so $V_B \geq R_L I$. Taking this limit into account together with condition $R_{MM} \approx R_L$ (to maximize dR_{MM}/dQ) gave $V_B \approx 2R_L I$ as the optimal bias voltage.

The only remaining free parameter is the load resistance. Factor dV_s/dR_{MM} will not depend on it (provided the optimal bias voltage is chosen). Factor dR_{MM}/dQ will increase for larger R_L and R_{MM}. The dependence of dQ/dP on R_{MM} (i.e. the size of the hot-spot) is unclear. After resiting the following load resistances $R_L = 1\,\Omega$, $10\,\Omega$, $50\,\Omega$, $100\,\Omega$ it has been found that the sensitivity of the metamaterial bolometer grew when R_L was increased. Higher resistances were not tested, as it became increasingly difficult to reach low substrate temperatures due to excessive heat dissipation dissipation at the metamaterial.

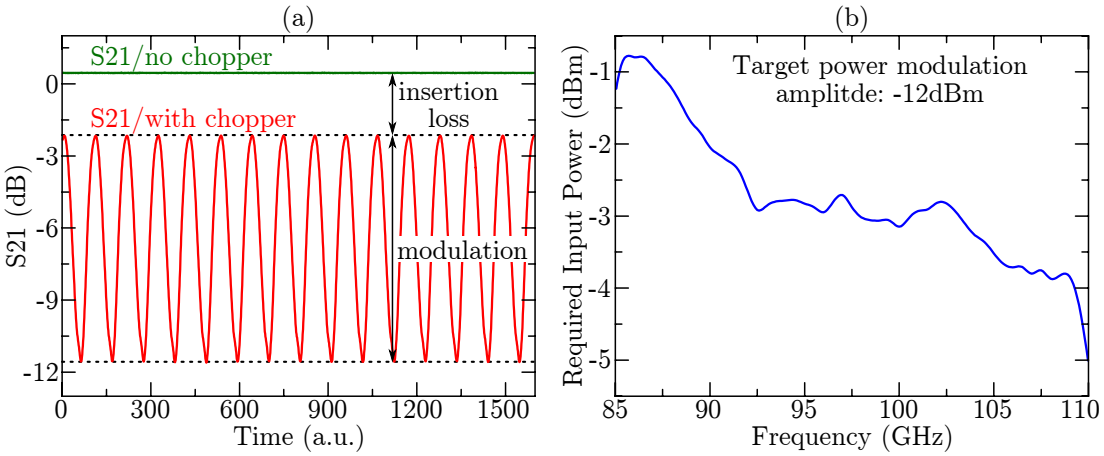

Figure B.1: ***Calibration of the optical chopper for use with sub-THz radiation.*** ***(a)*** *Transmission (S21) through the spinning chopper (red) and transmission without the chopper (green). The normalization of both traces is arbitrary (but the same).* ***(b)*** *The level of power output from the mm-wave modules (see Sec. 2.2.2) that is required in order to maintain constant amplitude of power modulation at the metamaterial plane. The target amplitude of power modulation, at metamaterial plane, is -12 dBm (≈ 63 μW). The curve plotted on the graph includes corrections due to optical chopper, reflections from the antennas and losses associated with propagation though the cryostat.*

Following the preliminary tests described above, all subsequent experiments were conducted using $R_L = 97.3\,\Omega$ and with bias voltage $V_B = 4\,\mathrm{V}$.

The hot-spot current (see Fig. A.1b) in combination with the chosen R_L and V_B allow to calculate the power dissipated at the hot-spot: about 40 mWat substrate temperature 5 K.

B Extracting sensitivity of metamaterial bolometer

This appendix will describe how the sensitivity of the metamaterial bolometer, presented in Sec. 3.3, was obtained in the experiment.

The experimental setup is shown schematically in Fig. 3.4a,b. The basic assumption of the experiment is that the incident radiation has negligible influence on the metamaterial properties[3]. The influence of the incident radiation on the sensing hot-spot within metamaterial is also assumed to be negligible[4]. The response of the metamaterial bolometer, i.e. voltage V_s across the load resistor as is shown in Fig. 3.4a, could therefore be assumed to depend linearly[5] on the power of radiation incident on the

[3]This assumption is supported by the experiments on the non-linear response of the selectively-etched superconducting metamaterial presented in Sec. 3.5. Even with selective etching (which was not carried out for the metamaterial bolometer) the nonlinear response of the selectively-etched metamaterial only became apparent at levels of radiation intensity above $1\,\mathrm{W/m^2}$ (700 μW total power reaching the metamaterial).

[4]Power dissipated on the hot-spot by the bias voltage was ∼ 40 mW (see App. A), which is significantly greater than the total power of the incident radiation (see the rest of this section).

[5]This assumption of the linear relationship between the signal voltage across the load resistor and radiation power is justified by the fixed-frequency power sweeps in the right-hand side inset on Fig. 3.5b.

metamaterial (P).

$$V_s = S \cdot P$$

The sensitivity of the bolometer is denoted with S. The power of radiation available at the time of the experiment was too low to observe changes in V_s directly, so a lock-in amplifier had to be used (Stanford Research Systems model SR830). For the lock-in detection, the beam of the sub-THz radiation incident on metamaterial bolometer was modulated at frequency[6] 420 Hz. The integration time used for the lock-in detection was[7] 3 s, which corresponds to bandwidth of $1/3\pi \approx 0.1$ Hz (page 3-11 in Ref. [267]).

A lock-in amplifier works by finding the amplitude of the oscillations of the input signal at the reference frequency. Given the long integration constant that was used in the experiments, the signal measured by the lock-in amplifier ($\left|\bar{V}_{lock-in}\right|$) can be approximated to a single frequency component (f_0 - modulation frequency):

$$\left|\bar{V}_{lock-in}(f_0)\right| = \left|\int dt\, \exp\left(\mathrm{i}2\pi f_0 t\right) \cdot V_s(t)\right| = S \cdot \left|\int dt\, \exp\left(\mathrm{i}2\pi f_0 t\right) \cdot P(t)\right| = S \cdot \left|\bar{P}(f_0)\right|$$

$$S = \left|\bar{V}_{lock-in}\right| / \left|\bar{P}\right|$$

Note that the lock-in amplifier actually outputs the root-mean-square value, so its output had to be multiplied by $\sqrt{2}$ to get to $\left|\bar{V}_{lock-in}\right|$ (page 3-3 in Ref. [267]).

For practical reasons, the optical chopper has been used to modulate the beam of sub-THz radiation incident on the metamaterial. Due to similar size of the chopper opening compared to the radiation beam size, the modulation created by the chopper suffered from insertion loss and modulation amplitude dependence on the frequency of sub-THz radiation (see Fig. B.1a).

To compensate for this, the chopper modulation wave-forms have been obtained for all relevant sub-THz frequencies (ν). The amplitudes of the fundamental Fourier components ($\left|\int dt\, \exp\left(\mathrm{i}2\pi f_0 t\right) \cdot P(t;\nu)\right|$) have been extracted. In the experiments, the output power of the mm-wave modules has been varied as a function of frequency (ν) in such a way as to keep the power modulation amplitude $\left|\bar{P}(f_0)\right|$ constant (independent of ν). Figure B.1b visualizes the look-up table used for the error correction described above. Apart from the chopper-related distortions, the look-up table, visualized in Fig. B.1b, includes the losses due to reflections from the antenna (on the way out of the transmitter) and losses due to propagation from the antenna, through the cryostat window, and within the cryostat up to the metamaterial plane. After the experiment, the output of the mm-wave modules has been verified with the external power-meter, which yielded fine corrections to the amplitude of the power modulation ($\left|\bar{P}(f_0)\right|$).

The sensitivity of the bolometer at each frequency has been obtained by measuring $\left|\bar{V}_{lock-in}\right|$ at two different modulation amplitudes of the incident power (63 μW and

[6] Modulation frequency has been chosen using an electrical spectrum analyzer. There was very little ambient noise at this frequency in the laboratory.

[7] Integration time had to be longer the period of the cryostat pump (1 second; see Sec. 2.1).

32 μW) and then estimating the sensitivity as the gradient of the straight line that passed through both data points.

C Efficiency of the metamaterial bolometer

In this appendix the efficiency of metamaterial bolometer from Sec. 3.3 will be estimated for the operating temperature $\theta = 5\,\mathrm{K}$.

The metamaterial is kept under voltage bias $V_B = 4\,\mathrm{V}$, in series with the load resistor $R_L = 97.3\,\Omega$ (see App. A). The resistance of the metamaterial in these circumstances is $R_{MM} = 142\,\Omega$ (experimental result). If the power of incident radiation oscillates with amplitude $\Delta P = 63\,\mu\mathrm{W}$ (see App. B), the signal voltage across the load resistor has been experimentally observed to oscillate with amplitude $\Delta V_s = 78.9\,\mu\mathrm{V}$ (at the peak of bolometer sensitivity).

First, one estimates the change in resistance of the metamaterial bolometer in response to oscillating radiation power:

$$\begin{aligned} V_s &= \frac{R_L}{R_{MM}+R_L}\cdot V_b \\ \Delta R_{MM} &= -\frac{\Delta V_s}{V_b}\cdot\frac{(R_{MM}+R_L)^2}{R_L} = 1.16\times 10^{-2}\,\Omega \end{aligned}$$

Next, one can use the knowledge of the width ($w = 30\,\mu\mathrm{m}$) and height ($h = 280\,\mathrm{nm}$) of the signal wire (see Sec. 3.3.1) that connects the ASRs in the metamaterial bolometer, to estimate the additional length (Δl) of the signal wire that needs to enter the normal state in order to increase the resistance of the metamaterial by ΔR_{MM}, given the conductivity of niobium at temperature 10 K is $\sigma_{Nb,\,10K} = 3.44\times 10^7\,\mathrm{S/m}$ [95]:

$$\Delta l = \Delta R_{MM}\cdot\sigma_{Nb,\,10K}\cdot wh = 3.4\,\mu\mathrm{m}$$

It is now possible to use the thermal resistance between the niobium film and the sapphire substrate $R_\theta = 3\times 10^{-3}\,\mathrm{m^2.K/W}$ (see App. F) to estimate how much power is required to sustain the section of signal wire of length Δl at temperature $\theta_w = 10\,\mathrm{K}$ if the substrate temperature is $\theta = 5\,\mathrm{K}$:

$$\Delta P_w = \frac{w\cdot\Delta l}{R_\theta}\cdot(\theta_w-\theta) = 0.2\,\mu\mathrm{W}$$

The efficiency of the metamaterial bolometer, that is the fraction of the incident radiation power converted to heating the sensitive part of the bolometer, is then given by:

$$100\%\times(\Delta P_w/\Delta P) = 0.3\%$$

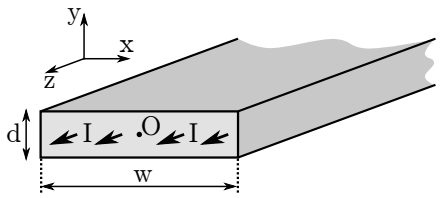

Figure D.1: ***Diagram of the flat superconducting wire with current I running through it.*** *The wire width is w and wire thickness is d ($w \gg d$). The position of the origin is denoted with O. In the metamaterial modulator without constrictions, described in Sec. 3.4, $w = 30\,\mu m$, $d = 280\,nm$.*

D Current threshold for sub-critical transmission modulation

Section 3.4.2 describes the sub-critical regime of metamaterial-assisted electro-optical modulation. The inset in Fig. 3.8a shows the amplitude of transmission modulation of the metamaterial electro-optical modulator as a function of the amplitude of sinusoidally oscillating control current. For the high control frequency (50 kHz) one can identify a non-zero threshold current $I_{th} \approx 80\,\text{mA}$ below which the transmission of the metamaterial is unaffected by the control current. This appendix will explain the nature of the threshold current.

Upper and lower critical fields of niobium film used for manufacturing the metamaterial electro-optical modulator

The basic behavior of superconductors in response to applied magnetic fields and electrical currents has been discussed in Sec. 1.2.1 and Sec. 1.2.2. Here a simplified model will be used to establish the distribution of magnetic field within a flat wire strip made out of type-II superconductor that carries currents comparable to critical current of the wire. The distribution of the magnetic field will then be used to estimate the lower and the upper critical fields of the niobium used for manufacturing the metamaterial electro-optical modulator.

Flat superconducting wire out of type-II superconductor that carries large current will be pierced through by the magnetic field in form of Abrikosov vortices. The wire will remain superconducting as long as vortices will remain pinned.

By assuming that all vortices within the flat superconducting wire were pinned with a constant pinning force, Huebener *et al.* [143] have shown that the distribution of the magnetic field within the wire, with geometry as displayed in Fig. D.1, is given by $\mathbf{H} = (H_y)\,\hat{\mathbf{y}}$, where $H_y = \text{sign}(x/w) \cdot H_{edge} \cdot \sqrt{2|x|/w}$ and H_{edge} is the strength of magnetic field at the edge of the wire.

If one assumes that the vortex pinning is always strong enough to withstand the Lorentz force due to current in the wire, then the critical current (I_c) of the wire will be reached when the (induced) magnetic field at the edge of the wire will reach the upper

critical field H_{c2}. The distribution of magnetic field within the wire that carries the current just below I_c will therefore be $H_y = \text{sign}(x/w) \cdot H_{c2} \cdot \sqrt{2|x|/w}$. The corresponding distribution of the current density is $\mathbf{J} = \nabla \times \mathbf{H} = (dH_y/dx)\,\hat{\mathbf{z}}$. Integrating the current density over the cross-section of the wire results in the full current carried by the wire, which, by definition, is just below I_c, so $I_c = 2 \times \int_0^{w/2} dx \cdot d \cdot J_z = 2d \cdot H_{c2}$. The critical current measured in the experiments was $I_c = 500\,\text{mA}$ (see Sec. 3.4.3), leading to $H_{c2} = 0.86\,\text{MA/m} \approx (1.1\,\text{T})/\mu_0$. While this is almost 4 times greater than the H_{c2} reported for the high-purity bulk niobium [142], it is in very good agreement with the measurements for thin niobium films with imperfections reported by Huebener *et al.* [143] and Ghenim *et al.* [268].

The lower critical field can be estimated from thermodynamic critical field $H_c \approx \sqrt{H_{c1} \cdot H_{c2}}$. Finnemore *et al.* reported $H_c = (162\,\text{mT})/\mu_0$ for high purity niobium wires [142]. The lower critical field is therefore $H_{c1} \approx (24\,\text{mT})/\mu_0$.

Vortex entry threshold

The transmission modulation of the metamaterial electro-optical modulator in the sub-critical regime, at high control frequency, can be explained by the suppression of niobium conductivity due to magnetic field (see App. E). The specific mechanism of conductivity suppression is the scattering of the sub-THz current, excited in the split-ring resonators, by the Abrikosov vortices induced by the control current. Consequently, the transmission modulation will only appear once the vortices will enter the intersection area between the split-ring arcs and the control wire (see Fig. 3.7c). The threshold current should therefore be related to the first entry of the vortices into the control wire.

Finding the threshold current for the first vortex entry is equivalent to finding the current at which the induced magnetic field at the edge of the control wire will reach the lower critical field H_{c1}. Huebener and Kampwirth have previously shown that the magnetic field at the edge of the flat superconducting wire strip, carrying current I that is confined to the thin surface layer[8] of the wire, is given by $H_{edge} = I/\pi d$, where d is the thickness of the wire [269]. Using the estimate for H_{c1} from the previous sub-section leads to the vortex entry current $I_w = \pi d \times H_{c1} = 17\,\text{mA}$. Alternatively one can rely on $H_{c2} = \kappa\sqrt{2} \cdot H_c$ and $H_{c1} = H_c \cdot \ln\kappa/\kappa\sqrt{2}$, so that $H_{c1} = H_{c2} \cdot \ln(\kappa)/2\kappa^2$ [27], where κ is the Ginzburg-Landau parameter [27]. Using $\kappa = 1.6$ provided by Ghenim *et al.* for 100 nm thick niobium film [268], $H_{c1} = (100\,\text{mT})/\mu_0$, consequently $I_w = 70\,\text{mA}$. This significantly improves the quantitative agreement with experimentally observed threshold current ($I_{th} \approx 80\,\text{mA}$), but one can question how acceptable it is to use a single Ginzburg-Landau parameter κ (as opposed to Maki parameters κ_1 and κ_2) [142].

The entry current (I_w) is more than 4 times smaller than the transmission modulation current threshold (I_{th}), signifying that the widening of the control wire at the point of

[8] If the current carried by the wire is weak enough to not to induce magnetic fields higher than H_{c1} at any point of the wire, the current will be confined to the thin surface layer, because the induced magnetic field will be screened from the bulk of the wire.

intersection with the split-ring arcs leads to much weaker magnetic field for any applied current. The field at those intersection points thus reaches H_{c1} at control currents larger than I_w.

E Estimate for fast sub-critical transmission modulation

In this appendix the transmission modulation of the metamaterial electro-optical modulator will be estimated for the fast modulation component in the sub-critical regime of operation (see Sec. 3.4.2).

The mechanism of modulation is assumed to be the scattering of the sub-THz currents (induced by the incident radiation) on the Abrikosov vortices within the control wire (induced by the control current). For brevity, only the transmission modulation by the control currents of maximum amplitude used in the experiment, i.e. $I = 250\,\mathrm{mA}$ (see Fig. 3.8a), will be considered here. Since the considered current is only two times smaller than the critical current ($\sim 500\,\mathrm{mA}$), it is assumed that the magnetic field distribution within the wire is the same as in the case of wire that carries critical current, i.e. $H_y = \mathrm{sign}(x/w).H_{edge}.\sqrt{2|x|/w}$ (see App. D), where $H_{edge} = H_{c2}/2$. More conveniently, the reduced magnetic field distribution is given by $h_y = H_y/H_{c2} = \mathrm{sign}(x/w).\sqrt{|x|/2w}$.

To estimate the change in the conductivity of niobium in response to applied magnetic field, the conductivity of niobium without the applied field, at 100 GHz, will be required both for superconducting niobium (at temperature 4 K) and for the niobium in the normal state (also at low temperature). There is published data for the conductivity of niobium at frequencies from 170 GHz upwards [95]. I have extrapolated from this data down to 100 GHz and adjusted the obtained value so that the model would match the experiment as well as possible. Figure E.1a shows the experimentally measured transmission of the metamaterial modulator at 4 K with no applied control current and the modeled transmission of the metamaterial, using the niobium conductivity $\tilde{\sigma}_0 = (1.96 - \mathrm{i}2.10) \times 10^8\,\mathrm{S/m}$ and sapphire dielectric constant $\tilde{\epsilon}_r = \epsilon_r \times (1 - \mathrm{i}\tan\delta)$, where $\epsilon_r = 9.51$ and $\tan\delta = 1.74 \times 10^{-7}$ [94]. The niobium film has been modeled as three-dimensional (i.e. with the correct thickness 280 nm). The sapphire substrates used in the experiments were polished with random orientation of the crystalline axis to the surface, so there was some uncertainty in the dielectric constant. At the stage of modeling the response of the metamaterial modulator ϵ_r has been tuned to give the best agreement with the experiment (the physically justified range is $9.3 \leq \epsilon_r \leq 11.4$ [94]). After obtaining a good numerical model for the metamaterial, the conductivity of the control wire (the area with the diagonal lines in the inset of Fig. E.1a) was varied in order to build a look-up table of change in transmission as a function of change in conductivity (see Fig. E.1b). The high-frequency conductivity of niobium in the normal state was also obtained through extrapolation from 170 GHz [95], resulting in $\sigma_n = 1.72 \times 10^8\,\mathrm{S/m}$ (at 10 K) .

The effective conductivity of niobium ($\tilde{\sigma}_{eff}$) that factors in the response to applied

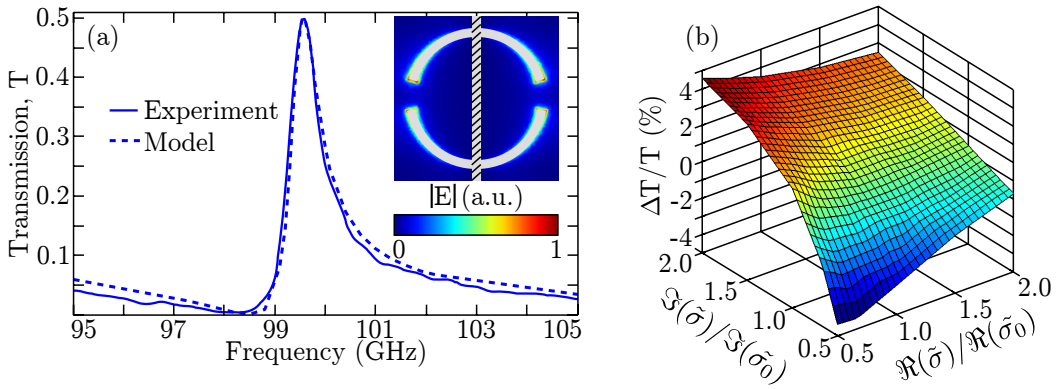

Figure E.1: ***Model for metamaterial electro-optical modulator. (a)*** *The measured (solid line) and the computed (dashed line) transmission of the metamaterial (no control current). The inset shows the distribution of the electric field (magnitude shown in arbitrary units) around the single meta-molecule at the resonance $\nu = 99.5 - 99.6$ GHz. The diagonal lines denote the area of the meta-molecule where the conductivity was varied to obtain (b).* ***(b)*** *The relative change in metamaterial (peak) transmission as a function of varying both real ($\Re$) and imaginary ($\Im$) components of niobium conductivity ($\tilde{\sigma}$) in the control wire. The initial conductivity of niobium, used for model in (a), is denoted with $\tilde{\sigma}_0$.*

magnetic field has been estimated using the model presented by Janjušević *et al.* [141]:

$$\frac{1}{\tilde{\sigma}_{eff}} = \frac{1 - b/\left[1 - \mathrm{i}\left(\omega_0/\omega\right)\right]}{(1-b)\cdot\tilde{\sigma}_0 + b\sigma_n} + \frac{1}{\sigma_n}\cdot\frac{b}{1 - \mathrm{i}\left(\omega_0/\omega\right)} \tag{E.1}$$

Here $b = b\left(H/H_{c2}\right)$ is a monotonously increasing function of the reduced magnetic field. The function $b(H/H_{c2})$ was recovered directly from Fig. 5b in Janjušević *et al.* [141]. Parameter ω_0 is the depinning frequency of Abrikosov vortices. As can be seen from Janjušević *et al.* [141], for niobium film of thickness above 200 nm, ω_0 is below 1 GHz. In the present case, working at typical frequencies around 100 GHz, $\omega_0/\omega \to 0$ is a good approximation. The resulting model is therefore:

$$\frac{\tilde{\sigma}}{\sigma_n} = \left[\frac{1-b}{(1-b)\cdot\tilde{\sigma}_0/\sigma_n + b} + b\right]^{-1} \tag{E.2}$$

The spatial distribution of high-frequency conductivity in the control wire, with current $I = 250$ mA running through it, is shown in Fig. E.2.

It is assumed that the spatial distribution of the control current does not change significantly at the point of intersection with the split-ring arcs (see Fig. E.1a). Since the high-frequency currents excited in the split-ring resonators flow perpendicularly to the control current, the spatial distribution of the conductivity inside the control wire is not important. The two assumptions above allow to replace the non-trivial distribution of conductivity inside the wire with the average (high-frequency) conductivity across the wire: $<\tilde{\sigma}>_{250\,\mathrm{mA}} = (2.1 - \mathrm{i}1.2) \times 10^8$ S/m. Knowledge of the average conductivity of the control wire can be directly translated to the transmission modulation via the look-up table visualized in Fig. E.1b.

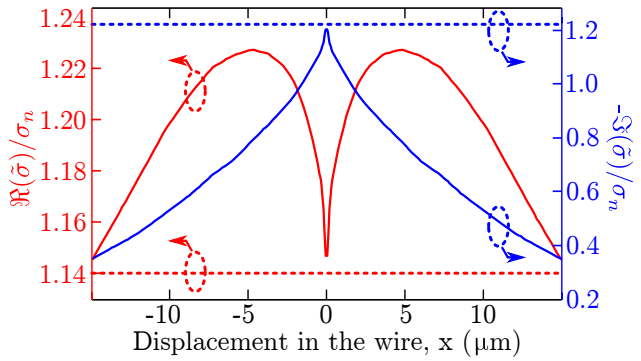

Figure E.2: ***High-frequency conductivity of niobium in the control wire.*** *The initial values of high-frequency niobium conductivity (4 K, superconducting state, no control current) are shown in dashed lines for both real (red) and imaginary (blue) components of the conductivity. The distribution of the conductivity in the wire with the applied current of $I = 250\,mA$ is shown in solid lines. In all cases, the conductivity is normalized with respect to the normal state conductivity (σ_n). The wire is assumed to be flat enough to ignore the variation in the conductivity across the shorter dimension (height).*

Based on the model described above, one can predict that the metamaterial transmission should be reduced by 3% ($\Delta T/T = -3\%$) when control current of magnitude $I = 250\,\text{mA}$ is passed through the metamaterial. This should be compared with the experimentally observed transmission modulation due to fast sub-critical modulation mechanism, which is observed at high modulation frequencies in the sub-critical regime. From Fig. 3.8a, the observed modulation in this regime (fast component, sub-critical modulation) is $\sim 1\%$. The model (derived in this appendix) therefore gives very good predictions of the metamaterial performance as an electro-optical modulator, considering the simplifications that had to be made.

F Heating dynamics of the metamaterial modulator in the super-critical regime

In this appendix, the dynamics of heating in the metamaterial modulator that operates in the super-critical regime (see Sec. 3.4.3), will be studied.

For brevity, the analysis will focus on the behavior of metamaterial when a 50 μs long voltage ramp of amplitude 38 V is applied across it (see Fig. 3.9a). From the electrical response of metamaterial modulator, shown in Fig. 3.9a, one can calculate the resistance of the metamaterial at the end of pulse $R_{50\,\mu\text{s},\,38\,\text{V}} = 390\,\Omega$. The resistance of the metamaterial in the normal state, at temperature 10 K, has been measured to be $R_{10\,\text{K}} = 2.6\,\text{k}\Omega$. The fractional resistance of the metamaterial at the end of the ramp pulse is therefore $R_{50\,\mu\text{s},\,38\,\text{V}}/R_{10\,\text{K}} = 0.15$. Since the resistance of the niobium at low temperature, when it is in the normal state, is largely independent of temperature, one can interpret the fractional resistance as the proportion of the metamaterial in the normal state.

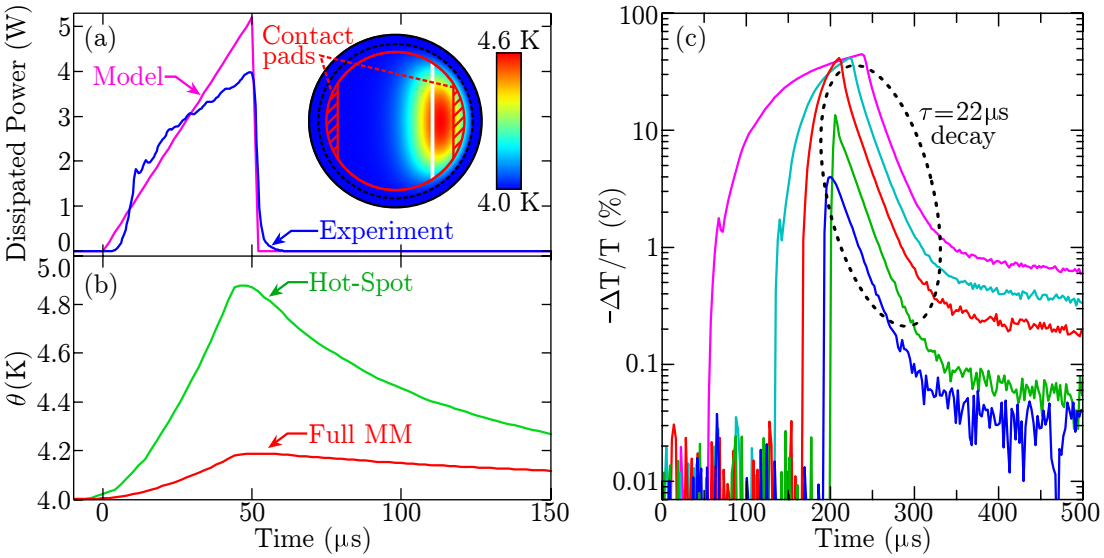

Figure F.1: ***The heating dynamics of the metamaterial modulator.*** ***(a)*** *The inset shows the sapphire slab used in the model. The area between the outer edge of the sapphire and the dashed circle is the overlap area of the sapphire substrate with the metallic sample holder (see Sec. 2.1). The overlap areas were modeled as heat sinks at temperature $\theta_b = 4\,K$. The red truncated circle denotes the area of the sapphire actually covered with the metamaterial (the circle is truncated by the electrical connection pads shown here with red diagonal stripes). The small area between the white line and the red contour denotes the 15% of the metamaterial that goes into the normal state at the end of 50 μs long control voltage ramp (38 V amplitude). The pink curve on the main plot shows the power dissipated in the 15%-portion of the metamaterial, as a function of time, as was used for the simulation. The blue curve shows the actual power dissipated on the metamaterial during a 50 μs long voltage ramp (38 V amplitude). The total energy supplied to the sapphire during the simulation (pink line) is 135 μJ, which is 5% larger than the experimentally supplied energy (blue curve; the difference is due to rounding errors). The colourmap in the inset shows the temperature distribution in the sapphire slab 50 μs after the voltage ramp is over (i.e. time $t = 100\,\mu s$). The sapphire substrate is modeled as a three-dimensional.* ***(b)*** *The average temperature of the 15% hot-spot (green) and of the whole metamaterial (red).* ***(c)*** *The change in metamaterial transmission in response to control ramps of various durations ($1 - 200\,\mu s$), showing the universal decay rate of $\tau = 22\,\mu s$ after the control voltage is switched off.*

The dynamics of transient temperature change of the sapphire substrate during (and after) the 50 μs long control voltage ramp were studied by numerical modeling using COMSOL 3.5a. In the model, the heat was supplied directly to 15% volume of the sapphire substrate, ignoring the fact that, in the experiment, the heat was initially created in the niobium film. The total heat supplied to the substrate during the single control ramp in the simulation was the same as in the experiment (see Fig. F.1a). The position of the 15% volume, into which the heat was supplied in the simulation, can be explained as follows. Since, in the experiment, the electrical contact pads heat up at all times when current is passed through the metamaterial (see discussion on the slow mechanism of sub-critical modulation in Sec. 3.4.2), it is logical to assume that the first area of the metamaterial to go into the normal state under the influence of voltage bias will be close to the contact pads. As soon as a single hot-spot appears, the current through the metamaterial modulator will drop rapidly (see Fig. 3.9a), making it unlikely

that any more hot-spots will appear. Consequently, in the simulation it was assumed that there was only one hot-spot, close to one of the contact pads.

The average temperature of the hot-spot and of the metamaterial, presented in Fig. F.1b, clearly shows that, during and after the control ramp, the temperature of the metamaterial substrate never gets high enough to fully explain the modulation of transmission observed in the super-critical regime. Section 3.4.3 explains the observed change in metamaterial transmission as a result of the establishment of the hot-spot in the niobium film, which suppresses the collective (trapped) mode response in the metamaterial through interactions between the meta-molecules. Figure F.1b shows that it is reasonable to assume that the substrate temperature remains roughly constant (and low), during the super-critical control ramp. However the temperature of the hot-spot in the niobium film will have to be close to 9 K. It follows, that there must be thermal resistance between the substrate and the niobium film, and that after the ramp is over, the hot-spot should cool down to substrate temperature following an exponential trend. The characteristic cooling down time of the film can be deduced from the recovery of metamaterial transmission after the pulse. Figure F.1c shows the transmission recovery after ramp pulses of various durations. In all cases, the recovery follows an exponential trend with an average decay time of $\tau = 22\,\mu s$.

One can estimate the thermal resistance from the decay time[9]:

$$R_\theta = |S.\Delta\theta/\dot{U}| = \frac{\tau}{C_n \rho d} = 3 \times 10^{-3}\,\mathrm{K.m^2/W}$$

Where S is the unit surface area of the niobium wire (in contact with substrate), $\Delta\theta$ is the temperature difference between niobium wire and the substrate,U is the heat in the unit volume of the niobium wire, $C_n = 2.7\,\mathrm{J/K.kg}$ is the heat capacity of niobium at temperatures just above θ_c [270], $\rho = 8.6 \times 10^3\,\mathrm{kg/m^3}$ is the density of niobium [270], and $d = 280\,\mathrm{nm}$ is the thickness of the niobium film. The obtained value of thermal resistance compares well with the literature data for thermal resistance between aluminum and sapphire ($R_\theta \sim 5 \times 10^{-3}\,\mathrm{K.m^2/W}$ at temperature $\theta = 1\,\mathrm{K}$, reported by Sahling *et al.* [271]), but it is two orders of magnitude higher than the thermal resistance between sapphire and lead [146].

G Test of the method used to determine the nonlinear sub-THz response in the superconducting metamaterial

Section 3.5.2 describes the procedure used to measure the nonlinear response of the selectively-etched superconducting metamaterial. In this appendix a similar procedure is

[9]To find the rate of heat loss of the niobium film $\dot{U} \equiv dU/dt$ assume that the temperature of the hot-spot decays exponentially and with the same time constant as the transmission, so $\theta = \theta_b + \Delta\theta = \theta_b + \alpha \cdot \exp(-t/\tau)$. Clearly the heat stored in the niobium film will depend on its temperature, so $U = U(\theta)$, therefore $\dot{U} = -dU/d\theta \cdot \Delta\theta/\tau$. By definition $dU/d\theta \equiv C_n \times \rho \times Sd$ is the heat capacity (of niobium).

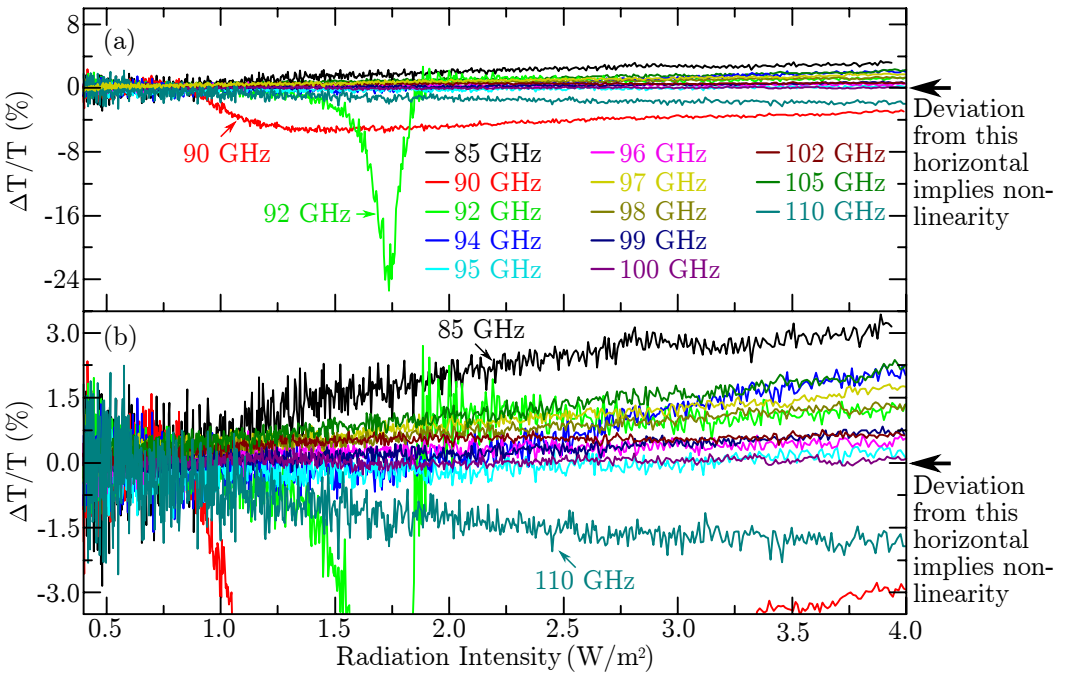

Figure G.1: ***Test of the procedure for measuring the nonlinear response of media in the sub-terahertz range. (a)*** *Measurement of the nonlinear response of the absorbing carbon foam. The graphs show the relative change in the transmission of the foam as a function of radiation intensity for different frequencies of incident radiation. The graphs are found by measuring the transmission through the foam and then normalizing the trace with respect to transmission without the foam in the path of radiation. This normalization step allows to eliminate systematic errors due to VNA and the mm-wave modules (see Sec. 2.2). An ideal linear medium would display no change in transmission ($\Delta T/T = 0\%$) in response to increasing radiation intensity. The electromagnetic response of the foam is assumed to be linear. The data presneted here, therfore, indicates the level of error due to experimental method used to find the nonlinear response of the medium.* ***(b)*** *Magnified version of plot (a).*

applied to a sheet of millimeter wave absorbing foam which should display strictly linear behavior at the level of radiation intensity used in the experiment (less than $10\,\mathrm{W/m^2}$). Measuring the nonlinear response of the foam thus allows to test the robustness of the procedure for measuring the nonlinear response.

In Sec. 3.5.2, the nonlinear response of the metamaterial was determined by measuring the transmission of the metamaterial in the superconducting state and then in the normal state, whilst increasing the intensity of the incident radiation. In order to remove the systematic errors due to VNA and the mm-wave modules, the transmission trace measured for the superconducting metamaterial was normalized with respect to the trace measured for the metamaterial in the normal state. The validity of this method is tested here by measuring the nonlinear response of the radiation absorbing carbon foam (Eccosorb AN 72 by Emerson & Cuming, US; -20 dB transmission attenuation), which was found by measuring the transmission of the foam as a function of radiation intensity and normalizing this trace with respect to transmission measured without the foam in the path of radiation. The resultant data is presented in Fig. G.1a,b as a relative

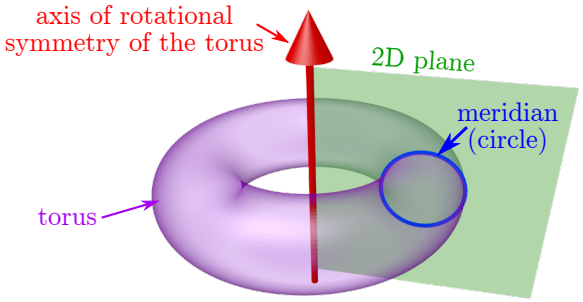

Figure H.1: ***A torus with a single meridian (blue circle) created through intersection with a plane.***

change in the transmission of the foam as a function of radiation intensity[10]. Different traces correspond to different frequencies of incident radiation. The sub-terahertz response of the foam is assumed to be linear, thus any deviation from the horizontal line $\Delta T/T = 0\%$ in Fig. G.1a,b should be treated as an error. One can see that, for most frequencies, the transmission of the foam changes by no more than $\pm 3\%$ when the intensity of the incident radiation is increased. The transmission of the carbon foam is significantly lower[11] than that of the selectively-etched metamaterial, yet despite the low level of transmission, the suggested method of determining the nonlinear response of the samples resulted in only a modest error in case of the carbon foam. However, there were two clear outliers at frequencies 90 GHz and 92 GHz. At low levels of radiation intensity these two traces displayed very large deviation from the horizontal line $\Delta T/T = 0\%$, only to return closer to it at higher levels of radiation intensity. Such behavior has not been observed in the experiments with selectively-etched metamaterial.

The intensity-dependent change in metamaterial transmission measured for the selectively etched metamaterial in Sec. 3.5 was, in some cases, as high as 13% (see Fig. 3.13a), i.e. significantly higher than the error level of roughly $\pm 3\%$ observed in Fig. G.1. One therefore concludes that the nonlinear response of the selectively-etched superconducting metamaterial reported in Sec. 3.5 is significant, i.e. it is not a result of experimental errors.

H Visualization of a meridian of a torus

The electrodynamic toroidal dipoles discussed in detail in Chap. 4, are created by oscillating meridional currents flowing on a torus. Figure H.1 shows a single meridian

[10] The experiments with foam were conducted outside the cryostat, by placing the foam on top of one of the cryostat windows. Consequently, the beam was not in focus when in reached the foam. For this reason, the intensity of radiation reaching the foam is lower than the intensity of radiation that reached the selectively-etched metamaterial from Sec. 3.5. However, the range of full power of radiation emitted by the mm-wave module, combined with power amplifier (see Sec. 2.2.7), was the same for both the experiment with the foam (reported here) and the experiments reported in Sec. 3.5.

[11] Transmission of the foam was close $-20\,\mathrm{dB}$, i.e. $\sim 1\%$. The transmission of the selectively-etched metamaterial was 2-8% (see Fig. 3.11d)

of a torus. This is a circle created through intersection of the torus with a plane that stretches from the axis of rotational symmetry of the torus (red vertical axis) to infinity.

I Multipoles and vector spherical harmonics

I.1 Electrodynamic multipole decomposition

This appendix will give a brief summary of the multipole decomposition of the electromagnetic fields emitted by the isolated sources of electromagnetic radiation. Detailed descriptions can be found in Refs. [175, 176, 217].

Electromagnetic radiation from an arbitrary charge ($\rho(\mathbf{r},t)$) and current ($\mathbf{J}(\mathbf{r},t)$) density distribution in vacuum is most conveniently described through electromagnetic scalar ($\phi(\mathbf{r},t)$) and vector ($\mathbf{A}(\mathbf{r},t)$) potentials. If ρ and $\mathbf{J}$ oscillate at a single (angular) frequency ω, the equations of motion for the electromagnetic potentials, in the Lorentz gauge, become[12] [174]:

$$\begin{aligned}(\nabla^2+k^2)\phi &= -4\pi\rho\\ (\nabla^2+k^2)\mathbf{A} &= -4\pi\mathbf{J}/c\\ k &= \omega/c\end{aligned}$$

Where c is the speed of light in vacuum and k is the wavenumber. A standard way of solving these two equations is through the scalar Green's function:

$$\begin{aligned}(\nabla^2+k^2)G_k(\mathbf{r},\mathbf{r}') &= -4\pi\delta^{(3)}(\mathbf{r}-\mathbf{r}')\\ G_k &= \exp\left(\mathrm{i}k\left|\mathbf{r}-\mathbf{r}'\right|\right)/\left|\mathbf{r}-\mathbf{r}'\right|\\ \phi(\mathbf{r},t) &= \int d^3r'\, G_k(\mathbf{r},\mathbf{r}')\rho(\mathbf{r}',t-\left|\mathbf{r}-\mathbf{r}'\right|/c)\end{aligned} \tag{I.1}$$

and vector Green's function:

$$\begin{aligned}(\nabla^2+k^2)\left[\mathbf{G}_k(\mathbf{r},\mathbf{r}')\right]_{\alpha,\beta} &= -4\pi\delta^{(3)}(\mathbf{r}-\mathbf{r}')\,\delta_{\alpha,\beta}\\ \left[\mathbf{G}_k(\mathbf{r},\mathbf{r}')\right]_{\alpha,\beta} &= \delta_{\alpha,\beta}G_k(\mathbf{r},\mathbf{r}')\\ \mathbf{A}(\mathbf{r},t) &= \frac{1}{c}\int d^3r'\,\mathbf{G}_k(\mathbf{r},\mathbf{r}').\mathbf{J}(\mathbf{r}',t-\left|\mathbf{r}-\mathbf{r}'\right|/c)\end{aligned} \tag{I.2}$$

The Greek letter sub-scripts above denote the Cartesian components of vectors and tensors, i.e. α can take values $\alpha = x$, y, z and the same applies to β (and any other Greek letter sub-scripts). The Kronecker delta is denoted with $\delta_{\alpha,\beta}$ ($\delta_{x,x}=\delta_{y,y}=\delta_{z,z}=1$ otherwise $\delta_{\alpha,\beta}=0$). The three-dimensional delta function is denoted with $\delta^{(3)}(\mathbf{r})$ ($\int d^3r\,\delta^{(3)}(\mathbf{r})\equiv 1$ and $\int d^3r\, f(\mathbf{r})\cdot\delta^{(3)}(\mathbf{r}-\mathbf{a})\equiv f(\mathbf{a})$ for any sufficiently smooth function

[12] Using CGS units.

$f(\mathbf{r})$). This notation will be used for the rest of this appendix.

The Green's functions can be represented in the following way:

$$\begin{aligned} G_k(\mathbf{r},\mathbf{r}') &= \frac{k}{4\pi}\sum_{l,m} F^{\dagger}_{lmk}(\mathbf{r}')\, H_{lmk}(\mathbf{r}) \\ \left[\mathbf{G}_k(\mathbf{r},\mathbf{r}')\right]_{\alpha,\beta} &= \frac{k}{4\pi}\sum_{\lambda,l,m} \left[\mathbf{F}^{(\lambda)}_{lmk}(\mathbf{r}')\right]^{\dagger}_{\alpha} \left[\mathbf{H}^{(\lambda)}_{lmk}(\mathbf{r})\right]_{\beta} \end{aligned} \tag{I.3}$$

Where indices take values $l = 0, 1, 2...$, $-l \leq m \leq l$, and where functions F_{lmk} and H_{lmk} are built from the spherical Bessel functions (j_l), spherical Hankel functions ($h_l^{(\pm)}$) and spherical harmonics (Y_{lm}) [176, 218]:

$$\begin{aligned} F_{lmk}(\mathbf{r}) &= j_l(kr)Y_{lm}(\hat{\mathbf{r}}) \\ H_{lmk}(\mathbf{r}) &= h_l^{(+)}(kr)Y_{lm}(\hat{\mathbf{r}}) \end{aligned}$$

The vectorial versions $\mathbf{F}^{(\lambda=0,\pm1)}_{lmk}(\mathbf{r})$, $\mathbf{H}^{(\lambda=0,\pm1)}_{lmk}(\mathbf{r})$ are created from the corresponding scalar functions using standard vector calculus operators, including the orbital angular momentum operator $\mathbf{L} = -\mathrm{i}\mathbf{r}\times\nabla$:

$$\begin{aligned} \mathbf{F}^{(0)}_{lmk} &= \frac{1}{\sqrt{l(l+1)}}\mathbf{L}\left(F_{lmk}\right) \\ &= j_l(kr)\mathbf{Y}_{llm}(\hat{\mathbf{r}}) \\ \mathbf{F}^{(+1)}_{lmk} &= \frac{-1}{k\sqrt{l(l+1)}}\nabla\times\mathbf{L}\left(F_{lmk}\right) \\ &= \frac{1}{\sqrt{2l+1}}\left(\sqrt{l}j_{l+1}(kr)\mathbf{Y}_{ll+1m}(\hat{\mathbf{r}}) + \sqrt{l+1}j_{l-1}(kr)\mathbf{Y}_{ll-1m}(\hat{\mathbf{r}})\right) \\ \mathbf{F}^{(-1)}_{lmk} &= \frac{\mathrm{i}}{k}\nabla F_{lmk} \\ &= \frac{1}{\sqrt{2l+1}}\left(\sqrt{l}j_{l-1}(kr)\mathbf{Y}_{ll-1m}(\hat{\mathbf{r}}) - \sqrt{l+1}j_{l+1}(kr)\mathbf{Y}_{ll+1m}(\hat{\mathbf{r}})\right) \end{aligned}$$

Expressions for $\mathbf{H}^{(\lambda=0,\pm1)}_{lmk}(\mathbf{r})$ are obtained by replacing $j_l(kr)$ with $h^{(+)}(kr)$ in the expressions above.

Functions $\mathbf{Y}_{ll'm}$ are the so-called vector spherical harmonics [175, 176, 217] (see App. I.3 for the explicit form of the vector spherical harmonics).

The multipole decomposition is accomplished by representing the charge density ρ

and current density $\mathbf{J}$ as series in F_{lmk} and $\mathbf{F}^{(\lambda)}_{lmk}$ [175, 176]:

$$\rho(\mathbf{r},t) = \frac{1}{(2\pi)^3}\sum_{lmk}(-\mathrm{i}k)^l\,\frac{\sqrt{4\pi(2l+1)}}{(2l+1)!!}\times Q_{lm}(-k^2,t)\times F_{lmk}(\mathbf{r}) \tag{I.4}$$

$$\begin{aligned}\mathbf{J}(\mathbf{r},t) =& \frac{c}{(2\pi)^3}\sum_{lmk}(-\mathrm{i}k)^{l-1}\,\frac{\sqrt{4\pi(2l+1)(l+1)}}{\sqrt{l}(2l+1)!!}\times\Big[kM_{lm}(-k^2,t)\times\mathbf{F}^{(0)}_{lmk}(\mathbf{r})+\\ &+\left(\frac{1}{c}\dot{Q}_{lm}(0,t)+k^2T_{lm}(-k^2,t)\right)\times\mathbf{F}^{(+1)}_{lmk}(\mathbf{r})+\\ &+\frac{1}{c}\sqrt{\frac{l}{l+1}}\dot{Q}_{lm}(-k^2,t)\times\mathbf{F}^{(-1)}_{lmk}(\mathbf{r})\Big]\end{aligned} \tag{I.5}$$

The three families of coefficients Q_{lm}, M_{lm}, T_{lm} correspond to electric, magnetic and toroidal multipoles (respectively). They arise as a result of three families of functions $\mathbf{F}^{(0)}_{lmk}$, $\mathbf{F}^{(+1)}_{lmk}$, $\mathbf{F}^{(-1)}_{lmk}$.

By substituting the multipole decomposition of the charge and current density (Eq. (I.4) and Eq. (I.5)) and Green's function decomposition (Eq. (I.3)) into Eq. (I.1) and Eq. (I.2) it is possible to find the general expressions for the scalar and vector potentials emitted by an arbitrary source (the full expression can be found in Ref. [176]). The electromagnetic potentials can then be used to find the electric field emitted by the source $\mathbf{E} = -\nabla\phi - \partial_t\mathbf{A}/c$. In the far-field approximation (obtained by expanding the Bessel and Hankel functions in the limit $r\to\infty$ and retaining terms of order $O(1/r)$) expression for the emitted electric field becomes (Eq (3.15) from Ref. [176]):

$$\begin{aligned}\mathbf{E}(\mathbf{r},t) \overset{O(1/r)}{=} \frac{1}{r}\sum_{l=1,-l\le m\le l}\frac{1}{c^{l+1}}\frac{\sqrt{4\pi(2l+1)(l+1)}}{\sqrt{l}(2l+1)!!}\Bigg\{&\\ -\left(\frac{d^{l+1}}{dt^{l+1}}\right)Q^{(0)}_{lm}\times&\\ \times\left[\sqrt{\frac{l}{2l+1}}\mathbf{Y}_{ll+1m}(\hat{\mathbf{r}})+\sqrt{\frac{l+1}{2l+1}}\mathbf{Y}_{ll-1m}(\hat{\mathbf{r}})\right]-&\\ -\mathrm{i}\sum_{n=0}\frac{1}{n!c^{2n}}\left(\frac{d^{l+2n+1}}{dt^{l+2n+1}}\right)M^{(n)}_{lm}\times\mathbf{Y}_{llm}(\hat{\mathbf{r}})+&\\ +\frac{1}{c}\sum_{n=0}\frac{1}{n!c^{2n}}\left(\frac{d^{l+2n+2}}{dt^{l+2n+2}}\right)T^{(n)}_{lm}\times&\\ \times\left[\sqrt{\frac{l}{2l+1}}\mathbf{Y}_{ll+1m}(\hat{\mathbf{r}})+\sqrt{\frac{l+1}{2l+1}}\mathbf{Y}_{ll-1m}(\hat{\mathbf{r}})\right]\Bigg\}&\end{aligned} \tag{I.6}$$

The bracketed super-script in the multipole coefficients denotes the Taylor expansion terms. The zeroth terms correspond to 'conventional' multipoles, i.e. $Q^{(0)}_{lm}\equiv Q_{lm}$ which is the spherical electric multipole (Q_{1m} is related to electric dipole, Q_{2m} to electric quadrupole, etc.). Terms with non-zero superscripts represent the corrections due to

(potentially) finite size of the charge-current density distribution that gives rise to the emitted radiation.

Equation (I.6) is in CGS units and for the case of arbitrary time dependence of the multipole moments (Q_{lm}, M_{lm}, T_{lm}). Converting this expression into SI units and for a complex-harmonic time dependence ($\sim \exp(+\mathrm{i}\omega t)$) results in:

$$\begin{aligned}\mathbf{E}(\mathbf{r},t) \overset{O(1/r)}{=} & \frac{\mu_0 c^2}{4\pi}\frac{\exp\left(\mathrm{i}\left[\omega t - kr\right]\right)}{r}\sum_{l=1,-l\leq m\leq l}\frac{1}{c^{l+1}}\frac{\sqrt{4\pi(2l+1)(l+1)}}{\sqrt{l}(2l+1)!!}\Bigg\{ \\ & -(\mathrm{i}\omega)^{l+1}Q_{lm}^{(0)}\times \\ & \times\left[\sqrt{\frac{l}{2l+1}}\mathbf{Y}_{ll+1m}(\hat{\mathbf{r}})+\sqrt{\frac{l+1}{2l+1}}\mathbf{Y}_{ll-1m}(\hat{\mathbf{r}})\right]- \\ & -\mathrm{i}\sum_{n=0}\frac{(\mathrm{i}\omega)^{l+2n+1}}{n!c^{2n}}M_{lm}^{(n)}\times\mathbf{Y}_{llm}(\hat{\mathbf{r}})+ \\ & +\frac{1}{c}\sum_{n=0}\frac{(\mathrm{i}\omega)^{l+2n+2}}{n!c^{2n}}T_{lm}^{(n)}\times \\ & \times\left[\sqrt{\frac{l}{2l+1}}\mathbf{Y}_{ll+1m}(\hat{\mathbf{r}})+\sqrt{\frac{l+1}{2l+1}}\mathbf{Y}_{ll-1m}(\hat{\mathbf{r}})\right]\Bigg\}\end{aligned} \tag{I.7}$$

The above expression served as a starting point in deriving Eq. (4.11) in Sec. 4.2.1.

I.2 Intensity scattered by the localized charge-current distribution

Vaman and Radescu provided the expression for the total power[13] radiated by the localized radiation source represented through multipole decomposition [176]. For convenience, this expression will be reproduced here in a truncated form (up to order $O(1/c^5)$) and for complex-harmonic time dependence:

$$\begin{aligned}I = & \frac{2\omega^4}{3c^3}\left|\mathbf{p}\right|^2+\frac{2\omega^4}{3c^3}\left|\mathbf{m}\right|^2+\frac{4\omega^5}{3c^4}\Im\left(\mathbf{p}^\dagger\mathbf{T}\right)+\frac{2\omega^6}{3c^5}\left|\mathbf{T}\right|^2+\frac{\omega^6}{5c^5}\left|\mathbf{Q}^{(e)}\right|^2+ \\ & +\frac{\omega^6}{20c^5}\left|\mathbf{Q}^{(m)}\right|^2-\frac{2\omega^6}{15c^5}\Re\left(\mathbf{m}^\dagger\mathbf{m}^{(1)}\right)\end{aligned}$$

Note that CGS units are used. The real part of an arbitrary complex number w is given by $\Re(w)$, the imaginary part is given by $\Im(w)$. The expressions for finding the multipole moments ($\mathbf{p}$, $\mathbf{m}$, etc.) are listed in App. K.

I.3 Explicit expressions for spherical vector harmonics

This appendix provides explicit expressions for the vector spherical harmonics in Cartesian coordinates. All expressions presented here have been adopted from the appendix of Ref. [176].

[13] Intensity of scattered radiation is integrated over all directions.

Let the Cartesian components of $\mathbf{Y}_{ll'm}$ be represented as the column vectors $\mathbf{Y}_{ll'm} = \left(\left(\mathbf{Y}_{ll'm}\right)_x, \left(\mathbf{Y}_{ll'm}\right)_y, \left(\mathbf{Y}_{ll'm}\right)_z\right)^T$, where $(...)^T$ denotes transposition, then:

$$\mathbf{Y}_{llm} = \begin{pmatrix} \frac{\sqrt{(l-m)(l+m+1)}}{\sqrt{2l(2l+2)}} & 0 & \frac{\sqrt{(l+m)(l-m+1)}}{\sqrt{2l(2l+2)}} \\ -\mathrm{i}\frac{\sqrt{(l-m)(l+m+1)}}{\sqrt{2l(2l+2)}} & 0 & \mathrm{i}\frac{\sqrt{(l+m)(l-m+1)}}{\sqrt{2l(2l+2)}} \\ 0 & \frac{m}{\sqrt{l(l+1)}} & 0 \end{pmatrix} \begin{pmatrix} Y_{l,m+1} \\ Y_{l,m} \\ Y_{l,m-1} \end{pmatrix}$$

$$\mathbf{Y}_{ll+1m} = \begin{pmatrix} \frac{\sqrt{(l+m+1)(l+m+2)}}{\sqrt{2(2l+2)(2l+3)}} & 0 & -\frac{\sqrt{(l-m+1)(l-m+2)}}{\sqrt{2(2l+2)(2l+3)}} \\ -\mathrm{i}\frac{\sqrt{(l+m+1)(l+m+2)}}{\sqrt{2(2l+2)(2l+3)}} & 0 & -\mathrm{i}\frac{\sqrt{(l-m+1)(l-m+2)}}{\sqrt{2(2l+2)(2l+3)}} \\ 0 & -\frac{\sqrt{(l+m+1)(l-m+1)}}{\sqrt{(l+1)(2l+3)}} & 0 \end{pmatrix} \begin{pmatrix} Y_{l+1,m+1} \\ Y_{l+1,m} \\ Y_{l+1,m-1} \end{pmatrix}$$

$$\mathbf{Y}_{ll-1m} = \begin{pmatrix} \frac{\sqrt{(l-m-1)(l-m)}}{\sqrt{4l(2l-1)}} & 0 & -\frac{\sqrt{(l+m-1)(l+m)}}{\sqrt{4l(2l-1)}} \\ -\mathrm{i}\frac{\sqrt{(l-m-1)(l-m)}}{\sqrt{4l(2l-1)}} & 0 & -\mathrm{i}\frac{\sqrt{(l+m-1)(l+m)}}{\sqrt{4l(2l-1)}} \\ 0 & \frac{\sqrt{(l-m)(l+m)}}{\sqrt{l(2l-1)}} & 0 \end{pmatrix} \begin{pmatrix} Y_{l-1,m+1} \\ Y_{l-1,m} \\ Y_{l-1,m-1} \end{pmatrix}$$

Where $Y_{l,m}$ are the standard spherical harmonics [218].

J Integral involving the Spherical Harmonics - $I_{l,m}$

In this appendix, the Eq. (4.8) and Eq. (4.9) from Sec. 4.2.1, will be derived. At the core of the derivation lies the evaluation of Eq. (4.8):

$$\int_R^\infty dr \left(\frac{R}{r}\right)^q \exp\left(-\mathrm{i}kr\right) \cong \frac{\exp\left(-\mathrm{i}kR\right)}{\mathrm{i}k}, \quad \Im\left(k\right) < 0$$

The case $q = 0$ can be found by the direct integration. Higher order cases can be evaluated by relating them to the exponential integrals. Abramowitz and Stegun define the exponential integral as (Eq. (5.1.4) of Ref. [272]):

$$E_n(z) = \int_1^\infty dt \, \frac{\exp\left(-zt\right)}{t^n}, \quad n = 0,\, 1,\, 2, ... \quad \Re\left(z\right) > 0$$

One is interested in the asymptotic expansion of the $E_n(z)$ for the case of large z given in Eq. (5.1.51) of Ref. [272]:

$$\lim_{z\to\infty} E_n(z) \cong \frac{\exp\left(-z\right)}{z}\left(1 - O\left(1/z\right)\right), \quad \left|\arg\left(z\right)\right| < \frac{3}{2}\pi$$

Equation (4.8) can therefore be evaluated as follows:

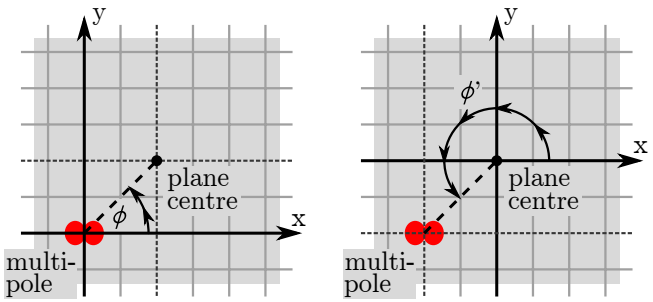

Figure J.1: ***The difference between*** ϕ ***and*** ϕ'***.*** *Angle* ϕ *is defined in the coordinate frame of a multipole under consideration, whilst the angle* ϕ' *is defined in the coordinate frame of the multipole array (also see Fig. 4.2). The observer is located directly above the origin of the array.*

$$\int_R^\infty dr \left(\frac{R}{r}\right)^q \exp\left(-\mathrm{i}kr\right) = R \cdot E_q(\mathrm{i}kR) \cong \quad R \cdot \tfrac{\exp(-\mathrm{i}kR)}{\mathrm{i}kR} \cdot \left(1 - O\left(1/kR\right)\right)$$

Note that $\Im(k) < 0$ implies $\Re(\mathrm{i}kR) > 0$, and $\Re(kR) > 0$ implies $|\arg(\mathrm{i}kR)| < \pi/2$. Up to order $O\left(1/kR\right)$ or, equivalently, up to $O\left(\lambda/R\right)$, the expression becomes:

$$\int_R^\infty dr \left(\frac{R}{r}\right)^q \exp\left(-\mathrm{i}kr\right) \cong \frac{\exp\left(-\mathrm{i}kR\right)}{\mathrm{i}k}$$

Next, consider Eq. (4.6) from Sec. 4.2.1:

$$I_{l,m} = \int d^2r \, Y_{l,m}(\theta, \phi) \exp\left(-\mathrm{i}kr\right)/r$$

The integration is understood to be over the area of the array of multipoles, as shown in Fig. 4.2. The position of each multipole in the plane of the array is given by ρ, the distance between the centre-point of the array and the considered multipole, and ϕ', the angle between the x-axis and the vector connecting the centre-point of the array and the multipole in question. There is also another angle ϕ that belongs together with r and θ, and denotes the position of the observer relative to the multipole under consideration (see Fig. 4.2). It is convenient to place the origin of the multipole array directly below the observer. In this case, the relation between ϕ and ϕ' takes a simple form $\phi = \phi' + \pi$, up to a full rotation around 2π. Figure J.1 helps to visualize the two angles. The same choice of origin establishes the relation $r^2 = \rho^2 + R^2$.

One can now rewrite the integral in a more accessible way:

$$I_{l,m} = \int_0^{2\pi} d\phi' \int_0^\infty \rho d\rho \, Y_{l,m}\left(\theta, \phi' + \pi\right) \frac{\exp\left(-\mathrm{i}kr\right)}{r}$$

From $r^2 = \rho^2 + R^2$, it follows that $r\,dr = \rho\,d\rho$, so

$$\begin{aligned} I_{l,m} &= \int_0^{2\pi} d\phi' \int_R^\infty r dr\, Y_{l,m}\left(\theta, \phi' + \pi\right) \frac{\exp\left(-\mathrm{i}kr\right)}{r} \\ &= (-1)^{m+m} \sqrt{\frac{2l+1}{4\pi} \frac{(l-m)!}{(l+m)!}} \cdot \int d\phi' \exp\left(\mathrm{i}m\phi'\right) \int_R^\infty dr\, P_l^m\left(\cos\theta\right) \exp\left(-\mathrm{i}kr\right) \end{aligned}$$

In the last step, the spherical harmonic has been expanded following the convention used by Arfken and Weber (see Chapter 12.6 in Ref. [218]), and $\exp\left(\mathrm{i}m\left(\pi + \phi'\right)\right) = (-1)^m \exp\left(\mathrm{i}m\phi'\right)$ has been substituted. Here the P_l^m denotes the Associated Legendre Functions. The expression above is simplified considerably by the fact that the integral over ϕ' is non-zero only for $m = 0$:

$$I_{l,m} = \pi\delta_{m,0} \sqrt{\frac{2l+1}{\pi}} \int_R^\infty dr\, P_l\left(\cos\theta\right) \exp\left(-\mathrm{i}kr\right)$$

Above, $P_l^0(x) = P_l(x)$ was used to replace the Associated Legendre Functions with Legendre Polynomials (respectively). The Kronecker delta is denoted with $\delta_{a,b}$ ($\delta_{a,b} = 1$ if $a = b$, otherwise $\delta_{a,b} = 0$).

From Fig. 4.2 it follows that $\cos\theta = R/r$ for $\mathbf{R} = R\hat{\mathbf{z}}$, and $\cos\theta = -R/r$ for $\mathbf{R} = -R\hat{\mathbf{z}}$, thus $\cos\theta = \left(\hat{\mathbf{R}}.\hat{\mathbf{z}}\right) \times R/r$. Using the parity property of Legendre Polynomials (Eq. 12.37 in Ref. [218]), one obtains $P_l\left(\cos\theta\right) = \left(\hat{\mathbf{R}}.\hat{\mathbf{z}}\right)^l P_l\left(R/r\right)$. Being a polynomial, $P_l(x)$ can be expressed as power series $P_l(x) = \sum_{s=0}^\infty a_s^{(l)} x^s$. The integral under consideration then becomes (with use of Eq. (4.8)):

$$\begin{aligned} I_{l,m} &= \pi\delta_{m,0} \sqrt{\frac{2l+1}{\pi}} \left(\hat{\mathbf{R}}.\hat{\mathbf{z}}\right)^l \cdot \sum_{s=0}^\infty a_s^{(l)} \int_R^\infty dr \left(\frac{R}{r}\right)^s \exp\left(-\mathrm{i}kr\right) \approxeq \\ &\approxeq \pi\delta_{m,0} \sqrt{\frac{2l+1}{\pi}} \left(\hat{\mathbf{R}}.\hat{\mathbf{z}}\right)^l \sum_{s=0}^\infty a_s^{(l)} \cdot \left(\frac{\exp\left(-\mathrm{i}kR\right)}{\mathrm{i}k} + O\left(\lambda/R\right)\right) \end{aligned}$$

Finally, one uses the normalization of the Legendre Polynomials to eliminate the sum $P_l(1) = 1 = \sum_{s=0}^\infty a_s^{(l)}$ (Eq. (12.31) in Ref. [218]). Thus

$$I_{l,m} \approxeq \frac{\pi\delta_{m,0} \left(\hat{\mathbf{R}}.\hat{\mathbf{z}}\right)^l}{\mathrm{i}k} \cdot \sqrt{\frac{2l+1}{\pi}} \cdot \exp\left(-\mathrm{i}kR\right)$$

which completes the derivation.

K Integrals for finding the multipoles from a current distribution

This appendix provides the expressions used to calculate the multipole moments from the current density distribution. The expressions have been adopted from Ref. [176]. Note that the electric and magnetic multipoles are exactly the same as the ones given in the standard texts on electrodynamics [174] (apart from the different normalization constants).

The Greek letter sub-scripts will be used to denote the Cartesian components of vectors and tensors ($\alpha, \beta, \gamma = x, y, z$). Cartesian multipoles are computed by integrating over the charge density[14] ($\rho(\mathbf{r})$) or current density ($\mathbf{J}(\mathbf{r})$) distribution within the unit cell.

Dipoles:

$$
\begin{aligned}
p_\alpha &= \int d^3r\, \rho\, r_\alpha = \frac{1}{\mathrm{i}\omega} \int d^3r\, J_\alpha \\
m_\alpha &= \frac{1}{2c} \int d^3r\, \left[\mathbf{r} \times \mathbf{J}\right]_\alpha \\
m_\alpha^{(1)} &= \frac{1}{2c} \int d^3r\, \left[\mathbf{r} \times \mathbf{J}\right]_\alpha r^2 \\
T_\alpha &= \frac{1}{10c} \int d^3r\, \left[(\mathbf{r}.\mathbf{J})\, r_\alpha - 2r^2 J_\alpha\right] \\
T_\alpha^{(1)} &= \frac{1}{28c} \int d^3r\, \left[3r^2 J_\alpha - 2r_\alpha(\mathbf{r}.\mathbf{J})\right] r^2
\end{aligned}
$$

Quadrupoles:

$$
\begin{aligned}
Q_{\alpha,\beta}^{(e)} &= \frac{1}{2} \int d^3r\, \rho \left[r_\alpha r_\beta - \frac{1}{3}\delta_{\alpha,\beta} r^2\right] = \frac{1}{\mathrm{i}2\omega} \int d^3r \left[r_\alpha J_\beta + r_\beta J_\alpha - \frac{2}{3}\delta_{\alpha,\beta}\,(\mathbf{r}.\mathbf{J})\right] \\
Q_{\alpha,\beta}^{(m)} &= \frac{1}{3c} \int d^3r\, \left[\mathbf{r} \times \mathbf{J}\right]_\alpha r_\beta + \{\alpha \leftrightarrow \beta\} \\
Q_{\alpha,\beta}^{(T)} &= \frac{1}{28c} \int d^3r \left[4 r_\alpha r_\beta\,(\mathbf{r}.\mathbf{J}) - 5r^2(r_\alpha J_\beta + r_\beta J_\alpha) + 2r^2\,(\mathbf{r}.\mathbf{J})\,\delta_{\alpha,\beta}\right]
\end{aligned}
$$

The Kronecker delta is denoted with $\delta_{\alpha,\beta}$ ($\delta_{x,x} = \delta_{y,y} = \delta_{z,z} = 1$ otherwise $\delta_{\alpha,\beta} = 0$).

Octupoles:

[14] Integrals over the charge density will be replaced with integrals over the current density by using the continuity equation $\mathrm{i}\omega\rho + \nabla.\mathbf{J} = 0$.

$$
\begin{aligned}
O^{(e)}_{\alpha,\beta,\gamma} =& \frac{1}{6}\int d^3r\,\rho\, r_\alpha \left(r_\beta r_\gamma - \frac{1}{5}r^2\delta_{\beta,\gamma}\right) + \{\alpha \leftrightarrow \beta,\gamma\} + \{\alpha \leftrightarrow \gamma,\beta\} \\
=& \frac{1}{\mathrm{i}6\omega}\int d^3r \left[J_\alpha\left(r_\beta r_\gamma - \frac{r^2}{5}\delta_{\beta,\gamma}\right) + r_\alpha\left(J_\beta r_\gamma + r_\beta J_\gamma - \frac{2}{5}(\mathbf{r}.\mathbf{J})\delta_{\beta,\gamma}\right)\right] + \\
&+ \{\alpha \leftrightarrow \beta,\gamma\} + \{\alpha \leftrightarrow \gamma,\beta\} \\
O^{(m)}_{\alpha,\beta,\gamma} =& \frac{15}{2c}\int d^3r \left(r_\alpha r_\beta - \frac{r^2}{5}\delta_{\alpha,\beta}\right)\cdot\left[\mathbf{r}\times\mathbf{J}\right]_\gamma + \{\alpha \leftrightarrow \beta,\gamma\} + \{\alpha \leftrightarrow \gamma,\beta\}
\end{aligned}
$$

For quadrupoles and octupoles a short-hand has been used to improve clarity. For example: $\int d^3r\,\left[\mathbf{r}\times\mathbf{J}\right]_\alpha r_\beta + \{\alpha \leftrightarrow \beta\} \equiv \int d^3r\,\left[\mathbf{r}\times\mathbf{J}\right]_\alpha r_\beta + \int d^3r\,\left[\mathbf{r}\times\mathbf{J}\right]_\beta r_\alpha$, i.e. the second term is obtained from the first term, with the exchanged positions of indices α and β. In case of octupoles (for example):

$$
\frac{1}{6}\int d^3r\,\rho\, r_\alpha \left(r_\beta r_\gamma - \frac{1}{5}r^2\delta_{\beta,\gamma}\right) + \{\alpha \leftrightarrow \beta,\gamma\} + \{\alpha \leftrightarrow \gamma,\beta\}
$$

means that the second term is obtained from the first term by exchanging α and β whilst leaving γ untouched. The third term is, again, obtained from the first term, but this time α and γ are exchanged, whilst β remains untouched.

In the case of harmonic oscillations of the current density (at a single frequency), there is no clear difference between the conduction and the displacement currents. In simulations, $\mathbf{J} = \mathrm{i}\omega\epsilon_0\left(\tilde{\epsilon}_r - 1\right)\mathbf{E}$ was used to find the current density within the media from the distribution of the electric field $\mathbf{E}(\mathbf{r})$. The relevant quantities are: ω-angular frequency, ϵ_0-free-space permittivity, c-speed of light and $\tilde{\epsilon}_r$-complex-valued dielectric constant (used to describe both the dielectrics and metals). For metals, it was sometimes more convenient to work with complex-valued conductivity $\tilde{\sigma}$ which is related to the dielectric constant via $\tilde{\epsilon}_r = 1 - \mathrm{i}\tilde{\sigma}/\omega\epsilon_0$.

The spherical multipoles are related to the Cartesian multipoles through following relations.

Dipoles:

$$
\begin{aligned}
Q_{1,0} &= p_z, & Q_{1,\pm1} &= \left(\mp p_x + \mathrm{i}p_y\right)/\sqrt{2} \\
M_{1,0} &= -m_z, & M_{1,\pm1} &= \left(\pm m_x - \mathrm{i}m_y\right)/\sqrt{2} \\
M^{(1)}_{1,0} &= -m^{(1)}_z, & M^{(1)}_{1,\pm1} &= \left(\pm m^{(1)}_x - \mathrm{i}m^{(1)}_y\right)/\sqrt{2} \\
T_{1,0} &= T_z, & T_{1,\pm1} &= \left(\mp T_x + \mathrm{i}T_y\right)/\sqrt{2} \\
T^{(1)}_{1,0} &= -T^{(1)}_z, & T^{(1)}_{1,\pm1} &= \left(\pm T^{(1)}_x - \mathrm{i}T^{(1)}_y\right)/\sqrt{2}
\end{aligned}
$$

Quadrupoles:

$$
\begin{aligned}
Q^{(e)}_{2,0} &= 3Q^{(e)}_{zz}, & Q^{(e)}_{2,\pm1} &= \sqrt{6}\left(\mp Q^{(e)}_{xz} + \mathrm{i}Q^{(e)}_{yz}\right), \\
& & Q^{(m)}_{2,\pm2} &= \frac{\sqrt{6}}{4}\left(-Q^{(m)}_{xx} \pm \mathrm{i}2Q^{(m)}_{xy} + Q^{(m)}_{yy}\right) \\
Q^{(m)}_{2,0} &= -\frac{3}{2}Q^{(m)}_{zz}, & Q^{(m)}_{2,\pm1} &= \sqrt{\frac{3}{2}}\left(\pm Q^{(m)}_{xz} - \mathrm{i}Q^{(m)}_{yz}\right), \\
& & Q^{(m)}_{2,\pm2} &= \frac{\sqrt{6}}{4}\left(-Q^{(m)}_{xx} \pm \mathrm{i}2Q^{(m)}_{xy} + Q^{(m)}_{yy}\right) \\
Q^{(T)}_{2,0} &= Q^{(T)}_{zz}, & Q^{(T)}_{2,\pm1} &= \sqrt{\frac{2}{3}}\left(\mp Q^{(T)}_{xz} + \mathrm{i}Q^{(T)}_{yz}\right), \\
& & Q^{(T)}_{2,\pm2} &= \left(Q^{(T)}_{xx} \mp \mathrm{i}2Q^{(T)}_{xy} - Q^{(T)}_{yy}\right)/\sqrt{6}
\end{aligned}
$$

Electric octupole:

$$
\begin{aligned}
O^{(e)}_{3,0} &= 15O^{(e)}_{zzz}, \\
O^{(e)}_{3,\pm1} &= \mp\frac{15\sqrt{3}}{2}\left(O^{(e)}_{zzx} \pm \mathrm{i}O^{(e)}_{yyy} \pm \mathrm{i}O^{(e)}_{xxy}\right), \\
O^{(e)}_{3,\pm2} &= -3\sqrt{\frac{15}{2}}\left(O^{(e)}_{zzz} + 2O^{(e)}_{yyz} \pm \mathrm{i}2O^{(e)}_{xyz}\right), \\
O^{(e)}_{3,\pm3} &= \mp\frac{3\sqrt{5}}{2}\left(O^{(e)}_{xxx} - 3O^{(e)}_{yyx} \pm \mathrm{i}O^{(e)}_{yyy} \mp \mathrm{i}3O^{(e)}_{xxy}\right)
\end{aligned}
$$

Magnetic octupole:

$$
\begin{aligned}
O^{(m)}_{3,0} &= -O^{(m)}_{zzz}/12, \\
O^{(m)}_{3,\pm1} &= \pm\left(O^{(m)}_{zzx} \pm \mathrm{i}O^{(m)}_{yyy} \pm \mathrm{i}O^{(m)}_{xxy}\right)/8\sqrt{3}, \\
O^{(m)}_{3,\pm2} &= \frac{\sqrt{2}}{8\sqrt{15}}\left(O^{(m)}_{zzz} + 2O^{(m)}_{yyz} \pm \mathrm{i}2O^{(m)}_{xyz}\right), \\
O^{(m)}_{3,\pm3} &= \pm\left(O^{(m)}_{xxx} - 3O^{(m)}_{yyx} \pm \mathrm{i}O^{(m)}_{yyy} \mp \mathrm{i}3O^{(m)}_{xxy}\right)/24\sqrt{5}
\end{aligned}
$$

L Full expression for radiation from the electric and the toroidal dipoles

In this appendix the expressions for the full radiation patterns of the electric and the toroidal dipoles will be derived from first principles. The interference between the two dipoles will also be considered. The approach mostly follows Afanasiev and Stepanovsky [183], but it was modified to keep the source-terms. Throughout the derivation, CGS units will be used and the complex-harmonic time-dependence will be assumed ($\exp(+\mathrm{i}\omega t)$ with angular frequency ω and wavenumber $k = \omega/c$).

As in other appendices, Greek letter sub-scripts will be used to denote the Cartesian components of vectors and tensors, e.g. α-th component of vector $\mathbf{E}$ will be denoted as

$(\mathbf{E})_\alpha \equiv E_\alpha$, where $\alpha = x, y, z$. Furthermore the summation convention will be used: if the *Greek sub-script*[15] is repeated (twice) within the linear term, the summation over this index is implied, e.g. $\mathbf{E}.\mathbf{J} = E_\alpha J_\alpha = E_x J_x + E_y J_y + E_z J_z$. The Kronecker delta will be denoted as $\delta_{\alpha,\beta}(\delta_{x,x} = \delta_{y,y} = \delta_{z,z} = 1$, otherwise $\delta_{\alpha,\beta} = 0)$. The three-dimensional delta function will be denoted as $\delta^{(3)}(\mathbf{r})$ ($\int d^3r\, \delta^{(3)}(\mathbf{r}) \equiv 1$, $\delta^{(3)}(\mathbf{r}) = 0$ if $\mathbf{r} \neq \mathbf{0}$, and $\int d^3r\, f(\mathbf{r}) \cdot \delta^{(3)}(\mathbf{r} - \mathbf{a}) \equiv f(\mathbf{a})$ for any sufficiently smooth function $f(\mathbf{r})$). Partial differentiation with respect to α-th coordinate will be denoted by $\partial_\alpha(...)$, e.g. $(\nabla\phi)_\alpha \equiv \partial_\alpha\phi$.

Electric dipole radiation pattern

It can be rigorously shown that the charge-current density that corresponds to an infinitesimally small electric dipole ($\mathbf{p}$), located at the origin, is given by [183]:

$$\rho^{(p)}(\mathbf{r}) = -\mathbf{p}.\nabla\delta^{(3)}(\mathbf{r})$$
$$\mathbf{J}^{(p)}(\mathbf{r}) = \mathrm{i}\omega\mathbf{p}\delta^{(3)}(\mathbf{r})$$

Instead of proving that this is the case, one can note that from the form of the expression for the current density it is clear that the only multipole this current-density will contribute to is the electric dipole. Using the integral from App. K, the contribution to the electric dipole will be $\mathbf{p} = \int d^3r \left(\mathrm{i}\omega\mathbf{p}\delta^{(3)}(\mathbf{r})\right) / (\mathrm{i}\omega) = \mathbf{p}\int d^3r\, \delta^{(3)}(\mathbf{r}) = \mathbf{p}$. The scalar ($\phi^{(p)}$) and vector potential ($\mathbf{A}^{(p)}$), that correspond to this charge and current density, can be found, in Lorentz gauge, using the Green's functions [174] (also see App. I):

$$\phi^{(p)}(\mathbf{r}) = \int d^3r' \frac{\exp\left(-\mathrm{i}k\left|\mathbf{r}-\mathbf{r}'\right|\right)}{\left|\mathbf{r}-\mathbf{r}'\right|}\rho(\mathbf{r}') = \mathbf{p}.\int d^3r'\,\nabla'\left(\frac{\exp\left(-\mathrm{i}k\left|\mathbf{r}-\mathbf{r}'\right|\right)}{\left|\mathbf{r}-\mathbf{r}'\right|}\right)\delta^{(3)}(\mathbf{r}') =$$
$$= \mathbf{p}.\left(-\nabla\right)\left(\int d^3r' \frac{\exp\left(-\mathrm{i}k\left|\mathbf{r}-\mathbf{r}'\right|\right)}{\left|\mathbf{r}-\mathbf{r}'\right|}\delta^{(3)}(\mathbf{r}')\right) = -\mathbf{p}.\nabla\left(\frac{\exp\left(-\mathrm{i}kr\right)}{r}\right)$$

$$\mathbf{A}^{(p)}(\mathbf{r}) = \int d^3r' \frac{\exp\left(-\mathrm{i}k\left|\mathbf{r}-\mathbf{r}'\right|\right)}{\left|\mathbf{r}-\mathbf{r}'\right|}\mathbf{J}(\mathbf{r}')/c = (\mathrm{i}k\mathbf{p})\frac{\exp\left(-\mathrm{i}kr\right)}{r}$$

Where c is the speed of light.

The radiated electric field is obtained in the normal fashion:

$$\left(\mathbf{E}^{(p)}\right)_\alpha = \left(-\nabla\phi - \mathrm{i}k\mathbf{A}\right)_\alpha = p_\beta\left(\partial_{\alpha\beta} + k^2\delta_{\alpha,\beta}\right)\frac{\exp\left(-\mathrm{i}kr\right)}{r}$$

The far-field component of the radiated field can be shown to be:

$$\mathbf{E}^{(p)} \overset{O(1/r)}{=} k^2\left(\mathbf{p} - \left(\mathbf{p}.\hat{\mathbf{r}}\right)\hat{\mathbf{r}}\right)\frac{\exp\left(-\mathrm{i}kr\right)}{r} = \left(k^2\left[\hat{\mathbf{r}}\times\mathbf{p}\right]\times\hat{\mathbf{r}}\right)\frac{\exp\left(-\mathrm{i}kr\right)}{r}$$

[15] Repetition of the Latin sub-script will not imply summation.

which is the same expression as the one found in the standard literature on electrodynamics [174].

Toroidal dipole radiation pattern

In a similar fashion, the rigorous expression for the charge-current density, that corresponds to infinitesimal toroidal dipole located at the origin, is given by [183, 227]:

$$\begin{aligned}\rho(\mathbf{r}) =& 0\\ \mathbf{J}(\mathbf{r}) =& \nabla\times\nabla\times\left(c\mathbf{T}\delta^{(3)}(\mathbf{r})\right)\end{aligned}$$

Again, it is possible to verify that the specified current-density will only contribute to the toroidal dipole, and that the contribution will be $\mathbf{T}$. The scalar potential that corresponds to this charge and current density vanishes ($\phi^{(T)}=0$), the vector potential is given by:

$$\begin{aligned}\mathbf{A}^{(T)}(\mathbf{r}) &= \int d^3r'\,\frac{\exp\left(-\mathrm{i}k\left|\mathbf{r}-\mathbf{r}'\right|\right)}{\left|\mathbf{r}-\mathbf{r}'\right|}\,\mathbf{J}(\mathbf{r}')/c\\ &= \nabla\left(\mathbf{T}.\nabla\left(\frac{\exp\left(-\mathrm{i}kr\right)}{r}\right)\right)-\mathbf{T}\nabla^2\left(\frac{\exp\left(-\mathrm{i}kr\right)}{r}\right)\end{aligned}$$

The radiated electric filed is given by:

$$\begin{aligned}\left(\mathbf{E}^{(T)}\right)_\alpha &= -\mathrm{i}k\left(\mathbf{A}^{(T)}\right)_\alpha = \left(-\mathrm{i}kT_\beta\right)\left(\partial_{\alpha\beta}-\delta_{\alpha,\beta}\nabla^2\right)\frac{\exp\left(-\mathrm{i}kr\right)}{r}\\ \mathbf{E}^{(T)} &\overset{O(1/r)}{=} \left(-\mathrm{i}k^3\right)\left(\mathbf{T}-\left(\mathbf{T}.\hat{\mathbf{r}}\right)\hat{\mathbf{r}}\right)\frac{\exp\left(-\mathrm{i}kr\right)}{r}\end{aligned}$$

Interference between the electric and the toroidal dipole

Whilst it is clear that the far-field distributions of the radiation from the electric and the toroidal dipoles are the same, the similarity goes deeper. Let the two dipoles be located at the same point and oriented along the same direction, also let the oscillations of the two dipoles be coherent, with electric dipole leading the toroidal dipole by quarter of a period, so that $\mathbf{p}=\mathrm{i}k\mathbf{T}$.

In this case, the net radiated electric field becomes:

$$\begin{aligned}\left(\mathbf{E}^{(\mathbf{p}+\mathbf{T})}\right)_\alpha &= \left(\mathbf{E}^{(\mathbf{p}=\mathrm{i}k\mathbf{T})}\right)_\alpha+\left(\mathbf{E}^{(T)}\right)_\alpha =\\ &= \left[\mathrm{i}kT_\beta\left(\partial_{\alpha\beta}+k^2\delta_{\alpha,\beta}\right)+\left(-\mathrm{i}kT_\beta\right)\left(\partial_{\alpha\beta}-\delta_{\alpha,\beta}\nabla^2\right)\right]\frac{\exp\left(-\mathrm{i}kr\right)}{r} =\\ &= \mathrm{i}kT_\beta\delta_{\alpha,\beta}\left[\nabla^2+k^2\right]\frac{\exp\left(-\mathrm{i}kr\right)}{r} = \mathrm{i}kT_\alpha\left(-4\pi\delta^{(3)}(\mathbf{r})\right)\\ \mathbf{E}^{(\mathbf{p}+\mathbf{T})} &= -\mathrm{i}4\pi k\mathbf{T}\delta^{(3)}(\mathbf{r})\end{aligned}$$

The electric field of the composite structure vanishes in the far-field *and* the near-

field. A single source-term remains due to fact that electric and toroidal dipoles correspond to different charge-current densities.

The expressions for the net scalar and vector potentials are also obtained by adding the expressions for the isolated electric and toroidal dipoles:

$$\phi^{(\mathbf{p}+\mathbf{T})} = -\mathrm{i}k\mathbf{T}.\nabla\left(\frac{\exp\left(-\mathrm{i}kr\right)}{r}\right) = \left(\hat{\mathbf{r}}.\mathbf{T}\right)\left(-k^2+\mathrm{i}k/r\right)\left(\frac{\exp\left(-\mathrm{i}kr\right)}{r}\right)$$

$$\begin{aligned}\left(\mathbf{A}^{(\mathbf{p}+\mathbf{T})}\right)_\alpha &= -k^2T_\beta\delta_{\alpha,\beta}\frac{\exp\left(-\mathrm{i}kr\right)}{r} + T_\beta\left(\partial_{\alpha\beta}-\delta_{\alpha,\beta}\nabla^2\right)\frac{\exp\left(-\mathrm{i}kr\right)}{r} = \\ &= T_\beta\partial_{\alpha\beta}\left(\frac{\exp\left(-\mathrm{i}kr\right)}{r}\right) - T_\beta\delta_{\alpha,\beta}\left[\nabla^2+k^2\right]\frac{\exp\left(-\mathrm{i}kr\right)}{r} = \\ &= T_\beta\partial_{\alpha\beta}\left(\frac{\exp\left(-\mathrm{i}kr\right)}{r}\right) + 4\pi T_\alpha\delta^{(3)}(\mathbf{r})\end{aligned}$$

The first derivative can be evaluated rigorously following the prescription $\partial_{\alpha\beta}\left(1/r\right) = \left(3r_\alpha r_\beta - r^2\delta_{\alpha\beta}\right)/r^5 - \left(4\pi/3\right)\delta_{\alpha\beta}\delta^{(3)}(\mathbf{r})$ [273]. The end-result can be written as:

$$\begin{aligned}\mathbf{A}^{(\mathbf{p}+\mathbf{T})} &= \left[\frac{(\mathbf{r}.\mathbf{T})\,F(\omega,r)}{c^2r^2}\mathbf{r} - \frac{D(\omega,r)}{cr}\mathbf{T}\right]\frac{\exp\left(-\mathrm{i}kr\right)}{r} + \frac{8\pi}{3}\mathbf{T}\delta^{(3)}(\mathbf{r}) \\ F(\omega,r) &= c^2\left(-k^2+\mathrm{i}3k/r+3/r^2\right) \\ D(\omega,r) &= c^2\left(-k^2+\mathrm{i}k/r+/r^2\right)\end{aligned}$$

M Angular momentum of a toroidal dipole in external electric field

This appendix presents the expression for the angular momentum of the static toroidal dipole immersed in externally applied electric field.

The angular momentum of electromagnetic field, in vacuum, is given by [174]:

$$\mathbf{L} = \epsilon_0\int d^3r\,\mathbf{r}\times\mathbf{E}\times\mathbf{B}$$

where $\mathbf{E}$ and $\mathbf{B}$ are the electric and magnetic fields (respectively), and ϵ_0 is the vacuum permittivity.

One can calculate the angular momentum of a toroidal dipole in the external electric field ($\mathbf{E}_{ext}$) by representing the current density of the dipole through magnetization[16] $\mathbf{M}$:

$$\begin{aligned}\mathbf{J}_{tor.\,dip.} &= \nabla\times\nabla\times\left(c\mathbf{T}\delta^{(3)}(\mathbf{r}-\mathbf{r}_0)\right) = \nabla\times\mathbf{M}_{tor.\,dip.} \\ \mathbf{M}_{tor.\,dip.} &= \nabla\times\left(c\mathbf{T}\delta^{(3)}(\mathbf{r}-\mathbf{r}_0)\right)\end{aligned}$$

[16] $\mathbf{J} = \nabla\times\nabla\times\left(c\mathbf{T}\delta^{(3)}(\mathbf{r})\right)$ is a standard way to represent the current density of an infinitesimal toroidal dipole ($\mathbf{T}$) [183, 227].

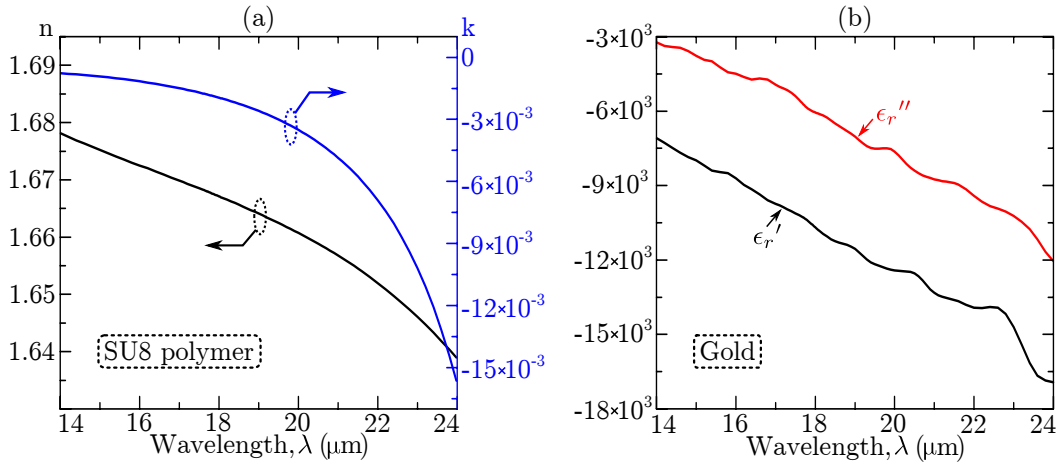

Figure N.1: ***Material constants for infrared toroidal metamaterial in Sec. 4.2.2.*** ***(a)*** *The refractive index of the polymer SU8. The complex-valued refractive index of SU8 is given by* $\tilde{n} = n + \mathrm{i}k$. ***(b)*** *The dielectric constant of the gold. The complex-valued dielectric constant is given by* $\tilde{\epsilon}_r = \epsilon_r' + \mathrm{i}\epsilon_r''$.

where c is the speed of light and $\mathbf{T}$ is the toroidal dipole moment. Substituting the external electric field ($\mathbf{E} \rightarrow \mathbf{E}_{ext}$) and toroidal dipole magnetization ($\mathbf{B} \rightarrow \mu_0 \mathbf{M}_{tor.\,dip.}$) into the expression for angular momentum leads to:

$$
\begin{aligned}
\mathbf{L} &= \frac{1}{c^2} \cdot \int d^3r\, \mathbf{r} \times \mathbf{E}_{ext} \times \mathbf{M}_{tor.\,dip.} \\
\mathbf{L} &= \frac{1}{c^2} \cdot \int d^3r\, \mathbf{r} \times \mathbf{E}_{ext} \times \nabla \times \left(c\mathbf{T}\delta^{(3)}(\mathbf{r} - \mathbf{r}_0) \right) \\
\mathbf{L} &= \frac{1}{c} \cdot \int d^3r\, \delta^{(3)}(\mathbf{r} - \mathbf{r}_0) \cdot [\mathbf{T} \times \mathbf{E}_{ext}] \\
\mathbf{L} &= \frac{1}{c} \cdot \mathbf{T} \times \mathbf{E}_{ext}(\mathbf{r}_0)
\end{aligned}
$$

Therefore, a system that consists of a static toroidal dipole $\mathbf{T}$ and an applied electric field $\mathbf{E}_{ext}$ will posses a non-vanishing angular momentum.

N Electromagnetic response of SU8 polymer and gold in the infrared spectrum

Figure N.1 presents the measured dielectric constant of gold and the refractive index of polymer SU8, used for simulations in Sec. 4.2.2. Measurements have been provided by Dr. I. Brener and Dr. D. B. Burckel from Sandia National Laboratories (US).

O Publications

O.1 Journal Publications

- V. Savinov, V. A. Fedotov, and N. I. Zheludev, "Macroscopic electromagnetic properties of metamaterials and the toroidal dipole". To be submitted

- V. A. Fedotov, A. V. Rogacheva, V. Savinov, D. P. Tsai, and N. I. Zheludev, "Resonant Transparency and Non-trivial Non-radiating Excitations in Toroidal Metamaterials", *Sci. Rep.* **3**, 2967 (2013)

- V. Savinov, V. A. Fedotov, P. A. J. de Groot, and N. I. Zheludev, "Radiation-harvesting resonant superconducting sub-THz metamaterial bolometer", *Supercond. Sci. Technol.* **26**, 084001 (2013)

- V. Savinov, V. A. Fedotov, S. M. Anlage, P. A. J. de Groot, and N. I. Zheludev, "Modulating sub-THz radiation with current in superconducting metamaterial" *Phys. Rev. Lett.* **109**, 243904 (2012).

- Y.-W. Huang, W. T. Chen, P. C. Wu, V. Fedotov, V. Savinov, Y. Z. Ho, Y.-F. Chau, N. I. Zheludev, and D. P. Tsai, "Design of plasmonic toroidal metamaterials at optical frequencies", *Optics Express* **20**, 1760 (2012).

- V. Savinov, A. Tsiatmas, A. R. Buckingham, V. A. Fedotov, P. A. J. de Groot, and N. I. Zheludev, "Flux exclusion superconducting quantum metamaterial: towards quantum-level switching", *Sci. Rep.* **2**, 450 (2012).

- Y. W. Huang, W. T. Chen, P. C. Wu, Y. Z. Ho, D. P. Tsai, V. Fedotov, V. Savinov, N. I. Zheludev, and Y. F. Chau, "Plasmonic toroidal resonance at optical frequencies", *SPIE Newsroom* (2012). doi: 10.1117/2.1201205.004193

O.2 Conference Contributions

- (oral) V. Savinov, V. A. Fedotov, P. A. J. de Groot, and N. I. Zheludev, "Radiation-harvesting resonant superconducting sub-THz metamaterial bolometer", CLEO/Europe - IQEC 2013, Munich, Germany, 12 - 16 May (2013)

- (poster) V. Savinov, V.A. Fedotov, A.V. Rogacheva, D.P. Tsai, and N.I. Zheludev, "Non-radiating excitations, vector potential waves and toroidal metamaterials" CLEO/Europe - IQEC 2013, Munich, Germany, 12 - 16 May (2013)

- (invited) V. Savinov, V. A. Fedotov, P. A. J. de Groot, N. I. Zheludev, "Superconducting metamaterial bolometer for harvesting the sub-THz radiation", IPS Meeting 2013, Singapore 4-6 March (2013)

- (oral) V. Savinov, V. A. Fedotov, A. V. Rogacheva, D. P. Tsai, N. I. Zheludev, "Non-trivial non-radiating excitations and vector potential", Nanometa 2013, Seefeld, Austria, Jan. 3-6 (2013).

- (poster) V. Savinov, V. A. Fedotov, P. A. J. de Groot, N. I. Zheludev, "Radiation-harvesting sub-THz bolometer based on resonant superconducting metamaterial", Nanometa 2013, Seefeld, Austria, Jan. 3-6 (2013).

- (oral) W. T. Chen, P. C. Wu, Y. W. Huang, C. T. Hsiao, K. Yu Yang, C. Y. Liao, V. Fedotov, V. Savinov, N. I. Zheludev, D. P. Tsai. "3D metamaterials: Erected U-shaped nano-rings and plasmonic toroidal metamaterials". E-MRS 2012 Symposium on control of light at the nanoscale: materials, techniques and applications, Strasbourg, France, May 14-18 (2012).

- (oral) V. Savinov, V. Fedotov, P. A. J. de Groot, N. I. Zheludev, "Electro-optical modulation of sub-terahertz radiation with superconducting metamaterial", CLEO: 2012 , San Jose, USA, 6-11 May 2012.

- (oral) V. Savinov, V. Fedotov, W. T. Chen, Y.-W. Huang, D. P. Tsai, D. Burckel, I. Brener. N. I. Zheludev, "Toroidal plasmonic metamaterial", CLEO: 2012 , San Jose, USA, 6-11 May 2012.

- (oral) V. Savinov, A. Tsiatmas, A. Buckingham, V. Fedotov, P. A. J. de Groot, N. I. Zheludev, "Flux Exclusion Quantum Superconducting Metamaterial", CLEO: 2012 , San Jose, USA, 6-11 May 2012.

- (oral) D. P. Tsai, W. T. Chen, P. C. Wu, C. T. Hsiao, K. Y. Yang, Y. W. Huang, C. Y. Liao, S. Sun, C. J. Chen, L. Zhou, G. Y. Guo, V. Fedotov, V. Savinov, N. I. Zheludev. "Magnetic response of upright meta-molecules in optical region" META'12, Paris, France, Apr. 19-22 (2012).

- (keynote) D. P. Tsai, N. I. Zheludev, V. Savinov, V. A. Fedotov, H. G. Tsai, C. Y. Liao, K. S. Chung, Y. Z. Ho, L. C. Kuo, Y. J. Liu, H. W. Huang, Y.-W. Huang, K.-Y. Yang, C. T. Hsiao, S. Sun, B. H. Cheng, Y. L. Chen, P. C. Wu, C. M. Chang, M. L. Tseng, W. T. Chen, "Three-dimensional metamaterials: from nano bumps to erected U-shape nano-rings and toroidal metamaterials in optical region", SPIE Photonics Europe, Brussels, Belgium, Apr. 16 - 19 (2012).

- (poster) V. Savinov, V. A. Fedotov, P. A. J. de Groot, N. I. Zheludev, "Electro-optical modulation of sub-terahertz radiation in a superconducting metamaterial", SPIE Photonics Europe, Brussels, Belgium, 16-19 Apr. 2012.

- (poster) V. Savinov, W. T. Chen, Y.-W. Huang, V. A. Fedotov, D. P. Tsai, D.B. Bruckel, I. Brener, N. I. Zheludev, "Toroidal plasmonic metamaterial", SPIE Photonics Europe, Brussels, Belgium, 16-19 Apr. 2012.

- (poster) V. Savinov, A. Tsiatmas, A. R. Buckingham, V. A. Fedotov, P. A. J de Groot, N. I. Zheludev , "Flux Exclusion Quantum Superconducting Metamaterial", SPIE Photonics Europe, Brussels, Belgium, 16-19 Apr. 2012.

- (invited) V. A. Fedotov, T. Kaelberer, N. Papasimakis, V. Savinov, A. V. Rogacheva, N. I. Zheludev, "Toroidal dipolar response in metamaterials: illusion or reality", Metamaterials Congress 2011, Barcelona, Spain 10-15, Oct. 2011.

- (oral) A. R. Buckingham, A. Tsiatmas, V. Savinov, V. A. Fedotov, P. A. J. de Groot, N. I. Zheludev, "Realising tunable quantum and low-loss metamaterials and plasmonics with superconductors", Metamaterials Congress 2011, Barcelona, Spain, 10-15 Oct. 2011.

- (invited) P.A.J. de Groot, A. R. Buckingham, V. Savinov, A. Tsiatmas, V. A. Fedotov, S. Wang, Y. Chen, and N. I. Zheludev, "Superconducting Metamaterials and Plasmonics. Vortex Matter in Nanostructured Superconductors", Rhodes, Greece, Sep. 10-17 (2011).

- (oral) Y.-W. Huang, W. T. Chen, P. C. Wu, Y.-F. Chau, D. P. Tsai, V. A. Fedotov, V. Savinov, N. I. Zheludev, "Plasmonic toroidal response at optical frequencies", SPIE Optics & Photonics (Plasmonics: Metallic Nanostructures and Their Optical Properties IX), San Diego, USA, 22 Aug. 2011.

- (oral) A. Tsiatmas, V. A. Fedotov, T. Kaelberer, N. Papasimakis, V. Savinov, A. Rogacheva, D. P. Ysai, N. I. Zheludev, "Demonstrating Elusive Toroidal Dipolar Response in Metamaterials", CLEO/Europe - EQEC 2011, Munich, Germany, 22-26 May 2011.

- (oral) A. Tsiatmas, A. R. Buckingham, V. Savinov, V. A. Fedotov, P. A. J. de Groot, N. I. Zheludev. "Superconducting Plasmonics and Quantum Metamaterials", SPP5, Busan, S. Korea, May 15 -20 (2011).

Bibliography

[1] N. I. Zheludev, "The road ahead for metamaterials," *Science*, vol. 328, p. 582, 2010.

[2] N. Papasimakis, V. A. Fedotov, Y. H. Fu, D. P. Tsai, and N. I. Zheludev, "Coherent and incoherent metamaterials and order-disorder transitions," *Phys. Rev. B*, vol. 80, p. 041102, 2009.

[3] C. Caloz and T. Itoh, *Electromagnetic metamaterials: Transmission line theory and microwave applications.* John Wiley & Sons, 2006.

[4] D. T. Emmerson, "The work of Jagadis Chandra Bose: 100 Years of millimeter-wave research," *IEEE Trans. Microw. Theory Tech.*, vol. 45, pp. 2267–2273, 1997.

[5] ——. [Online]. Available: https://www.cv.nrao.edu/~demerson/bose/bose.html

[6] D. R. Smith, W. J. Padilla, D. C. Vier, S. C. Nemat-Nasser, and S. Schultz, "Composite medium with simultaneously negative permeability and permittivity," *Phys. Rev. Lett.*, vol. 84, pp. 4184–4187, 2000.

[7] R.A. Shelby, D.R. Smith, and S. Schultz, "Experimental verification of a negative index of refraction," *Science*, vol. 292, p. 77, 2001.

[8] V. G. Veselago, "The electrodynamics of substances with simultaneously negative values of ϵ and μ," *Sov. Phys. Usp.*, vol. 10, pp. 509–514, 1968; 1967 in Russian.

[9] L. S. Dolin, "To the possibility of comparison of three-dimensional electromagnetic systems with nonuniform anisotropic filling," *Izv. Vyssh. Uchebn. Zaved. Radiofizika*, vol. 4, pp. 964–967, 1961.

[10] U. Leonhardt, "Optical conformal mapping," *Science*, vol. 312, pp. 1777–1780, 2006.

[11] D. Schurig, J. J. Mock, B. J. Justice, S. A. Cummer, J. B. Pendry, A. F. Starr, and D. R. Smith, "Metamaterial electromagnetic cloak at microwave frequencies," *Science*, vol. 314, p. 977, 2006.

[12] J. B. Pendry, D. Schurig, and D. R. Smith, "Controlling electromagnetic fields," *Science*, vol. 312, p. 1780, 2006.

[13] J. B. Pendry, "Negative Refraction Makes a Perfect Lens," *Phys. Rev. Lett.*, vol. 85, p. 3966, 2000.

[14] A. Grbic and G. V. Eleftheriades, "Overcoming the diffraction limit with a planar left-handed transmission-line lens," *Phys. Rev. Lett.*, vol. 92, p. 117403, 2004.

[15] Z. Jacob, L. V. Alekseyev, and E. Narimanov, "Optical hyperlens: far-field imaging beyond the diffraction limit," *Opt. Express*, vol. 14, pp. 8247–8256, 2006.

[16] Z. Liu, H. Lee, Y. Xiong, C. Sun, and X. Zhang, "Far-field optical hyperlens magnifying sub-diffraction-limited objects," *Science*, vol. 315, p. 1686, 2007.

[17] T. Kaelberer, V. A. Fedotov, N. Papasimakis, D. P. Tsai, N. I. Zheludev, "Toroidal Dipolar Response in a Metamaterial," *Science*, vol. 330, p. 1510, 2010.

[18] A. D. Boardman, V. V. Grimalsky, Y. S. Kivshar, S. V. Koshevaya, M. Lapine, N. M. Litchinitser, V. N. Malnev, M. Noginov, Y. G. Rapoport, and V. M. Shalaev, "Active and tunable metamaterials," *Laser Photonics Rev.*, vol. 5, pp. 287–307, 2010.

[19] C. M. Soukolis and M. Wegener, "Past achievements and future challenges in the development of three-dimensional photonic metamaterials," *Nature Photon.*, vol. 5, pp. 523–530, 2011.

[20] A. Q. Liu, W. M. Zhu, D. P. Tsai, and N. I. Zheludev, "Micromachined tunable metamaterials: a review," *J. Opt.*, vol. 14, p. 114009, 2012.

[21] N. I. Zheludev and Yu. S. Kivshar, "From metamaterials to metadevices," *Nature Mater.*, vol. 11, pp. 917–924, 2012.

[22] O. Hess, J. B. Pendry, S. A. Maier, R. F. Oulton, J. M. Hamm, and K. L. Tsakmakidis, "Active nanoplasmonic metamaterials," *Nature Mater.*, vol. 11, pp. 573–584, 2012.

[23] E. Plum, V. A. Fedotov, P. Kuo, D. P. Tsai, and N. I. Zheludev, "Towards the lasing spaser: controlling metamaterial optical response with semiconductor quantum dots," *Opt. Express*, vol. 17, p. 8548, 2009.

[24] H.-T. Chen, W. J. Padilla, J. M. O. Zide, A. C. Gossard, A. J. Taylor, and R. D. Averitt, "Active terahertz metamaterial devices," *Nature*, vol. 444, p. 597, 2006.

[25] F. B. P. Niesler, J. K. Gansel, S. Fishbach, and M. Wegener, "Metamaterial metal-based bolometers," *Appl. Phys. Lett.*, vol. 100, p. 203508, 2012.

[26] K. M. Dani, Z. Ku, P. C. Upadhya, R. P. Prasankumar, S. R. J. Brueck, and A. J. Taylor, "Subpicosecond optical switching with a negative index metamaterial," *Nano Lett.*, vol. 9, pp. 3565–3569, 2009.

[27] M. Tinkham, *Introduction to superconductivity. 2nd ed.* New York: Dover Publications Inc., 1996.

[28] V. V. Schmidt, *The Physics of Superconductors*, P. Mueller, A. V. Ustinov, Ed. Springer, 1997.

[29] V. Moshchalkov, M. Menghini, T. Nishio, Q. H. Chen, A. V. Silhanek, V. H. Dao, L. F. Chibotaru, N. D. Zhigadlo, and J. Karpinski, "Type-1.5 superconductivity," *Phys. Rev. Lett.*, vol. 102, p. 117001, 2009.

[30] H. Eisaki and H. Takagi, R. J. Cava, B. Batlogg, J. J. Krajewski, W. F. Peck, Jr., K. Mizuhashi, J. O. Lee, and S. Uchida, "Competition between magnetism and superconductivity in rare-earth nickel boride carbides," *Phys. Rev. B*, vol. 50, pp. 647–650, 1994.

[31] D. Dew-Hughes, "The critical current of superconductors: an historical review," *Low. Temp. Phys.*, vol. 27, pp. 713–722, 2001.

[32] J. Bardeen, L. N. Cooper, and J. R. Schrieffer, "Theory of superconductivity," *Phys. Rev.*, vol. 108, pp. 1175–1204, 1957.

[33] T. van Duzer, C. W. Turner, *Principles of Superconductive Devices and Circuits.* Edward Arnold, 1981.

[34] H. L. Edwards, J. T. Markert, and A. L. de Lozanne, "Energy gap and surface structure of $YBa_2Cu_3O_{7-x}$ probed by scanning tunneling microscopy," *Phys. Rev. Lett.*, vol. 69, pp. 2967–2970, 1992.

[35] S. Lin and X. Hu, "Possible dynamic states in inductively coupled intrinsic Josephson junctions of layered high-T_c superconductors," *Phys. Rev. Lett.*, vol. 100, p. 247006, 2008.

[36] L. F. Stokes, M. Chodorow, and H. J. Shaw, "All-single-mode fibre resonator," *Opt. Lett.*, vol. 7, pp. 288–290, 1982.

[37] J. Q. You and F. Nori, "Atomic physics and quantum optics using superconducting circuits," *Nature*, vol. 474, pp. 589–597, 2011.

[38] H. Tou, Y. Kitaoka, K. Asayama, N. Kimura, Y. Ōnuki, E. Yamamoto, and K. Maezawa, "Odd-parity superconductivity with parallel spin [airing in UPt_3: evidence from ^{195}Pt Knight shift study," *Phys. Rev. Lett.*, vol. 77, pp. 1374–1377, 1996.

[39] K. Ishida, H. Mukuda, Y. Kitaoka, K. Asayama, Z. Q. Mao, Y. Mori, and Y. Maeno, "Spin-triplet superconductivity in Sr_2RuO_4 identified by ^{17}O Knight shift," *Nature*, vol. 396, pp. 658–660, 1998.

[40] M. J. Lancaster, *Passive Microwave Device Applications of High-Temperature Superconductors*. Cambridge Univesity Press, 2006.

[41] K. K. Likharev, *Dynamics of Josephson Junctions and Circuits*. Gordon and Breach Science Publishers, 1984.

[42] K. Kitazawa, "Superconductivity: 100th anniversary of its discovery and its future," *Jpn. J. Appl. Phys.*, vol. 51, p. 010001, 2012.

[43] National Health Service Wales. United Kingdom. [Online]. Available: http://www.wales.nhs.uk/sitesplus/863/page/39408

[44] Central Japan Railway Company. Japan. [Online]. Available: http://english.jr-central.co.jp/company/company/others/eco-report/_pdf/p38-p41.pdf

[45] Tore Supra, EURATOM-CEA. France. [Online]. Available: http://www-fusion-magnetique.cea.fr/gb/accueil/index.htm

[46] B. H. Eom, P. K. Day, H. G. LeDuc, and J. Zmuidzinas, "A wideband, low-noise superconducting amplifier with high dynamic range," *Nature Phys.*, vol. 8, pp. 623–627, 2012.

[47] S. Cibella, M. Ortolani, R. Leoni, G. Torrioli, L. Mahler, Ji-Hua Xu, A. Tredicucci, H. E. Beere, and D. A. Ritchie, "Wide dynamic range terahertz detector pixel for active spectroscopic imaging with quantum cascade lasers," *Appl. Phys. Lett.*, vol. 95, p. 213501, 2009.

[48] National Institute of Standards and Technology, USA. [Online]. Available: http://www.nist.gov/pml/history-volt/superconductivity_2000s.cfm

[49] H. Padamsee, "The science and technology of superconducting cavities for accelerators," *Supercond. Sci. Technol.*, vol. 14, pp. R28–R51, 2001.

[50] J. Zmuidzinas and P. L. Richards, "Superconducting detectors and mixers for millimeter and submillimeter astrophysics," *Proc. IEEE*, vol. 92, pp. 1597–1616, 2004.

[51] J. Clarke and F. K. Wilhelm, "Superconducting quantum bits," *Nature*, vol. 453, pp. 1031–1042, 2008.

[52] Hts film coating data sheet. THEVA (Germany). E-type and M-type YBCO was used in my experiments. [Online]. Available: http://www.theva.com/user/eesy.de/theva.biz/dwn/Datasheet_Coatings.pdf

[53] D. M. Pozar, *Microwave Engineering*, 4th ed. John WIley & Sons, Inc., 2011.

[54] M. Tonouchi, "Cutting-edge terahertz technology," *Nature Photon.*, vol. 1, pp. 97–105, 2007.

[55] *Agilent 1287-1, Understanding the Fundamental Principles of Vector Network Analysis*, Agilent, 2012.

[56] *Agilent AN 1287-3, Applying Error correction to Network Analyzer Measurements*, Agilent, 2002.

[57] M Born, E. Wolf, *Principles of Optics, 7th expanded edition.* University Press, Cambridge, 2009.

[58] B. Komiyama, M. Kiyokawa, and T. Matsui, "Open resonator for precision dielectric measurements in the 100 GHz band," *IEEE Trans. Microw. Theory Tech.*, vol. 39, pp. 1792–1796, 1991.

[59] M. N. Afsar and H. Ding, "A novel open-resonator system for precise measurement of permittivity and loss-tangent," *IEEE Trans. Instrum. Meas.*, vol. 50, pp. 402–405, 2001.

[60] H. P. Hsu, *Signals and Systems*, 2nd ed. McGraw-Hill, 2011.

[61] B. Ferguson and X.-C. Zhang, "Materials for terahertz science and technology," *Nature Mater.*, vol. 1, pp. 26–33, 2002.

[62] W. L. Chan, J. Deibel, and D. M. Mittleman, "Imaging with terahertz radiation," *Rep. Prog. Phys.*, vol. 70, pp. 1325–1379, 2007.

[63] J. Federici and L. Moeller, "Review of terahertz and subterahertzwireless communications," *J. Appl. Phys.*, vol. 107, p. 111101, 2010.

[64] I. B. Vendik, O. G. Vendik, M. A. Odit, D. V. Kholodnyak, S. P. Zubko, M. F. Sitnikova, P. A. Turalchuk, K. N. Zemlyakov, I. V. Munina, D. S. Kozlov, V. M. Turgaliev, A. B. Ustinov, Y. Park, J. Kihm, C.-W. Lee, "Tunable Metamaterials for Controlling THz Radiation," *IEEE Trans. Terahertz Sci. Technol.*, vol. 2, pp. 538–549, 2012.

[65] M. D. Sherrill and K. Rose, "Microwave nonlinearities in thin superconducting films," *Rev. Mod. Phys.*, vol. 36, pp. 312–315, 1964.

[66] C. C. Chin, D. E. Oates, G. Dresselhaus, and M. S. Dresselhaus, "Nonlinear electrodynamics of superconducting NbN and Nb thin films at microwave frequencies," *Phys. Rev. B*, vol. 45, pp. 4788–4798, 1992.

[67] C. Zhang, B. Jin, A. Glossner, L. Kang, J. Chen, I. Kawayama, H. Murakami, P. Müller, P. Wu, and M. Tonouchi, "Pair-breaking in superconducting NbN films induced by intense THz field," *J. Infrared Milli. Terahz. Waves*, vol. 33, pp. 1071–1075, 2012.

[68] S. M. Anlage, "The physics and applications of superconducting metamaterials," *J. Opt*, vol. 13, p. 024001, 2011.

[69] R. R. Mansour, "Microwave superconductivity," *IEEE Trans. Microw. Theory Tech.*, vol. 50, p. 750, 2002.

[70] V. A. Fedotov, N. Papasimakis, E. Plum, A. Bitzer, M. Walther, P. Kuo, D. P. Tsai, and N. I. Zheludev, "Spectral Collapse in Ensembles of Metamolecules," *Phys. Rev. Lett.*, vol. 104, p. 223901, 2010.

[71] V. A. Fedotov, M. Rose, S. L. Prosvirnin, N. Papasimakis, and N. I. Zheludev, "Sharp trapped-mode resonances in planar metamaterials with a broken structural symmetry," *Phys. Rev. Lett.*, vol. 99, pp. 147 401–4, 2007.

[72] J. Halbritter, "rf residual losses, surface impedance, and granularity in superconducting cuprates ," *J. Appl. Phys.*, vol. 68, p. 6315, 1990.

[73] M. A. Golosovsky, H. J. Snortland, and M. R. Beasly, "Nonlinear microwave properties of superconductlng Nb microstnp resonators," *Phys. Rev. B*, vol. 51, p. 6462, 1995.

[74] E. Shamonina and L. Solymar, "Magneto-inductive waves supported by metamaterial elements: components for a one-dimensional waveguide," *J. Phys. D: Appl. Phys.*, vol. 37, p. 362, 2004.

[75] N. I. Zheludev, S. L. Prosvirnin, N. Papasimakis, and V. A. Fedotov, "Lasing Spaser," *Nature Photon.*, vol. 2, p. 351, 2008.

[76] V.A. Fedotov, A. Tsiatmas, J. H. Shi, R. Buckingham, P. A. J. de Groot, Y. Chen, S. Wang, and N.I. Zheludev, "Temperature control of Fano resonances and transmission in superconducting metamaterials," *Opt. Express*, vol. 18, p. 9015, 2010.

[77] B. Luk'yanchuk, N. I. Zheludev, S. A. Maier, N. J. Halas, P. Nordlander, H. Giessen, and C. T. Chong, "The Fano resonance in plasmonic nanostructures and metamaterials," *Nature Mater.*, vol. 9, pp. 707–715, 2010.

[78] S. D. Jenkins and J. Ruostekoski, "Resonance linewidth and inhomogeneous broadening in a metamaterial array," *Phys. Rev. B*, vol. 86, p. 205128, 2012.

[79] H. Goldstein, C. Poole, J. Safko, *Classical Mechanics.* Addison-Wesley Publishing Company, 2002.

[80] S. D. Jenkins and J. Ruostekoski, "Theoretical formalism for collective electromagnetic response of discrete metamaterial systems," *Phys. Rev. B*, vol. 86, p. 085116, 2012.

[81] C. A. Schmuttenmaer, "Exploring dynamics in the far-infrared with terahertz spectroscopy," *Chem. Rev.*, vol. 104, p. 1759, 2004.

[82] F. Sizov, "THz radiation sensors," *Opto-Electron. Rev.*, vol. 18, pp. 10–36, 2010.

[83] C. E. Groppi and J. H. Kawamura, "Coherent detector arrays for terahertz astrophysics applications," *IEEE Trans. Terahertz Sci. Technol.*, vol. 1, p. 85, 2011.

[84] P. L. Richards, "Bolometers for infrared and millimeter waves," *J. Appl. Phys.*, vol. 76, pp. 1–24, 1994.

[85] M. Kenyon, P. K. Day, C. M. Bradford, J. J. Bock, and H. G. Leduc, "Electrical properties of background-limited membrane-isolated transition-edge sensing bolometers for far-IR/Submillimeter direct-detection spectroscopy," *J. Low. Temp. Phys.*, vol. 151, pp. 112–118, 2008.

[86] J. Wei, D. Olaya, B. S. Karasik, S. V. Pereverzev, A. V. Segeev, and M. E. Gershenson, "Ultrasensitive hot-electron nanobolometers for terahertz astrophysics," *Nature Nanotech.*, vol. 3, pp. 496–500, 2008.

[87] B. S. Karasik, A. V. Sergeev, and D. E. Prober, "Nanobolometers for THz photon detection," *IEEE Trans. Terahertz Sci. Technol.*, vol. 1, p. 97, 2011.

[88] G. M. Rebeiz, "Millimeter-wave and terahertz integrated circuit antennas," *Proc. IEEE*, vol. 80, p. 1748, 1992.

[89] S. E. Schwarz and B. T. Ulrich, "Antenna-coupled infrared detectors," *J. Appl. Phys.*, vol. 48, pp. 1870–1873, 1977.

[90] V. Savinov, V. A. Fedotov, P. A. J. de Groot, and N. I. Zheludev, "Radiation-harvesting resonant sub-THz metamaterial bolometer," *Supercond. Sci. Technol.*, vol. 26, p. 084001, 2013.

[91] V. Savinov, V. A. Fedotov, S. M. Anlage, P. A. J. de Groot, and N. I. Zheludev, "Modulating Sub-THz Radiation with Current in Superconducting Metamaterial," *Phys. Rev. Lett.*, vol. 109, p. 243904, 2012.

[92] S. D. Jenkins and J. Ruostekoski, "Cooperative resonance linewidth narrowing in a planar metamaterial," *New. J. Phys.*, vol. 14, p. 103003, 2012.

[93] W. J. Skocpol, M. R. Beasley, and M. Tinkham, "Self-heating hotspots in superconducting thin-film microbridges," *J. Appl. Phys.*, vol. 45, pp. 4054–4066, 1974.

[94] J. Krupka, K. Derzakowski, M. Tobar, J. Harnett, and R. G. Geyer, "Complex permittivity of some ultralow loss dielectric crystals at cryogenic temperatures," *Meas. Sci. Technol.*, vol. 10, p. 387, 1999.

[95] A. A. V. Pronin, M. Dressel, A. Pimenov, A. Loidl, I. V. Roshchin, and L. H. Greene, "Direct observation of the superconducting energy gap developing in the conductivity spectra of niobium," *Phys. Rev. B*, vol. 57, pp. 14 416–14 421, 1998.

[96] K. D. Irwin, "An application of the electrothermal feedback for high resolution cyogenic particle detection," *Appl. Phys. Lett.*, vol. 66, pp. 1998–2000, 1995.

[97] A. Luukanen and J. P. Pekola, "A superconducting antenna-coupled hot-spot microbolometer," *Appl. Phys. Lett.*, vol. 82, pp. 3970–3972, 2003.

[98] A. Luukanen, E. N. Grossman, A. J. Miller, P. Helisto, J. S. Penttila, H. Sipola, and H. Seppa, "An ultra-low noise superconducting antenna-coupled microbolometer with a room-temperature read-out," *IEEE Microw. Wireless Compon. Lett.*, vol. 16, pp. 464–466, 2006.

[99] A. D. Semenov, H. Richter, H.-W. Hubers, B. Gunther, A. Smirnov, K. S. Il'in, M. Siegel, and J. P. Karamarkovic, "Terahertz performance of integrated lens antennas with a hot-electron bolometer," *IEEE Trans. Microw. Theory Techn.*, vol. 55, pp. 239–247, 2007.

[100] T. Maier and H. Brückl , "Wavelength-tunable microbolometers with metamaterial absorbers," *Opt. Lett.*, vol. 34, pp. 3012–3014, 2009.

[101] D. Shrekenhamer, W. Xu, S. Venkatesh, D. Schurig, S. Sonkusale, and W. Padilla, "Experimental realization of a metamaterial detector focal plane array," *Phys. Rev. Lett.*, vol. 109, p. 177401, 2012.

[102] S. Ogawa, K. Okada, N. Fukushima, and M. Kimata, "Wavelength selective uncooled infrared sensor by plasmonics," *Appl. Phys. Lett.*, vol. 100, p. 021111, 2012.

[103] J. E. Stewart, *Infrared Spectroscopy.* New York: Marcel Dekker, Inc., 1970.

[104] M. J. Buckingham, *Noise in electronic devices and systems.* Chichester: Ellis Horwood, 1983.

[105] F. J. Low and A. R. Hoffman, "The detectivity of cryogenic bolometers," *Appl. Opt.*, vol. 2, pp. 649–650, 1963.

[106] J. C. Mather, "Bolometer noise: nonequilibrium theory," *Appl. Opt.*, vol. 21, pp. 1125–1129, 1982.

[107] M. Rahm, J.-S. Li, and W. J. Padilla, "THz Wave Modulators: A Brief Review on different Modulation Techniques," *J. Infrared Milli. Terahz. Waves*, vol. 34, pp. 1–27, 2013.

[108] H. Takahashi, T. Kosugi, A. Hirata, K. Murata, and N. Kukutsu, "10-Gbit/s Quadrature Phase-Shift-Keying Modulator and Demodulator for 120-GHz-Band Wireless Links," *IEEE Trans. Microw. Theory Tech.*, vol. 58, pp. 4072–4078, 2010.

[109] I. H. Libon, S. Baumgärtner, M. Hempel, N. E. Hecker, J. Feldmann, M. Koch, and P. Dawson, "An optically controllable terahertz filter," *Appl. Phys. Lett.*, vol. 76, pp. 2821–2823, 2000.

[110] T. Kleine-Ostmann, P. Dawson, K. Pierz, G. Hein, and M. Koch, "Room-temperature operation of an electrically driven terahertz modulator," *Appl. Phys. Lett.*, vol. 84, pp. 3555–3557, 2004.

[111] T. Kleine-Ostmann, K. Pierz, G. Hein, P. Dawson, M. Marso, and M. Koch, "Spatially resolved measurements of depletion properties of large gate twodimensional electron gas semiconductor terahertz modulators," *J. Appl. Phys.*, vol. 105, p. 093707, 2009.

[112] B. Sensale-Rodriguez, R. Yan, S. Rafique, M. Zhu, W. Li, X. Liang, D. Gundlach, V. Protasenko, M. M. Kelly, D. Jena, L. Liu, and H. G. Xing, "Extraordinary Control of Terahertz Beam Reflectance in Graphene Electro-absorption Modulators," *Nano Lett.*, vol. 12, pp. 4518–4522, 2012.

[113] S. Busch, B. Scherger, M. Scheller, and M. Koch, "Optically controlled terahertz beam steering and imaging," *Opt. Lett.*, vol. 37, pp. 1391–1393, 2012.

[114] A. Hirata, M. Harada, and T. Nagatsuma, "120-GHz Wireless Link Using Photonic Techniques for Generation, Modulation, and Emission of Millimeter-Wave Signals," *J. Lightwave Technol.*, vol. 21, pp. 2145–2153, 2003.

[115] A. Hirata, T. Kosugi, H. Takahashi, R. Yamaguchi, F. Nakajima, T. Furuta, H. Ito, H. Sugahara, Y. Sato, and T. Nagatsuma, "120-GHz-Band Millimeter-Wave Photonic Wireless Link for 10-Gb/s Data Transmission," *IEEE Trans. Microw. Theory Tech.*, vol. 54, pp. 1937–1944, 2006.

[116] H.-M. Chen, J. Su, J.-L. Wang, and X.-Y. Zhao, "Optically-controlled high-speed terahertz wave modulator based on nonlinear photonic crystals," *Opt. Express*, vol. 19, pp. 3599–3603, 2011.

[117] J.-S. Li, "A novel ultrafast terahertz wave modulator based on nonlinear medium," *Opt. Commun.*, vol. 296, pp. 137–140, 2013.

[118] Z. Ghattan, T. Hasek, R. Wilk, M. Shahabadi and M. Koch, "Sub-terahertz on-off switch based on a two-dimensional photonic crystal infiltrated by liquid crystals," *Opt. Commun.*, vol. 281, pp. 4623–4625, 2008.

[119] R. Wilk, N. Vieweg, O. Kopschinski, and M. Koch, "Liquid crystal based electrically switchable Bragg structure for THz waves," *Opt. Express*, vol. 17, pp. 7377–7382, 2009.

[120] R. Kowerdzieja, M. Olifierczuka, B, Salskib, and J. Parka, "Tunable negative index metamaterial employing in-plane switching mode at terahertz frequencies," *Liq. Cryst.*, vol. 39, pp. 827–831, 2012.

[121] D. Shrekenhamer, W.-C. Chen, and W. J. Padilla, "Liquid Crystal Tunable Metamaterial Absorber," *Phys. Rev. Lett.*, vol. 110, p. 177403, 2013.

[122] H.-T. Chen, S. Palit, T. Tyler, C. M. Bingham, J. M. O. Zide, J. F. O'Hara, D. R. Smith, A. C. Gossard, R. D. Averitt, W. J. Padilla, N. M. Jokerst, and A. J. Taylor, "Hybrid metamaterials enable fast electrical modulation of freely propagating terahertz waves," *Appl. Phys. Lett.*, vol. 93, p. 091117, 2008.

[123] H. Chen, J. F. O'Hara, A. K. Azad, A. J. Taylor, R. D. Averitt, D. B. Shrekenhamer, and W. J. Padilla, "Experimental demonstration of frequency-agile terahertz metamaterials," *Nature Photon.*, vol. 2, p. 295, 2008.

[124] N.-H. Shen, M. Kafesaki, T. Koschny, L. Zhang, E. N. Economou, and C. M. Soukoulis, "Broadband blueshift tunable metamaterials and dual-band switches," *Phys. Rev. B*, vol. 79, p. 161102, 2009.

[125] H.-T. Chen, W. J. Padilla, M. J. Cich, A. K. Azad, R. D. Averitt, and A. J. Taylor, "A metamaterial solid-state terahertz phase modulator," *Nature Photon.*, vol. 3, pp. 148–151, 2009.

[126] W. L. Chan, H.-T. Chen, A. J. Taylor, I. Brener, M. J. Cich, and D. M. Mittleman, "A spatial light modulator for terahertz beams," *Appl. Phys. Lett.*, vol. 94, p. 213511, 2009.

[127] N. Kanda, K. Konishi, and M. Kuwata-Gonokami, "Light-induced terahertz optical activity," *Opt. Lett.*, vol. 34, pp. 3000–3002, 2009.

[128] D. R. Chowdhury, R. Singh, J. F. O'Hara, H.-T. Chen, A. J. Taylor, and A. K. Azad, "Dynamically reconfigurable terahertz metamaterial through photo-doped semiconductor," *Appl. Phys. Lett.*, vol. 99, p. 231101, 2011.

[129] D. Shrekenhamer, S. Rout, A. C. Strikwerda, C. Bingham, R. D. Averitt, S. Sonkusale, and W. J. Padilla, "High speed terahertz modulation from metamaterials with embedded high electron mobility transistors," *Opt. Express*, vol. 19, p. 9968, 2011.

[130] J. Shu, C. Qiu, V. Astley, D. Nickel, D. M. Mittleman, and Q. Xu, "High-contrast terahertz modulator based on extraordinary transmission through a ring aperture," *Opt. Express*, vol. 19, p. 26666, 2011.

[131] Y. Y. Urzhumov, J. S. Lee, T. Tyler, S. Dhar, V. Nguyen, N. M. Jokerst, P. Schmalenberg, and D. R. Smith, "Electronically reconfigurable metal-on-silicon metamaterial," *Phys. Rev. B*, vol. 86, p. 075112, 2012.

[132] S. H. Lee, M. Choi, T.-T. Kim, S. Lee, M. Liu, X. Yin, H. K. Choi, S. S. Lee, C.-Gi Choi, S.-Y. Choi, X. Zhang, and Bumki Min, "Switching terahertz waves with gate-controlled active graphene metamaterials," *Nature Mater.*, vol. 11, pp. 936–941, 2012.

[133] J. Zhou, D. Roy Chowdhury, R. Zhao, A. K. Azad, H.-T. Chen, C. M. Soukoulis, A. J. Taylor, and J. F. O'Hara, "Terahertz chiral metamaterials with giant and dynamically tunable optical activity," *Phys. Rev. B*, vol. 86, p. 035448, 2012.

[134] G. Scalari, C. Maissen, D. Turčinková, D. Hagenmüller, S. De Liberato, C. Ciuti, C. Reichl, D. Schuh, W. Wegscheider, M. Beck, and J. Faist, "Ultrastrong Coupling of the Cyclotron Transition of a 2D Electron Gas to a THz Metamaterial," *Science*, vol. 335, pp. 1323–1326, 2012.

[135] H. Tao, A. C. Strikwerda, K. Fan, W. J. Padilla, X. Zhang, and R. D. Averitt, "MEMS Based Structurally Tunable Metamaterials at Terahertz Frequencies," *J. Infrared Milli. Terahz. Waves*, vol. 32, pp. 580–595, 2011.

[136] W. M. Zhu, A. Q. Liu, T. Bourouina, D. P. Tsai, J. H. Teng, X. H. Zhang, G. Q. Lo, D. L. Kwong, and N. I. Zheludev, "Microelectromechanical Maltese-cross metamaterial with tunable terahertz anisotropy," *Nat. Commun.*, vol. 3, p. 1274, 2012.

[137] J. Li, C. M. Shah, W. Withayachumnankul, B. S.-Y. Ung, A. Mitchell, S. Sriram, M. Bhaskaran, S. Chang, and D. Abbott, "Mechanically tunable terahertz metamaterials," *Appl. Phys. Lett.*, vol. 102, p. 121101, 2013.

[138] W. Zhang, W. M. Zhu, H. Cai, M.-L.J Tsai, G.-Q. Lo, D. P. Tsai, H. Tanoto, J.-H. Teng, X.-H. Zhang, D.-L. Kwong, and A.-Q. Liu, "Resonance Switchable Metamaterials Using MEMS Fabrications," *IEEE J. Sel. Top. Quant. Electron.*, vol. 19, p. 4700306, 2013.

[139] G. W. Webb, "Low-temperature electrical resistivity of pure niobiulm," *Phys. Rev.*, vol. 181, pp. 1127–1135, 1969.

[140] D. A. Neeper and J. R. Dillinger, "Thermal resistance at indium-sapphire boundaries between 1.1 and 2.1°K," *Phys. Rev.*, vol. 135, pp. A1028–A1033, 1964.

[141] D. Janjušević, M. S. Grbić, M, Požek, A. Dulčić, D. Paar, B. Nebendahl, and T. Wagner, "Microwave response of thin niobium films under perpendicular static magnetic fields," *Phys. Rev. B*, vol. 74, p. 104501, 2006.

[142] D. K. Finnemore, T. F. Stromberg, and C. A. Swenson, "Superconducting properties of high-purity niobium," *Phys. Rev.*, vol. 149, pp. 231–243, 1966.

[143] R. P. Huebener, R. T. Kampwirth, R. L. Martin, T. W. Barbee Jr., and R. B. Zubeek, "Critical current density in superconducting niobium films," *J. Low Temp. Phys.*, vol. 19, pp. 247–258, 1975.

[144] A. P. Zhuravel, C. Kurter, A. V. Ustinov, and S. M. Anlage, "Unconventional rf photoresponse from a superconducting spiral resonator," *Phys. Rev. B*, vol. 85, p. 134535, 2012.

[145] K. E. Gray, R. T. Kampwirth, J. F. Zasadzinski, and S. P. Ducharme, "Thermal propagation and stability in superconducting films," *J. Phys. F: Met. Phys.*, vol. 13, pp. 405–430, 1983.

[146] F. Nitsche and B. Schumann, "Heat transfer between sapphire and lead," *J. Low Temp. Phys.*, vol. 39, pp. 119–130, 1979.

[147] J. T. Gittleman and S. Bozowski, "Switching times of the current-induced, superconducting-to-normal transition in filaments of tin and indium," *Phys. Rev.*, vol. 135, pp. A297–A299, 1964.

[148] F. B. Hagedron, "Silsbee-limit critical currents in a 1700å film of tim," *Phys. Rev. Lett.*, vol. 12, pp. 322–324, 1964.

[149] B. S. Karasik, M. A. Zorin, I. I. Milostnaya, A. I. Elantev, G. N. Gol'tsman, and E. M. Gershenzon, "Subnanosecond switching of YBaCuO films between superconducting and normal states induced by current pulse," *J. Appl. Phys.*, vol. 77, pp. 4064–4070, 1995.

[150] H.-T. Chen, H. Yang, R. Singh, J. F. O'Hara, A. K. Azad, S. A. Trugman, Q. X. Jia, and A. J. Taylor, "Tuning the resonance in high-temperature superconducting terahertz metamaterials," *Phys. Rev. Lett.*, vol. 105, p. 247402, 2010.

[151] J. Gu, R. Singh, Z. Tian, W. Cao, Q. Xing, M. He, J. W. Zhang, J. Han, H.-T. Chen, and W. Zhang, "Terahertz superconductor metamaterial," *Appl. Phys. Lett.*, vol. 97, p. 071102, 2010.

[152] H.-T. Chen, J. F. O'Hara, A. K. Azad, A. J. Taylor, R. D. Averitt, D. B. Shrekenhamer, and W. J. Padilla, "Experimental demonstration of frequency-agile terahertz metamaterials," *Nature Photon.*, vol. 2, pp. 295–298, 2008.

[153] O. Paul, C. Imhof, B. Lägel, S. Wolff, J. Heinrich, S. Höfling, A. Forchel, R. Zengerle, R. Beigang, and M. Rahm, "Polarization-independent active metamaterial for high-frequency terahertz modulation," *Opt. Express*, vol. 17, p. 819, 2009.

[154] D. Shrekenhamer, S. Rout, A. C. Strikwerda, C. Bingham, R. D. Averitt, S. Sonkusale, and W. J. Padilla, "High speed terahertz modulation from metamaterials with embedded high electron mobility transistors," *Opt. Express*, vol. 19, pp. 9968–9975, 2011.

[155] G. Grimaldia, A. Leoa, A. Nigroa, S. Pacea, C. Cirilloa, and C. Attanasioa, "Thickness dependence of vortex critical velocity in wide Nb films," *Physica C*, vol. 468, pp. 765–768, 2008.

[156] P. Horowitz, *The Art of Electronics*, 2nd ed. Cambridge Univesity Press, 1989.

[157] M. Moskovits, "Surface-enhanced spectrocopy," *Rev. Mod. Phys.*, vol. 57, pp. 783–826, 1985.

[158] D. Cotter, R. J. Manning, K. J. Blow, A. D. Ellis, A. E. Kelly, D. Nesset, I. D. Phillips, A. J. Poustie, and D. C. Rogers, "Nonlinear optics for high-speed digital information processing," *Science*, vol. 286, pp. 1523–1528, 1999.

[159] J. Hebling, G. Almási, and I. Z. Kozma, "Velocity matching by pulse front tilting for large area THz-pulse generation," *Opt. Express*, vol. 10, pp. 1161–1166, 2002.

[160] A. Stepanov, J. Kuhl, I. Kozma, E. Riedle , G. Almási and J. Hebling, "Scaling up the energy of THz pulses created by optical rectification," *Opt. Express*, vol. 13, p. 57625768, 2005.

[161] K.-L. Yeh, M. C. Hoffmann, J. Hebling, and K. A. Nelson, "Generation of 10 μJ ultrashort terahertz pulses by optical rectification," *Appl. Phys. Lett.*, vol. 90, p. 171121, 2007.

[162] H. Hirori, A. Doi, F. Blanchard, and K. Tanaka, "Single-cycle terahertz pulses with amplitudes exceeding 1 MV/cm generated by optical rectification in $LiNbO_3$," *Appl. Phys. Lett.*, vol. 98, p. 091106, 2011.

[163] J. Hebling , K.-L. Yeh , M. C. Hoffmann , B. Bartal, and K. A. Nelson, "Generation of high-power terahertz pulses by tilted-pulse-front excitation and their application possibilities," *J. Opt. Soc. Am. B*, vol. 25, pp. B6–B19, 2008.

[164] K. Tanaka, H. Hirori, and M. Nagai, "THz nonlinear spectroscopy of solids," *IEEE Trans. Terahertz Sci. Technol.*, vol. 1, pp. 301–312, 2011.

[165] M. Liu, H. Y. Hwang, H. Tao, A. C. Strikwerda, K. Fan, G. R. Keiser, A. J. Sternbach, K. G. West, S. Kittiwatanakul, J. Lu, S. A. Wolf, F. G. Omenetto, X. Zhang, K. A. Nelson, and R. D. Averitt, "Terahertz-field-induced insulator-to-metal transition in vanadium dioxide metamaterial," *Nature*, vol. 487, pp. 345–348, 2012.

[166] K. Fan, H. Y. Hwang, M. Liu, A. C. Strikwerda, A. Sternbach, J. Zhang, X. Zhao, X. Zhang, K. A. Nelson, and R. D. Averitt, "Nonlinear Terahertz Metamaterials via Field-Enhanced Carrier Dynamics in GaAs," *Phys. Rev. Lett.*, vol. 110, p. 217404, 2013.

[167] C. Kurter, A. P. Zhuravel, A. V. Ustinov, and S. M. Anlage, "Microscopic examination of hot spots giving rise to nonlinearity in superconducting resonators," *Phys. Rev. B*, vol. 84, p. 104515, 2011.

[168] C. Zhang, B. Jin, J. Han, I. Kawayama, H. Murakami, J. Wu, L. Kang, J. Chen, P. Wu, and M. Tonouchi, "Terahertz nonlinear superconducting metamaterials," *Appl. Phys. Lett.*, vol. 102, p. 081121, 2013.

[169] C. Zhang, B. Jin, J. Han, I. Kawayama, H. Murakami, X. Jia, L. Liang, L. Kang, J. Chen, P. Wu, and M. Tonouchi, "Nonlinear response of superconducting NbN thin film and NbN metamaterial induced by intense terahertz pulses," *New J. Phys.*, vol. 15, p. 055017, 2013.

[170] Y. Asada and H. Nosé, "Superconductivity of niobium films," *J. Phys. Soc. Jpn.*, vol. 26, pp. 347–354, 1969.

[171] M. S. M. Minhaj, S. Meepagala, J. T. Chen, and L. E. Wenger, "Thickness dependence on the superconducting properties of thin Nb films," *Phys. Rev. B*, vol. 49, pp. 15 235–15 240, 1994.

[172] M. C. Ricci, H. Xu, R. Prozorov, A. P. Zhuravel, A. V. Ustinov, and S. M. Anlage, "Tunability of superconducting metamaterials," *IEEE Trans. Appl. Supercond.*, vol. 17, p. 918, 2007.

[173] C. Kurter, P. Tassin, A. P. Zhuravel, L. Zhang, T. Koschny, A.V. Ustinov, C.M. Soukoulis, and S. M. Anlage, "Switching nonlinearity in a superconductor-enhanced metamaterial," *Appl. Phys. Lett.*, vol. 100, p. 121906, 2012.

[174] J. D. Jackson, *Classical Electrodynamics*. Wiley, New York ed. 3, 1999.

[175] V. M. Dubovik and A. A. Cheshkov, "Multipole expansion in classical and quantum field theory and radiation," *Sov. J. Part. Nucl.*, vol. 5, p. 318, 1975.

[176] E. E. Radescu and G. Vaman, "Exact calculation of the angular momentum loss, recoil force, and radiation intensity for an arbitrary source in terms of electric, magnetic, and toroid multipoles," *Phys. Rev. E*, vol. 65, p. 046609, 2002.

[177] T. A. Gongora and E. Ley-Koo, "Complete electromagnetic multipole expansion including toroidal moments," *Rev. Mex. Fis. E*, vol. 65, p. 188, 2002.

[178] Ia. B. Zel'dovich, "Electromagnetic interaction with parity violation," *Sov. Phys. JETP*, vol. 33, p. 1531, 1957.

[179] C. S. Wood, S. C. Bennett, D. Cho, B. P. Masterson, J. L. Roberts, C. E. Tanner, and C. E. Wieman, "Measurement of Parity Nonconservation and an Anapole Moment in Cseium," *Science*, vol. 275, p. 1759, 1997.

[180] W. C. Haxton and C. E. Wieman, "Atomic parity nonconservation and nuclear anapole moments," *Annu. Rev. Nucl. Part. Sci.*, vol. 51, pp. 261–293, 2001.

[181] J. S. M. Ginges and V. V. Flambaum, "Violations of fundamental symmetries in atoms and tests of unification theories of elementary particles," *Phys. Rep.*, vol. 397, pp. 63–154, 2004.

[182] G. N. Afanasiev, "Simplest sources of electromagnetic fields as a tool for testing the reciprocity-like theorems," *J. Phys. D: Appl. Phys.*, vol. 34, p. 539, 2001.

[183] G. N. Afanasiev and Yu. P. Stepanovsky, "The electromagnetic field of elementary time-dependent toroidal sources," *J. Appl. Phys. A*, vol. 28, p. 4565, 1995.

[184] E. A. Marengo and R. W. Ziolkowski, "Nonradiating sources, the Aharonov-Bohm effect, and the question of measurability of electromagnetic potentials," *Radio Sci.*, vol. 37, p. 19, 2002.

[185] L. D. Landau and E. M. Lifschitz, *The Classical Theory of Fields*, 4th ed. New York: Pergamon Press, 1975.

[186] V. A. Fedotov, A. V. Rogacheva, V. Savinov, D. P. Tsai, and N. I. Zheludev, "Non-Trivial Non-Radiating Excitation as a Mechanism of Resonant Transparency in Toroidal Metamaterials," *arXiv:1211.3840v1*, vol. , p. , 2012.

[187] Y. Fan, Z. Wei, H. Li, H. Chen, and C. M. Soukoulis, "Low-loss and high-Q planar metamaterial with toroidal moment," *Phys. Rev. B*, vol. 87, p. 115417, 2013.

[188] Z.-G. Dong, P. Ni, J. Zhu, and X. Zhang, "Toroidal dipole response in a multifold double-ring metamaterial," *Opt. Express*, vol. 20, p. 13065, 2012.

[189] B. Q̈güt, N. Talebi, R. Vogelgesang, W. Sigle, and P. A. van Aken, "Toroidal plamonic eigenmodes in oligomer nanocavities for the visible," *Nano Lett.*, vol. 12, pp. 5239–5244, 2012.

[190] Y.-W. Huang, W. T. Chen, P. C. Wu, V. Fedotov, V. Savinov, Y. Z. Ho, Y.-F. Chau, N. I. Zheludev, and D. P. Tsai, "Design of plasmonic toroidal metamaterials at optical frequencies," *Opt. Express*, vol. 20, p. 1760, 2012.

[191] Z.-G. Dong, J. Zhu, J. Rho, J.-Q. Li, C. Lu, X. Yin, and X. Zhang, "Optical toroidal dipolar response by an asymmetric double-bar metamaterial," *Appl. Phys. Lett.*, vol. 101, p. 144105, 2012.

[192] Y.-W. Huang, W. T. Chen, P. C. Wu, V. A. Fedotov, N. I. Zheludev, and D. P. Tsai, "Toroidal lasing spaser," *Sci. Rep.*, vol. 3, p. 1237, 2013.

[193] S. A. Maier and H. A. Atwater, "Plasmonics: Localization and guiding of electromagnetic energy in metal/dielectric structures," *J. Appl. Phys.*, vol. 98, p. 011101, 2005.

[194] K. A. Willets and R. P. Van Duyne, "Localized Surface Plasmon Resonance Spectroscopy and Sensing," *Annu. Rev. Phys. Chem.*, vol. 58, pp. 267–297, 2007.

[195] S. Lal, S. Link, and N. J. Halas, "Nano-optics from sensing to waveguiding," *Nature Photon.*, vol. 1, pp. 641–648, 2007.

[196] M. A. Noginov, G. Zhu, A. M. Belgrave, R. Bakker, V. M. Shalaev, E. E. Narimanov, S. Stout, E. Herz, T. Suteewong, and U. Wiesner, "Demonstration of a spaser-based nanolaser," *Nature*, vol. 460, pp. 1110–1113, 2009.

[197] H. Wang, E. C. Y. Yan, E. Borguet, and K. B. Eisenthal, "Second harmonic generation from the surface of centrosymmetric particles in bulk solution," *Chem. Phys. Lett.*, vol. 259, p. 15, 1996.

[198] J. Shan, J. I. Dadap, I. Stiopkin, G. A. Reider, and T. F. Heinz, "Experimental study of optical second-harmonic scattering from spherical nanoparticles," *Phys. Rev. A*, vol. 73, p. 023819, 2006.

[199] B. K. Canfield, S. Kujala, H. Husu, M. Kauranen, B. Bai, J. Laukkanen, M. Kuittinen, Y. Svirko, and J. Turunen, "Local-field and multipolar effects in the second-harmonic response of arrays of metal nanoparticles," *J. Nonlin. Opt. Phys. Mater.*, vol. 16, p. 317, 2007.

[200] S. Kujala, B. K. Canfield, M. Kauranen, Y. Svirko, and J. Turunen, "Multipolar analysis of second-harmonic radiation from gold nanoparticles," *Opt. Express*, vol. 16, p. 17196, 2008.

[201] M. Zdanowicz, S. Kujala, H. Husu, and M. Kauranen, "Effective medium multipolar tensor analysis of second-harmonic generation from metal nanoparticles," *New J. Phys.*, vol. 13, p. 023025, 2011.

[202] M. Ren, B. Jia, J.-Y. Ou, E. Plum, J. Zhang, K. F. MacDonald, A. E. Nikolaenko, J. Xu, M. Gu, and N. I. Zheludev , "Nanostructured plasmonic medium for terahertz bandwidth all-optical switching," *Adv. Mater.*, vol. 23, p. 5540, 2011.

[203] N. Engheta, W. D. Murphy, V. Rokhlin, and M. S. Vassiliou, "The Fast Multipole Method (FMM) for electromagnetic scattering problems," *IEEE Trans. Antennas Propag.*, vol. 40, pp. 634–641, 1992.

[204] R. Coifman, V. Rokhlin, and S. Wandzura, "The Fast Multipole Method for the wave equation: a pedestrian prescription," *IEEE Antennas Propag. Mag.*, vol. 35, pp. 7–12, 1993.

[205] C. C. Lu and W. C. Chew, "Fast algorithm for solving hybrid integral equations [EM wave scattering]," *IEE Proc. H, Microw. Antennas Propag.*, vol. 140, pp. 455–460, 1993.

[206] C. Craeye, "A fast Impedance and pattern computation scheme for finite antenna arrays," *IEEE Trans. Antennas Propag.*, vol. 54, pp. 3030–3034, 2006.

[207] W. B. Lu and T. J. Cui, "Efficient method for full-wave analysis of large-scale finite-sized periodic structures," *J. of Electromagn. Waves and Appl.*, vol. 21, pp. 2157–2168, 2007.

[208] R. M. Shubair, and Y. L. Chow, "Efficient Compuation of the periodic Green's Function in layered dielectric media," *IEEE Trans. Microw. Theory Techn.*, vol. 41, p. 498, 1993.

[209] A. L. Fructos, R. R. Boix, F. Mesa, and F. Medina, "An efficient approach for the computation of 2-D Green's Functions with 1-D and 2-D periodicities in homogeneous media," *IEEE Trans. Antennas Propag.*, vol. 56, pp. 3733–3742, 2008.

[210] G. Valerio, P. Baccarelli, P. Burghignoli, and A. Galli, "Comparative analysis of acceleration techniques for 2-D and 3-D Green's Functions in periodic structures along one and two directions," *IEEE Trans. Antennas Propag.*, vol. 55, p. 1630, 2007.

[211] V. Savinov, V. A. Fedotov, and N. I. Zheludev, "Macroscopic electromagnetic response of metamaterials with toroidal resonances," *arXiv:1310.0106v1*, 2013.

[212] M. M. I. Saadoun and N. Engheta, "Theoretical study of electromagnetic properties of non-local Ω media," *PIER*, vol. 9, pp. 351–397, 1994.

[213] A. J. Bahr and K. R. Clausig, "An approximate model for artificial chiral material," *IEEE Trans. Antennas Propag.*, vol. 42, pp. 1592–1599, 1994.

[214] J. B. Pendry, A. J. Holden, D. J. Robbins, and W. J. Stewart, "Magnetism from conductors and enhanced nonlinear phenomena," *IEEE Trans. Microw. Theory Techn.*, vol. 47, pp. 2075–2084, 1999.

[215] C. Rockstuhl, T. Zentgraf, E. Pshenay-Severin, J. Petschulat, A. Chipouline, J. Kuhl, T. Pertsch, H. Giessen, and Falk Lederer , "The origin of magnetic polarizability in metamaterials at optical frequencies - an electrodynamic approach," *Opt. Express*, vol. 15, pp. 8871–8883, 2007.

[216] J. C.-E. Sten and D. Sjöberg, "Low-frequency scattering analysis and homogentization of split-ring elements," *PIER B*, vol. 35, pp. 187–212, 2011.

[217] A. I. Akhiezer and V. B. Berestetskii, *Quantum Electrodynamics*, 2nd ed. New York: Interscience Publishers, 1965.

[218] G. B. Arfken and H. J. Weber, *Mathematical Methods for Physicists*, 5th ed. Harcourt/Academic Press, 2001.

[219] D. B. Burckel , J. R. Wendt, G. A. Ten Eyck, A. R. Ellis, I. Brener, and M. B. Sinclair, "Fabrication of 3D metamaterial resonators using self-aligned membrane projection lithography," *Adv. Mater.*, vol. 22, p. 3171, 2010.

[220] D. B. Bruckel, J. R. Wendt, G. A. Ten Eyck, J. C. Ginn, A. R. Ellis, I. Brenner, and M. B. Sinclair, "Micrometer-Scale Cubic Unit Cell 3D Metmaterial Layers," *Adv. Mater.*, vol. 22, p. 5053, 2010.

[221] G. Müller, N. Klein, A. Brust, H. Chaloupka, and M. Hein, "Survey of microwave surface impedance data of High-$T_c$superconductors - evidence for non-pairing charge carriers," *J. Supercond.*, vol. 3, pp. 235–242, 1990.

[222] Y. Akahane, T. Asano, B.-S. Song, and S. Noda, "High-Q photonic nanocavity in a two-dimensional photonic crystal," *Nature*, vol. 425, pp. 944–947, 2003.

[223] F. Xia, L. Sekaric, Y. Vlasov, "Ultracompact optical buffers on a silicon chip," *Nature Photon.*, vol. 1, pp. 65–71, 2007.

[224] Y. Aharonov and D. Bohm, "Significance of electromagnetic potentials in the quantum theory," *Phys. Rev.*, vol. 115, pp. 485–491, 1959.

[225] A. Tonomura, N. Osakabe, T. Matsuda, T. Kawasaki, J. Endo, S. Yano, and H. Yamada , "Evidence for Aharonov-Bohm effect with magnetic field completely shielded from electron wave," *Phys. Rev. Lett.*, vol. 56, pp. 792–795, 1986.

[226] V. A. Fedotov, A. V. Rogacheva, V. Savinov, D. P. Tsai, and N. I. Zheludev, "Resonant transparency and non-trivial non-radiating excitations in toroidal metamaterials," *Sci. Rep.*, vol. 3, p. 2967, 2013.

[227] A. D. Broadman, K. Marinov, N. I. Zheludev, and V. A. Fedotov, "Disperion properties of nonradiating configurations: Finite-difference time-domain modelling," *Phys. Rev. E*, vol. 72, p. 036603, 2005.

[228] G. N. Afanasiev and V. M. Dubovik, "Some remarkable charge-current configurations," *Phys. Part. Nucl.*, vol. 29, pp. 366–391, 1998.

[229] S. Zaric, G. N. Ostojic, J. Kono, J. Shaver, V. C. Moore, M. S. Strano, R. H. Hauge, R. E. Smalley, and X. Wei, "Optical signatures of the Aharonov-Bohm phase in single-walled carbon nanotubes," *Science*, vol. 304, pp. 1129–1131, 2004.

[230] A. Tonomura and F. Nori, "Quantum physics: Disturbance without the force," *Nature*, vol. 452, pp. 298–299, 2008.

[231] H. Batelann and A. Tonomura, "The Aharonov - Bohm effects: Variations on a subtle theme," *Phys. Today*, vol. 62, p. 38, 2009.

[232] B. Lee, E. Yin, T. K. Gustafson, and R. Chiao, "Analysis of Aharonov-Bohm effect due to time-dependent vector potentials," *Phys. Rev. A*, vol. 45, pp. 4319–4325, 1992.

[233] L. Novotny and N. van Hulst, "Antennas for light," *Nature Photon.*, vol. 5, p. 83, 2011.

[234] B. S. Deaver Jr. and W. M. Fairbank , "Experimental Evidence for Quantized Flux in Superconducting Cylinders," *Phys. Rev. Lett.*, vol. 7, p. 43, 1961.

[235] R. Doll and M. Näbauer , "Experimental Proof of Magnetic Flux Quantization in a Superconducting Ring," *Phys. Rev. Lett.*, vol. 7, p. 51, 1961.

[236] R. Kleiner, D. Koelle, F. Ludwig, and J. Clarke, "Superconducting quantum interference devices: state of the art and applications," *Proc. IEEE*, vol. 92, pp. 1534–1548, 2004.

[237] A. M. Zagoskin, "Superconducting quantum metamaterials in 3D: possible realizations," *J. Opt.*, vol. 14, p. 114011, 2012.

[238] C. Du, H. Chen, and S. Li, "Quantum left-handed metamaterial from superconducting quantum-interference devices," *Phys. Rev. B*, vol. 74, p. 113105, 2006.

[239] N. Lazarides and G. P. Tsironis, "RF superconducting quantum interference device metamaterials," *Appl. Phys. Lett.*, vol. 90, p. 163501, 2007.

[240] M. A. Castellanos-Beltran, K. D. Irwin, G. C. Hilton, L. R. Vale, and K. W. Lehnert, "Amplification and squeezing of quantum noise with a tunable Josephson metamaterial," *Nautre Phys.*, vol. 4, p. 928, 2008.

[241] A. L. Rakhmanov, A. M. Zagoskin, S. Savel'ev, and F. Nori, "Quantum metamaterials: Electromagnetic waves in a Josephson qubit line," *Phys. Rev. B*, vol. 77, p. 144507, 2008.

[242] P. D. Nation, M. P. Blencowe, A. J. Rimberg, and E. Buks, "Analogue Hawking radiation in a dc-SQUID array transmission line," *Phys. Rev. Lett.*, vol. 103, p. 087004, 2009.

[243] O. Astafiev, A. M. Zagoskin, A. A. Abdumalikov Jr., Yu. A. Pashkin, T. Yamamoto, K. Inomata, Y. Nakamura, and J. S. Tsai, "Resonance Fluorescence of a Single Artificial Atom," *Science*, vol. 327, p. 840, 2010.

[244] A. A. Abdumalikov, Jr., O. Astafiev, A. M. Zagoskin, Yu.A. Pashkin, Y. Nakamura, and J. S. Tsai, "Electromagnetically Induced Transparency on a Single Artificial Atom," *Phys. Rev. Lett.*, vol. 104, p. 193601, 2010.

[245] A. I. Maimistov and I. R. Gabitov, "Nonlinear response of a thin metamaterial film containing Josephson Junctions," *Opt. Commun.*, vol. 283, p. 1633, 2010.

[246] C. Hutter, E. A. Tholén, K. Stannigel, J. Lidmar, and D. B. Haviland, "Josephson junction transmission lines as tunable artificial crystals," *Phys. Rev. B*, vol. 83, p. 014511, 2011.

[247] D. Zueco, J. J. Mazo, E. Solano, and J. J. García-Ripoll, "Microwave photonics with Josephson junction arrays: Negative refraction index and entanglement through disorder," *Phys. Rev. B*, vol. 86, p. 024503, 2012.

[248] P. Lähteenmäki, G. S. Paraoanu, J. Hassel, and P. J. Hakonen, "Dynamical Casimir effect in a Josephson metamaterial," *Proc. Natl. Acad. Sci. USA*, vol. 110, pp. 4234–4238, 2013.

[249] S. I. Mukhin and M. V. Fistul, "Generation of non-classical photon states in superconducting quantum metamaterials," *Supercond. Sci. Technol.*, vol. 26, p. 084003, 2013.

[250] V. Savinov, A. Tsiatmas, A. R. Buckingham, V. A. Fedotov, P. A. J. de Groot, and N. I. Zheludev, "Flux exclusion superconducting quantum metamaterial: Towards quantum-level switching," *Sci. Rep.*, vol. 2, p. 450, 2012.

[251] R. P. Huebener, *Magnetic Flux Structures in Superconductors.* Berlin Heidelberg New York: Springer-Verlag, 1979.

[252] L. E. Reichl, *A Modern Course in Statistical Physics*, 2nd ed. John Wiley & Sons, 1998.

[253] A. H. Silver and J. E. Zimmerman, "Quantum states and transitions in weakly connected superconducting rings," *Phys. Rev.*, vol. 157, pp. 317–341, 1967.

[254] S. G. Doettinger, R. P. Huebener, R. Gerdemann, A. Kühle, S. Anders, T. G. Träuble, and J. C. Villégier, "Electronic instability at high flux-flow velocities in high-T_c, superconducting films," *Phys. Rev. Lett.*, vol. 73, p. 1691, 1994.

[255] F. S. Jelila, J-P Maneval, F-R Ladan, F. Chibane, A. Marie-de-Ficquelmont, L. Méchin, J-C Villégier, and M. Aprili, J. Lesueur, "Time of Nucleation of Phase-Slip Centers in $YBa_2Cu_3O_7$ Superconducting Bridges," *Phys. Rev. Lett.*, vol. 81, p. 1933, 1998.

[256] G. Sabouret, C. Williams, and R. Sobolewski, "Resistive switching dynamics in current-biased $YBa_2Cu_3O_{7-x}$ microbridges excited by nanosecond electrical pulses," *Phys. Rev. B*, vol. 66, p. 132501, 2002.

[257] S. Pedersen, G. R. Kofod, J. C. Hollingbery, C. B. Sørensen, and P. E. Lindelof, "Dilation of the giant vortex state in a mesoscopic superconducting loop," *Phys. Rev. B*, vol. 64, p. 104522, 2001.

[258] D. Y. Vodolazov, F. M. Peeters, S. V. Dubonos, and A. K. Geim, "Multiple flux jumps and irreversible behavior of thin Al superconducting rings," *Phys. Rev. B*, vol. 67, p. 054506, 2003.

[259] K. E. Gray, Ed., *Nonequilibrium superconductivity, phonons, and Kapitza boundaries*, ser. NATO ASI Series. New York: Plenum, 1981.

[260] A. Glossner, C. Zhang, S. Kikuta, I. Kawayama, H. Murakami, P. Müller, and M. Tonouchi, "Cooper pair breakup in $YBa_2Cu_3O_{7-\delta}$ under strong terahertz fields," *arXiv:1205.1684v1*, 2012.

[261] R. D. Averitt, G. Rodriguez, A. I. Lobad, J. L. W. Siders, S. A. Trugman, and A. J. Taylor, "Nonequilibrium superconductivity and quasiparticle dynamics in $YBa_2Cu_3O_{7-\delta}$," *Phys. Rev. B*, vol. 63, p. 140502, 2001.

[262] M. Johnson, "Direct real time measurement of quasiparticle lifetimes in a superconductor," *Phys. Rev. Lett.*, vol. 67, pp. 374–377, 1991.

[263] A. Tsiatmas, V. A. Fedotov, F. J. G. de Abajo, and N. I. Zheludev, "Low-loss terahertz superconducting plasmonics," *New. J. Phys.*, vol. 14, p. 115006, 2012.

[264] M. T. González, J. Viña, S. R. Currás, J. A. Veira, J. Maza, and F. Vidal, "Normal-superconducting transition induced by high current densities in $YBa_2Cu_3O_{7-\delta}$ melt-textured samples and thin films: Similarities and differences," *Phys. Rev. B*, vol. 68, p. 054514, 2003.

[265] J. Gu, R. Singh, Z. Tian, W. Cao, Q. Xing, M. He, J. W. Zhang, J. Han, H.-T. Chen, and W. Zhang, "Terahertz superconductor metamaterial," *Appl. Phys. Lett.*, vol. 97, p. 071102, 2010.

[266] M. A. Jensen and J. W. Wallace, "A review of antennas and propagation for MIMO wireless communications," *IEEE Trans. Antennas Propag.*, vol. 52, pp. 2810–2824, 2004.

[267] *DSP Lock-In Amplifier, Model SR830 (Manual)*, 1.5 11/99 ed., Stanford Research Systems, 1999.

[268] L. Ghenim, J.-Y. Fortin, G. Wen, Z. Zhang, C. Baraduc, and J.-C. Villegier, "Transport and vortex pinning in micron-size superconducting Nb films," *Phys. Rev. B*, vol. 69, p. 064513, 2004.

[269] R. P. Huebener and R. T. Kampwirth, "Meissner shielding currents and magnetic flux penetration in thin-film superconductors," *J. Low Temp. Phys.*, vol. 6, pp. 275–285, 1972.

[270] C. Chou, D. White and H. L. Johnston, "Heat capacity in the normal and superconducting states and critical field of niobium," *Phys. Rev.*, vol. 109, pp. 788–796, 1958.

[271] S. Sahling, J. Engert, A. Galdun, and R. Knöner, "The thermal boundary resistance between sapphire and aluminium monocrystals at low temperature," *J. Low Temp. Phys.*, vol. 45, pp. 457–469, 1981.

[272] M. Abramowitz and I. A. Stegun, *Handbook of Mathematical Functions with Forumulas, Graphs, and Mathematical Tables*, 10th ed. Dover Publications, 1972.

[273] C. P. Frahm, "Some novel delta-function identities," *Am. J. Phys.*, vol. 51, pp. 826–828, 1983.